

DUAL-COMB SPECTROSCOPY OF LASER-PRODUCED PLASMAS

by

Reagan R. D. Weeks

---

Copyright © Reagan R. D. Weeks 2023

A Dissertation Submitted to the Faculty of the

WYANT COLLEGE OF OPTICAL SCIENCES

In Partial Fulfillment of the Requirements

For the Degree of

DOCTOR OF PHILOSOPHY

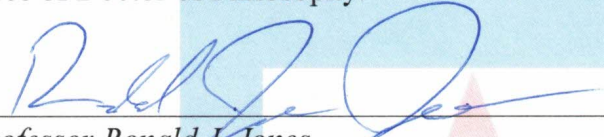
In the Graduate College

THE UNIVERSITY OF ARIZONA

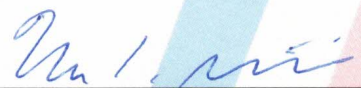
2023

THE UNIVERSITY OF ARIZONA  
GRADUATE COLLEGE

As members of the Dissertation Committee, we certify that we have read the dissertation prepared by **Reagan Robert Dewayne Weeks**, titled ***Dual-Comb Spectroscopy of Laser-Produced Plasmas*** and recommend that it be accepted as fulfilling the dissertation requirement for the Degree of Doctor of Philosophy.

  
\_\_\_\_\_  
Professor Ronald J. Jones Date: 4/12/2023

  
\_\_\_\_\_  
Professor Khanh Q. Kieu Date: 04/12/2023

  
\_\_\_\_\_  
Professor Mark Christopher Phillips Date: 04/12/23

  
\_\_\_\_\_  
Dr. Gregory Pitz Date: 4/12/2023

Final approval and acceptance of this dissertation is contingent upon the candidate's submission of the final copies of the dissertation to the Graduate College.

I hereby certify that I have read this dissertation prepared under my direction and recommend that it be accepted as fulfilling the dissertation requirement.

  
\_\_\_\_\_  
Professor Ronald J. Jones  
Dissertation Committee Chair  
Wyant College of Optical Sciences Date: 4/12/2023

## ACKNOWLEDGMENTS

I owe a debt of gratitude to the many people who helped me during my graduate studies, both in and out of the lab. Foremost is my advisor, Prof. Jason Jones, who graciously accepted me into his lab and trained me to be a well-rounded scientist. Only by trusting me with his fragile experiments did he teach me to be an experimentalist, and he invested nearly seven years in me only for me to graduate and leave once I became competent (as is an advisor's lot). I want to acknowledge the balancing act he had to constantly perform in guiding me while also letting me learn on my own so I could slowly become self-sufficient. Similarly, I am grateful to Prof. Mark Phillips, who was a second mentor. I appreciate his efforts to mold me into a thorough scientist, and I note that he particularly guided my work developing spectral models and codes, assisted me with manuscript writing, and was our resident expert on laser-produced plasmas. I appreciate both mentors allowing me to share in their ideas so I could gain the necessary experience to begin forming my own insights. My hope is that their investment in me will lead to fruitful collaborations in the future.

I thank my mentors at the Air Force Research Lab, Drs. Greg Pitz and Tony Hostutler, who trained me in the summers of my undergraduate years and provided me a place as a contractor in their labs before I began graduate school. It was during these times that I learned basic experimental lab skills, and I began my graduate work well prepared because of them. I appreciate their unwavering support while I was away in Tucson, as they have provided me with opportunities including the DoD SMART Scholarship that has supported me these past four years. I look forward to working alongside them in the coming years once I transition to AFRL as a full-time researcher.

There are many professors, both graduate and undergraduate, that I thank for their role in my development as a scientist. I particularly thank Prof. Hans Hallen, my undergraduate advisor, and Prof. Russell Philbrick, both of whom started me in optics and always

encouraged my efforts, despite my initial insecurity and awkwardness working in the lab.

My success in the PhD program is due in no small part to my colleagues in the lab. I worked with Dr. Caroline Lecaplain and Yu “Kane” Zhang in the first years of my studies, and together we developed many of the techniques that made dual-comb spectroscopic measurements on laser-produced plasmas successful. I am also deeply indebted to my graduate colleagues Ryan Rhoades and Seth Erickson for the many technical conversations as well as the many non-technical ones (perhaps too many in lab for Dr. Jones’s liking). I believe our collaboration benefited each of us, but I particularly asked a lot of questions and often received good answers. Perhaps more importantly, I learned the value of having affable colleagues who are there to share in the good and difficult times in the lab. Ryan and Seth were generous with their time and expertise, and my insights and ideas were usually inspired by them. They pushed me to become better a scientist and even a better person, and my recognition of this encourages me to strive to be such a colleague and friend to my future coworkers.

My friends, both in and out of school, have supported me and my studies, and I am thankful. I am particularly appreciative of my friend and former undergraduate colleague Brady Ells, who, by listening to my constant explanations and complaints of the lab, probably learned more about spectroscopy and plasmas than he ever wanted. I also appreciate the occasional technical assistance he provided on issues in MATLAB, LaTeX, and PowerPoint.

To my cat Pippin, I am thankful for the seemingly countless hours he spent by my side as I worked from home, often not receiving as much attention as he would have liked. He provided crucial moral support to me as he oversaw all my coding, data processing, and writing. These efforts have paid off, and I would credit his wonderful supervision.

Lastly, I am grateful to my family, all members having been my constant supporters, particularly in encouraging my schoolwork since I was young. I was fortunate to be raised in a home that valued learning and knowledge, as well as being taught to strive for and reflect on leading a virtuous and meaningful life. I am inspired by my parents, Ryan and Jamie, and my sisters, Devon and Savannah, all of whom have never lost the desire to learn. Thank you.



## LAND ACKNOWLEDGMENT

We respectfully acknowledge the University of Arizona is on the land and territories of Indigenous peoples. Today, Arizona is home to 22 federally recognized tribes, with Tucson being home to the O'odham and the Yaqui. Committed to diversity and inclusion, the University strives to build sustainable relationships with sovereign Native Nations and Indigenous communities through education offerings, partnerships, and community service.

## TABLE OF CONTENTS

|   |    |
|---|----|
| <b>LIST OF FIGURES</b> . . . . .  | 9  |
| <b>LIST OF TABLES</b> . . . . .   | 25 |
| <b>ABSTRACT</b> . . . . .   | 26 |
| <b>CHAPTER 1 Dual-Comb Spectroscopy of Laser-Produced Plasmas</b> . . . . | 27 |
| <b>1.1 Introduction</b> . . . . .   | 27 |
| <b>1.2 Spectroscopic Techniques for Studying LPPs</b> . . . . .           | 28 |
| <i>1.2.1 Laser-Induced Breakdown Spectroscopy</i> . . . . .               | 28 |
| <i>1.2.2 Absorption Spectroscopy of LPPs</i> . . . . .                    | 29 |
| <b>1.3 Overview of Dual-Comb Spectroscopy of LPPs Experiments</b> . . . . | 30 |
| <b>1.4 Dual-Comb Spectroscopy</b> . . . . .                               | 32 |
| <i>1.4.1 Time and Frequency Domain Paradigms</i> . . . . .                | 32 |
| <i>1.4.2 Apodization and Frequency Resolution</i> . . . . .               | 36 |
| <i>1.4.3 Measurement Optimization in DCS</i> . . . . .                    | 45 |
| <i>1.4.4 DCS Signal Processing</i> . . . . .                              | 48 |
| <b>CHAPTER 2 Experimental Setup</b> . . . . .                             | 57 |
| <b>2.1 Frequency Combs</b> . . . . .                                      | 57 |
| <i>2.1.1 Yb-Fiber Oscillators and Amplifiers</i> . . . . .                | 58 |
| <i>2.1.2 Er-Fiber Oscillators and Amplifiers</i> . . . . .                | 61 |
| <b>2.2 Comb Stabilization</b> . . . . .                                   | 67 |
| <i>2.2.1 Er-DCS Stabilization</i> . . . . .                               | 69 |
| <i>2.2.2 Yb-DCS Stabilization</i> . . . . .                               | 76 |

|   |     |
|---|-----|
| 2.3 DCS Detection . . . . .   | 79  |
| 2.4 LPP Ablation Timing and Electronics . . . . .   | 82  |
| CHAPTER 3 Quantitative Spectral Analysis . . . . .  | 84  |
| 3.1 Absorption Spectra Theory . . . . .   | 84  |
| 3.2 Spectral Fitting . . . . .  | 87  |
| 3.3 Boltzmann-Plot Analysis . . . . .   | 90  |
| CHAPTER 4 Measurement of Neutral Gadolinium Oscillator Strengths<br>using DCS in LPPs . . . . . | 94  |
| 4.1 Introduction . . . . .  | 94  |
| 4.2 Experiment . . . . .  | 99  |
| 4.3 Theory . . . . .  | 101 |
| 4.4 Time-Resolved Absorption Spectra of Gd . . . . .  | 102 |
| 4.5 Analysis of Spectra . . . . .   | 105 |
| 4.6 Determination of Temperature and Atomic Density . . . . .                                   | 107 |
| 4.7 Determination of Gd I Oscillator Strengths . . . . .  | 110 |
| 4.8 Discussion . . . . .  | 113 |
| 4.9 Summary and Conclusions . . . . .   | 119 |
| CHAPTER 5 Multi-Species Temperature and Number Density Analysis<br>of a LPP using DCS . . . . . | 121 |
| 5.1 Introduction . . . . .  | 121 |
| 5.2 Experiment . . . . .  | 122 |
| 5.3 Time-Resolved Absorption Spectra of Multi-Element Alloy and Anal-<br>ysis . . . . .         | 124 |
| 5.4 Determination of Temperature and Atomic Density . . . . .                                   | 127 |
| 5.5 Discussion . . . . .  | 129 |
| 5.6 Sample Concentration/Measured Number Densities Calibration . .                              | 138 |
| 5.7 Summary and Conclusions . . . . .   | 147 |
| APPENDIX A Multicolor DCS with Optical Pumping . . . . .  | 150 |

|   |     |
|---|-----|
| APPENDIX B Codes . . . . .                      | 157 |
| B.1 Signal Processing . . . . .                 | 157 |
| B.2 Absorption Spectra Modelling . . . . .      | 163 |
| B.3 Spectral Fitting . . . . .                  | 166 |
| B.4 Boltzmann-Plot Analysis . . . . .           | 168 |
| B.5 Averaging-Size Looping Variations . . . . . | 169 |
| REFERENCES . . . . .                            | 186 |

## LIST OF FIGURES

|     |  |    |
|-----|--|----|
| 1.1 | Illustration of the ultrashort pulse train emitted by a mode-locked laser, and the corresponding frequency spectrum which exhibits the comb structure. . .   | 33 |
| 1.2 | (a) Illustration of the interference of the pulse trains from two frequency combs with slightly different repetition rates to generate an interferogram. The Fourier transform yields the overlap power spectrum in (b), called the SBS. Here, the reference SBS contains no absorption, whereas the signal SBS was measured with an absorptive sample present. The spectral fringing present in both spectra is due to etaloning and divides out when calculating transmittance.  | 35 |
| 1.3 | Illustration of the interference of two frequency combs with slightly different repetition rates to generate a directly detectable RF comb. . . . .  | 37 |
| 1.4 | Illustration expanding on Fig. 1.3 to show the aliasing of RF beatnotes which occur at 0 Hz and $f_{rep}/2$ . The combs are differentiated by solid and dashed lines. Aliased beatnotes are depicted with dotted lines. Note that all comb teeth present beat against each other in DCS: teeth from the same comb beat to produce RF frequencies at $f_{rep}$ and its harmonics, and beatnotes generated between the combs have frequencies $f_{RF}$ between 0 Hz and $f_{rep}/2$ that also repeat according to $f'_{RF} = f_{RF} + n f_{rep}$ . Only some beatnotes and their aliases are shown here for clarity. . . . . | 38 |
| 1.5 | Plots of various 100 $\mu s$ wide apodization windows. Their associated ILFs are shown in Fig. 1.6. 100 $\mu s$ represents a common apodization window size (equal to $T_{meas}$ ) in DCS measurements of LPPs. . . . .  | 40 |

|      |   |    |
|------|---|----|
| 1.6  | The associated ILFs of the apodization windows plotted in Fig. 1.5. The associated optical linewidth of each is listed in GHz, calculated assuming $f_{rep} = 80$ MHz and $\Delta f_{rep} = 500$ Hz. Note that 500 $\mu$ s of 0s were padded to each side of the apodization window to decrease the frequency spacing to better resolve the functional shape of the ILF for better viewing. Padding 0s does not change the ILF linewidth, which is dependent only on the temporal duration of nonzero window ( $T_{meas}$ ). . . . .  | 41 |
| 1.7  | Comparison of absorbance spectra processed using a rectangular apodization function versus a Blackman-Harris function. The absorption lineshapes of the rectangular window case are narrower but feature ringing in the baseline. . .   | 42 |
| 1.8  | Comb-resolved reflection measurement of the transmission of a Fabry-Perot cavity. . . . .   | 43 |
| 1.9  | Illustration of the relationship between time-delay and apodization window width ( $T_{meas}$ ) in DCS-LPP experiments. The interferogram following ablation probes absorption in the LPP. For a symmetric apodization window, the maximum $T_{meas}$ is twice the time-delay (shown in dashed red), so that no times before ablation are included. A smaller value of $T_{meas}$ can be used (shown in dashed blue) but results in poorer frequency resolution. Thus, the time-delay effectively sets a limit on best frequency resolution $\delta f_{meas}$ achievable via $T_{meas}$ . Also shown is the preceding interferogram, recorded as a reference for background absorption when no LPP is present, discussed in Sec. 1.4.3. . . . | 44 |
| 1.10 | Measurement of the standard deviation (STD) of the noise floor in absorbance for a DCS-LPP measurement with bandwidth of 4.7 THz centered near 783 nm. The signal was detected using a balanced detector. Error bars represent the STD of the plotted values across multiple averaging bins. . . . .  | 48 |
| 1.11 | Comparison of the center-burst of an unaveraged centerburst and the inverse Fourier transform of its Mertz phase corrected (MPC) Fourier transform. The symmetry of the Mertz phase corrected centerburst is due to the Mertz phase corrected frequency spectrum being real (in a complex number sense). . . . .  | 50 |

|      |   |    |
|------|---|----|
| 1.12 | Comparison between a Mertz phase corrected (MPC) SBS and the magnitude of the Fourier transform of the same signal. Note the amplitude bias of the noise floor as well as within the optical window. . . . .  | 51 |
| 1.13 | Comparison of absorbance spectra processed using a rectangular apodization function processed with zero-padding and none. 163 $\mu$ s of 0s were padded to each side of the 58 $\mu$ s apodized signals in the former case. The sampling of the non-zero-padded spectrum causes the lineshape centers to appear to be shifted due to the plotted point sampling being so low. . . . .   | 52 |
| 1.14 | Comparison of the centerbursts of five recorded shots and the time-domain average of 750 centerbursts. Each shot was 0.1 ms apart, dictated by the ablation rate. All centerbursts were shifted so that their maximum centerburst values aligned. Here, phase-slippage was not extreme enough to completely degrade the averaged signal. Note that the chosen alignment procedure forces the cycles to overlap. As such, phase-slippage is expected to manifest as variations in the amplitude of the cycles due to their position changing under the centerburst envelope. Such behavior is indicated here, though measurement noise also plays a role. Alignment of the cycles would not occur if the centers of the centerburst envelopes were instead aligned, which can be done by utilizing Hilbert transformations. Note that consecutive interferograms are neither plotted nor were recorded due to the ablation frequency, and so a "re-phasing" of centerbursts may occur over these longer time-scales (10s seconds). . . . . | 53 |
| 1.15 | Comparison of the centerbursts of a time-averaged set of 750 interferograms and the inverse Fourier transform of the Mertz phase correction (MPC) of the same data. The time-averaged centerbursts were aligned so that their maximum value overlapped. Note that frequency averaging the Mertz phase corrected spectra and then inverse Fourier transforming into the time domain produces the same result as inverse Fourier transforming each of the Mertz phase corrected spectra and then averaging them in the time domain. . . . .   | 54 |

|      |  |    |
|------|--|----|
| 1.16 | Comparison of the absorbance spectra of 750 SBS averaged in the frequency domain after Mertz phase correction versus averaging of the interferograms in the time domain before Fourier transform and Mertz phase correction. The time-averaged interferograms were aligned so that their maximum centerburst value overlapped. . . . .   | 55 |
| 1.17 | Example of a signal SBS with narrow, weakly absorbing features and a pseudo-reference SBS generated from the weakly low-passed signal. Both are Mertz phase-corrected by the same strongly low-passed phase $\theta_{MPC}(\nu)$ . . . . .  | 56 |
| 2.1  | Schematic of the oscillators used for the Yb-DCS system. The black beamlines are guided within optical fiber, whereas the red are in free-space. HWP: half-waveplate, QWP: quarter-waveplate, COL: fiber collimation package, PBS: polarizing beamsplitter, WDM: wavelength division multiplexer, ISO: optical isolator, GP: transmission grating pair, M: mirror, EOM: electro-optic modulator. M+PM is a mirror mounted on a stage with a picometer motor, used for relatively large cavity length changes. M+PZT is a mirror mounted to a PZT used in stabilization (see Sec. 2.2.2). The mirror M* is placed such that the first optical beam passes over the mirror, and the reflection from M+PZT is incident. . . . . | 60 |
| 2.2  | Schematic of the optical layout for the pre-amplifiers of Combs 1 and 2 in the Yb-DCS system. The black beamlines are guided within optical fiber, whereas the red are in free-space. HWP: half-waveplate, AL: aspheric lens, COL: fiber collimation package, Comb.: pump combiner, ISO: optical isolator, SPL: fiber splitter, AOM: acousto-optic modulator, DCF: double-clad fiber, PC: fiber-based polarization controller, POL: inline fiber polarizer, UVFS: UV fused silica. . . . .   | 61 |



|     |  |    |
|-----|--|----|
| 2.3 | Schematic of the optical layout for Combs 1 and 2 of the Yb-DCS system after their pre-amplifiers and up to the PCF amplifiers. The interlock signal comes from the p-polarized light which leaks through the mirror just before the PFC amplifier. The black beamlines are guided within optical fiber, whereas the red are in free-space. HWP: half-waveplate, D: dichroic mirror, L: lens, followed by focal length, COL: fiber collimation package, ISO: optical isolator, M: mirror, G: transmission grating, UVFS: UV fused silica, PCF: photonic crystal fiber, representing the PCF amplifier. . . . . | 62 |
| 2.4 | Schematic of Comb 1 oscillator in the Er-DCS system. Er-doped gain fiber is indicated in green, which has negative dispersion. PM980 and PM1550 both have positive dispersion. The focusing lens has a focal length of 1.45 mm, producing a spot-size of $3.57 \mu\text{m}$ on the SESAM. WDM: wavelength division multiplexer, EDFA: erbium-doped fiber amplifier, SESAM: semiconductor saturable absorber mirror. . . . .  | 63 |
| 2.5 | Schematic of Comb 2 oscillator in the Er-DCS system. Er-doped gain fiber is indicated in green, which has negative dispersion. PM980 and PM1550 both have positive dispersion. The focusing lens has a focal length of 2.45 mm, producing a spot-size of $3.02 \mu\text{m}$ on the SESAM. WDM: wavelength division multiplexer, EDFA: erbium-doped fiber amplifier, SESAM: semiconductor saturable absorber mirror, EOM: electro-optic modulator. . . . .  | 64 |
| 2.6 | Oscillator spectra of the Er-DCS system, recorded 09/16/2022. The oscillator pump currents were 140 mA and 125 mA for Combs 1 and 2, respectively. The case temperature was $83^\circ \text{F}$ . . . . .  | 65 |
| 2.7 | Schematic of the optical layout of the EDFA and HNLF portion of the Er-DCS system for each comb. The pulses are optimized just before the HNLF. All beamlines are guided within optical fiber. WDM: wavelength division multiplexer, ISO: optical fiber isolator, SPL: fiber splitter, HNLF: highly-nonlinear fiber, COL: fiber collimation package. . . . .   | 65 |
| 2.8 | PI curves of the EDFAs in the Er-DCS system, measured just before the HNLF.  | 66 |

|      |   |    |
|------|---|----|
| 2.9  | Amplifier spectra of the Er-DCS system just before HNLF, recorded 05/17/2021.<br>The amplifier pump currents were 1200 mA for both combs. . . . .   | 66 |
| 2.10 | Broadband amplifier spectra of the Er-DCS system generated in HNLF, recorded<br>09/26/2022. The amplifier pump currents were 775 mA and 650 mA for<br>Combs 1 and 2, respectively. . . . .  | 67 |
| 2.11 | General arrangement of a phase-locked loop, used in stabilizing the frequency<br>combs. . . . .   | 70 |
| 2.12 | Schematic of the optical layout used to generate Beatnotes 1 and 2 in the Er-<br>DCS system. All beamlines are guided within non-PM fiber. ISO: fiber-based<br>isolator, 50:50: 50:50 fiber beamsplitter, FBG: fiber Bragg grating. . . . .   | 70 |
| 2.13 | Schematic of the optical layout used to generate Beatnotes 3 and 4 in the<br>Er-DCS system. All beamlines are guided within PM fiber. ISO: fiber-<br>based isolator, 50:50: 50:50 fiber beamsplitter, FBG: fiber Bragg grating,<br>RC: reflection-type combiner. . . . .  | 71 |
| 2.14 | Schematic of the circuit used to acquire $f_{rep}$ and $\Delta f_{rep}$ from Beatnotes 1 and<br>2 in the Er-DCS system. The outputs “to Lock #1” and “to Lock #2” are<br>the inputs in Fig. 2.15. RF amplifiers, represented by triangles, provide $\sim 25$<br>dB of amplification. SPL: splitter, CPL: directional coupler, BPF: bandpass<br>filter, LPF: lowpass filter, MXR: mixer. . . . . | 72 |
| 2.15 | Schematic of Locks 1 and 2 in the Er-DCS system, used to condition and lock<br>Beatnotes 1 and 2. RF amplifiers, represented by triangles, provide $\sim 25$ dB of<br>amplification. SPL: splitter, CPL: directional coupler, BPF: bandpass filter,<br>LPF: lowpass filter, MXR: mixer, ATT: attenuator. . . . .  | 73 |
| 2.16 | Schematic of Locks 3 and 4 in the Er-DCS system, used to condition and lock<br>Beatnotes 3 and 4. RF amplifiers, represented by triangles, provide $\sim 25$ dB of<br>amplification. SPL: splitter, CPL: directional coupler, BPF: bandpass filter,<br>LPF: lowpass filter, MXR: mixer, ATT: attenuator, DL: diode limiter. . . . .   | 75 |

|      |  |    |
|------|--|----|
| 2.17 | Schematic of the optical layout used to generate Beatnotes 1-4 as well as the optical signal for the reference laser locking in the Yb-DCS system. The black beamlines are guided within optical fiber, whereas the red are in free-space. PC: polarization controller, SPL: splitter, ISO: fiber optical isolator, 50:50: 50:50 fiber beamsplitter, FBG: fiber Bragg grating, Comb: fiber beam combiner, COL: fiber collimation package, G: transmission grating. . . . .           | 77 |
| 2.18 | Schematic of the optical layout used to generate PDH signals for the reference laser locking in the Yb-DCS system. The black beamlines are guided within optical fiber, whereas the red are in free-space. COL: fiber collimation package, ISO: optical isolator, G: transmission grating, EOM: electro-optic modulator, HWP: half-waveplate, QWP: quarter-waveplate, L: lens, with focal length following, PBS: polarization beamsplitter, ULEC: ultralow-expansion cavity. . . . . | 78 |
| 2.19 | Schematic of PDH locks for CW 1 and CW 2 in the Yb-DCS system. RF amplifiers, represented by triangles, provide $\sim 25$ dB of amplification. SPL: splitter, CPL: directional coupler, BPF: bandpass filter, LPF: lowpass filter, MXR: mixer, ATT: attenuator, VCO: voltage-controlled oscillator. . . . .  | 78 |
| 2.20 | Schematic of Locks 1 and 2 in the Yb-DCS system, used to condition and lock Beatnotes 1 and 2. RF amplifiers, represented by triangles, provide $\sim 25$ dB of amplification. Two PZT drivers are used to manually adjust the comb mode frequencies for locking. SPL: splitter, CPL: directional coupler, BPF: bandpass filter, LPF: lowpass filter, MXR: mixer, ATT: attenuator, Comp.: Phase Comparator. . . . .  | 79 |
| 2.21 | Schematic of Locks 3 and 4 in the Yb-DCS system, used to condition and lock Beatnotes 3 and 4. RF amplifiers, represented by triangles, provide $\sim 25$ dB of amplification. Comb 2 $f_{rep}$ can be used to clock the DAQ for synchronous sampling of the interferograms. SPL: splitter, CPL: directional coupler, BPF: bandpass filter, LPF: lowpass filter, MXR: mixer, ATT: attenuator, Comp.: Phase Comparator. . . . .   | 80 |

|      |   |    |
|------|---|----|
| 2.22 | Schematic of the optical setup used for combining the two post-amplification comb beamlines, which pass to the experiment, and the detection setup after the measurement. The black beamlines are guided within optical fiber, whereas the red are in free-space. HWP: half-wave plate, COL: fiber collimation package, PBS: polarizing beamsplitter, G: reflection grating, M: mirror, FM: flipper mirror, L: lens, followed by focal length, VA: variable attenuator, BD: balanced detector, DAQ: data-acquisition board. The mirror M* is placed such that the first optical beam passes over the mirror, and the reflection from the 4f optical filter is incident. . . . .                   | 81 |
| 2.23 | Representation of the timing of DCS-LPP experiments. The blue dashed box shows detail zoomed in time. . . . .   | 83 |
| 2.24 | Schematic of the electrical setup for generating $f_{rep}$ and using it to synchronize the triggers for the ablation system. . . . .  | 83 |
| 3.1  | Example of a spectral fit of Nd I in which $T$ and $n_{tot}$ were fit directly as parameters, with residuals included. The residuals are as large as $\sim 1$ absorbance unit. As is discussed in Sec. 5.5, the oscillator strength for the 561.5879 THz transition is believed to be incorrect in the literature. The fitting algorithm attempts to minimize the residuals of this transition by compensating with larger residuals for all other transitions. The transition can be excluded from the fitting to improve performance, but it is not always known which spectroscopic input may be incorrect, and small inconsistencies in a few transitions will affect the entire fit. . . . . | 89 |
| 3.2  | Example Boltzmann plots for three species, showing alloy data from Ch. 5. (Figure from [30]) . . . . .  | 92 |

|     |  |     |
|-----|--|-----|
| 4.1 | (a) Experimental schematic of the dual-comb setup. BS: beamsplitter; AOM: acousto-optic modulator; M: mirror; HWP: half-wave plate; PBS: polarizing beamsplitter; L: lens; PD: photodetector. (b) Schematic of the time-domain interferograms generated by the dual-comb signal. The interferograms repeat with a frequency equal to the inverse of the difference between the repetition rates of the two frequency combs. Only the interferograms coming directly before and after the ablation events repeating at $\sim 10$ Hz are recorded. The first interferogram is used as a reference, and the second is the signal containing the absorption information due to the ablation plume. The measured time-delay is defined as the length of time between the ablation event and the centerburst of the signal interferogram. (Figure from [29]) . . . . . | 100 |
| 4.2 | Experimental absorbance spectra (each averaged over 750 ablation shots) for the measured time-delays indicated in the figure. Spectra are offset for clarity. (Figure from [29]) . . . . .   | 102 |
| 4.3 | Experimental absorbance spectrum (averaged over 750 ablation shots) measured at $88 \mu\text{s}$ . . . . .   | 103 |
| 4.4 | (a) Portion of experimental spectrum at $72 \mu\text{s}$ showing strong and weak Gd I absorption lines. Dotted lines indicate transitions listed in the Kurucz database with known oscillator strengths. (b) Experimental spectrum at $154 \mu\text{s}$ over the same range. At later times, weaker lines are no longer visible, and the spectral resolution is improved. (Figure from [29]) . . . . .   | 104 |
| 4.5 | Spectral fit for the absorption spectrum at $88 \mu\text{s}$ . The solid red line shows the experimental data, and the solid blue line shows the best-fit spectrum. The black arrows indicate frequencies of Gd I transitions with known oscillator strengths, and magenta arrows indicate frequencies of additional dipole-allowed Gd I transitions with unknown oscillator strengths. . . . .  | 106 |

|      |   |     |
|------|---|-----|
| 4.6  | Examples of experimental data and fits for portions of the absorption spectrum at (a) 53 $\mu\text{s}$ and (b) 154 $\mu\text{s}$ . The dotted points show experimental data, and the solid blue line shows the best-fit spectrum. Vertical dashed lines show frequencies of Gd I transitions with known oscillator strengths, and vertical dotted lines show frequencies of additional dipole-allowed Gd I transitions with unknown oscillator strengths. The lower panels show the fit residuals. (Figure from [29]) . . . . .   | 107 |
| 4.7  | Boltzmann plots for all time-delays. Solid points were calculated from fits to peak areas for experimental data, along with oscillator strengths, level degeneracies, and lower-level energy from the Kurucz database. The solid red lines are linear fits to the data points. Error bars were calculated from the uncertainties in peak areas and oscillator strengths. . . . .  | 110 |
| 4.8  | (a) Excitation temperature and (b) total column density of Gd I for each time-delay measurement. Data points were determined from fits to the Boltzmann plots at each time-delay and error bars were calculated based on standard errors of fits and propagation of errors. The solid lines are guides for the eye. (Figure from [29]) . . . . .  | 111 |
| 4.9  | $\log(gf)$ values vs. time-delay for selected transitions. The frequency and lower energy for each transition is noted in the figure. Plots with filled markers indicate transitions listed in the Kurucz database whose oscillator strengths were recalculated; those with unfilled markers are for previously unreported, dipole-allowed transitions. (Figure from [29]) . . . . .  | 112 |
| 4.10 | Plot comparing this work's calculated $\log(gf)$ values from the Boltzmann fit (in red) with reported values in Kurucz and Lawler et al. (in black and blue, respectively). The line frequency and lower transition level energy identify the transition corresponding to each $\log(gf)$ value. Each bar's width along the y-axis indicates the value and its spread, given as $\log(gf)$ plus/minus its reported absolute log-space uncertainty. Note that the uncertainties used for the values from this work are the average errors shown in Table 4.1. (Figure from [29]) . . . . . | 115 |

|      |   |     |
|------|---|-----|
| 4.11 | Example of overlapped Gd I peaks in experimental data. The transition listed by Kurucz et al. is differentiated in the figure from the those identified by calculating all dipole-allowed transitions. The Kurucz-listed transition is somewhat resolved from the nearby unlisted lower-frequency transition but is not well-resolved from the even closer higher-frequency transition. Inclusion of all three in the fitting model improves the fitted area accuracy of the peaks. The uncertainty of the fit takes into account the presence of nearby transitions, increasing as the separate transitions are less resolved from one another. (Figure from [29]) . . . . . | 116 |
| 5.1  | (a) Example SBS for the recorded reference and signal interferograms, each the result of spectral averaging across 750 ablation shots. Atomic absorption features due to atoms present in the plume coincident with the DCS beampath are clear in the signal SBS. Spectral fringing seen in the SBS due to residual reflections from optical components is eliminated by signal normalization with the reference in calculating absorbance, shown in (b). . . . .   | 123 |
| 5.2  | Experimental absorbance DCS spectra measured at seven time-delays after ablation. Each is the average of 750 shots. Atomic transitions of Fe, Nd, and Gd are visible, along with some ionic lines at early times, but only the two Nd I resonant transitions are visible at 250 $\mu$ s. A single atomic transition for each species is indicated as an example. Spectra offset for clarity. (Figure from [30]) . . . . .   | 126 |
| 5.3  | Example spectral fits at (a) 51 and (b) 151 $\mu$ s, plotted over a narrow spectral region to show agreement between measurements (points) and spectral fits (lines). Transitions used in the spectral fitting are labelled by element. Additional absorption lines visible in the spectrum were not included in the fits because oscillator strength data were not available. Note the absorbance range in (a) is smaller. (Figure from [30]) . . . . .  | 127 |

|     |  |     |
|-----|--|-----|
| 5.4 | State column densities for selected high-lying (blue triangles) and low-lying (red circles) energy levels of (a) Nd I, (b) Gd I, and (c) Fe I as a function of time after ablation. Higher energy levels lose population as the plume cools in time, whereas atoms accumulate in the lower energy states. The Nd I resonant transition trace comes from the calculated column density using the 561.8511 THz transition fitted peak area. (Figure from [30]) . . . . . | 128 |
| 5.5 | Boltzmann plots for Nd I, Gd I, and Fe I at 31, 51, and 71 $\mu$ s. Red lines are linear fits calculated from the plots to determine temperature and total column density for each species. Error bars include both reported oscillator strength uncertainties and standard error from the spectral fits. . . . .  | 129 |
| 5.6 | Boltzmann plots for Nd I, Gd I, and Fe I at 87, 110, and 151 $\mu$ s. Red lines are linear fits calculated from the plots to determine temperature and total column density for each species. Error bars include both reported oscillator strength uncertainties and standard error from the spectral fits. . . . .  | 130 |
| 5.7 | Temperature (a) and total column density (b) as a function of time after ablation for Nd I, Gd I, and Fe I. (c) is a vertically-zoomed copy of (b) to show detail of Nd I and Gd I total column densities. The ratio of Gd I/Nd I is shown in (d). (Figure from [30]) . . . . .  | 131 |
| 5.8 | Time evolution of absorbance spectra of LPP containing CeO molecular bands and prominent Ce atomic lines (positions indicated by arrows). The measurement spectral resolution varies with time-delay (from top to bottom: 7.60 GHz, 4.96 GHz, 3.72 GHz, 2.56 GHz, 1.91 GHz, 1.50 GHz, and 1.25 GHz). Spectra offset for clarity. (Figure from [31]) . . . . .  | 133 |



|      |  |     |
|------|--|-----|
| 5.9  | (a) Absorbance measurement of LPP showing molecular CeO rovibrational electronic transition lines originating predominantly from the P and Q branches of the $X_2(^3\Phi_3) - A_2(^3\Delta_2)(0-0)$ band. The spectrum is the result of 400 averaged shots and was acquired at 302 $\mu\text{s}$ after ablation with a resolution of 1.24 GHz. No cleaning shots were performed for this measurement, resulting in increased CeO absorption and decreased Ce I absorption. (b) Zoomed-in portions of (a) emphasizing different 0.1 THz portions of the spectra and lines position reported by Linton et al. [121]: (b1) P-branch lines at approximately 379.65 THz; (b2) P and Q-branch lines at approximately 380.05 THz; (b3) Q-branch lines with bandhead at approximately 380.35 THz. (Figure from [31]) | 134 |
| 5.10 | Plot of (a) fitted peak areas and (b) their ratio for the two resonant transitions of Nd I within the DCS measurement bandwidth. Solid line denotes mean value across all time-delays and dashed lines one standard deviation, $1.71 \pm 0.12$ . Error bars on the fitted peak areas come from the fit error, which is propagated and plotted for the ratios. (Figure from [30])   | 136 |
| 5.11 | Excitation temperature (a) and total column density (b) for Nd I and Gd I for seven repeated measurements of 750 ablation shots each at 110 $\mu\text{s}$ . Solid horizontal lines denote mean values across all seven measurements, and dashed lines mark one standard deviation. (Figure from [30])  | 137 |
| 5.12 | Determined excitation temperatures for Nd and Gd as a function of sample concentration.  | 139 |
| 5.13 | Determined excitation temperatures for Nd and Gd as a function of Nd concentration. Note that Gd has an inverse concentration to Nd, so pairs of points that share a common x-value were taken in the same measurement.  | 140 |
| 5.14 | Determined total column densities for Nd and Gd as a function of sample concentration. The linear fits have y-intercepts forced to 0.  | 141 |
| 5.15 | Fitted peak areas for three transitions with 750 averages as a function of sample concentration. Note, Fe was kept at a constant 90% concentration.  | 142 |
| 5.16 | Determined total column densities for Nd I for various sample concentrations as a function of averaging number.  | 144 |

|      |   |     |
|------|---|-----|
| 5.17 | Determined total column densities for Gd I for various sample concentrations as a function of averaging number. . . . .   | 144 |
| 5.18 | Determined excitation temperatures for Nd I for various sample concentrations as a function of averaging number. . . . .  | 145 |
| 5.19 | Determined excitation temperatures for Gd I for various sample concentrations as a function of averaging number. . . . .  | 145 |
| 5.20 | Histogram showing the distribution of fitted peak areas for the 560.7151 THz Gd I transition with 0% Gd sample concentration. . . . .   | 146 |
| 5.21 | Histogram showing the distribution of fitted peak areas for the 561.8511 THz Nd I transition with 10% Nd sample concentration. . . . .  | 147 |
| A.1  | Schematic showing the layout of the Er-DCS system used for probing a LPP with 780 nm and 1550 nm light simultaneously. PPLN: periodically-poled lithium niobate, DM: dichroic mirror, Pol. Comb.: fiber-based polarization combiner, M: mirror, L: lens, HWP: half-wave plate, BPD: balanced photodetector, FPGA: field-programmable gate array, DAQ: data-acquisition board. . . . . | 151 |
| A.2  | Energy level diagram for Rb, showing the energy levels and transitions of interest in boldface. The other levels and transitions are other possible candidates for measurement. . . . .   | 152 |
| A.3  | Absorption spectra of three Rb transitions measured using the fundamental and second-harmonic of the Er-DCS. The dashed lines show the theoretical frequency location of the 1530 nm transitions. . . . .   | 153 |
| A.4  | Optical layout for pumping Rb atoms in a LPP with a CW laser locked to the D2 transition, allowing detection of excited state transitions by the Er-DCS system for longer times. . . . .  | 154 |
| A.5  | DCS absorbance spectrum of the 1530 nm excited-state transitions of Rb, measured in a late-time LPP using optical pumping. . . . .  | 155 |
| B.1  | Example of calculated $\Delta f_{rep}(i)$ with statistics listed in the annotation. . . .   | 170 |
| B.2  | Example SBS for both signal and reference of a DCS-LPP experiment. Both are Mertz phase-corrected by their own low-passed phase information. . . . .  | 171 |

|      |  |     |
|------|--|-----|
| B.3  | Example transmittance function. . . . .  | 172 |
| B.4  | Example absorbance function, plotted against the uncalibrated optical frequency axis. The frequency spacings are calibrated but a global offset is required for absolute calibration. . . . .  | 173 |
| B.5  | Example Blackman-Harris apodization window with zero-padding. . . . .  | 174 |
| B.6  | Example ILF, which is the Fourier transform of the Blackman-Harris apodization window in Fig. B.5. Note the measured FWHM reported in the annotation, which is the instrumental resolution. . . . .  | 175 |
| B.7  | Example absorbance function with background subtraction and absolute calibration. . . . .  | 176 |
| B.8  | Example calibrated absorbance overlaid with a modelled spectrum to check feature alignment. . . . .  | 177 |
| B.9  | Example calibrated absorbance function with calculated peak heights, linewidths, and integrated peak areas. . . . .  | 178 |
| B.10 | Partition function $Z(T)$ and the 20 <sup>th</sup> degree fitted polynomial for Gd I used in the absorption spectrum calculations. . . . .   | 179 |
| B.11 | Modelled absorption spectrum for Nd I, Gd I, and Fe I, all at 5000 K excitation temperature with total number densities of $10^{15}$ , $10^{15}$ , and $10^{16}$ cm <sup>-3</sup> , respectively. All species were modelled with Lorentzian widths (FWHM) of 2 GHz and kinetic temperatures of 5000 K. This model also included ILF broadening effect due to a 170 $\mu$ s wide Blackman-Harris apodization window with a 3.02 GHz linewidth (FWHM). . . . . | 180 |
| B.12 | Example plot produced by the spectral fitting code, showing the experimental data overlaid with the fitted model, as well as the fit residuals at the bottom. The fit points indicated by red circles are the points around the fitting transitions which were used in the fit. The experimental data shown here come from the multispecies LPP-DCS data discussed in Ch. 5. . . . .   | 181 |
| B.13 | Zoomed-in portion of Fig. B.12. . . . .  | 182 |

- B.14 Example plot produced by the Boltzmann-plot analysis code, showing the Boltzmann plot for 20 transitions of Gd I measured in a LPP at 87  $\mu\text{s}$  after ablation. The code generates a plot like this for each species in the analysis. 183
- B.15 Example plot produced by the Boltzmann-plot time-series code, showing the calculated temperatures for Fe I, Nd I, and Gd I as a function of time-delay. Note that Fe I results after 87  $\mu\text{s}$  were discarded after analysis due to having too few points for the Boltzmann fit. . . . . 184
- B.16 Example plot produced by the Boltzmann-plot time-series code, showing the calculated total column-densities for Fe I, Nd I, and Gd I as a function of time-delay. Note that Fe I results after 87  $\mu\text{s}$  were discarded after analysis due to having too few points for the Boltzmann fit. . . . . 185

## LIST OF TABLES

|     |  |     |
|-----|--|-----|
| 4.1 | Oscillator strengths of Gd I transitions determined in this work, and comparison to literature. . . . .                  | 108 |
| 4.2 | List of Gd I transitions calculated $\log(gf)$ values for previously unreported transition oscillator strengths. . . . . | 109 |
| 5.1 | Atomic transitions of Fe, Nd, and Gd used in the spectral fit and Boltzmann analysis. . . . .                            | 125 |

## ABSTRACT

Dual-comb spectroscopy (DCS) represents a novel method of using absorption spectroscopy as a diagnostic tool for time-resolved multispecies analysis of excitation temperatures and column densities in laser-produced plasmas (LPPs). DCS utilizes two stabilized modelocked lasers to generate a pair of mutually-coherent frequency combs and enables broadband spectroscopic measurements with high spectral and temporal resolution that are well-suited for studying the quickly evolving conditions of LPPs. The ablation plume of an LPP evolves both spatially and temporally and, when combined with optical diagnostics, has proved useful both as a means for preparing high-temperature gas-phase atomic/molecular species and for non-contact elemental analysis of solid materials. Temperature and number density studies involving ionic, atomic, and molecular species present in the LPP are applicable to quantitative analysis of sample composition as well as plasma diagnostic research focused on plume formation and expansion, molecular formation, diffusion rates, and condensation processes, both spatially and temporally. LPPs can be studied by DCS with both the necessary time and spectral resolutions required to probe many absorption transitions within the timescales of late-time LPP evolution. Recent work has shown that the technique's high spectral resolutions enable measurements of congested optical spectra, such as those from heavy elements and molecules, to be resolved and more accurately analyzed. Broadband detection of multiple transitions, combined with Boltzmann-plot style analysis commonly used in laser-induced breakdown spectroscopy (LIBS), provides the ability to determine time-resolved excitation temperatures and total column densities of atomic species. Using efficient harmonic conversion in nonlinear crystals (e.g., second harmonic generation), DCS can easily access multiple wavelength regions. The ability to measure spectrally and temporally resolved broadband spectra within many wavelength regions makes DCS an effective optical technique for studying LPPs as well as additional spectroscopic applications.

## Chapter 1

### Dual-Comb Spectroscopy of Laser-Produced Plasmas

#### 1.1 Introduction

Using ultrafast lasers to generate frequency combs, dual-comb spectroscopy (DCS) provides a high-brightness source for absorption spectroscopy which enables both high spectral resolution and broad spectral bandwidth with significant impact in a wide range of applications [1, 2]. DCS utilizes the broad spectrum of a pair of femtosecond frequency combs to probe an absorptive sample. Absorption spectra can be measured with a single fast photodiode in a massively parallel heterodyne measurement, achieved when the two combs are interfered while operating at slightly different repetition rates. In this work, DCS is used for time-resolved studies of laser-produced plasmas (LPPs). LPPs provide a powerful tool for the analysis of solid materials. Optical spectroscopy of LPPs has been applied to fields such as astronomy [3, 4], geochemistry [5], archaeology [6], pharmaceuticals [7], atmospheric sensing [8], nuclear nonproliferation [9], isotopic analysis of nuclear materials [10], nuclear fusion [11, 12], amongst others. LPPs may be generated by ablating the surface of a solid sample with a high-energy laser pulse. The resulting ablation plume evolves both spatially and temporally and, when combined with optical diagnostics, has proved useful both as a means for preparing high-temperature gas-phase atomic/molecular species and for non-contact elemental analysis of solid materials [13, 14]. A better understanding of the evolution of physical and chemical properties of the LPP, including temperature and number densities of various ionic, atomic, and molecular species, is becoming essential to progress in current and future applications [15–17]. Studies involving multiple species present in the LPP are applicable to quantitative analysis of sample composition as well as plasma diagnostic research focused on plume formation and expansion, molecular formation, diffusion rates, and con-

densation processes, both spatially and temporally. This dissertation presents several DCS experiments studying the characteristics of LPPs, as well as background on LPPs, DCS, and absorption spectra theory. Also provided are extensive details on the frequency-comb systems used, their construction and stabilization, the detection and synchronization of the DCS-LPP experiments, and the processing and analysis techniques employed.

## 1.2 Spectroscopic Techniques for Studying LPPs

### 1.2.1 *Laser-Induced Breakdown Spectroscopy*

Several spectroscopic techniques are employed for plasma diagnostic studies of LPPs, utilizing both emission and absorption methods. The commonly used emission spectroscopy technique laser-induced breakdown spectroscopy (LIBS) measures optical emission from the LPP, typically using a spectrograph and time-gated CCD detector [18]. LIBS is used for sample composition analysis and has also been used to determine electron densities via Stark broadenings and shifts and electronic excitation temperatures via Boltzmann analysis. LIBS measurements may be performed with high time resolution but are often limited to early times of plasma evolution with corresponding high temperatures to produce sufficient optical emission for detection [19, 20]. At early times, the emission signal is strong, but dominated by Stark broadening (see Sec. 3.1 for a brief discussion of spectral lineshape broadening mechanisms in LPPs). At late times, the Stark broadening decreases, but the emission also decreases as the plasma cools, limiting its capability to track late-time plasma evolution. Moreover, emission spectroscopy suffers from self-absorption and self-reversal, which have the effect of distorting and broadening the spectral lines for optically thick plasmas, especially for transitions to states with low energy levels, including ground states. Performing LIBS with high spectral resolution is challenging, and measured spectra nearly always contain instrumental broadening effects. High spectral resolution becomes increasingly important as the number of species increases and for elements with high atomic mass, due to a corresponding increased number and density of spectral lines with potential for overlap. LIBS is capable of measuring the optical emission from multiple elements and transitions over a broad spectral range and can be used for plasma diagnostics such as determining excitation



temperature.

### 1.2.2 Absorption Spectroscopy of LPPs

Absorption spectroscopy techniques such as laser absorption spectroscopy (LAS) [21, 22] and laser-induced fluorescence using tunable continuous-wave (CW) lasers [23] do not suffer from some of the limitations of LIBS. Absorption techniques are well-suited to late-time measurements of LPPs (10s-1000s of  $\mu$ s, when temperatures are too low to measure optical emission) due to probing of lower-energy states of transitions [24]. As a result, absorption spectroscopy is well-suited to measuring resonant, metastable, and other transitions with low energy levels which are often problematic for LIBS due to self-absorption. In addition, because absorption measurements may be performed at the lower temperatures and electron densities present at later times in the LPP evolution, narrower spectral linewidths are measured due to reduced Doppler and Stark broadening. LAS can probe ground-state resonance lines to quantify number densities more accurately and can be used for characterizing LPPs at later times throughout the plasma evolution. Self-absorption effects are avoided with absorption spectroscopy, and absorption in high optical density conditions can be measured using narrow-linewidth continuous-wave (CW) lasers [10] or compensated using COG methods for lower-resolution measurements [25]. Tunable LAS measures species in the LPP by scanning over individual transitions with high spectral resolution, and lineshape analysis is used to determine kinetic temperatures, state column densities, and pressure broadening characteristics [20, 22, 26]. However, determination of excitation temperatures requires measurement of at least two—and preferably many—transitions, which is challenging using tunable lasers. Limited scanning ranges and speeds similarly limit the ability to probe many transitions as is often desired for multispecies analysis. Absorption spectroscopy using flashlamps or optical parametric oscillator (OPO) light sources in conjunction with high-resolution spectrometers are one solution to this problem, but use of an incoherent light source imposes trade-offs between sensitivity, spectral resolution, and bandwidth. Recent work has shown the potential for broadband absorption spectroscopy of LPPs for measurement of multiple U and UO absorption lines and determination of excitation temperatures [27].

### 1.3 Overview of Dual-Comb Spectroscopy of LPPs Experiments

LPPs can be studied by DCS with both the necessary time and spectral resolutions required to probe many absorption transitions within the timescales of late-time LPP evolution. Recent work [28–32] has shown that the technique’s high spectral resolutions enable measurements of congested optical spectra, such as those from heavy elements, to be resolved and more accurately analyzed. Broadband detection of multiple transitions, combined with Boltzmann-plot style analysis commonly used in LIBS (see Sec. 3.3), provides the ability to determine time-resolved excitation temperatures and total column densities of atomic species.

The first measurements of DCS of LPPs demonstrated broad spectral coverage of 13 nm (5 THz) to simultaneously measure Rb and K absorption in a single-shot LPP at high spectral resolution of  $< 0.2$  GHz (0.4 pm) adequate to resolve the ground-state hyperfine splitting and isotopic shift of  $^{85}\text{Rb}$  and  $^{87}\text{Rb}$  [33]. These measurements were made just before I started my graduate work. The next experiment used DCS absorption spectroscopy to determine time-resolved excitation temperatures and number densities of Fe in a LPP with time resolutions down to  $\sim 20$   $\mu\text{s}$ . For this work, published in Optics Letters [28], I and my graduate colleague Yu ”Kane” Zhang worked together to build the LPP experimental setup and determine the proper parameters that enabled detection. Zhang and postdoctoral researcher Caroline Lecaplain led the work of manuscript preparation and data analysis while I worked on maintaining the existing Yb-fiber combs and rebuilding the amplifiers and locking setups (described in Ch. 2). The ablation timing controls were designed and built by me and are described in Sec. 2.4. After finishing the modifications with Zhang, we worked together to develop a technique used to measure multiple time-delays in the LPP simultaneously, which was named burst-mode DCS and published in Optics Letters (also written by Zhang) [32].

In [32], a broadband measurement at 535 nm of a LPP containing Nd revealed many transitions which were unreported in the literature. Lack of spectroscopic data, particularly oscillator strengths of transitions, for the heavier elements precludes complete spectral analyses utilizing these elements. Chapter 4 presents DCS measurements of a Gd-containing

LPP in which high spectral resolution and frequency accuracy allowed positive identification of many previously unidentified Gd I lines from their correspondence with frequencies of dipole-allowed Gd I transitions. Using the temperatures and number densities calculated via Boltzmann-plot analyses using the transitions with known oscillator strengths, the unknown oscillator strengths of the previously unreported transitions were determined. This work was published in *Spectrochimica Acta Part B: Atomic Spectroscopy* [29], for which Zhang and I worked together on the experiment and I led the writing and analysis.

Chapter 5 presents an analysis of multiple species measured simultaneously in a LPP to determine time-resolved excitation temperatures and number densities. The experimental work was again performed by me and Zhang, and I led the analysis and writing, which was published in the *Journal of Applied Physics* [30]. Prior studies of DCS of LPPs for determination of excitation temperatures focus on characterizing single elements. Here, DCS was performed on a LPP generated by ablating a multi-element alloy containing Nd, Gd, and Fe, and individual excitation temperatures and column densities were determined for the three atomic species using Boltzmann plots. The measured excitation temperatures of Nd I and Gd I showed good agreement at all time-delays, whereas the Fe I temperature was found to be higher, and the ratios between the column densities varied with delay. The observations are understood via effects of LPP spatial averaging, elemental fractionation, and molecular formation and are compared and contextualized with previous work studying LPPs using other spectroscopic techniques. A brief discussion of the precision and accuracy of the determined excitation temperatures and column densities is also presented. Measurement and comparison of late-time excitation temperatures of multiple species in LPPs aids in understanding thermal and spatial inhomogeneities within the plume and their effects on line-of-sight measurements.

Work of using DCS to detect molecules in a LPP is also presented in Ch. 5 within the context of understanding the effects of oxide formation. This study was performed by me and my graduate colleague Ryan Rhoades using the Er-DCS system (described in Ch. 2) and was published in *Optics Letters*, with the molecular analysis and manuscript preparation being led by Rhoades. Additionally, unpublished work studying alloys of various concentrations is included in this chapter, experimental work being done by me and Zhang on the Yb-DCS

system and analyzed by me. Measurements performed across varying concentrations of the sample help to calibrate the spectroscopic results to better understand their relationship with the sample and experimental conditions.

Appendix A presents an experiment performed with the Er-DCS system in which transitions of Rb I in a LPP were measured with the fundamental and second-harmonic light of the Er-DCS system simultaneously. The transitions at 1530 nm, being of higher energy, were only detectable at hotter early times when DCS frequency resolution is poorer. To achieve higher resolution measurements, the lower energy state of the transitions was populated via optical pumping with a CW laser. This scheme results in measurement of transition lineshapes with no Doppler-broadening.

The rest of this chapter presents background and important topics on DCS and its application to LPPs. Chapter 2 provides details on the frequency combs and optical setups used in these experiments, including the stabilization, detection, and synchronization with ablation. Chapter 3 presents the mathematical theory for absorption spectra, modelling, spectral fitting, and Boltzmann-plot analyses. Chapters 4 and 5 and App. A present the details, results, and analysis of the DCS of LPP experiments discussed above. Appendix B contains details on the implementation in code of the data-processing and spectral analysis.

## 1.4 Dual-Comb Spectroscopy

### 1.4.1 Time and Frequency Domain Paradigms

Dual-comb spectroscopy employs two frequency combs to measure the absorption function of a sample. The frequency combs are generated by a pair of mode-locked lasers that emit a train of ultrashort pulses at repetition rates typically from 10s of MHz to GHz, dependent on the cavity length. The spectra of frequency combs consist of narrow laser lines, or “comb teeth”, spaced precisely at the repetition rate of the laser that can span over an octave of optical bandwidth (Fig. 1.1) [34]. With high levels of stabilization, linewidths of individual comb teeth can reach  $\sim$ Hz levels. The frequency of every comb tooth can be known based on the comb’s repetition rate  $f_{rep}$  and the carrier-envelope offset frequency  $f_{ceo}$ , which is the offset of the first tooth from 0 Hz and is related to the pulse-to-pulse phase shift  $\Phi_{ceo}$  by

$f_{ceo} = \frac{f_{rep}\Phi_{ceo}}{2\pi}$ . That is, the frequency  $f_n$  of comb tooth  $n$  is given by

$$f_n = nf_{rep} + f_{ceo}. \quad (1.1)$$

The pulse train and spectrum are related via Fourier transform such that broader spectral bandwidths generate shorter Fourier-limited pulses. The phenomenon of comb teeth can be understood as an extreme case of spectral fringing which occurs because of the temporal interference of the train of laser pulses.

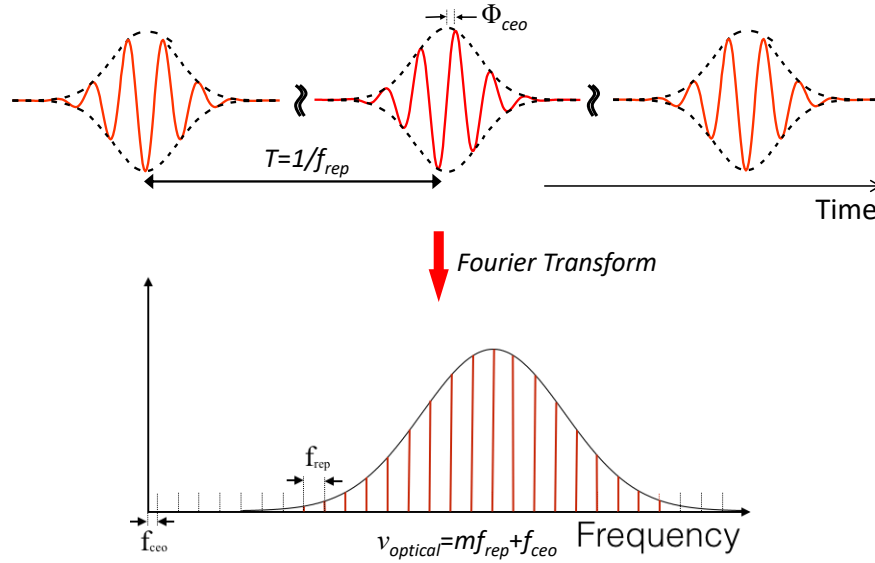


**Figure 1.1:** Illustration of the ultrashort pulse train emitted by a mode-locked laser, and the corresponding frequency spectrum which exhibits the comb structure.

Absorption spectroscopy performed with a frequency comb can be thought of as many parallel CW-laser absorption measurements. Direct detection of optical frequencies, however, is not possible with standard electronics nor with most spectrometers due to their limited resolution. To measure the absorption at many optical frequencies simultaneously, an interferometric measurement can be performed with a second frequency comb, a technique analogous to Fourier-transform spectroscopy (FTS) [35]. FTS consists of a variety of related techniques, but the most common method employs a broadband incoherent source that is collimated and passed through an absorptive sample (removing the sample provides

the background spectrum). The light enters a Michelson interferometer, in which it is split into two beams by a beamsplitter, each propagating down a separate arm. The light is retroreflected at the end of each arm, recombined at the original beamsplitter, and then incident on a photodetector. The position of one arm's mirror is scanned perpendicular to the beam propagation direction, so that the path difference between the two arms is varied, typically from 0 to as much as a meter. The scanning mirror produces a varying delay between the two copies of the light source, generating a time-dependent interference pattern called an interferogram. In DCS, the scanning mirror is replaced with a slight difference in the repetition rates of the two interfered combs. Successive pulses from each comb pass through each other, resulting in a discretely sampled first-order cross-correlation of the electric field amplitudes (Fig. 1.2(a)). This interferogram consists of a short centerburst, which occurs when the ultrashort pulses overlap, with long tails where free-induction decay may be detectable due to any absorption present. According to the Wiener-Khinchin theorem, the Fourier transform of an autocorrelation gives the power spectrum, or spectral decomposition, of the original signal. Thus, the Fourier transform of the signal generated via detection of the interferogram with a fast photodetector yields the portion of the optical power spectrum common to both lasers (Fig. 1.2(b)). The frequency spectrum is called the single-beam spectrum (SBS), per the terminology used in Fourier transform infrared spectroscopy (FTIR). The absorption signal of a sample within the combs' beampaths will be written onto the power spectrum.

The interferograms in DCS repeat with frequency

$$\Delta f_{rep} = |f_{rep,Comb1} - f_{rep,Comb2}| \quad (1.2)$$

so that the time between centerbursts is given by

$$T_{IFG} = \frac{1}{\Delta f_{rep}}. \quad (1.3)$$

Also note that the interferogram shown in Fig. 1.2(a) is double-sided, which results when the combs are interfered before they both probe the sample (called a colinear measurement). In a dispersive measurement, only one comb probes the sample before comb interference, and

a single-sided interferogram is produced that has the added benefit of containing the phase information of the absorbance function. Only double-sided interferograms were utilized in the experiments contained in this work, due to their being more straightforward to process (see Sec. 1.4.4).

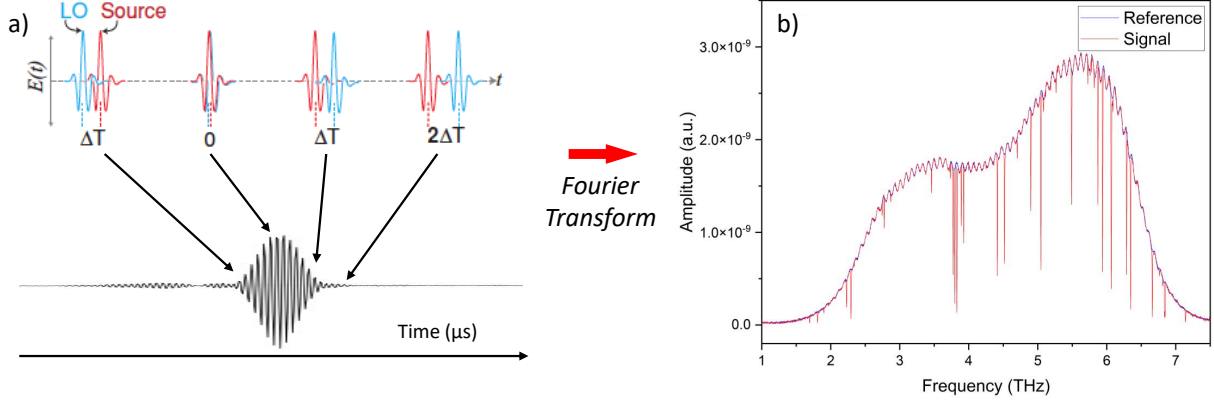


**Figure 1.2:** (a) Illustration of the interference of the pulse trains from two frequency combs with slightly different repetition rates to generate an interferogram. The Fourier transform yields the overlap power spectrum in (b), called the SBS. Here, the reference SBS contains no absorption, whereas the signal SBS was measured with an absorptive sample present. The spectral fringing present in both spectra is due to etaloning and divides out when calculating transmittance.

DCS can also be understood in the frequency-domain paradigm (Fig. 1.3). When spatially overlapped and mixed on a photodetector, the frequency modes of the combs generate beat frequencies offset by  $\Delta f_{rep}$  in a massively-parallel heterodyne measurement. The beatnotes form an RF comb that can be directly detected by electronics. An absorption feature which reduces the intensity of any of the optical comb teeth will reduce the intensity of the corresponding RF comb teeth. This RF comb is the overlap power spectrum described above. The measured RF frequencies directly map to their associated optical frequencies according to

$$f_{optical} = f_{RF} \cdot \frac{f_{rep}}{\Delta f_{rep}} + f_{offset}, \quad (1.4)$$

where  $f_{offset}$  is a constant shift applied to the frequency spectrum for absolute calibration. The need for  $f_{offset}$  comes from the fact that the RF beatnotes are not unique across the full bandwidth of the combs. They instead repeat/alias, with reflection points at  $0$  Hz and  $f_{rep}/2$ .  $f_{rep}/2$  is a reflection point due to the fact that, given a tooth of one

comb, there always exists a tooth of the other comb such that their frequency difference is  $\leq f_{rep}/2$ , assuming the repetition rates of the combs are similar (more specifically, that  $\frac{1}{2}f_{rep,Comb1} \leq f_{rep,Comb2} \leq 2f_{rep,Comb1}$ ). The maximum *optical* bandwidth that can be measured without beatnote aliasing is given by

$$\Delta\nu = f_{rep}^2 / (2\Delta f_{rep}). \quad (1.5)$$

Figure 1.4 illustrates this phenomenon and how aliasing of the RF beatnote frequencies occurs if the measured optical bandwidth extends beyond the reflection points of the corresponding RF region. To avoid aliasing in the RF domain, the measured optical band must be  $\leq \Delta\nu$  and must not include pairs of comb teeth with beatnotes that cross the reflection points. Note that filtering in the RF domain does not prevent beatnote aliasing; only the optical frequencies can be filtered to prevent the generation of aliased beatnotes. The optical bandwidth and center frequency can be controlled by dispersing the comb light and using spatial filtering, such as a mask or slit, as discussed in Sec. 2.3. The measured RF band can also be shifted away from reflection points by shifting the one comb's teeth by a constant value, such as with an AOM, as is done in Ch. 4.

The value of  $f_{offset}$  used for calibration, mentioned in Eq. 1.4, can be determined via calibration to a measured optical transition whose center frequency is known. Alternatively,  $f_{offset}$  can be known without measurement of an absorption feature if the frequencies of the comb teeth are known, i.e., if the parameters which define the combs according to Eq. 1.1 are known. These parameters can be determined based on the parameters of the comb stabilization (see Sec. 2.2), as is done in App. B.1. Note that  $f_{offset} \approx f_{j,Comb1} \approx f_{k,Comb2}$ , for comb teeth  $j$  and  $k$  of each comb which are nearest the measurement bandwidth and have a frequency difference of  $\sim 0$  Hz (as shown in Fig. 1.4). This approximation is good to within  $f_{rep}$ .

#### 1.4.2 Apodization and Frequency Resolution

Apart from the recorded interferograms being discretely sampled rather than continuous, the method is completely analogous to FTS, with the mechanical delay arm replaced with



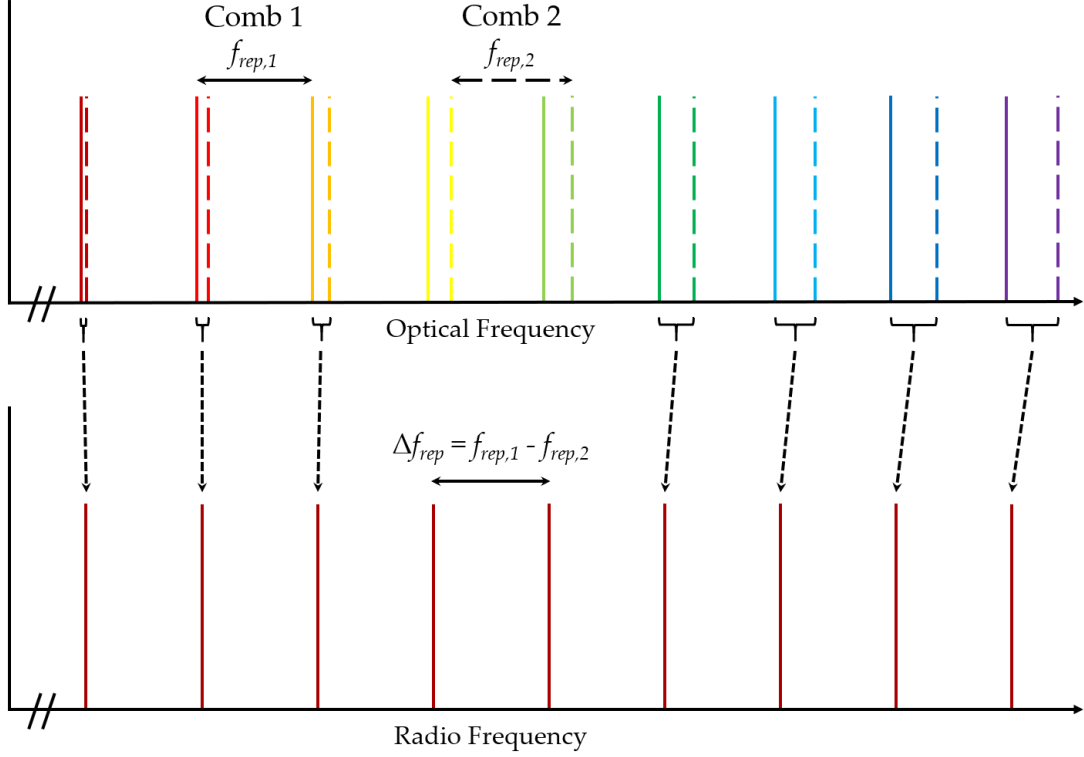


**Figure 1.3:** Illustration of the interference of two frequency combs with slightly different repetition rates to generate a directly detectable RF comb.

the precision, accuracy and rapid all-optical delay offered by the frequency combs. Scan speeds of  $T_{IFG}$  (Eq. 1.3) are on the order of  $\sim$ ms for values of  $\Delta f_{rep}$  used in this work, which are much faster than FTIR scan speeds ( $\sim$ seconds). As noted above, the interferograms in DCS repeat with a period between centerbursts of  $T_{IFG}$ . The DCS signal is present for as long as the combs are interfered, but it can only be recorded for a finite length of time ( $T_{meas}$ ). The signal, then, is effectively multiplied by some function with width equal to  $T_{meas}$ . This function is called an apodization window. The convolution theorem of Fourier transform theory states that the multiplication of two functions results in the convolution in the Fourier domain of the Fourier transform of the two functions. When the recorded signal is Fourier transformed to produce a frequency spectrum, the resulting SBS is necessarily convolved with the Fourier transform of the apodization window, called the instrumental lineshape function (ILF). The convolution causes the absorption features to be broadened

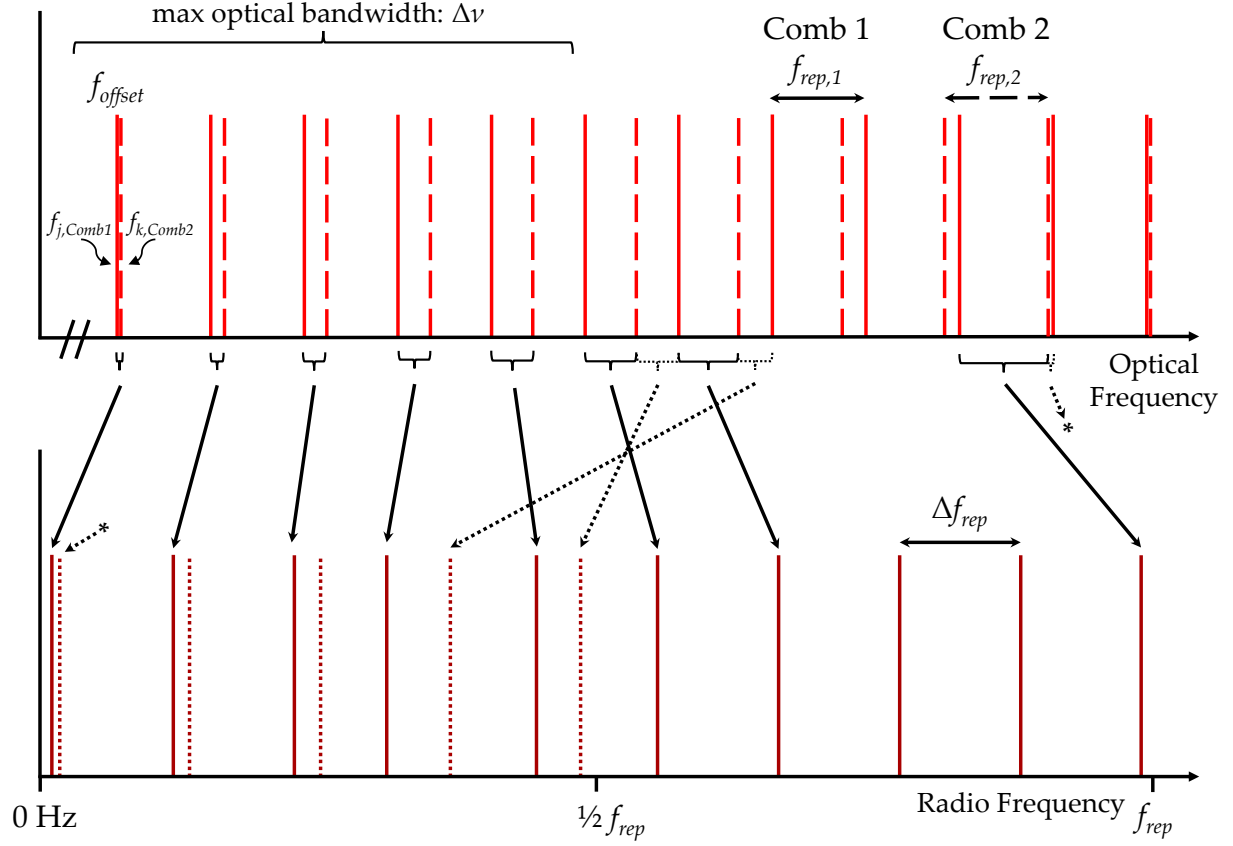


**Figure 1.4:** Illustration expanding on Fig. 1.3 to show the aliasing of RF beatnotes which occur at 0 Hz and  $f_{\text{rep}}/2$ . The combs are differentiated by solid and dashed lines. Aliased beatnotes are depicted with dotted lines. Note that all comb teeth present beat against each other in DCS: teeth from the same comb beat to produce RF frequencies at  $f_{\text{rep}}$  and its harmonics, and beatnotes generated between the combs have frequencies  $f_{\text{RF}}$  between 0 Hz and  $f_{\text{rep}}/2$  that also repeat according to  $f'_{\text{RF}} = f_{\text{RF}} + n f_{\text{rep}}$ . Only some beatnotes and their aliases are shown here for clarity.

based on the shape and width of the ILF (broadening is negligible if the ILF width is much smaller than the linewidth of the features). Therefore, the ILF width is an important parameter inherent to the measurement process and is called the instrumental resolution ( $\delta f_{\text{inst}}$ ). There are multiple definitions of the ILF width, and here we will choose to define it as the full-width at half-maximum (FWHM) linewidth of the ILF. For all definitions, though,  $\delta f_{\text{inst}}$  is inversely proportional to the time-duration of the measurement. That is,

$$\delta f_{\text{inst}} \propto \frac{1}{T_{\text{meas}}}, \quad (1.6)$$

and the proportionality constant depends on the shape of ILF as well as the definition chosen. The absorption lineshapes cannot be measured with a resolution better than  $\delta f_{inst}$  due to the convolution. Thus, the measurement resolution,  $\delta f_{meas}$ , is limited by  $\delta f_{inst}$ , but not always equivalent, as will be shown.

The above discussion refers to absorption linewidths and measurement resolutions using the terms of FTS. Within the context of DCS, though, all measured RF frequencies are directly mappable to optical frequencies according to Eq. 1.1. The mapping of frequency deltas (e.g., linewidths and bandwidths), is given by the relation

$$\Delta f_{opt} = \Delta f_{RF} \cdot \frac{f_{rep}}{\Delta f_{rep}}, \quad (1.7)$$

which is easily derived from Eq. 1.1. It is more informative to discuss linewidths and resolutions in DCS in terms of optical frequencies. Thus, all future instances of  $\delta f_{inst}$  and  $\delta f_{meas}$  will indicate the optical frequency versions (calculated via the conversion in Eq. 1.7), and only  $\delta f_{inst,RF}$  will indicate the instrumental resolution in the RF domain. The relation that  $\delta f_{meas}$  is limited by  $\delta f_{inst}$  still holds in the optical frequency domain given the linear nature of the conversion in Eq. 1.7. Note, however, that Eq. 1.7 implies that  $\delta f_{inst}$  is dictated by  $\delta f_{inst,RF}$  (and thus  $T_{meas}$ , based on Eq. 1.6) as well as the comb parameters  $f_{rep}$  and  $\Delta f_{rep}$ .

The simplest apodization window, a rectangular function, is the effective apodization which occurs if a more complex function is not used to multiply the finite signal, as it simply weights the signal with 1s at every time recorded and with 0s at all other times. The ILF of a rectangular apodization window is a sinc function, which has oscillations in the function wings. Convolution with the signal's frequency spectrum often results in ringing in the wings of the absorption lineshapes in the SBS. The high frequency ringing is caused by the discontinuity of the rectangular function. Apodization windows which are continuous, or at least feature smaller discontinuities at the edges, mitigate ringing in the SBS. Figure 1.5 shows the functional form for a number of popular apodization windows. Their associated ILFs are shown in Fig. 1.6. Note that the FWHM linewidth is smallest for the rectangular apodization window. The best instrumental resolution  $\delta f_{inst}$  in Fourier transform spectroscopic measurements is achieved when using a rectangular apodization

function. The spectral ringing which may occur in this case can be mitigated, however, with the use of other apodization windows, at the expense of  $\delta f_{inst}$ . Figure. 1.7 shows an example of this trade-off: The Blackman-Harris apodization window smooths the ringing in the lineshape wings, but at the cost of broadening the lineshapes. Many apodization functions have been studied [36], and the choice of function often depends on application. Note that the apodization windows here are applied symmetrically about the centerburst, since only double-sided interferograms are being utilized in the experiments discussed in following chapters.

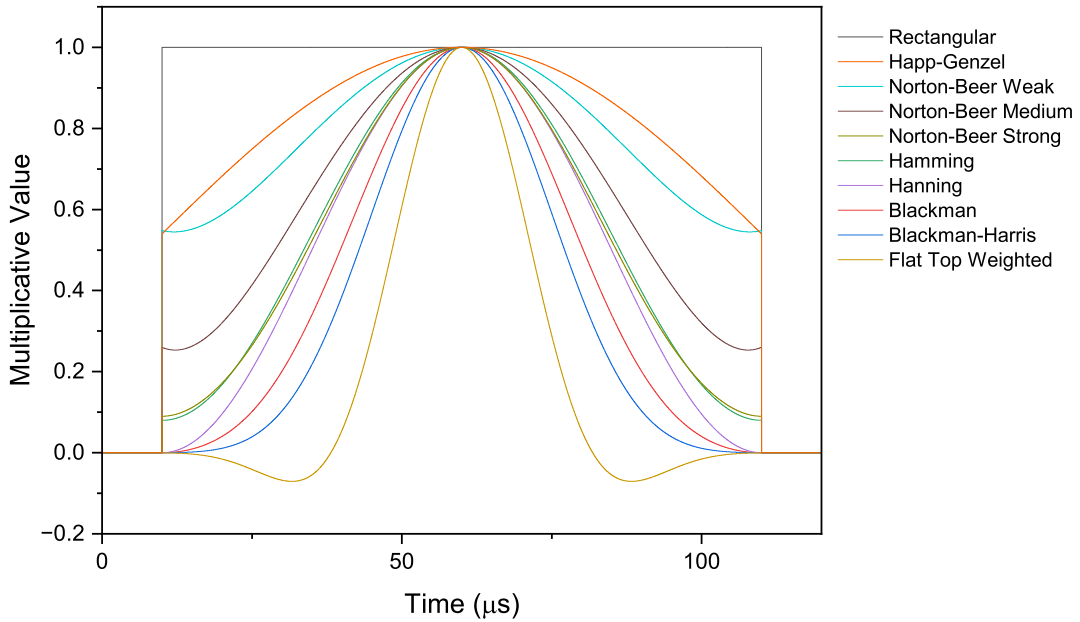


**Figure 1.5:** Plots of various 100  $\mu\text{s}$  wide apodization windows. Their associated ILFs are shown in Fig. 1.6. 100  $\mu\text{s}$  represents a common apodization window size (equal to  $T_{meas}$ ) in DCS measurements of LPPs.

Note that any spectral analysis which utilizes peak areas measured with Fourier transform spectroscopic techniques must account for these instrumental broadening effects (see Sec. 3.2). Furthermore, the convolution with the ILF has the effect of breaking the linearity between peak area and number density as described by Beer’s Law for strongly absorbing lines [36]. The cause is that the SBS, as opposed to the absorbance spectrum, is convolved with the ILF in the measurement process. In transmission, strong absorbance causes the bot-

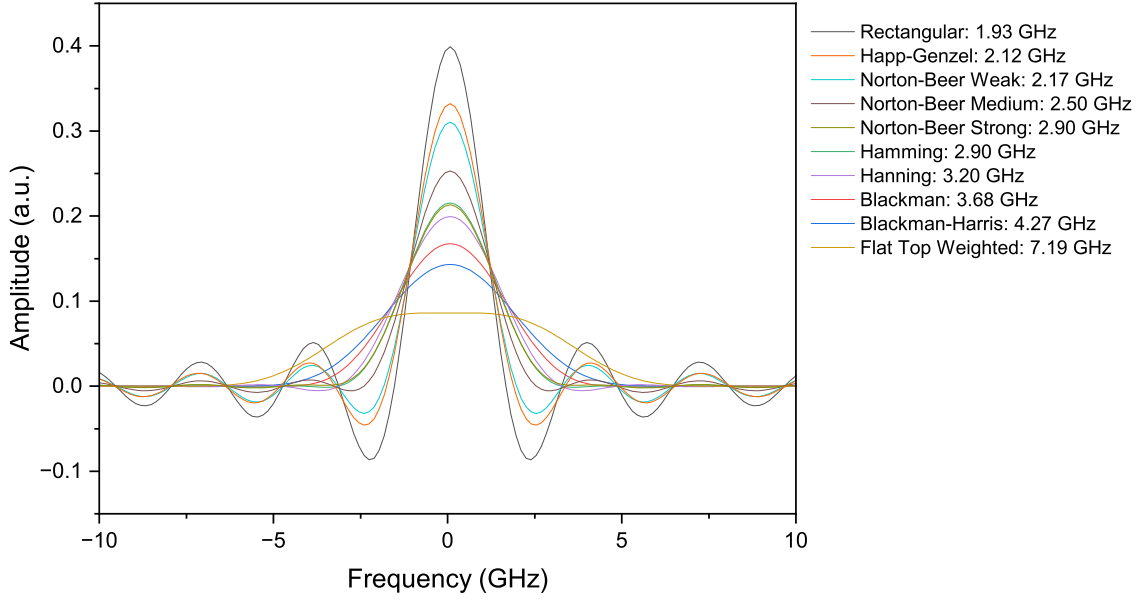


**Figure 1.6:** The associated ILFs of the apodization windows plotted in Fig. 1.5. The associated optical linewidth of each is listed in GHz, calculated assuming  $f_{rep} = 80$  MHz and  $\Delta f_{rep} = 500$  Hz. Note that 500  $\mu$ s of 0s were padded to each side of the apodization window to decrease the frequency spacing to better resolve the functional shape of the ILF for better viewing. Padding 0s does not change the ILF linewidth, which is dependent only on the temporal duration of nonzero window ( $T_{meas}$ ).

tom of the lineshape to approach, but never reach, 0. Note that transmittance is calculated by dividing an SBS containing absorption features with a second absorption-free reference SBS, the procurement of which is discussed in the next section and which is generally unaffected by the ILF convolution as it contains no lineshapes. For very strong absorbances, the part of the lineshape near 0 transmission becomes flattened and is distorted in the process of convolution with the ILF. For this reason, it is important that this effect be accounted for in a spectral model and that the convolution be applied in transmittance, as is also discussed in Sec. 3.2. A more detailed explanation of this effect is presented by Griffiths and de Haseth on p. 178 in [35].

A signal measured over the time of one period of the interferograms will have an instrumental linewidth roughly equal to the repetition rate. That is, if  $T_{meas} \approx T_{IFG}$ , then  $\delta f_{inst} \approx f_{rep}$ . Approximations are used here due to small variations between the different apodization function, many of which have time-bandwidth products close but not equal to

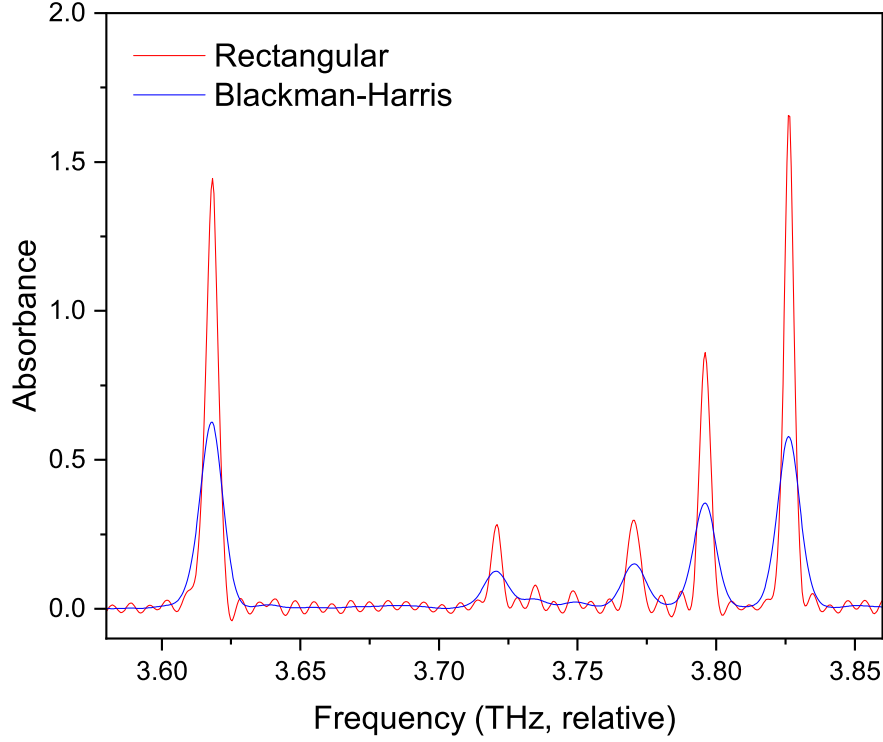


**Figure 1.7:** Comparison of absorbance spectra processed using a rectangular apodization function versus a Blackman-Harris function. The absorption lineshapes of the rectangular window case are narrower but feature ringing in the baseline.

1. Taking into account Eq. 1.6, if  $T_{meas} > T_{IFG}$ , then  $\delta f_{inst} < f_{rep}$ , and negligible broadening of the absorption lineshapes occurs, as mentioned above. Furthermore, the linewidths of the comb teeth will be resolved. An example of a "comb-tooth resolved" measurement is shown in Fig. 1.8, in which DCS was used to measure the reflection from a Fabry-Perot cavity. To highly resolve the comb teeth,  $T_{meas}$  must be  $\gg T_{IFG}$ . Note that in such measurements, the absorption lineshapes are not significantly broadened in the convolution with  $\delta f_{inst}$ , but they are also not measured/probed at the resolution  $\delta f_{inst}$ . Rather, they are probed at the frequency spacing of the comb teeth, i.e.,  $f_{rep}$ . Thus, the effective resolution of the absorption measurement,  $\delta f_{meas}$ , does not equal  $\delta f_{inst}$  and is instead limited to  $f_{rep}$ , i.e.,  $\delta f_{meas} = f_{rep}$ . For example, in Fig. 1.8, the individual comb teeth are resolved, but the modes of the Fabry-Perot cavity are probed only at each comb tooth. This is because no light that can be absorbed and measured exists between the comb teeth. Absorption features

narrower than  $f_{rep}$  will be unresolved since there are no more than at least one comb tooth to probe them. However, higher resolution spectra ( $\delta f_{meas} < f_{rep}$ ) can be achieved by scanning the frequencies of the comb teeth across multiple measurements.

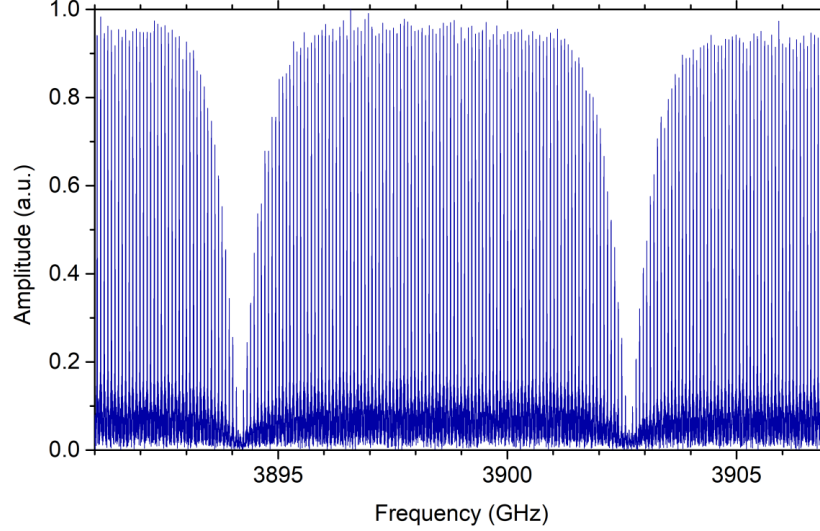


**Figure 1.8:** Comb-resolved reflection measurement of the transmission of a Fabry-Perot cavity.

The opposite case of  $T_{meas} < T_{IFG}$  results in  $\delta f_{inst} > f_{rep}$ . Here, the comb teeth are not resolved and the effective measurement resolution is set by the instrumental resolution, i.e.,  $\delta f_{meas} = \delta f_{inst}$ . In this case, absorption lineshapes are broadened via the convolution with the ILF, as previously mentioned. Smaller values of  $T_{meas}$  may be necessary in measurements with time-resolution requirements, such as measurement of samples with absorption functions that are changing in time. Spectroscopy in LPPs is one example, and the need for time-resolved measurements usually precludes operation of DCS at its maximum spectral resolution of  $f_{rep}$ . LPPs are short-lived, and DCS measurements probe the plume within 10s to 100s of  $\mu s$  of ablation. Figure 1.9 illustrates how the ablation/centerburst time-separation sets an upper limit on the apodization window width ( $T_{meas}$ ) of twice the time-delay being probed. The time-delay is defined as the time between ablation and the center of the envelope of the following centerburst. If a wider apodization window (larger  $T_{meas}$ ) is used on the signal, then times before ablation will be included (unacceptably) in the data. Measurements

of later-time delays can be apodized with wider windows (larger  $T_{meas}$ ) to achieve better frequency resolution, since in this case  $\delta f_{meas} = \delta f_{inst}$  (and recalling Eq. 1.6). By the same logic, at a given time-delay, apodization windows narrower than twice the time-delay can be used to achieve higher time resolution (shorter  $T_{meas}$ ) at the expense of poorer spectral resolution. Note that each time-delay requires a separate measurement, unless burst-mode DCS is utilized, mentioned above and presented in [32].

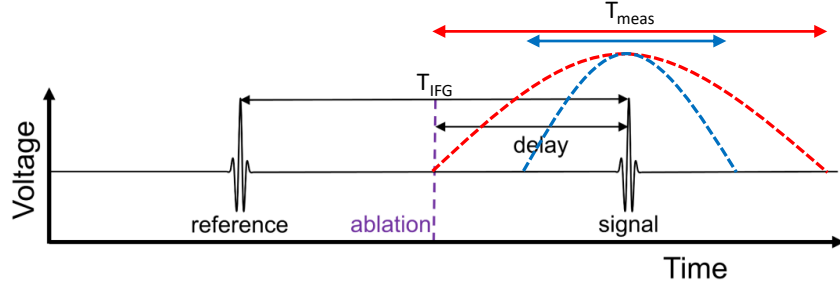


**Figure 1.9:** Illustration of the relationship between time-delay and apodization window width ( $T_{meas}$ ) in DCS-LPP experiments. The interferogram following ablation probes absorption in the LPP. For a symmetric apodization window, the maximum  $T_{meas}$  is twice the time-delay (shown in dashed red), so that no times before ablation are included. A smaller value of  $T_{meas}$  can be used (shown in dashed blue) but results in poorer frequency resolution. Thus, the time-delay effectively sets a limit on best frequency resolution  $\delta f_{meas}$  achievable via  $T_{meas}$ . Also shown is the preceding interferogram, recorded as a reference for background absorption when no LPP is present, discussed in Sec. 1.4.3.

The true time resolution of DCS measurements remains an open topic of study. At worst, the time resolution is the full width of the apodization window ( $T_{meas}$ ). However, preliminary studies that involved applying apodization windows of various lengths to a time-dependent DCS signal have shown that absorbance strength does not change significantly when portions of the signal far from the centerburst are excluded/heavily attenuated. The result indicates that the time-averaging that occurs over the signal window is more strongly weighted to regions around the centerburst, making the time-resolution better than  $T_{meas}$ . More testing is needed to better understand the form of the time-average weighting function, which is expected to be dependent on the shapes of the apodization window and the interferogram/centerburst.



### 1.4.3 Measurement Optimization in DCS

The preceding discussion of frequency resolution assumes that the frequencies of the comb teeth do not change in time. However, the comb cavities are typically susceptible to mechanical vibrations as well as temperature, pressure, and humidity fluctuations. Given the high precision and accuracy of frequency combs, small variations can be detected through changes in the comb teeth frequencies. As such, a high degree of active stabilization of the comb frequencies is required to prevent unwanted frequency and phase noise in the measurement. Section 2.2 discusses the methods of stabilization used for the experiments in this work, used to ensure that the drift of the comb frequencies is tolerably small within the measurement times. Note that some DCS techniques do not utilize active stabilization but use signal-processing correction techniques in conjunction with free-running combs [37]. For instance,  $\Delta f_{rep}$  can be recorded as it changes in time and used in post-processing to correct for drift. Bi-directional cavities can also be employed, in which both combs are generated within the same laser cavity but with opposite propagation directions so that the relative noise between the combs is reduced [38].

When studying LPPs, absorption is typically measured over hundreds of ablation shots and the spectra averaged (discussed in the next section). DCS interferograms repeat with period  $T_{IFG}$ , with typical values of 1.25-4 ms (given  $\Delta f_{rep}$  values of 250-800 Hz). The ablation lasers used in this work, however, operate at 10 Hz (100 ms period). Thus, the LPPs have a low duty cycle since absorption occurs for only a few ms at most. Only the interferogram whose centerburst comes directly after ablation is recorded to measure absorption (and only a portion of that interferogram is used, selected via an apodization window with width  $T_{meas}$ , as discussed above). Thus, the total acquisition time in a DCS-LPP experiment over  $N$  ablation events is given by  $T_{acq} = N \times 100$  ms. Figure 1.9, discussed above, shows the interferogram immediately following ablation that is measured for absorption as well as the interferogram immediately preceding ablation. At times just before ablation, any remaining absorption due to the previous ablation event is too weak to detect. Thus, the aforementioned interferogram can be used to obtain a reference SBS. The reference SBS provides the background (LPP-free) absorption profile, and is required for the calculation

of transmittance and absorbance discussed in the next section. Typically in absorption spectroscopy, a second beamline which circumvents the sample is used for this background, but there can be differences between the reference and signal dependent on the optics used in the separate paths. Alternatively, the sample can be removed and a second measurement recorded. In the case of DCS, however, interferometric drift over the timescales of making two measurements can introduce background variations. The low duty cycle of the LPPs is convenient for reference SBS obtainment, and these reference SBSs typically have excellent agreement with the signal SBS.

Since one of the advantages of DCS is the ability to make absorption measurements over broad bandwidths, it may be desirable to maximize the bandwidth to measure as many transitions as possible. An upper limit to the measurement bandwidth is the overlap of the optical bandwidths of the two combs. The output spectral bandwidth of passively mode-locked frequency combs is often 10s of nm and can be greatly extended through nonlinear frequency generation techniques to achieve supercontinua [39]. The effective measurement bandwidth, however, will be limited by the alias-free bandwidth  $\Delta\nu$ , defined above in Eq. 1.5. This bandwidth can be increased by increasing  $f_{rep}$ . However, the upper limit for  $f_{rep}$  is set by the required spectral resolution of the measurement in the case of  $T_{meas} > T_{IFG}$  (in which  $\delta f_{meas} = f_{rep}$ , as discussed above). For example, absorption lineshapes with 1 GHz linewidths cannot not be resolved in a DCS measurement using combs with  $f_{rep} = 2$  GHz (and will also not be resolved if  $T_{meas} < T_{IFG}$  causing  $\delta f_{meas} > f_{rep} = 2$ ). Also, increasing  $f_{rep}$  decreases the energy per pulse, causing higher average powers to be necessary to drive nonlinear frequency conversion processes that may be necessary to reach wavelengths of interest. Alternatively for increasing  $\Delta\nu$ ,  $\Delta f_{rep}$  can be decreased, which has the effect of increasing  $T_{IFG}$  according to Eq. 1.3. Thus, in the case of measuring  $N$  consecutive interferograms, the acquisition time  $T_{acq}$  is increased according to the simple relation  $T_{acq} = N \cdot T_{IFG}$ . Note this is a different case than discussed above for LPP measurements, in which non-consecutive interferograms are recorded and the acquisition time is set by the ablation rate. However, in DCS-LPP measurements,  $T_{meas}$  is nearly always  $< T_{IFG}$  and is held constant as  $\Delta f_{rep}$  is varied. Here, as discussed above in Sec. 1.4.2,  $\delta f_{meas} = \delta f_{inst}$ , which will vary according to Eq. 1.7 due to the variation of  $\Delta f_{rep}$ . Note that  $f_{inst,RF}$  remains unchanged since

$T_{meas}$  is constant (Eq. 1.6). Therefore, if  $\Delta f_{rep}$  is decreased to increase  $\Delta\nu$ ,  $\delta f_{meas}$  increases (becomes poorer) if  $T_{meas}$  remains unchanged. In other words, the interferogram periodicity becomes longer when  $\Delta f_{rep}$  is increased, and so measurement of longer time windows is required to achieve the same optical resolution. Such a trade-off may be unacceptable in time-sensitive measurements, such as studies of LPPs. Note that the same trade-off occurs if  $f_{rep}$  is increased (though bandwidth is gained more quickly since it goes with the square of  $f_{rep}$ ). A solution is to increase  $f_{rep}$  and  $\Delta f_{rep}$  in tandem so that their ratio remains constant.

An additional advantage of DCS is the large dynamic range of measurements, with the ability to measure both strongly and weakly absorbing features simultaneously. However, the signal-to-noise ratio (SNR) of DCS spectra must often be improved via averaging, which decreases the standard deviation of the noise floor so that weakly absorbing signals are detectable above the noise. For Gaussian noise, the SNR will increase as  $1/\sqrt{N}$  for  $N$  averaged spectra, as shown in Fig. 1.10. For the DCS systems discussed here, values for  $N$  of 500-1000 typically results in minimum detectable absorbances of  $\sim 0.01$  absorbance units. The implementation of averaging in DCS signal processing is discussed in the next section. SNR can also be improved by increasing the absorption path length in order to increase the amount of absorption.

In CW-LAS, increasing the optical power generally improves the SNR. In DCS, increasing the bandwidth increases the incident power, but it also has the effect of increasing the shot noise since there are more comb teeth detected without additional signal detected. It can be shown that for DCS,  $SNR \propto 1/M$ , for  $M$  spectral elements incident on the photodetector (i.e.,  $M$  comb teeth) [1, 40]. For a shot-noise limited measurement, which is the ideal case,  $SNR \propto 1/M$  remains true, but many factors often play a role which change the SNR calculation, including detector noise (noise equivalent power), relative intensity noise of the combs, and the dynamic range of the detector (DCS measurements often saturate most photodetectors and the combs must be attenuated). Derivations and discussions of the SNR in DCS measurements are presented in [1] and [40].

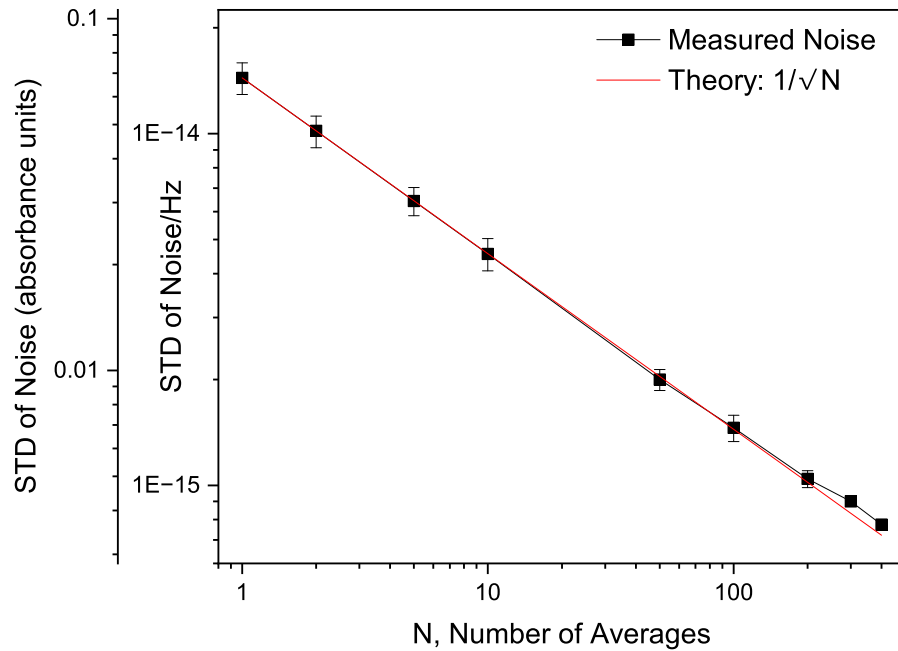


**Figure 1.10:** Measurement of the standard deviation (STD) of the noise floor in absorbance for a DCS-LPP measurement with bandwidth of 4.7 THz centered near 783 nm. The signal was detected using a balanced detector. Error bars represent the STD of the plotted values across multiple averaging bins.

#### 1.4.4 DCS Signal Processing

Once DCS data are collected, several post-processing steps must be taken to generate absorption spectra. If absorption strengths are to be used for analysis, care must be taken that the photometric accuracy of the spectra is conserved. A large part of my doctoral work consisted of developing a suite of codes used for generating and analyzing DCS absorption spectra. Much of the work focused on determining the best processing methods as well as developing codes which were robust, efficient, and user-friendly to minimize processing time and allow others to utilize them. An overview of some of the important topics is presented here, and details regarding implementation in code are found in App. B.1.

Raw DCS data consist of a discrete interferogram detected by a fast photodetector ( $\sim 100$  MHz bandwidth). The voltage of the detector is discretely sampled in time by a fast data-acquisition board (DAQ) and recorded. Post-processing the raw DCS data means trans-

forming the recorded time-domain signal into a calibrated absorption spectrum based on the theory described in the previous sections. To use the spectra in analysis, e.g., using absorption peak areas in a Boltzmann-plot analysis (see Sec. 3.3), the photometric accuracy of the spectra must be ensured. Griffiths and de Haseth discuss the major contributors to photometric accuracy degradation in FTIR spectrometry in [35]. Several of these apply to DCS as a Fourier-transform type of spectroscopy. These include apodization effects, baseline offsets, and the effect on strongly absorbing lines due to detector response nonlinearity [41, 42].

The heart of the post-process is the Fourier transform. The frequency spectrum  $\hat{f}'(\nu)$  of the time-domain signal  $f(t)$  is calculated via Fourier transform as

$$\hat{f}'(\nu) = \int_{-\infty}^{+\infty} f(t) \exp(-i2\pi\nu t) dt. \quad (1.8)$$

Note that  $f(t)$  has a time-width of  $T_{meas}$ . If the interferogram  $f(t)$  has any asymmetry, the frequency spectrum will be complex:

$$\hat{f}'(\nu) = Re(\nu) + Im(\nu). \quad (1.9)$$

The full complex spectrum  $\hat{f}'(\nu)$  exists across two planes and cannot be plotted as a single spectrum. The magnitude of  $\hat{f}'(\nu)$ ,

$$|\hat{f}'(\nu)| = \sqrt{Re(\nu)^2 + Im(\nu)^2}, \quad (1.10)$$

can be shown as a single spectrum and contains both complex parts but exhibits noise nonlinearities. Specifically, the noise floor will be above zero since all values are squared. Since this is a nonphysical result and purely a mathematical effect, a solution is to utilize phase-correction:

$$\hat{f}(\nu) = Re(\nu) \cdot \cos \theta_{MPC}(\nu) + Im(\nu) \cdot \sin \theta_{MPC}(\nu) \quad (1.11)$$

gives the Mertz phase-corrected spectrum, where  $\theta_{MPC}(\nu)$  is the low-passed, slowly varying

phase of the complex spectrum [35, 43, 44]. The low-passed phase  $\theta_{MPC}(\nu)$  is estimated from the Fourier transform of a short, symmetric portion of the centerburst. The resulting spectrum is real, and the inverse Fourier transform will be symmetric (Fig. 1.11). More specifically,  $\theta_{MPC}(\nu)$  is estimated as the phase of Fourier transform of  $f_{MPC}(t)$ , calculated by multiplication of  $f(t)$  with a very narrow rectangular function centered about the centerburst of  $f(t)$ . For example, in DCS-LPP experiments,  $f_{MPC}(t)$  typically consists of only the central 80 ns of  $f(t)$ . Figure 1.12 shows a Mertz phase corrected spectrum along with magnitude of the Fourier transform of the same signal. Other methods of phase-correction must be utilized for single-sided interferograms, such as the Forman method [35, 43, 45].

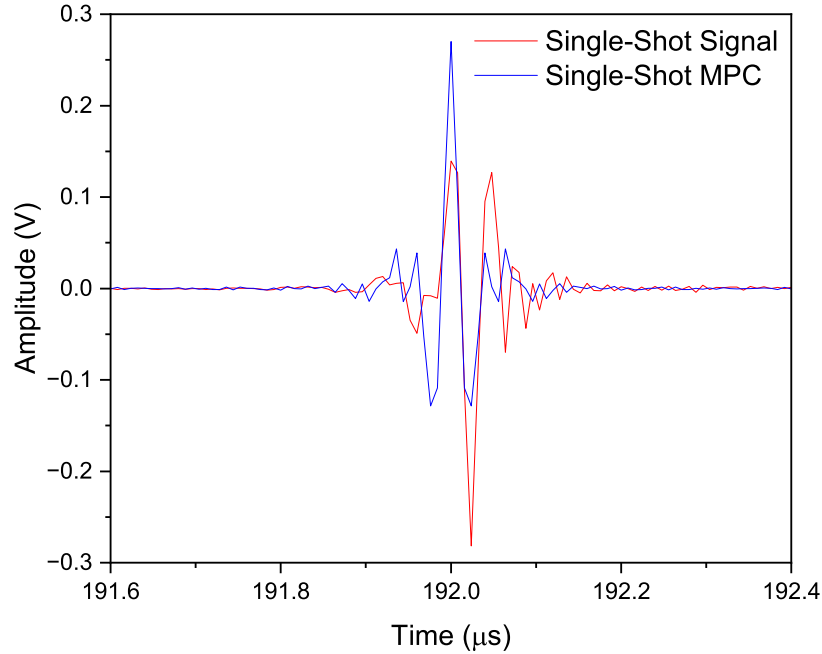


**Figure 1.11:** Comparison of the center-burst of an unaveraged centerburst and the inverse Fourier transform of its Mertz phase corrected (MPC) Fourier transform. The symmetry of the Mertz phase corrected centerburst is due to the Mertz phase corrected frequency spectrum being real (in a complex number sense).

The apodized time-domain signal can be zero-padded by simply appending 0s symmetrically to both ends of the data for inclusion in the Fourier transform. The effect is to “smooth” the data by adding more points within the same RF frequency bandwidth, much

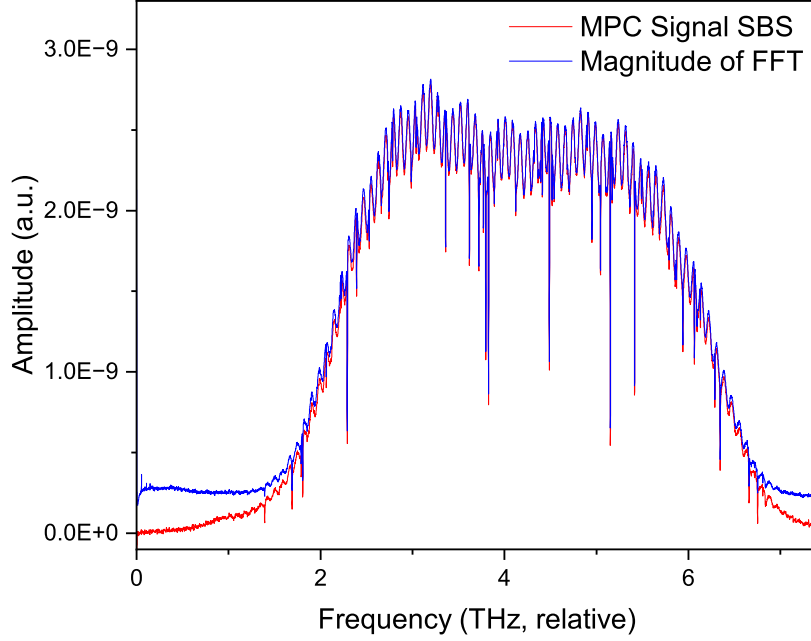


**Figure 1.12:** Comparison between a Mertz phase corrected (MPC) SBS and the magnitude of the Fourier transform of the same signal. Note the amplitude bias of the noise floor as well as within the optical window.

like an interpolation, as shown in Fig 1.13. Though the frequency-domain point spacing will be smaller,  $\delta f_{meas}$  is not decreased (since  $T_{meas}$  is not increased since it describes the width of the nonzero portion of the signal) and higher frequency components will not be introduced.

For Fourier transform spectroscopic techniques, the data can be averaged either in the time or frequency domain. For time-domain averaging, centerbursts need to be nearly identical. Otherwise, phase-slippage degrades the average centerburst (Fig. 1.14), which can average to zero if extreme phase-slipping is present over the averaging time. To prevent this, several techniques can be employed to realign the phases of the centerburst carrier frequencies. A simple time-shift of the signal can be used, and alignment can optimize overlap of the centerburst cycles (either by aligning the centerburst peak values or maximizing their cross-correlation) or optimize overlap of the centerburst envelopes (by utilizing Hilbert transformations). None of these techniques, however, utilize any phase corrections, which may be necessary if an appreciable amount of phase error is present. Such techniques are

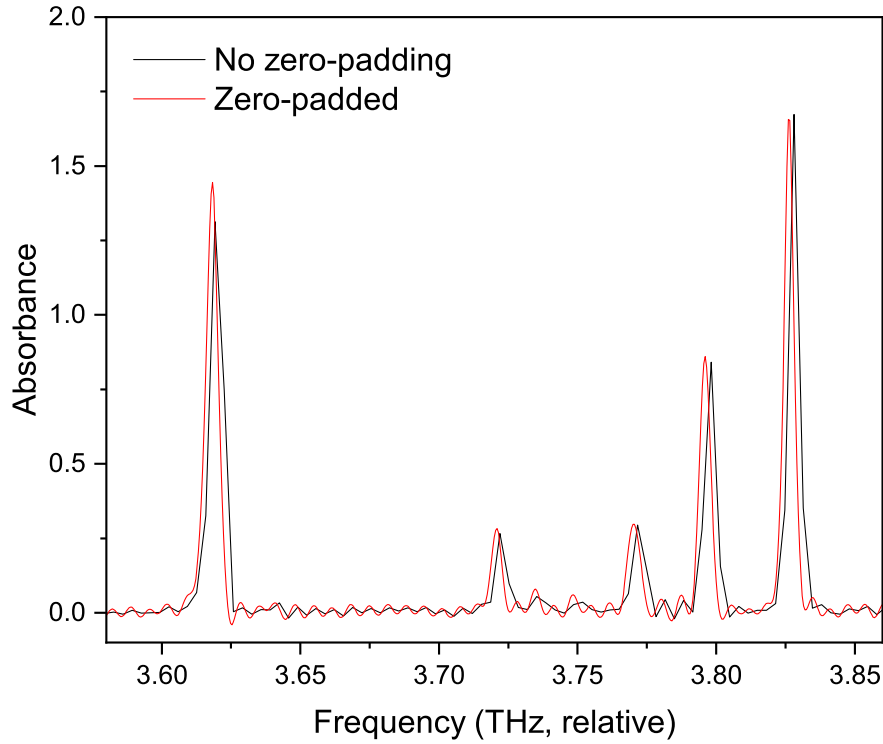


**Figure 1.13:** Comparison of absorbance spectra processed using a rectangular apodization function processed with zero-padding and none.  $163 \mu\text{s}$  of 0s were padded to each side of the  $58 \mu\text{s}$  apodized signals in the former case. The sampling of the non-zero-padded spectrum causes the lineshape centers to appear to be shifted due to the plotted point sampling being so low.

possible but beyond the scope of this work. Care must be taken when performing time-domain averaging without applying phase correction methods because photometric accuracy will likely be lost if the data are recorded over an amount of time long enough for sufficient phase-slippage to occur (observed to be  $\sim 0.1 \text{ s}$  for the Yb-DCS system). Therefore, for symmetric time-windows, it is recommended to use the Mertz phase correction (Eq. 1.11) on the unaveraged SBS and then average in the frequency domain. It is possible to Mertz phase-correct the spectra in the frequency domain and then inverse Fourier transform back into the time domain, where the centerbursts will now be much more similar as well as aligned in time (Fig. 1.15). Time-domain averaging can then be implemented and the result Fourier transformed back into the frequency domain. However, this method is computationally more expensive with generally no benefit over frequency-domain averaging immediately



after Mertz phase correction. Figure 1.16 shows a comparison of absorbance spectra for using time-domain averaging versus frequency-domain averaging.

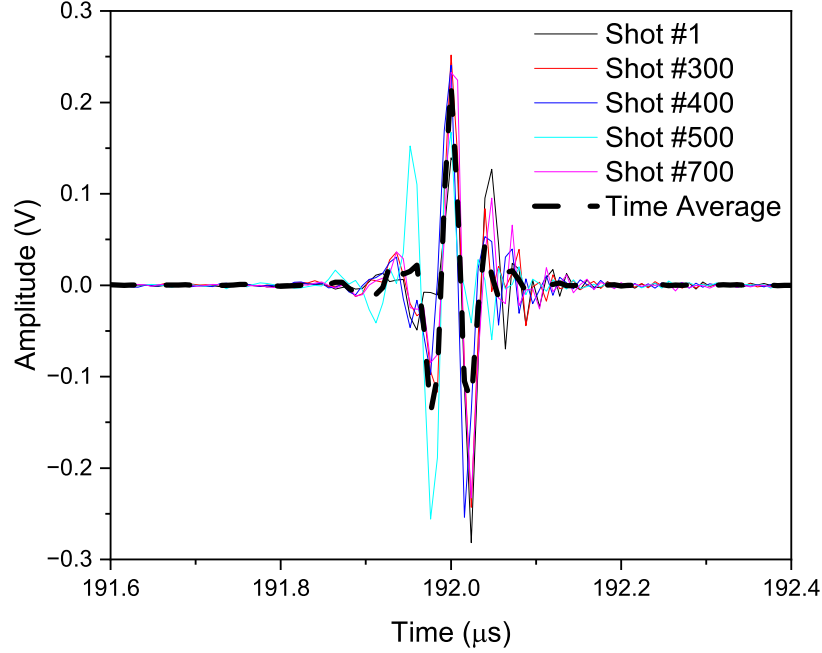


**Figure 1.14:** Comparison of the centerbursts of five recorded shots and the time-domain average of 750 centerbursts. Each shot was 0.1 ms apart, dictated by the ablation rate. All centerbursts were shifted so that their maximum centerburst values aligned. Here, phase-slippage was not extreme enough to completely degrade the averaged signal. Note that the chosen alignment procedure forces the cycles to overlap. As such, phase-slippage is expected to manifest as variations in the amplitude of the cycles due to their position changing under the centerburst envelope. Such behavior is indicated here, though measurement noise also plays a role. Alignment of the cycles would not occur if the centers of the centerburst envelopes were instead aligned, which can be done by utilizing Hilbert transformations. Note that consecutive interferograms are neither plotted nor were recorded due to the ablation frequency, and so a "re-phasing" of centerbursts may occur over these longer time-scales (10s seconds).

For frequency-domain averaging, the signal and reference SBS are typically averaged before the calculation of transmittance according to

$$T(\nu) = \frac{\overline{SBS}_{sig}(\nu)}{\overline{SBS}_{ref}(\nu)}. \quad (1.12)$$

Single-shot signal SBS sometimes have values for strong absorbances that go below zero,

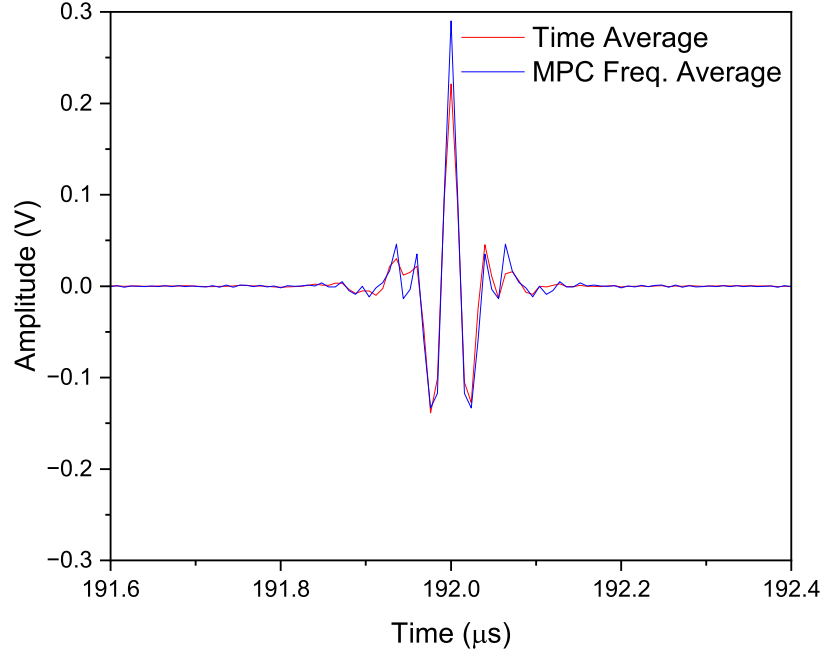


**Figure 1.15:** Comparison of the centerbursts of a time-averaged set of 750 interferograms and the inverse Fourier transform of the Mertz phase correction (MPC) of the same data. The time-averaged centerbursts were aligned so that their maximum value overlapped. Note that frequency averaging the Mertz phase corrected spectra and then inverse Fourier transforming into the time domain produces the same result as inverse Fourier transforming each of the Mertz phase corrected spectra and then averaging them in the time domain.

considered to be an effect of noise. Averaging the SBS before division decreases the noise influence so that that negative values are much more rare within the optical window. This prevents negative transmittance values and thus imaginary absorbance values, noting that absorbance is given by

$$A(\nu) = \ln\left(\frac{1}{T(\nu)}\right). \quad (1.13)$$

A similar method to Mertz phase correction can be used to generate pseudo-reference SBS for calculating transmittance when a true reference is unavailable. The reference spectra collected in LPP-DCS experiments with low-duty cycle ablation, discussed above, are nearly ideal. However, measurement of a static sample requires removing the sample for a reference measurement or using a separate reference beam-line. Over the time required for

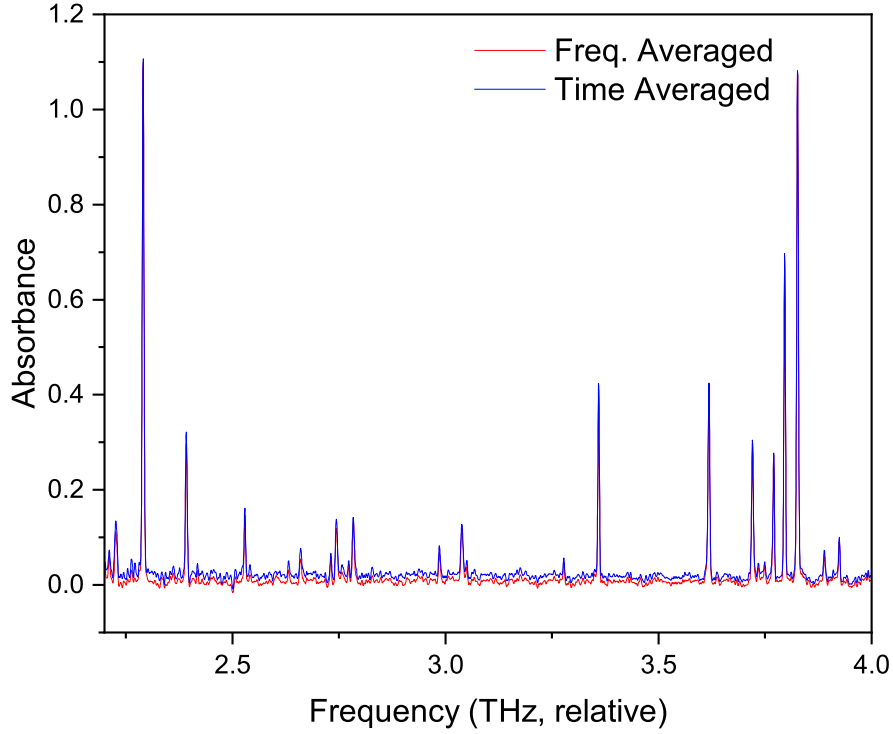


**Figure 1.16:** Comparison of the absorbance spectra of 750 SBS averaged in the frequency domain after Mertz phase correction versus averaging of the interferograms in the time domain before Fourier transform and Mertz phase correction. The time-averaged interferograms were aligned so that their maximum centerburst value overlapped.

the former method, spectral variations are often observed in DCS, and such variations are introduced by slight differences in optics and detection when using the latter method. A pseudo-reference, which includes the low-frequency components of the shape of the optical window without the high-frequency components of the absorption features, can be generated from the signal data by Fourier transforming  $f_{p-ref}(t)$  which contains only a small region about the centerburst.  $f_{p-ref}(t)$  is calculated in the same way as  $f_{MPC}(t)$  discussed above, but with a wider rectangular function so that the shape of the optical window in the SBS is captured. The Fourier transform of  $f_{p-ref}(t)$ ,  $\hat{f}'_{p-ref}(\nu)$ , will be complex just as  $\hat{f}'(\nu)$  is, and the same Mertz phase correction applied to  $\hat{f}'(\nu)$  can be applied to  $\hat{f}'_{p-ref}(\nu)$ , both utilizing  $\theta_{MPC}(\nu)$  derived from the very narrow  $f_{MPC}(t)$ . The signal and pseudo-reference SBS,  $SBS_{sig}$  and  $SBS_{p-ref}$ , are then real and can be divided for transmittance. If  $f_{p-ref}(t)$  is too

narrow,  $SBS_{p-ref}$  will not effectively capture the shape of the optical envelope of  $SBS_{sig}$ . If  $f_{p-ref}(t)$  is too wide,  $SBS_{p-ref}$  will exhibit broad, shallow depressions at the position of each absorption line in  $SBS_{sig}$ . Note that care must be taken when utilizing a pseudo-reference in this way, as broad absorption features present in  $SBS_{sig}$  will be indistinguishable from the optical envelope structure. As such, a pseudo-reference cannot fully replace a true reference in determining absorption features.

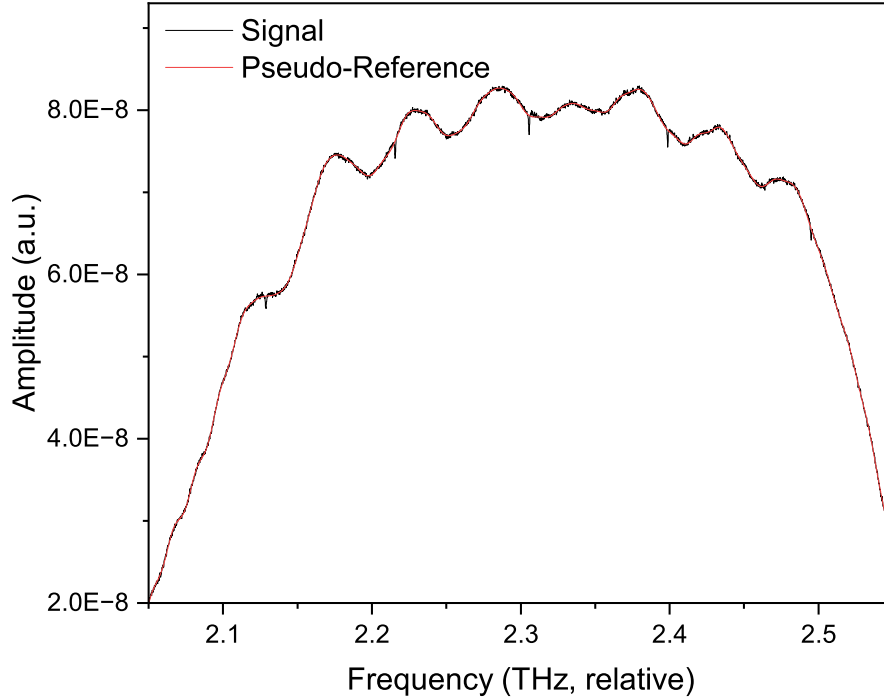


**Figure 1.17:** Example of a signal SBS with narrow, weakly absorbing features and a pseudo-reference SBS generated from the weakly low-passed signal. Both are Mertz phase-corrected by the same strongly low-passed phase  $\theta_{MPC}(\nu)$ .

## Chapter 2

### Experimental Setup

#### 2.1 Frequency Combs

Frequency combs consist of many evenly spaced narrow-linewidth laser lines, the frequencies of which can be known with high precision and accuracy according to Eq. 1.1. A popular source for broadband frequency combs are passively mode-locked lasers. Mode-locking lasers are designed so that higher-intensity intracavity pulses experience less roundtrip loss than CW light so that pulsed-operation is preferred under specific conditions. An intracavity pulse forms when the many cavity modes within the gain bandwidth are phase-coherent. Techniques used for passive mode-locking include Kerr lensing within gain crystals, nonlinear-polarization rotation, figure-8 and -9 fiber cavities, and use of saturable absorbers within linear cavities. With the right parameters, mode-locked lasers can generate sub-100 fs pulses.

Dispersion is an issue for such broadband and intense laser light, particularly for light guided in optical fiber due to the typically small mode areas and long interaction lengths involved. Dispersion occurs when the group and phase velocities within a medium are dependent on the frequency of the light. Without proper dispersion control, chirping and temporal breakup of ultrashort pulses can occur within dispersive materials as the lower and higher frequencies travel at different speeds. The group velocity dispersion (GVD, units of  $\text{s}^2/\text{m}$ ) is typically the focus of most dispersion control engineering since the effects of higher order dispersion are increasingly smaller and less important in most applications (with fiber lasers being the exception, where third order dispersion is often significant). A positive GVD is known as normal dispersion, and results in lower frequencies travelling faster than higher frequencies. A negative GVD is called anomalous dispersion, and results in the opposite chirp. To maintain a Fourier-limited pulse, the effects of normal and anomalous dispersion

must be balanced for a total of  $\sim 0 \text{ s}^2/\text{m}$ , with optics and media which introduce positive and negative dispersion utilized as needed. For some applications, such as chirped-pulse amplification, pulse-spreading is utilized to lower the pulse intensity and reduce nonlinear effects within media such as amplifiers. Dispersion control of the cavities and amplifiers used in this work are described in detail in Secs. 2.1.1 and 2.1.2.

A variety of lasers are used to generate frequency combs with differing specifications. Though Ti:sapphire lasers have long been the workhorse for frequency combs, fiber-based lasers offer advantages in robustness and access to wavelengths in the visible and IR, where many atomic and molecular transitions exist. Doped fibers used as a gain media offer long interaction path lengths that allow efficient photon conversion. Ytterbium and erbium, with gain bandwidths centered about  $1 \mu\text{m}$  and  $1.5 \mu\text{m}$ , respectively, are popular dopants. Erbium is a particularly convenient choice since  $1.5 \mu\text{m}$  telecom components are widely available, including 980 nm diode pump lasers. The following sections discuss the Yb- and Er-fiber based frequency combs utilized in this work. Most of the experiments presented here were performed with the Yb-DCS system; the CeO-LPP measurements in Sec. 5.5 and two-color Rb-LPP experiments in App. A were performed using the Er-DCS system. The Er-DCS system is included here because the last couple of years of my graduate work focused on this system. Also, the Er-DCS system will be used in my future work and presents an opportunity here to describe in detail an alternative setup with several notable differences from the Yb-DCS system. The Yb-based combs and amplifiers and their stabilization were originally constructed by previous graduate students (David Carlson and Tsung-Han Wu), but were heavily modified by me and Zhang, with the additional construction of the LPP-centric portions. The Er-fiber combs and amplifiers and their stabilization were originally constructed by my graduate colleague Seth Erickson alongside Lecaplain before Rhoades and I took over construction of the LPP system and rebuilt the locking mechanisms.

### 2.1.1 Yb-Fiber Oscillators and Amplifiers

The oscillators of the Yb-DCS system utilize Yb-doped fiber to lase near 1060 nm and modelock via nonlinear polarization rotation (Fig. 2.1). The waveplates within the free-space section are set to ensure a round-trip polarization evolution that causes CW light to

experience a high level of loss via dumping from the cavity by the upper PBS. However, phase fluctuations that randomly result in coherence of the cavity modes create weak pulses, which experience a different polarization evolution within the non-PM fiber sections. The polarization change is the result self- and cross-phase modulation of the light driven by the higher intensity of the weak pulse relative to CW light. With appropriate waveplate orientations, these weak pulses have the proper polarization to pass through the PBS and re-seed the oscillator to drive lasing that favors pulsed-operation. The free-space section also contains a grating pair used to introduce negative dispersion and bring the round-trip cavity dispersion close to zero, since both passive and active silica fiber have normal dispersion near 1060 nm. Output powers of the oscillators are roughly 48 and 47 mW for Combs 1 and 2, respectively.

Both combs have pre-amplifiers used to boost the power before seeding high-power photonic-crystal fiber (PCF) amplifiers (Fig. 2.2). Double-clad Yb-doped gain fiber makes up the active portion of the pre-amp. Double-clad fiber is used because it allows the comb (seed) light to be guided single-mode within a small core while the pump is guided within the much larger area of the inner cladding. This allows high-power pump diode light, which usually has poor beam quality, to be coupled more efficiently into the fiber. Some light is picked-off before the pre-amplifiers in both combs for input into a spectrometer to monitor the oscillator spectra. Light from Comb 2 is also tapped for use in Beatnote 2 in the comb stabilization, measured before the AOM used in the feed-forward locking arrangement described in Sec. 2.2.2. The ends of the fiber portions are angle-cleaved to reduce back-reflections. 32 mW and 35 mW are coupled into each amplifier, and 1.5 W and 1.6 W are output at 8.2 mA and 4.3 mA pumping currents for Combs 1 and 2, respectively.

Figure 2.3 shows the layout used in both combs between the pre-amplifiers and PCF amplifiers. Dichroic mirrors strip the residual pre-amplifier pump-light, and an isolator prevents back-reflections. A transmission grating and slit combination are used in a 4f arrangement to select and limit the spectral bandwidth before insertion into the PCF. The purpose is to reduce third-order dispersion (TOD) while remaining in the linear amplification regime within the high-power amplifier. Positive TOD is introduced within the system mainly through the gratings and material dispersion of the fiber. To compensate, negative

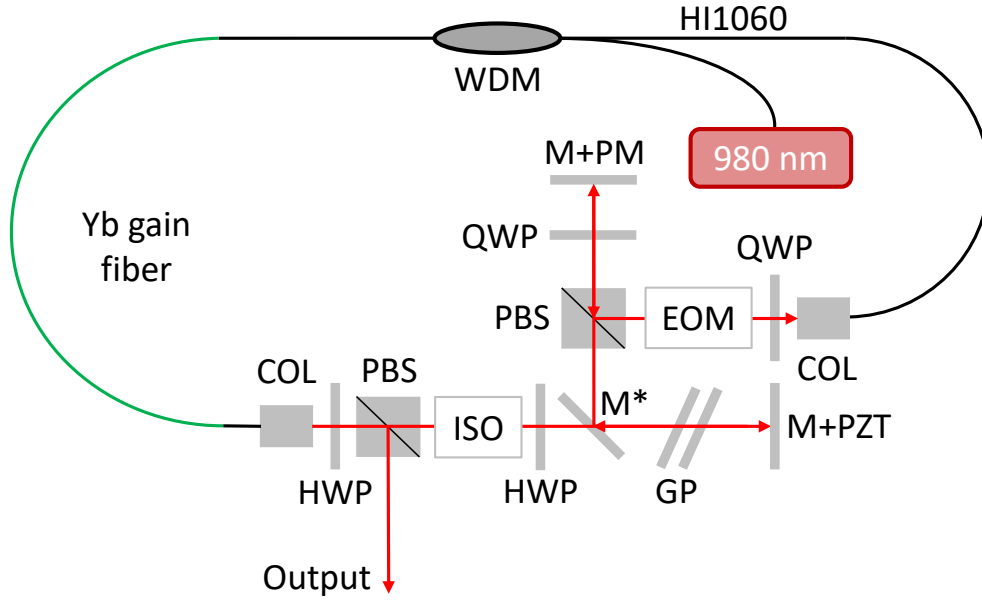


**Figure 2.1:** Schematic of the oscillators used for the Yb-DCS system. The black beamlines are guided within optical fiber, whereas the red are in free-space. HWP: half-waveplate, QWP: quarter-waveplate, COL: fiber collimation package, PBS: polarizing beamsplitter, WDM: wave-length division multiplexer, ISO: optical isolator, GP: transmission grating pair, M: mirror, EOM: electro-optic modulator. M+PM is a mirror mounted on a stage with a picometer motor, used for relatively large cavity length changes. M+PZT is a mirror mounted to a PZT used in stabilization (see Sec. 2.2.2). The mirror M\* is placed such that the first optical beam passes over the mirror, and the reflection from M+PZT is incident.

TOD can be added in the nonlinear amplification regime, in which a short, intense pulse is amplified. For this, a pulse broadened by the pre-amplifier is compressed using gratings just before the PCF amplifier. Clean pulses of 60-70 fs can be generated. However, extreme self-phase modulation (SPM) generally occurs in nonlinear amplification, resulting in highly-structured comb spectra which may not overlap properly for the purpose of DCS. In the linear amplification regime, sending a stretched pulse directly into the amplifier results in the intensity, and therefore SPM, being reduced, leaving the output spectrum smoother. Less TOD compensation occurs in the linear amplification regime, however, and output pulses are generally broken apart with side-lobes and shoulders. Note that high-harmonic generation (HHG) for which the Yb-DCS system is purposed requires well-structured pulses



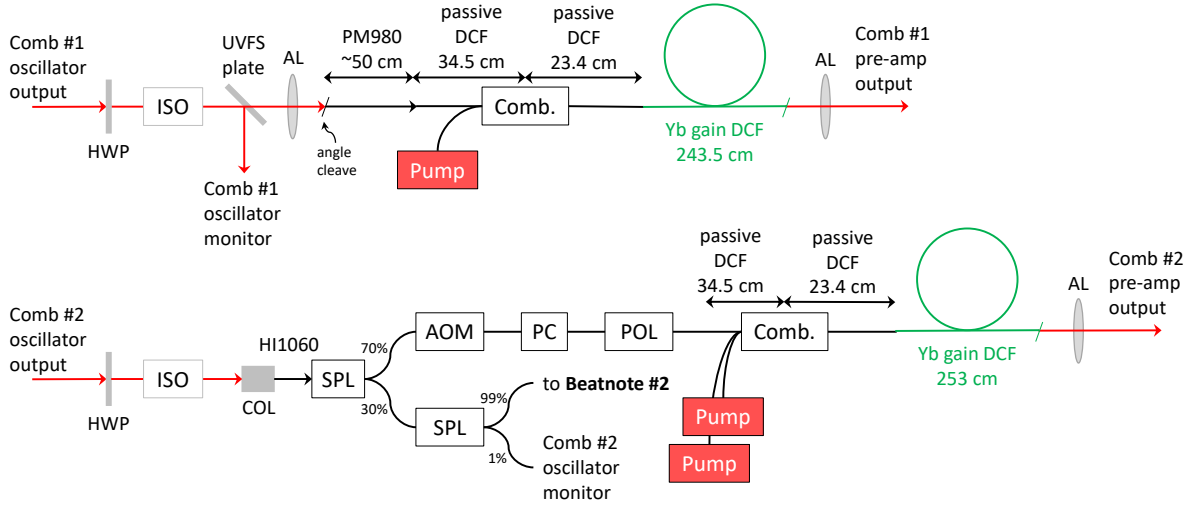


**Figure 2.2:** Schematic of the optical layout for the pre-amplifiers of Combs 1 and 2 in the Yb-DCS system. The black beamlines are guided within optical fiber, whereas the red are in free-space. HWP: half-waveplate, AL: aspheric lens, COL: fiber collimation package, Comb.: pump combiner, ISO: optical isolator, SPL: fiber splitter, AOM: acousto-optic modulator, DCF: double-clad fiber, PC: fiber-based polarization controller, POL: inline fiber polarizer, UVFS: UV fused silica.

that contain most of the power in a compressed pulse to achieve higher intensities. The negative effects of TOD can be curbed by limiting the spectral bandwidth of the pulse to produce clean  $\sim 150$  fs pulses. In this way, laser pulses with necessary intensities for HHG can be generated while maintaining the smooth spectra necessary for DCS. Comb 1 outputs 155 fs pulses with 2.5 W at 1.2 A and 31.2 W at 5.4 A PCF amplifier pumping current.

Before final amplification, a UV fused silica plate taps off two beamlines, one used for locking and the other for monitoring the comb spectrum at this point. P-polarized light which leaks through a turning mirror is also used for the interlock system meant to turn off the high-power pumps to the PCF amplifier to prevent catastrophic failure in the case of the amplifier not being seeded by comb light. The amplifier output, typically at low-pumping powers, is used for the experiments described in later chapters.

### 2.1.2 Er-Fiber Oscillators and Amplifiers

The Er-DCS oscillators utilize Er-doped gain fiber in a linear cavity that utilizes a saturable absorber for modelocking. Erbium is a popular dopant as it has a wide gain bandwidth

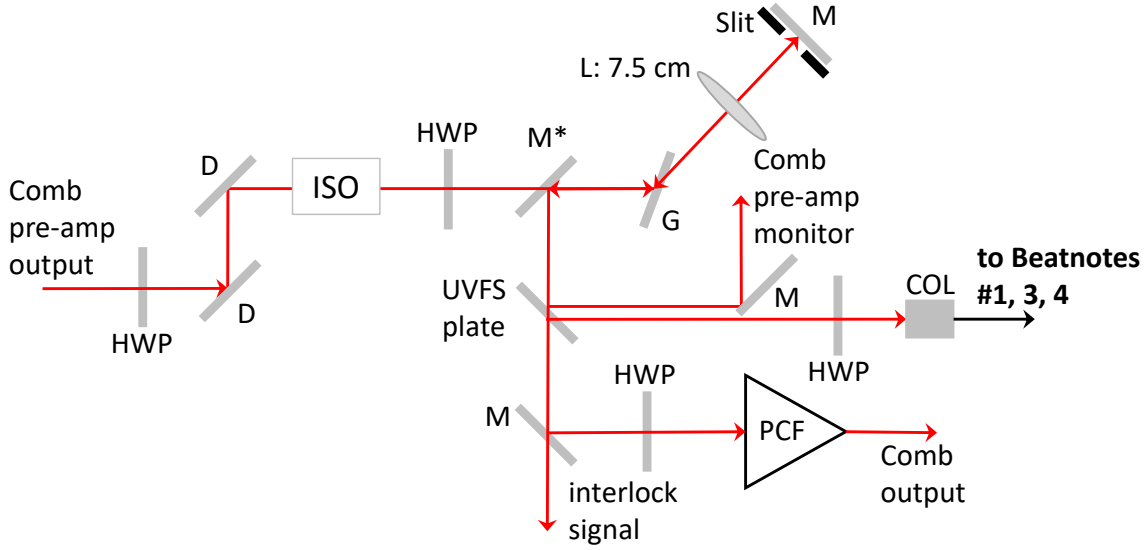


**Figure 2.3:** Schematic of the optical layout for Combs 1 and 2 of the Yb-DCS system after their pre-amplifiers and up to the PCF amplifiers. The interlock signal comes from the p-polarized light which leaks through the mirror just before the PFC amplifier. The black beamlines are guided within optical fiber, whereas the red are in free-space. HWP: half-waveplate, D: dichroic mirror, L: lens, followed by focal length, COL: fiber collimation package, ISO: optical isolator, M: mirror, G: transmission grating, UVFS: UV fused silica, PCF: photonic crystal fiber, representing the PCF amplifier.

around  $1.5 \mu\text{m}$ , a region for which many telecom components are widely available including diode pump lasers. Polarization-maintaining (PM) fiber is used throughout the cavity to improve robustness, so that the laser is less sensitive to the fiber position.

Figures 2.4 and 2.5 show the schematics for the oscillators of Combs 1 and 2, respectively. The pump light from a diode laser at 980 nm is inserted into the cavity via a wavelength-division multiplexer (WDM). This light pumps the Er-doped gain fiber, causing spontaneous emission. The emitted light near 1550 nm is reflected via a fiber retroreflector and passes again through the gain fiber, now inducing amplified spontaneous emission and stimulated emission. On the other end of the cavity, the light is reflected by a semiconductor saturable absorber mirror (SESAM), which is a type of Bragg mirror with a built-in saturable absorber on a GaAs substrate. The Bragg mirror is engineered to control the modulation depth

and fluence in the saturable absorber region as well as the bandwidth and dispersion of the SESAM. Use of a saturable absorber initiates passive mode-locking, in which a higher-intensity pulse is favored in the cavity over lower-intensity CW operation.

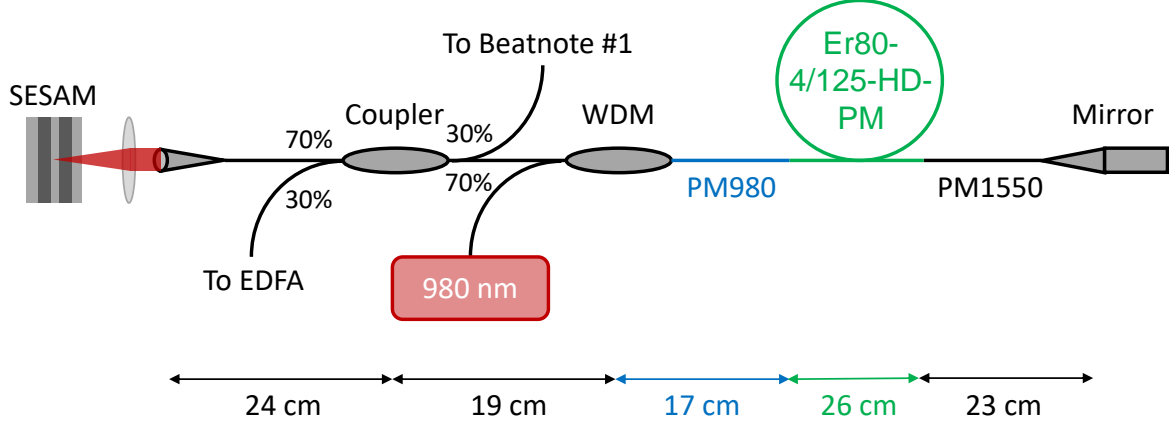


**Figure 2.4:** Schematic of Comb 1 oscillator in the Er-DCS system. Er-doped gain fiber is indicated in green, which has negative dispersion. PM980 and PM1550 both have positive dispersion. The focusing lens has a focal length of 1.45 mm, producing a spot-size of  $3.57 \mu\text{m}$  on the SESAM. WDM: wavelength division multiplexer, EDFA: erbium-doped fiber amplifier, SESAM: semiconductor saturable absorber mirror.

The dispersion parameters are 11.36, 18.00, and  $-22.00 \text{ ps}/(\text{nm}\cdot\text{km})$  for PM980, PM1550, and the Er-doped gain fiber, respectively. Note that dispersion parameters for the first two had to be estimated based on similar fibers since their own values were not readily available. Given the fiber lengths (shown in the figures), the roundtrip GDD of the cavities is  $-0.0207 \text{ ps}^2$  and  $-0.0191 \text{ ps}^2$ , for Combs 1 and 2, respectively.

The oscillator spectra are shown in Fig. 2.6. The oscillators are stored together, along with the amplifiers described below, in a homemade acrylic case lined with insulating weather stripping. The case serves to protect the oscillators as well as keep the temperature, humidity, and pressure relatively stable. Desiccants are placed within the case since humidity changes have been observed to affect modelocking conditions. Pressure changes can also affect the oscillators, mainly by changing the cavity lengths, as can be observed by watching frequency changes in the locking beatnotes when pressure is applied to the case. To stabilize the

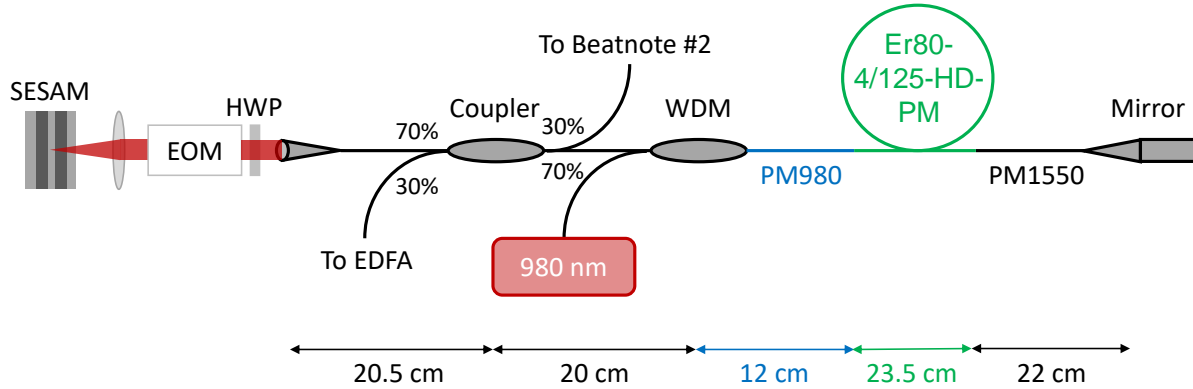


**Figure 2.5:** Schematic of Comb 2 oscillator in the Er-DCS system. Er-doped gain fiber is indicated in green, which has negative dispersion. PM980 and PM1550 both have positive dispersion. The focusing lens has a focal length of 2.45 mm, producing a spot-size of  $3.02 \mu\text{m}$  on the SESAM. WDM: wavelength division multiplexer, EDFA: erbium-doped fiber amplifier, SESAM: semiconductor saturable absorber mirror, EOM: electro-optic modulator.

temperature, a large heating pad was attached to the inside of the case lid, which runs on a simple PID circuit to maintain a stable internal temperature, e.g.,  $83^\circ \text{F}$ , to within  $0.2^\circ$ . Note, if the heater current cycles (e.g., when the setpoint temperature is being actively maintained), the comb frequencies may be observed to shift with each cycle, affecting the integrity of the stabilization locks (described in Sec. 2.2.1). For this reason, it is recommended to set the target temperature above room temperature and tune the gain of the PID controller to a low setting so that the temperature remains stable just below the setpoint while the heater remains constantly on.

The erbium-doped fiber amplifier (EDFA, Fig. 2.7) consists entirely of PM fiber and components. An isolator protects the oscillator from back-reflections, and a WDM comes just before the EDFA to strip out the residual pump light. The gain fiber is followed by the pump-combining WDM in a backward-pumping arrangement so that more gain is present in the downstream portion of the gain fiber where the signal is more intense. Since the active fiber introduces anomalous dispersion at  $1.5 \mu\text{m}$ , the amplifier is followed by a length of normally dispersive passive fiber, the length of which was determined by measuring the output pulse with an autocorrelator and optimizing for the shortest and cleanest pulse possible.

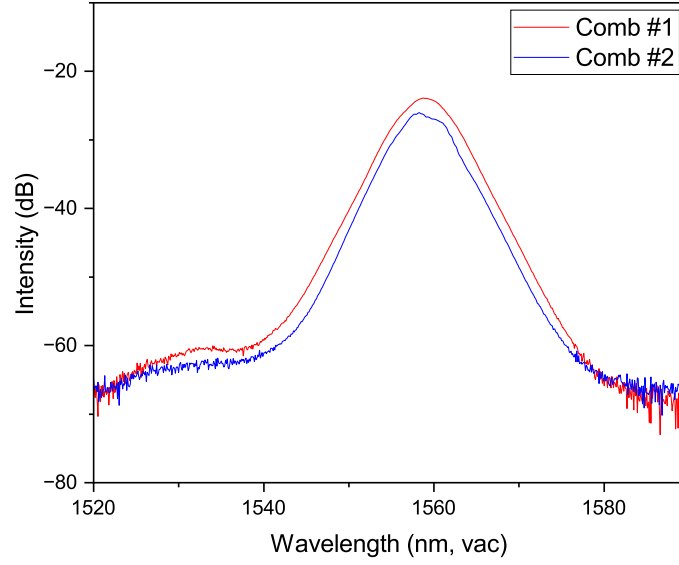


**Figure 2.6:** Oscillator spectra of the Er-DCS system, recorded 09/16/2022. The oscillator pump currents were 140 mA and 125 mA for Combs 1 and 2, respectively. The case temperature was 83° F.

The PI curves and output spectra of both combs' amplifiers are shown in Figs. 2.8 and 2.9, and the pulses were  $\sim 100$  fs. A 10% tap is used to obtain some of the comb light for the optical beatnotes of Locks 3 and 4 (see Sec. 2.2.1).

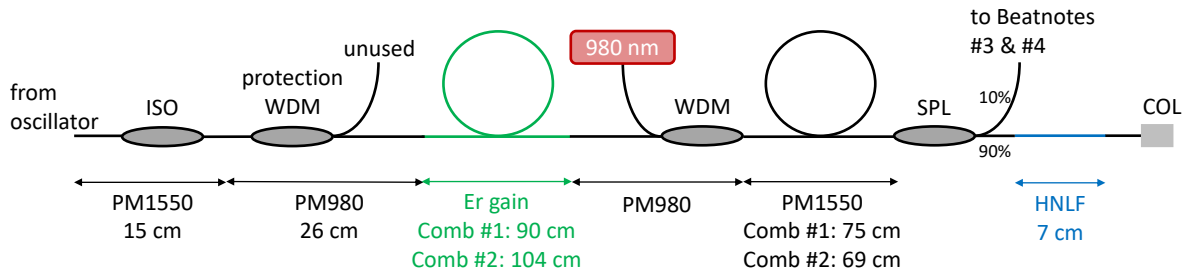


**Figure 2.7:** Schematic of the optical layout of the EDFA and HNLF portion of the Er-DCS system for each comb. The pulses are optimized just before the HNLF. All beamlines are guided within optical fiber. WDM: wavelength division multiplexer, ISO: optical fiber isolator, SPL: fiber splitter, HNLF: highly-nonlinear fiber, COL: fiber collimation package.

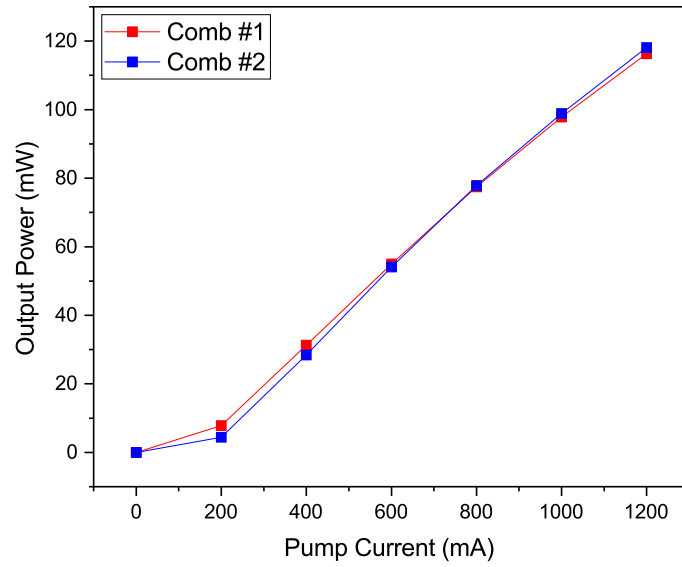


**Figure 2.8:** PI curves of the EDFAs in the Er-DCS system, measured just before the HNLF.

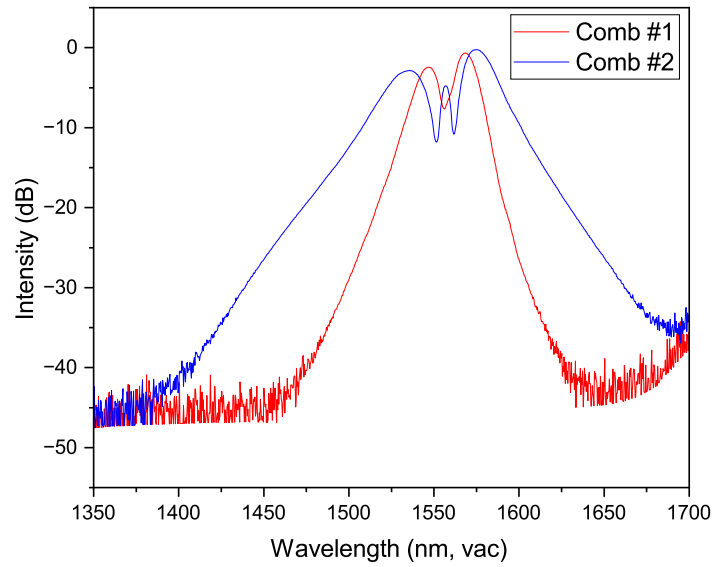


**Figure 2.9:** Amplifier spectra of the Er-DCS system just before HNLF, recorded 05/17/2021. The amplifier pump currents were 1200 mA for both combs.

To broaden the output spectra, 7 cm of anomalous highly-nonlinear fiber (HNLF) was spliced to the end of each amplifier, and the output spectra are shown in Fig. 2.10. The fiber length was optimized by measuring the output spectra at various input powers. A shorter length can achieve the same broadening at a higher input power as a longer length without displaying strong spectral fringing and gaps caused by SPM. A smooth comb spectrum with higher power is desirable for better spectral coverage and easier detection. 40 mW and 46 mW are output from the fiber collimation packages spliced to the HNLF at 1200 mA amplifier pump currents for Combs 1 and 2, respectively.

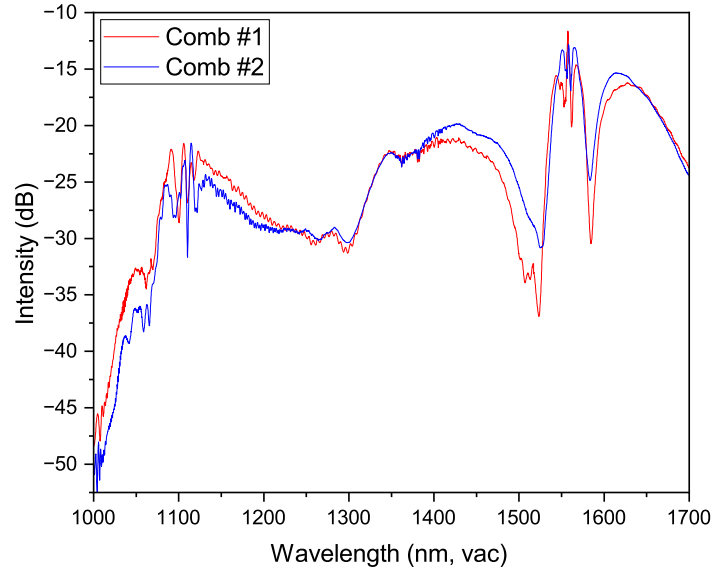


**Figure 2.10:** Broadband amplifier spectra of the Er-DCS system generated in HNLF, recorded 09/26/2022. The amplifier pump currents were 775 mA and 650 mA for Combs 1 and 2, respectively.

## 2.2 Comb Stabilization

For high-resolution DCS measurements, the combs must be made highly phase-coherent, often via active stabilization of the cavities using phase-locked feedback loops. If the comb teeth frequencies are drifting over the measurement time, the measured lineshape will be broadened. This can occur if the comb tooth initially at the measurement frequency drifts by at least  $f_{rep}$  so that the measurement frequency is probed by an adjacent tooth at a

later time. This is a relatively large drift, however, and the level of stabilization required to prevent such drift is generally easy to achieve. More importantly, the combs must be stabilized to one another, such that they have a high degree of mutual coherence. In DCS, when one comb tooth drifts relative to the other (a change in  $\Delta f_{rep}$ ), the RF frequency corresponding to a given optical frequency changes according to Eq. 1.4. Thus, the center of any lineshape will shift in the RF domain with any change in  $\Delta f_{rep}$ . For example, consider a DCS measurement in the NIR with  $f_{rep} = 80$  MHz and  $\Delta f_{rep} = 500$  Hz. If the combs are locked such that a pair of comb teeth overlap at 300 THz ( $\sim 1 \mu\text{m}$ ), and an absorption feature is measured at  $f_{RF} = 20$  MHz ( $f_{optical} = 303.2$  THz), then a change in  $\Delta f_{rep}$  of  $\pm 0.1$  Hz will result in the measured  $f_{RF}$  of the absorption feature changing by  $\pm 2$  kHz. The equivalent drift of the measured optical frequency is then  $\pm 0.64$  GHz. These are typical values for the DCS measurements presented in this work, and a drift of 0.64 GHz over the measurement time will effectively "smear" a measured absorption feature with a comparable or smaller linewidth. Note, the measurement drift is proportional to the number of comb teeth between the measurement frequency and the frequency of the nearest locking point. The further a measurement is made from a locking point, the more drift will be measured for a given change in  $\Delta f_{rep}$ . Thus, to better stabilize  $\Delta f_{rep}$ , the combs are locked to one another via a reference CW laser, as described in Secs. 2.2.2 and 2.2.1. In this work, the absolute frequency drift of the DCS system is dictated by the frequency stability of the reference lasers (or cavity to which they are locked, in the case of the Yb-DCS system). The  $>100$ s MHz linewidth features measured here were not broadened by the slow, small drifts of the reference lasers.

In the studies presented here, the combs were actively stabilized by controlling actuators within the laser cavities (with the exception of a feed-forward setup used for Comb 2 in the Yb-DCS system described in 2.2.2) in order to maintain a phase-lock between specific comb teeth and reference CW lasers. Note that the phase of the two signals is compared rather than the frequencies because phase measurements are much more sensitive. For example, it is difficult to detect a 1 Hz difference between two MHz-level signals by measuring their frequencies. However, the phase difference between the signals changes by  $2\pi$  every second. Figure 2.11 shows a general layout for a phase-locked loop used to stabilize the



combs. Interfering the relatively stable, narrow linewidth reference lasers with each comb and detecting the beatnotes gives a set of RF (10s MHz) signals which increase/decrease according to the frequency change of the comb (assuming the CW drift is much smaller than the comb drift). One of these beatnotes is compared to an RF clock to generate an error signal which drives a servo controlling the cavity actuators, creating a phase-locked loop. Combinations of actuators are used that have complimentary bandwidths and actuating ranges, e.g., electro- and acousto-optic modulators (EOM/AOM) (higher bandwidth, lower range) and piezo-electric transducers (PZT) (lower bandwidth, higher range). EOMs and AOMs can be placed directly into the comb cavities, and PZTs can be utilized as mounts for cavity mirrors and within translation stages that can mount both mirrors and gratings (used in the Yb-DCS system). The combs are each referenced to the same CW laser at some wavelength and then referenced to a second CW laser at another wavelength to indirectly control both degrees of freedom of the combs. This can be thought of as clamping a single comb tooth to a specific frequency, around which, like the bellows of an accordion, “stretching” of the other teeth frequencies will occur. A second comb tooth some distance away is then also clamped to eliminate this stretching. A higher degree of stabilization over a larger wavelength region can generally be achieved by using a larger wavelength spacing between the two reference lasers so that the locking points are spaced farther in frequency. A more thorough description of the phase-locking mechanisms and setup for each DCS system is given in the following sections.

### *2.2.1 Er-DCS Stabilization*

The details of the Er-DCS system stabilization are presented here before those of the Yb-DCS system, as the former system is slightly more straightforward than the latter. In the Er-DCS system, the optical beatnotes used for comb stabilization with reference lasers are generated completely within optical fiber. Figure 2.12 shows the layout for combining and filtering the light from both combs and CW 1 (RIO ORION at 1563.867 nm) to generate Beatnotes 1 and 2. The comb light is obtained from the second output of the oscillator output couplers. Fiber Bragg gratings (FBG) filter the comb light to a small bandwidth centered around the CW 1 wavelength to prevent unnecessary light from reaching the detector to

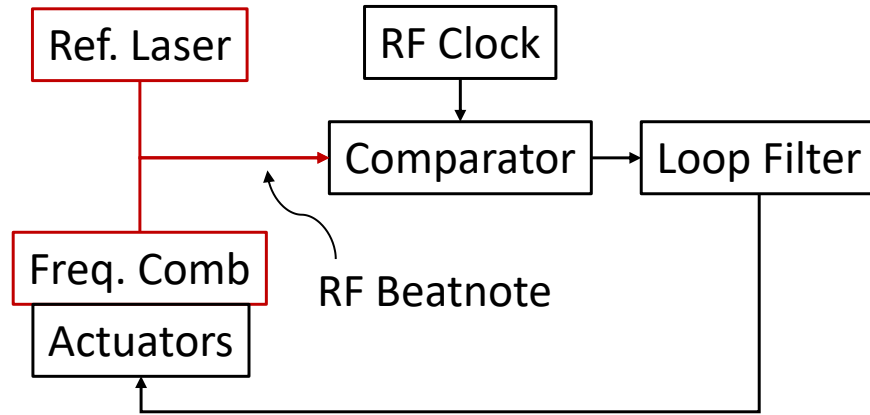


**Figure 2.11:** General arrangement of a phase-locked loop, used in stabilizing the frequency combs.

improve the detected beatnote SNR. The other outputs of the splitters are used to monitor the oscillator spectra of the combs.

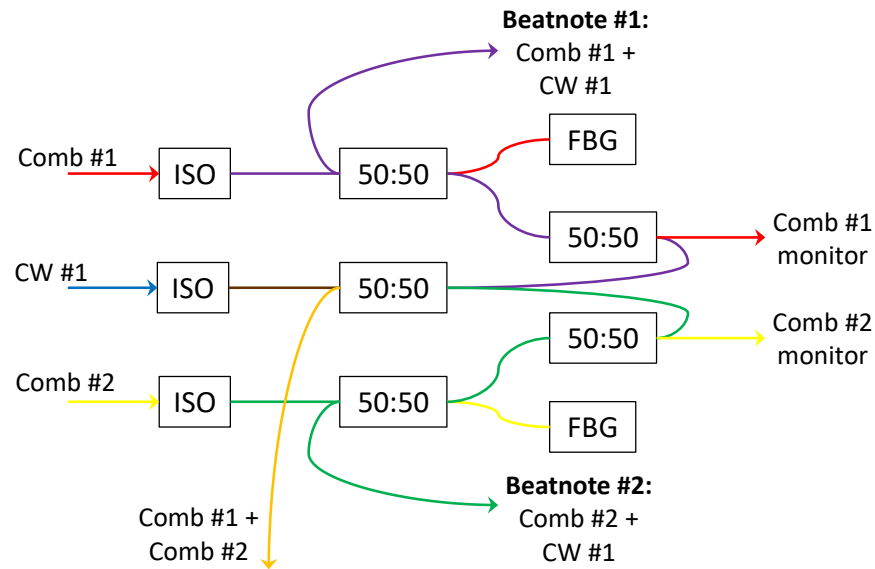


**Figure 2.12:** Schematic of the optical layout used to generate Beatnotes 1 and 2 in the Er-DCS system. All beamlines are guided within non-PM fiber. ISO: fiber-based isolator, 50:50: 50:50 fiber beamsplitter, FBG: fiber Bragg grating.

The setup for obtaining Beatnotes 3 and 4 utilizes fiber circulators for a simpler layout, shown in Fig. 2.13. Here, the center wavelength of the FBGs must be shifted via TEC cooling to overlap with the CW 2 wavelength (RIO PLANEX at 1542 nm). In both layouts, the optical beatnotes are incident on fast photodetectors ( $\sim 100$  MHz bandwidth), and the signal is sent into the electrical setups.

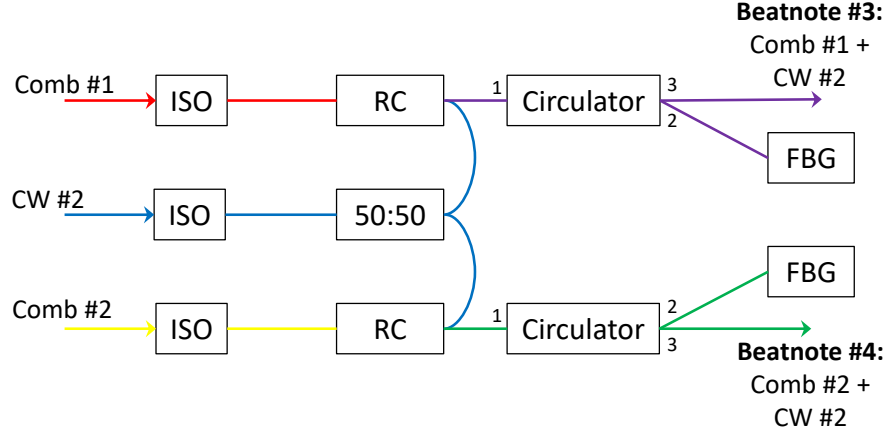


**Figure 2.13:** Schematic of the optical layout used to generate Beatnotes 3 and 4 in the Er-DCS system. All beamlines are guided within PM fiber. ISO: fiber-based isolator, 50:50: 50:50 fiber beamsplitter, FBG: fiber Bragg grating, RC: reflection-type combiner.

Figure 2.14 shows the electrical setup used to obtain countable signals for  $f_{rep}$  of Comb 1 and  $\Delta f_{rep}$ . The frequencies are split from the beatnote signals generated with CW 1. A tunable bandpass filter centered near 248 MHz isolates the third harmonic of  $f_{rep}$  for counting since no filters with an appropriate bandpass at the fundamental frequency were available. Frequency counters detect and display the frequencies, which are used for keeping the combs within a targeted range and calculating the conversion factor between measured RF and optical frequencies.

The passed beatnote signals proceed into the schematic shown in Fig. 2.15 to be conditioned and locked to reference frequencies. The setup consists of two phase-locked loops, each containing a “fast” lock and its subsidiary “slow” lock. Lock 1 stabilizes Comb 1 to CW 1, and Lock 2 stabilizes Comb 2 to Comb 1 via CW 1. A small bit of power of each signal is tapped using RF directional couplers for beatnote observation on an electronic spectrum

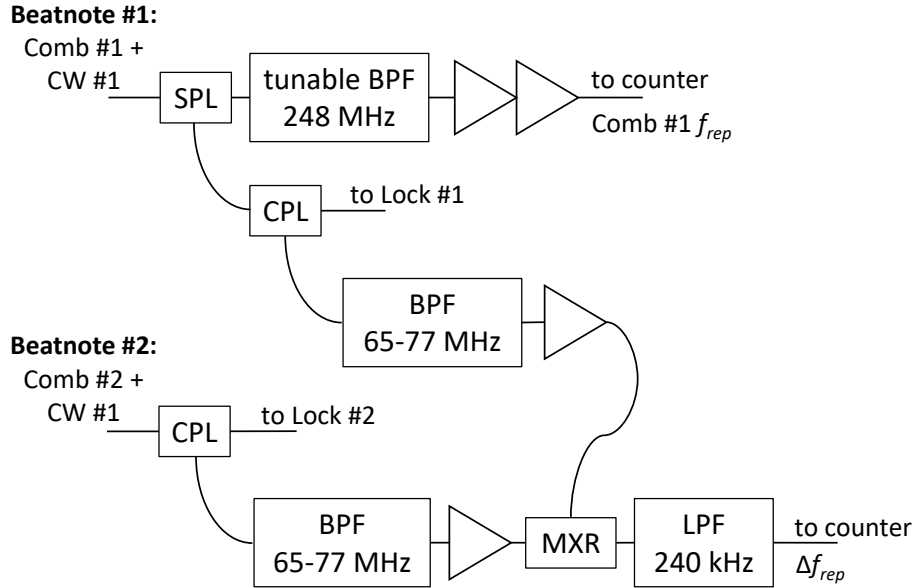


**Figure 2.14:** Schematic of the circuit used to acquire  $f_{rep}$  and  $\Delta f_{rep}$  from Beatnotes 1 and 2 in the Er-DCS system. The outputs “to Lock #1” and “to Lock #2” are the inputs in Fig. 2.15. RF amplifiers, represented by triangles, provide  $\sim 25$  dB of amplification. SPL: splitter, CPL: directional coupler, BPF: bandpass filter, LPF: lowpass filter, MXR: mixer.

analyzer.

Before locking, the beatnotes must be amplified and filtered at their target locking frequencies. Note, some filtering typically occurs before amplification to prevent amplification of noise outside the filter bandpass, enhancing the amplification efficiency within the bandpass. The beatnotes are conditioned such that they have  $\sim 0$  dBm of peak power (based on the required input power of the servo) and are ideally at least  $\sim 40$  dB above their surrounding noise floor. Note, Beatnote 1 (for Lock 1) is split, and a portion is mixed with Beatnote 2. Lock 2, thus, locks Comb 2 to Comb 1 via CW 1 to increase the coherence between the combs rather than their coherence with the reference laser by subtracting out the noise of CW 1.

In the Er-DCS system, a pair of Red Pitaya field-programmable gate array (FPGA) controlled boards provide the locking reference frequencies and act as the phase comparator and servos and output the feedback signals used to drive the locking actuators. A single

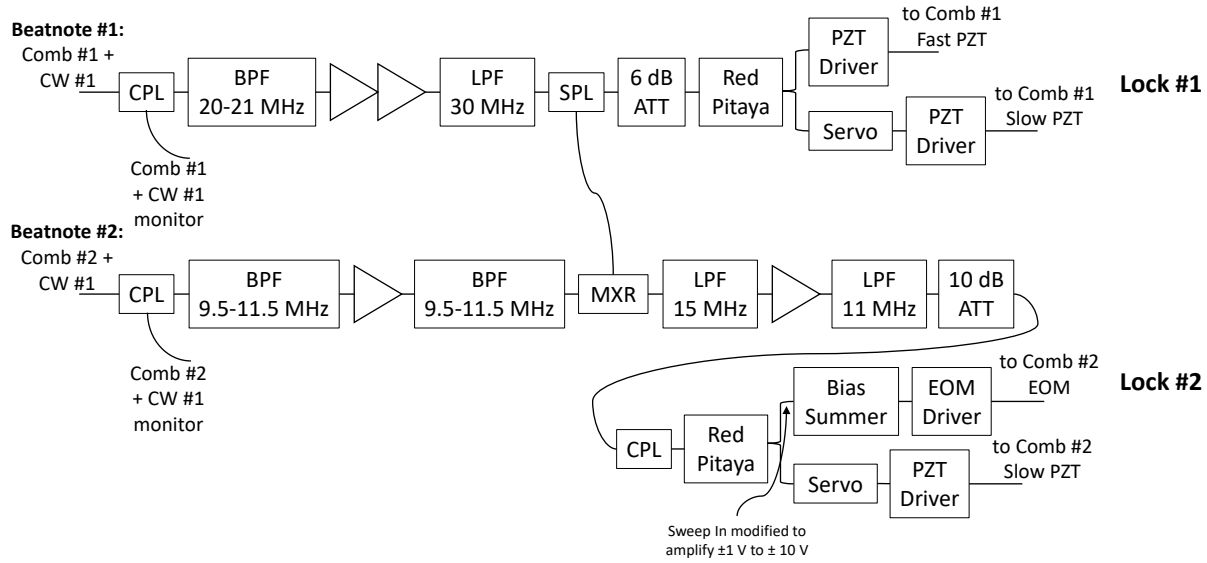


**Figure 2.15:** Schematic of Locks 1 and 2 in the Er-DCS system, used to condition and lock Beatnotes 1 and 2. RF amplifiers, represented by triangles, provide  $\sim 25$  dB of amplification. SPL: splitter, CPL: directional coupler, BPF: bandpass filter, LPF: lowpass filter, MXR: mixer, ATT: attenuator.

Red Pitaya can support two inputs and two outputs; here, one Red Pitaya is sufficient for Locks 1 and 2. The Red Pitayas are controlled by and communicate with a computer via an ethernet cable. A Python program for optical phase-locking developed at NIST [46, 47] is used to set the reference frequency as well as the loop filter gain function, controlled by the frequencies of the “corners” of the constituent proportional, integral, and derivative gain profiles.

The feedback signal from each servo is split. The first must be appropriately conditioned before being sent to the “fast” locking actuator, usually an EOM or “fast” PZT. For the Er-DCS system, a fast-PZT assembly consists of a comb cavity mirror mounted to a PZT mounted to a resonance-damping slug of copper filled with lead. Conditioning typically requires amplification and maybe the addition of a bias. Sensitive actuators, such as pump diodes, may require protective voltage limiters, which can be achieved with diodes as is done in Lock 2. The fast actuator typically has relatively high bandwidth (100s kHz - MHz) and chiefly dictates the level of coherence between the locked lasers. Electro-optic modulators (EOMs) are well-suited but often have a short actuating range, which motivates the usage

of a secondary “slow” lock.

The second portion of the feedback signal is sent to a secondary servo, having its own loop filter gain function set to generate a “slow” feedback signal by reducing the gain of higher frequencies. The slow signal is conditioned and sent to an actuator, such as a PZT adjusting the comb cavity length via the displacement of a translation stage with a mounted mirror. The slow actuator supports the fast actuator by providing extra locking range to account for slow, long-term drifts of the comb frequencies.

Lock 1 achieves a phase noise standard deviation of  $\sim 3$  radians with the following settings. For the fast lock of Comb 1 Fast PZT using the Red Pitaya: reference frequency 20.5 MHz, negative VCO gain sign, VCO gain  $2e7$ ,  $Kp -3.5e1$ ,  $fi 4.37e3$ ,  $fii 2.34e3$ ,  $fd$  off, and  $fdf$  off, for proportional, first integrator, second integrator, first derivative, and second derivative gains, respectively. For the slow lock of Comb 1 Slow PZT using an analog servo: PI corner 3.3 kHz, -9 dB corner 10 Hz, servo gain  $100 \times 1$ , with input bias off.

Lock 2 achieves a phase noise standard deviation of  $\sim 0.15$  radians with the following settings. For the fast lock of Comb 2 EOM using the Red Pitaya: reference frequency 11 MHz, positive VCO gain sign, VCO gain  $1e5$ ,  $Kp -4.3e1$ ,  $fi 1.12e3$ ,  $fii 1.41e3$ ,  $fd 4.57e5$ , and  $fdf 5.5e2$ . For the slow lock of Comb 2 Slow PZT using an analog servo: PI corner 3.3 kHz, -9 dB corner 10 Hz, servo gain  $300 \times 1$ , with input bias off.

Though Locks 1 and 2 provide a high degree of stability at the reference CW frequency, the comb may be insufficiently stable at far-removed frequencies due to comb mode “stretching” caused by changes in  $f_{rep}$  and  $f_{ceo}$ . Thus, the combs are stabilized to a second CW reference laser. The larger the difference in the two reference laser frequencies, the larger the optical bandwidth over which the combs will be sufficiently stable. Note, care must be taken in choosing the locking actuators and their gain functions to avoid “fighting” between each lock at the two reference frequencies for a single comb. This is because each lock manipulates the comb by affecting both  $f_{rep}$  and  $f_{ceo}$  in combination, which together are a complete orthogonal basis of the comb modes.

Lock 3 locks CW 2 to Comb 2, and Lock 4 locks Comb 1 to Comb 2 via CW 2, as shown in Fig. 2.16. The signal conditioning is like that described for Locks 1 and 2. The locking actuator for CW 2 is the drive current. Thus, CW 2 is adjusted to the nearest frequency

mode of Comb 2. The locking actuator for Comb 1 is the oscillator diode pump's current. Care must be taken to set the lower and upper bounds of the pump current. If too low, the comb will un-modelock. If too high, Kelly sidebands and CW spikes may appear in the oscillator spectrum, affecting the pulse characteristics. To this end, the sweep channel of a bias/summer is used to control the gain of the feedback signal. A diode voltage limiter is also included to stop very large voltages from going to the pump driver to prevent damage. Since the combs are somewhat stabilized at the CW 2 frequency by Locks 1 and 2, Locks 3 and 4 do not require subsidiary slow actuators.

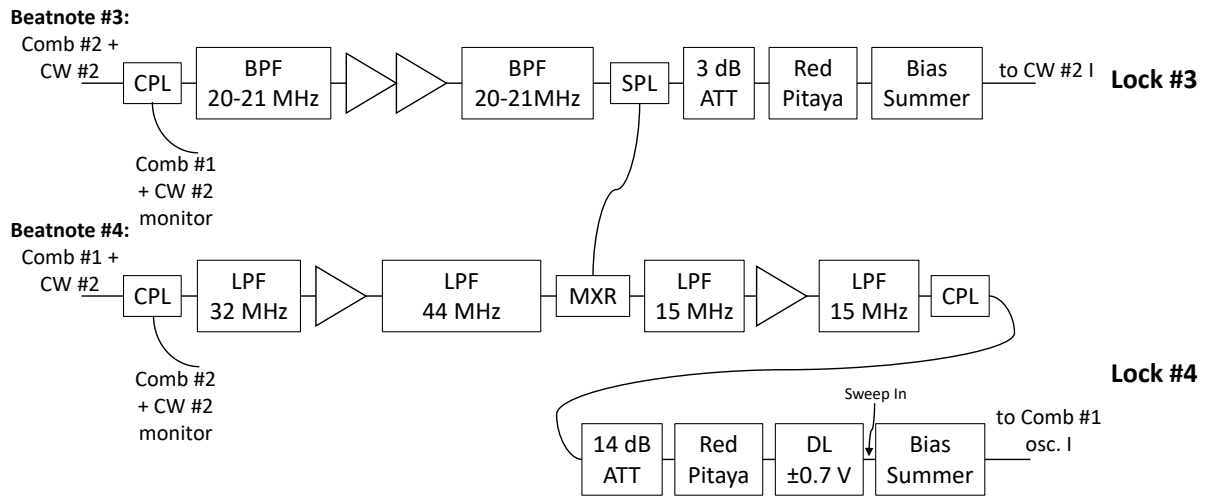


**Figure 2.16:** Schematic of Locks 3 and 4 in the Er-DCS system, used to condition and lock Beatnotes 3 and 4. RF amplifiers, represented by triangles, provide  $\sim 25$  dB of amplification. SPL: splitter, CPL: directional coupler, BPF: bandpass filter, LPF: lowpass filter, MXR: mixer, ATT: attenuator, DL: diode limiter.

Lock 3 achieves a phase noise standard deviation of  $\sim 0.5$  radians with the following settings. For the lock to CW 2 current using the Red Pitaya: reference frequency 20.5 MHz, positive VCO gain sign, VCO gain  $1e10$ ,  $Kp$   $4e1$ ,  $fi$   $1e7$ ,  $fii$   $6.17e3$ ,  $fd$  off, and  $fdf$  off. Lock 4 achieves a phase noise standard deviation of  $\sim 0.5$  radians, but with larger amplitude variation, with the following settings. For the lock to Comb 1 oscillator pump current using the Red Pitaya: positive VCO gain sign, VCO gain  $1e3$ ,  $Kp$   $-7.5e0$ ,  $fi$   $2e1$ ,  $fii$   $2e1$ ,  $fd$   $1e1$ , and  $fdf$  0. The reference frequency for Lock 4 is tuned to the beatnote frequency before locking, typically 4-6 MHz. Locking times are typically greater than 30 minutes.

### 2.2.2 Yb-DCS Stabilization

In the Yb-DCS system, the comb light for generation of the beatnotes used in phase-locking are combined with the CW reference lasers within fiber as shown in Fig. 2.17. Note that each comb is combined with both reference lasers, and the two beatnote signals are separated in free-space using transmission gratings and then incident on separate photodetectors. The detected beatnotes feed into the phase-locking schematics described later in this section. The two CW reference lasers (CW 1: NPRO at 1064 nm, CW 2: ROCK at 1050 nm) are also combined and sent to the setup shown in Fig. 2.18 used for Pound-Drever-Hall (PDH) stabilization of the lasers to an ultralow-expansion Fabry-Perot cavity. Referencing the CW lasers to a cavity reduces the relative frequency drift between them, leaving mainly common-mode frequency changes between them dictated by the drift of the cavity that occurs over longer timescales. An EOM modulates both beams' frequencies, adding sidebands. Lenses mode-match the beam to the cavity, and the reflected light is detected. The transmitted light is monitored using a camera and oscilloscope. The reflected beams of each reference laser are incident on separate photodetectors, and the signals are used as the input for the locking schematic shown in Fig. 2.19. The signals are filtered, mixed with the 13.5 MHz PDH phase-modulating frequency, and filtered again. Analog servos generate the feedback signals, which are split and sent to fast (CW 1: internal PZT, CW 2: external AOM) and slow actuators (CW 1: oscillator temperature, CW 2: internal PZT).

Locks 1 and 2 operate similarly to those of the Er-DCS system, but analog electronics replace the functions of the Red Pitayas (Fig. 2.20). Each conditioned beatnote signal is divided down to increase the effective locking range since most analog servos are incapable of tracking phase changes of more than  $\pi$ . RF generators produce the reference locking frequencies, which are compared to each beatnote signal using phase comparators. A voltage is produced which is 0 when the beatnote frequency matches the reference and changes linearly with phase deviation. This error signal is input to a servo, which generates the feedback signal. As before, the high-bandwidth signal feeds back to fast actuators, while a portion is low-passed and sent to slower actuators for long-term ( $\sim 10$ s minutes) stabilization.

Lock 1 locks Comb 1 to CW 1 via feedback to Comb 1 EOM with slow stabilization





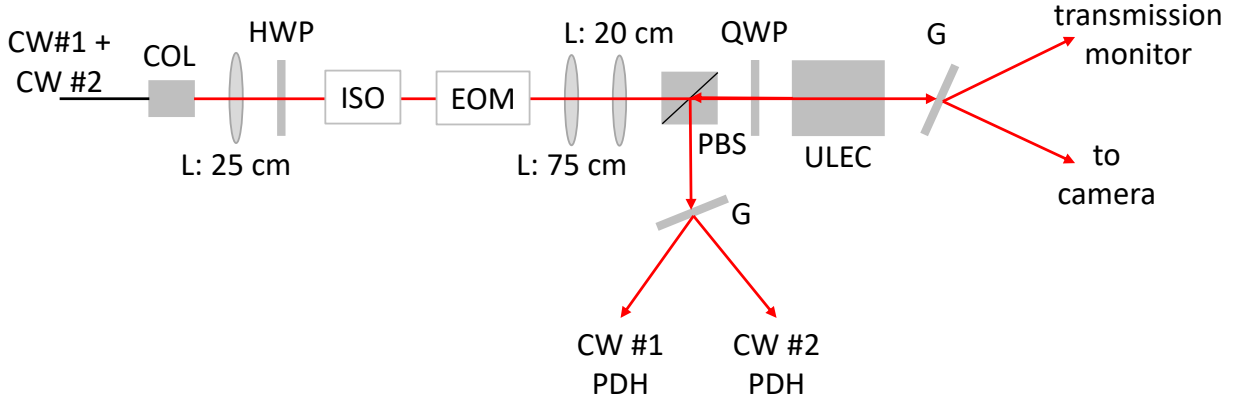


**Figure 2.18:** Schematic of the optical layout used to generate PDH signals for the reference laser locking in the Yb-DCS system. The black beamlines are guided within optical fiber, whereas the red are in free-space. COL: fiber collimation package, ISO: optical isolator, G: transmission grating, EOM: electro-optic modulator, HWP: half-waveplate, QWP: quarter-waveplate, L: lens, with focal length following, PBS: polarization beamsplitter, ULEC: ultralow-expansion cavity.

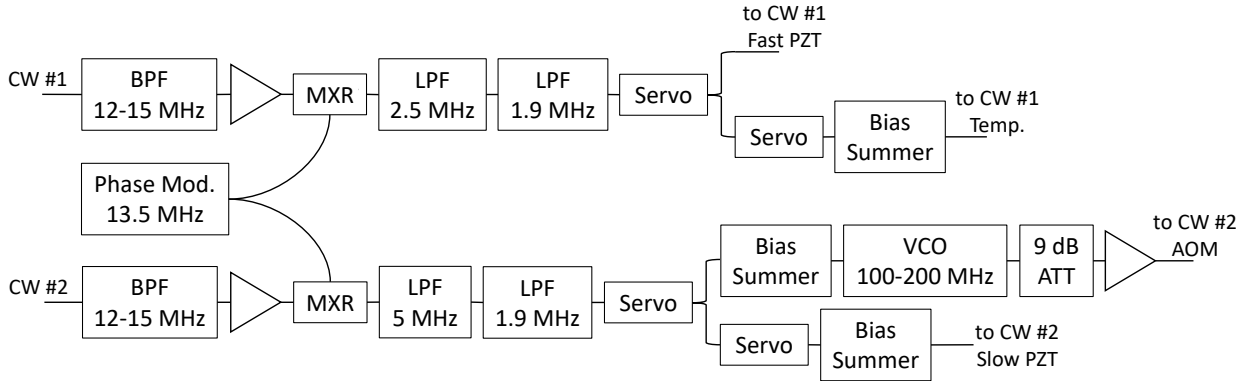


**Figure 2.19:** Schematic of PDH locks for CW 1 and CW 2 in the Yb-DCS system. RF amplifiers, represented by triangles, provide  $\sim 25$  dB of amplification. SPL: splitter, CPL: directional coupler, BPF: bandpass filter, LPF: lowpass filter, MXR: mixer, ATT: attenuator, VCO: voltage-controlled oscillator.

Lock 3 locks Comb 1 to CW 2 via a tip/tilt PZT to which a cavity mirror is mounted (Fig. 2.21). Lock 4 locks Comb 2 to Comb 1 via CW 2 using an EOM for fast actuation as well as a fast PZT for slower actuation, both within the comb oscillator. The locking frequencies are set to ensure that each comb's nearest mode to the CW 2 optical frequency differ by  $\frac{1}{4}f_{rep}$ . Thus, comb modes overlap near 1064 nm and 1008 nm with the number of

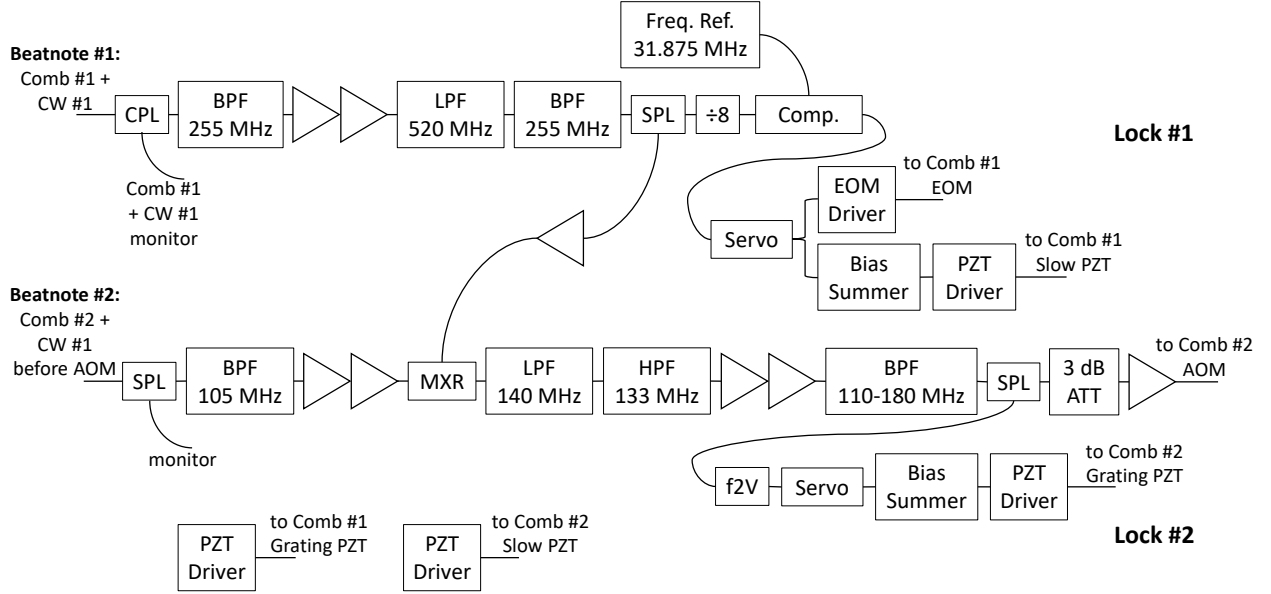


**Figure 2.20:** Schematic of Locks 1 and 2 in the Yb-DCS system, used to condition and lock Beatnotes 1 and 2. RF amplifiers, represented by triangles, provide  $\sim 25$  dB of amplification. Two PZT drivers are used to manually adjust the comb mode frequencies for locking. SPL: splitter, CPL: directional coupler, BPF: bandpass filter, LPF: lowpass filter, MXR: mixer, ATT: attenuator, Comp.: Phase Comparator.

modes between these frequencies differing by exactly one between the combs. A frequency difference of  $\frac{1}{4}f_{rep}$  was chosen at the CW 2 locking point as opposed to 0 so that would  $\Delta f_{rep}$  be 404.873 Hz rather than an unsuitably smaller or larger value. Since  $\Delta f_{ceo}/\Delta f_{rep} \in \mathbb{N}$ , interferograms are identical besides phase errors introduced by sources such as interferometer drift (after the locking detection points) and DCS detection. This is accomplished by mixing  $\frac{1}{4}f_{rep,Comb2}$  with Beatnote 4 and using  $\frac{1}{2}f_{rep,Comb2}$  as the locking frequency.

### 2.3 DCS Detection

As discussed in 1.4, the two frequency combs are interfered at a fast photodetector to measure the dual-comb signal which contains the absorption information. The two combs can be combined after or before passing through the measurement sample, resulting in either one or both combs probing the sample and referred to as asymmetric/dispersive or symmetric/colinear measurements, respectively. Figure 2.22 shows the setup for a typical symmetric measurement, this particular arrangement being used in the Er-DCS system. Here, the comb

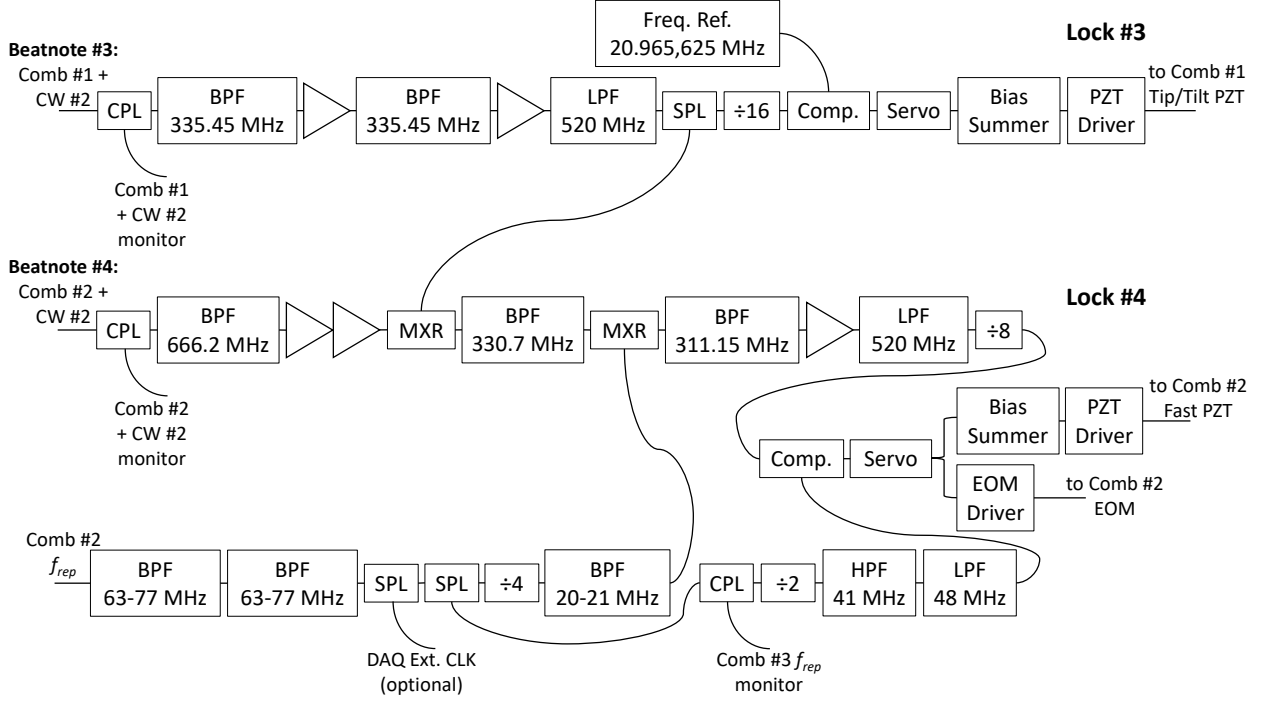


**Figure 2.21:** Schematic of Locks 3 and 4 in the Yb-DCS system, used to condition and lock Beatnotes 3 and 4. RF amplifiers, represented by triangles, provide  $\sim 25$  dB of amplification. Comb 2  $f_{rep}$  can be used to clock the DAQ for synchronous sampling of the interferograms. SPL: splitter, CPL: directional coupler, BPF: bandpass filter, LPF: lowpass filter, MXR: mixer, ATT: attenuator, Comp.: Phase Comparator.

beamlines are coupled into free-space for combining since fiber components do not have the necessary bandwidth to prevent loss over the full  $1\text{-}2\ \mu\text{m}$  comb bandwidth of the Er-DCS supercontinuum (the combs can be transported, however, within appropriate fibers without significant loss). The combs are combined using a polarizing beamsplitter (PBS) and re-coupled into fiber with orthogonal linear polarizations. A half-wave plate (HWP) in one comb beamline is used to balance the powers of the combs.

After sample measurement, the combs are coupled into free-space and spectrally filtered using a grating/slit combination in a  $4f$  arrangement. Limiting the optical bandwidth of the measurement to a narrower region of interest prevents aliasing of the RF signal as well as generally improves the SNR by reducing the number of comb teeth incident on the detector (as discussed in Sec. 1.4.3). A lens is placed such that the grating and retro-reflecting mirror are each one focal length away. The filtering slit is placed at the mirror (Fourier plane) to achieve the highest spectral resolution. The slit can be translated and have its width varied

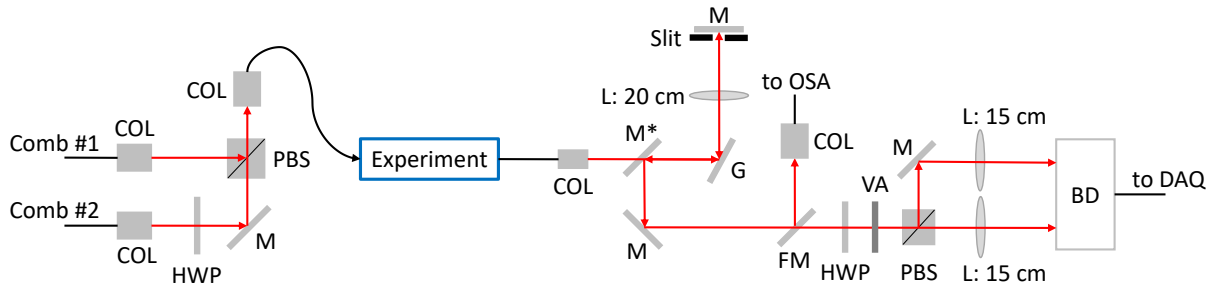


**Figure 2.22:** Schematic of the optical setup used for combining the two post-amplification comb beamlines, which pass to the experiment, and the detection setup after the measurement. The black beamlines are guided within optical fiber, whereas the red are in free-space. HWP: half-wave plate, COL: fiber collimation package, PBS: polarizing beamsplitter, G: reflection grating, M: mirror, FM: flipper mirror, L: lens, followed by focal length, VA: variable attenuator, BD: balanced detector, DAQ: data-acquisition board. The mirror M\* is placed such that the first optical beam passes over the mirror, and the reflection from the 4f optical filter is incident.

to choose a desired portion of the comb spectra for detection. A mask of multiple slits can be used to detect multiple spectral bands, but care must be taken that the RF dual-comb detection is not aliased, resulting in overlap and ambiguity of the detected spectral bands. The beamline after filtering can be directed into an OSA using a mirror on a flipper mount to aid in setting the slit for passing desired wavelengths. The dual-comb signal is detected by a balanced detector, which removes common-mode noise between the combs. For this, the dual-comb beamline is split using a PBS, and a preceding HWP rotates the polarization so that each comb is split equally between the two ports of the detector ( $45^\circ$  if the combs are originally set to p- and s-polarization each). The comb powers must also be balanced for proper detection by using the HWP in the beam-combining section mentioned in the previous paragraph. A variable attenuator is useful for controlling the powers incident on the detector since detection nonlinearities are observed with high powers. Total power incident on each port must typically be kept below  $\sim 50 \mu\text{W}$ . Measurements which utilize more narrowband light, such as the second-harmonic Er-DCS measurements in Ch. 5 and App. A, can employ the same basic setup but largely contained within PM fiber (with the exception of the 4f filtering system, which can be in free-space or replaced in fiber with another filtering device such as a FBG so long as the passband is appropriate).

## 2.4 LPP Ablation Timing and Electronics

For DCS-LPP experiments, the dual-comb interferometer and ablation laser timing must be synchronous so that the same time-delay is measured over multiple shots. Here, a shot is defined as a single pair of an ablation laser shot and signal interferogram. A general illustration of the DCS-LPP timing was shown in Fig. 1.9. Since the timing between interferograms is determined by the dual-comb locking conditions, the ablation laser timing is made to follow the combs' timing. The Nd:YAG ablation lasers used in the above experiments have a repetition rate of roughly 10 Hz (100 ms between shots) and require flashlamp and Q-switch triggers. Since  $\Delta f_{rep}$  is rarely perfectly divisible by 10 Hz, the actual ablation timing must be adjusted slightly so the time-delay remains constant across shots.

The ablation timing is controlled by a FPGA, which receives  $\Delta f_{rep}$  as an input and outputs either a  $\sim 10$  Hz trigger to a delay generator, which generates the flashlamp and Q-switch triggers with the appropriate delays, or the laser triggers directly. The ablation timing is made to be  $\sim 10$  Hz but synchronous with  $\Delta f_{rep}$  by the FPGA beginning an ablation cycle at a positive edge of input  $\Delta f_{rep}$  (Fig. 2.23). The FPGA waits 100 ms then begins the next ablation cycle at the next positive edge of  $\Delta f_{rep}$ . To ensure each ablation cycle is  $\sim 10$  Hz, the FPGA ignores positive edges of  $\Delta f_{rep}$  during the 100 ms waiting period. The flashlamp, Q-switch, and DAQ trigger timings relative to the start of each ablation cycle can be adjusted within the FPGA code. In the Er-DCS system, the user can update  $\Delta f_{rep}$  in real-time to control the timing between the reference and signal DAQ triggers.

To reliably trigger the FPGA,  $\Delta f_{rep}$  should be converted into a square wave. Fig. 2.24 shows the schematic of the electrical setup which generates  $\Delta f_{rep}$  by mixing the detected  $f_{rep}$  of each comb. A Butterworth filter is used to filter and amplify  $\Delta f_{rep}$ . A large amount of amplification in conjunction with a diode limiter can approximate a square-wave, but a function generator is nonetheless triggered by  $\Delta f_{rep}$  and used to output a square wave of the same frequency. Using the function generator, a variable phase-delay can be added, which allows the user to control the timing between the interferogram centerbursts and the positive edge of the associated square  $\Delta f_{rep}$ , which effectively allows the user to control the time-delay being probed by the DCS signal in the LPP experiment. In Fig. 2.23, changing the phase-

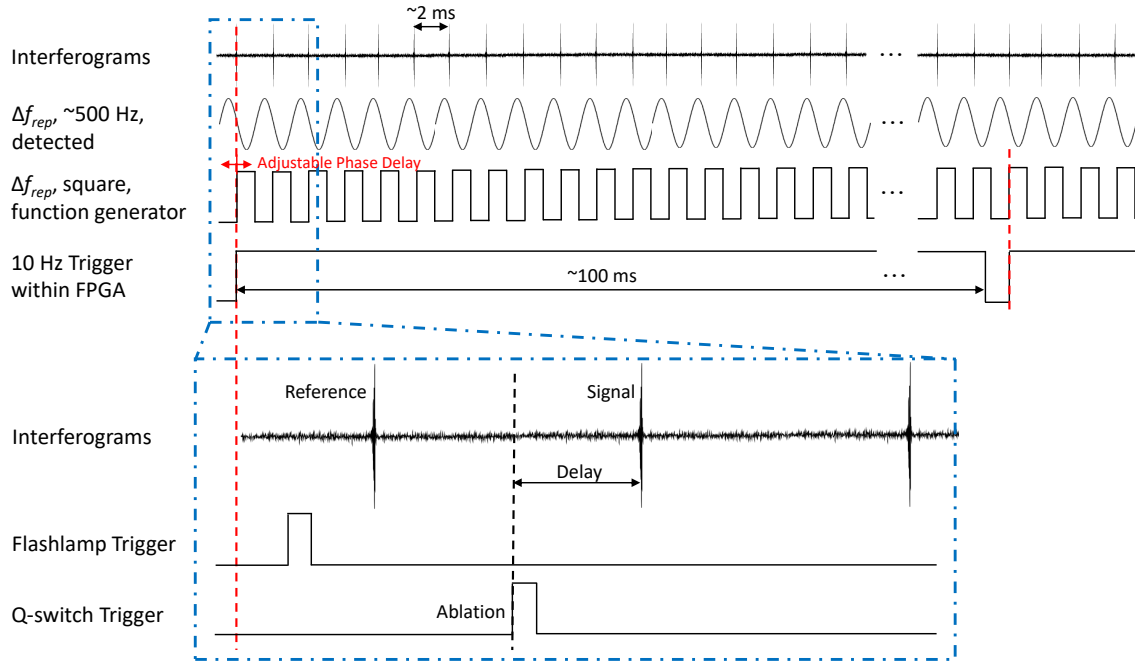


**Figure 2.23:** Representation of the timing of DCS-LPP experiments. The blue dashed box shows detail zoomed in time.

delay shifts the traces in time relative to the interferogram signal and the sinusoidal  $\Delta f_{rep}$ . The time-delay can be adjusted in real-time by adjusting this phase-delay and viewing the relative timing of the interferograms and trigger signals on an oscilloscope/DAQ. Typically, jitter of the time-delay from shot to shot was  $\sim 1 \mu s$  or less.

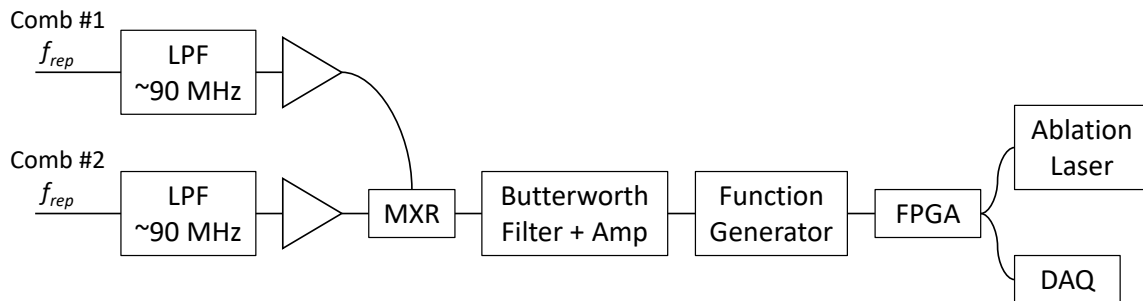


**Figure 2.24:** Schematic of the electrical setup for generating  $f_{rep}$  and using it to synchronize the triggers for the ablation system.

## Chapter 3

### Quantitative Spectral Analysis

#### 3.1 Absorption Spectra Theory

Many references present the mathematical theory for absorption spectroscopy that forms the basis of DCS work [49–51]. A brief review is given here of the relevant equations used in the following analyses. These equations form the foundation of the scientific model of absorption spectra and are also used here in simulating spectra. Modelling atomic absorption spectra serves two main purposes in the DCS studies of LPPs. Firstly, they are used predictively to inform experimental parameters. The choice of sample is partly based on whether strong and numerous enough absorption lines exist for a species within the frequency combs’ optical bandwidth, and whether they have the appropriate spacings and linewidths. Also of importance is whether the transitions originate from energy levels that will be adequately populated at a given LPP excitation temperature for detection of absorption. A simulated spectrum works as a tool to aid the spectroscopist differentiate signal from noise while an experiment is being optimized, as well as to know whether real-time and even processed data match expectations. Secondly, a spectral model, in conjunction with spectral fitting, is used to determine the physical parameters of the sample which directly affect the spectrum. The model is calculated from these parameters (chiefly excitation temperature and number density), which are varied until the difference between the model and the experimental spectra is adequately minimized. This can be done manually or, often necessarily for more complex spectra, using a nonlinear least-squares regression algorithm, which is discussed in the next section. Note, however, that it was determined that directly fitting individual absorption peak areas was superior in mitigating fit-quality diminishment caused by erroneous input information (e.g., poorly measured peaks or incorrect oscillator strengths listed in the liter-



ature). Section 3.2 describes the direct peak-area modelling and fitting that was ultimately used. The absorption modelling presented here is still utilized, however, as a tool for predicting and checking spectra (typically in the early stages of experiments), and serves to present the necessary mathematical background. The details related to the implementation of these equations in code are related in App. B.2.

Atomic absorption spectra consist of lineshapes scaled by an absorption amount. Here, the lineshapes are modelled as Voigt profiles, which are the convolution of a Gaussian lineshape with a Lorentzian lineshape. Gaussian broadening is caused by inhomogeneous mechanisms, dominated by Doppler broadening (so that  $\delta\nu_{Gaussian} = \delta\nu_{Doppler}$ ), which is given by

$$\delta\nu_{Doppler} = \frac{2\nu_0}{c} \sqrt{\frac{2 \ln(2) k_B T_{kinetic}}{m}}, \quad (3.1)$$

given speed of light  $c$  and a transition with center frequency  $\nu_0$  for a species with mass  $m$  at kinetic temperature  $T_{kinetic}$  [50]. The Lorentzian component is generated by homogeneous broadening mechanisms, dominated here by pressure broadening. Stark broadening is another homogeneous broadening mechanism and is caused by the interaction with the electric fields of nearby charged particles, such as ions. Stark broadening can be large at early times in LPPs, as mentioned above in Sec. 1.2.1, but is considered too weak at the late times probed by DCS to be included in this model. Here, a Lorentzian linewidth  $\delta\nu_{Lorentzian}$  is estimated for pressure broadening based on values from previous work rather than calculated. The normalized Voigt lineshape is calculated as

$$\chi_{Voigt}(\nu) = \frac{2\sqrt{\ln(2)}}{\sqrt{\pi}\delta\nu_{Gaussian}} \text{Real}[w(z)], \quad (3.2)$$

where  $w(z)$  is the Faddeeva function with input  $z = x + iy$ , for

$$x = 2\sqrt{\ln(2)} \frac{\nu - \nu_0}{\delta\nu_{Gaussian}}, \quad (3.3)$$

$$y = \sqrt{\ln(2)} \frac{\delta\nu_{Lorentzian}}{\delta\nu_{Gaussian}}. \quad (3.4)$$

The normalized Voigt lineshapes must be scaled based on the amount of absorbance,

which is dictated by sample path length, transition strength, and the relative populations in the lower (initial, denoted  $i$ ) and upper (final, denoted  $f$ ) energy levels of the transition. Specifically, absorbance is given by

$$A(\nu) = \alpha_{i,f}(\nu)L \quad (3.5)$$

(under spatially-uniform conditions) for path length  $L$  and absorbance coefficient

$$\alpha_{i,f}(\nu) = \tilde{\sigma}_0 g_i f_{if} \left( \frac{n_i}{g_i} - \frac{n_f}{g_f} \right) \chi_{Voigt}(\nu). \quad (3.6)$$

Here,  $g_{i,f}$  are the level degeneracies,  $f_{if}$  is the oscillator strength,  $n_{i,f}$  are the level populations, and  $\tilde{\sigma}_0 = \frac{e^2}{4\epsilon_0 m_e c} = 2.654 \times 10^{-6} \text{ m}^2/\text{s}$  is the integrated absorption cross-section constant. The values for  $g_{i,f}$  and  $f_{if}$  are often derived from transition databases which list  $J_{i,f}$  and  $\log(gf)$  for various transitions, noting that  $g_{i,f} = 2J_{i,f} + 1$ .

A Boltzmann distribution of states is assumed to calculate the energy level populations  $n_{i,f}$ , given a thermal distribution of states applies. The state populations are then given by

$$n_{i,f} = n_{tot} \cdot \frac{g_{i,f} \exp(\frac{-E_{i,f}}{k_B T})}{Z(T)}, \quad (3.7)$$

for level energies  $E_{i,f}$  (given by the transition database), excitation temperature  $T$ , and partition function  $Z(T)$ . The partition function is given by

$$Z(T) = \sum_{j=1}^n g_j \exp(\frac{-E_j}{k_B T}) \quad (3.8)$$

and must be calculated over all  $n$  states of the atom.

Thus, the absorbance spectrum  $A(\nu)$  can be calculated by providing  $T$  (excitation),  $n_{tot}$ ,  $T_{kinetic}$ ,  $L$ ,  $m$ ,  $\delta\nu_{Lorentzian}$ ,  $E_{i,f}$ ,  $g_{i,f}$ , and  $f_{if}$ , noting  $\nu_0 = c(E_f - E_i)$  with state energies in  $\text{cm}^{-1}$ . The fit shown in Fig. 3.1 utilized this model.

## 3.2 Spectral Fitting

To extract physical values from absorption spectra, such as temperatures and number densities, absorption peak areas (area under the curve) are necessary. Direct integration is not practical in congested spectra (e.g., DCS spectra of heavy elements). Firstly, absorption features of spectra of heavy elements or containing multiple elements often overlap with one another, even if only partially such as in the lineshape wings. Secondly, as a Fourier transform spectroscopic technique, DCS spectra are necessarily convolved with ILF, which is the Fourier transform of the apodization window (see Sec. 1.4), typically causing lineshape broadening. Also, instrumental broadening effects are known to introduce nonlinearities in Beer's Law when computing absorbance of strong peaks, thereby breaking the linearity between column density and apparent absorbance computed from transmittance spectra (see Sec. 1.4.4). By determining peak areas via fitting an appropriate spectral model to experimental data, an analysis can account for both effects.

In spectral fitting, the goal is to determine the set of input parameters for a spectral model that create a spectrum that matches the experimental data as closely as possible. The spectral model is generated using an initial guess for the input parameters and compared to the experimental data. A nonlinear least-squares regression algorithm varies the input parameters until, ideally, the model matches the experimental data. Practically, theory and experiment will never completely agree, and the algorithm has several stopping conditions, including optimality tolerance ( $10^{-10}$ ), function tolerance ( $10^{-10}$ ), step-size tolerance ( $10^{-10}$ ), maximum number of iterations ( $10^{10}$ ), and maximum number of function evaluations ( $10^{10}$ ), with values that have worked well for DCS applications listed in parentheses. Once the fitting is complete, the quality of the fit can be judged based on the  $R^2$  value, the mean RMS sum of the residuals, and the standard errors of the fitting parameters. Note, these estimations of the fit reflect the statistical errors of the fit rather than experimental errors.

To avoid errors from overlapping lines or wings of nearby lines, it is important to include as many transitions as possible in the fitting model. Transition information can be acquired from literature, typically for stronger and isolated lines. However, the literature for heavier elements in particular is often incomplete. Including dipole-allowed transitions which do not

appear in literature sources is important in fitting so that peak areas are not erroneously assigned, particularly in regions of overlap. All dipole-allowed transitions between lower-state  $i$  and upper-state  $f$  for a species can be calculated knowing the energies  $E_{i,f}$ , degeneracies  $J_{i,f}$ , and parities of all states, which are available online through NIST [52]. Dipole-allowed transitions occur between states of differing parity and obey the selection rule  $\Delta J = 0, \pm 1$ .

The model used for the fitting routine was not the same absorbance spectrum model described in Sec. 3.1. There, the input parameters included excitation temperatures and total number densities for each species, which dictated the absolute and relative heights of the peaks. Here, the transitions are modelled with their own independent parameters, excluding the absorbance baseline offset value. Such a model was found to be superior for use in fitting because any problem with one transition's fit did not affect the fit of the others. When using temperature and total number density as input parameters, the fitting algorithm adjusts these two parameters so that all transitions closely match the experimental spectrum. But in the case of any single transition having been measured poorly (e.g., being located at the spectral window edge where the noise baseline is higher), having incorrect database information (e.g., incorrect listed oscillator strength), or overlap with an unknown line, the fitting algorithm will degrade the fit of all other lines to better fit this erroneous line rather than ignoring it. An example of this occurred in the studies of Nd I. One of the ground-state lines near 533.5 nm is believed to have an incorrect oscillator strength listed in the Kurucz database, as discussed in more detail in Ch. 5. Fitting temperature and number density directly for Nd I spectra which included this line resulted in poor results with large residuals (Fig. 3.1). By fitting the lineshape parameters for each transition independently, the results of the fit can be analyzed for each transition separately, and any erroneous lines can be excluded post-fit.

Using the list of transition frequencies, the model spectrum is constructed as a sum of Voigt functions, each corresponding to a center frequency  $\nu_0$  from the list of input transitions but with independent area/height and Gaussian/Lorentzian width  $w_G$  and  $w_L$ . Nonlinear least squares algorithms, such as the Levenberg-Marquardt and the trust-region-reflective, are used to vary the model parameters and minimize the difference to the experimental spectrum. The center frequency of each peak should be bound to a range (e.g.,  $\nu_0 \pm w_V$ , where  $w_V$  is the

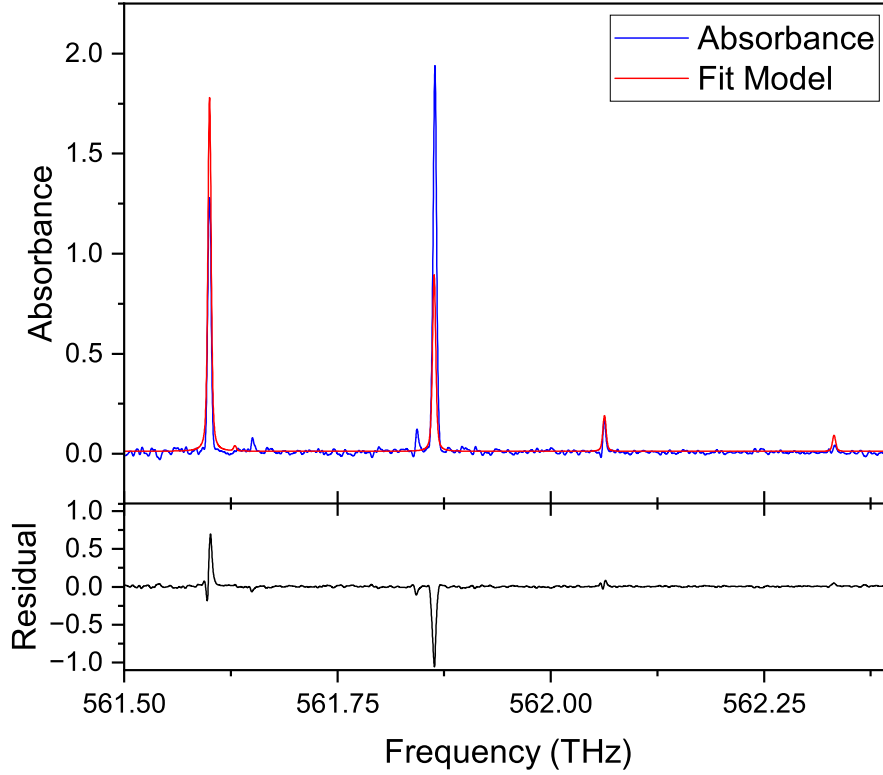


**Figure 3.1:** Example of a spectral fit of Nd I in which  $T$  and  $n_{tot}$  were fit directly as parameters, with residuals included. The residuals are as large as  $\sim 1$  absorbance unit. As is discussed in Sec. 5.5, the oscillator strength for the 561.5879 THz transition is believed to be incorrect in the literature. The fitting algorithm attempts to minimize the residuals of this transition by compensating with larger residuals for all other transitions. The transition can be excluded from the fitting to improve performance, but it is not always known which spectroscopic input may be incorrect, and small inconsistencies in a few transitions will affect the entire fit.

FWHM of the Voigt profile), to allow for small variations in calibration of the experimental frequency axis across the spectrum or variations in actual line center frequency potentially due to line-shifts (Stark and/or van der Waals) or unresolved hyperfine/isotope structure. The peak finding is initialized by manually setting expected values for  $w_G$  and  $w_L$  and using a numerical estimation of the peak areas from the experimental data. The widths  $w_G$  and  $w_L$  should also be bound (e.g., to values no larger than  $3 \times$  the initial estimates). A weighting function is used so that only spectral regions with transitions to be fit are included. An example weighting function has values of 1 at frequencies of all input peaks  $\nu_0 \pm 10w_V$  and 0s elsewhere. In this way, anomalous peaks and noise well-separated from the targeted peaks

can be excluded in the fitting optimization.

After summation of all Voigt functions over the frequency axis corresponding to the experimental data, the model spectrum is effectively convolved with the ILF corresponding to the apodization window used on the original experimental signal. This convolution is performed in the Fourier time-domain by converting the simulated spectrum to transmittance, taking the inverse Fourier transform, multiplying by the apodization window, computing the Fourier transform, then calculating the absorbance spectrum which now includes the instrumental broadening. As discussed in Sec. 1.4.4, proper inclusion of the apodization is essential to convert the model absorption spectrum (where peak areas are linearly related to column densities) to the apparent absorption plotted in the experimental spectrum.

Figures 4.5, 4.6, 4.11, and 5.3 show examples of spectral fits. Appendix B.3 describes some of the details of the implementation of the fitting routine in code.

### 3.3 Boltzmann-Plot Analysis

Boltzmann plots are a method of obtaining excitation temperature  $T$  and total column density  $n_{tot}L$  for a species based on measured absorbance strengths. The technique assumes a thermal distribution of states for the species, and, given the oscillator strengths of the transitions,  $T$  and  $n_{tot}L$  are calculated based on the relative and absolute absorbance strengths measured. Within the context of LPPs, assumption of a Boltzmann distribution is part of a larger assumption of local thermodynamic equilibrium (LTE), which states that a thermal distribution exists at each point in the plume. This condition does not imply, however, that the excitation temperature is the same at all points in the plume. Evaluation of LTE is a focus of LPP studies and is discussed more in Chs. 4 and 5. Each transition measured is a single point on a Boltzmann plot, and multiple transitions should lie along a line.  $T$  and  $n_{tot}L$  are related to the points by the slope and y-intercept of the line they form. Therefore, multiple transitions are needed for a Boltzmann-plot analysis in order to fit them to a line. More transitions measured decrease the uncertainty of the fitted line. Moreover, including transitions over a range of energies aids analysis, the effects of which are also discussed in Ch. 5.

If  $n_i \gg n_f$ , which is valid for the temperature ranges probed in these late-time LPP

experiments, stimulated emission may be neglected, and Eq. 3.6 may be simplified so that Eq. 3.5 integrated over frequency gives:

$$S_{if} = \int A(\nu) d\nu = \tilde{\sigma}_0 f_{if} n_i L. \quad (3.9)$$

Therefore, the spectrally-integrated area  $S_{if}$  of an absorbance line is proportional to the column density  $n_i L$  in the lower level of the transition multiplied by the oscillator strength of the transition, subject to the approximations given. Combining Eqs. 3.7 and 3.9 and expressing as a linear equation of the form  $y = b + mx$  yields:

$$\ln\left(\frac{n_i L}{g_i}\right) = \ln\left(\frac{S_{if}}{\tilde{\sigma}_0 g_i f_{if}}\right) = \ln\left(\frac{n_{tot} L}{Z(T)}\right) - \frac{E_i}{k_B T}. \quad (3.10)$$

Using this relationship, a “Boltzmann plot” may be constructed by plotting  $\ln(\frac{n_i L}{g_i})$  versus  $E_i$  for a set of measured transitions, an example of which is shown in Fig. 3.2. When fit with a linear function, the slope and y-intercept are directly related to  $T$  and  $n_{tot} L$ , respectively. As noted, confidence in the Boltzmann plot is increased by including more transitions over a variety of energies. The error propagation is described in the next paragraph, with the uncertainties coming from the oscillator strengths, the fitted peak areas, and the error of the linear fit of the Boltzmann plot. Oscillator strength uncertainties  $\sigma(f_{if})$  must be obtained from literature and are often reported in the relative error form  $\frac{\sigma(g_i f_{if})}{g_i f_{if}}$ . The best estimate of uncertainty in the fitted peak areas,  $\sigma(S_{if})$ , is the standard error given by the fit statistics. It must be noted that this is a purely statistical measure and is not calculated from any physical uncertainties.

Each transition’s value on the Boltzmann plot is calculated as

$$y_{if} = \ln\left(\frac{S_{if} [\text{Hz}]}{\tilde{\sigma}_0 [\text{m}^2/\text{s}] \cdot 100^2 \cdot 10^{\log(gf)_{if}}}\right), \quad (3.11)$$

which has units of  $[\ln(\text{cm}^{-2})]$  and uses each transition’s oscillator strength in the commonly reported  $\log(gf)$  form. This is simply a slightly altered form of the middle expression in

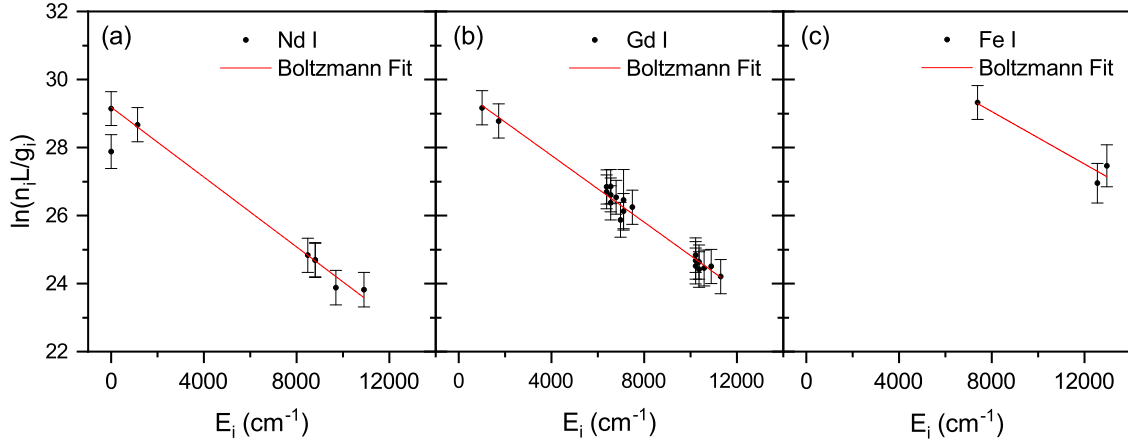


**Figure 3.2:** Example Boltzmann plots for three species, showing alloy data from Ch. 5. (Figure from [30])

Eq. 3.10. The uncertainty is given by

$$\sigma(y_{if}) = \sqrt{\left[\frac{\sigma(S_{if})}{S_{if}}\right]^2 + \left[\frac{\sigma(g_i f_{if})}{g_i f_{if}}\right]^2}. \quad (3.12)$$

The values of  $y_{if}$  are fit to a line of the form  $\tilde{y} = mx + b$  such that  $x = E_i$ ,  $m = \frac{-1}{k_b T}$ ,  $b = \ln(\frac{ntotL}{Z(T)})$ , and  $\tilde{y}_{if} = \tilde{y}(E_i)$ . The uncertainties of the slope and y-intercept are

$$\sigma(m) = RMSE \frac{1}{\sqrt{\sum_i [(E_i - \bar{E})^2]}} \quad (3.13)$$

and

$$\sigma(b) = RMSE \cdot \sqrt{\frac{\sum_i (E_i^2)}{N \sum_i [(E_i - \bar{E})^2]}}, \quad (3.14)$$

respectively, for average value  $\bar{E} = \text{mean}(E_i)$ , number of fit points  $N$ , and root-mean-square error

$$RMSE = \sqrt{\frac{\sum_{if} (y_{if} - \tilde{y}_{if})^2}{N - 2}}. \quad (3.15)$$

Temperature  $T$  is given by

$$T = \frac{-1}{k_B m} \quad (3.16)$$



with uncertainty

$$\sigma(T) = \frac{\sigma(m)}{k_B m^2} \quad (3.17)$$

in units of K.

Total column-density  $n_{tot}L$  is given by

$$n_{tot}L = e^b Z(T) \quad (3.18)$$

with uncertainty

$$\sigma(n_{tot}L) = n_{tot}L \cdot \sqrt{\sigma(b)^2 + \left(\frac{\sigma(Z(T))}{Z(T)}\right)^2} \quad (3.19)$$

in units of  $\text{cm}^{-2}$ . Here,  $\sigma(Z(T))$  is calculated as

$$\sigma(Z(T)) = 1/2(|Z[T + \sigma(T)] - Z[T]| + |Z[T - \sigma(T)] - Z[T]|), \quad (3.20)$$

which is the average value of the difference between the partition function evaluated at  $T$  and evaluated at  $T \pm \sigma(T)$ .

Note, one can also calculate individual state column-densities as

$$n_i L = \frac{S_{if}}{\tilde{\sigma}_0 f_{if}} = g_i e^{y_{if}} \quad (3.21)$$

with uncertainty

$$\sigma(n_i L) = n_i L \cdot \sigma(y_{if}), \quad (3.22)$$

as was done in Fig. 5.4.

To calculate a theoretical oscillator strength given a transition peak area and the relevant Boltzmann-plot fit, as is done for Table 4.2, the oscillator strength in the form of  $\log(gf)$  is given by

$$\log(gf)_{if} = \log\left(\frac{S_{if}}{\tilde{\sigma}_0} \cdot e^{-\tilde{y}_{if}}\right) = \log(e)[\ln(S_{if}) - \ln(\tilde{\sigma}_0) - \tilde{y}_{if}] \quad (3.23)$$

with uncertainty

$$\sigma(\log(gf)_{if}) = \log(e) \cdot \sqrt{\left(\frac{\sigma(S_{if})}{S_{if}}\right)^2 + \sigma(\tilde{y}_{if})^2}. \quad (3.24)$$

## Chapter 4

### Measurement of Neutral Gadolinium Oscillator Strengths using DCS in LPPs

#### 4.1 Introduction

This chapter presents the measurement and analysis of a Gd-containing LPP using the Yb-DCS system, which was published in *Spectrochimica Acta Part B: Atomic Spectroscopy* [29]. The oscillator strengths of 43 transitions of neutral Gd from 530 to 535 nm were determined based on high-resolution absorption spectra measured by probing a laser-produced plasma using time-resolved dual-comb spectroscopy. Absorption spectra were measured at various time-delays, ranging from 33 to 252  $\mu\text{s}$  after the onset of the plasma formation, over which the temperature and number density varied as the ablation plume evolved. A Boltzmann analysis was used to determine the excitation temperature and column density of Gd in the ablation plume, based on measured absorption from 20 Gd I spectral lines with known oscillator strengths. Oscillator strengths were then determined for additional dipole-allowed Gd I transitions identified in the absorption spectra, 19 of which were previously unreported. Oscillator strengths of all measured transitions were compared with literature values when available and show good agreement in most cases. Time-resolved measurement of atomic absorption in the cooling plasma provides access to a range of excitation temperatures and optical densities for the atoms in the ablation plume, allowing repeated measurements under different conditions, thereby improving confidence in the results. Our results also highlight that the high spectral bandwidth and resolution capabilities of dual-comb spectroscopy make it well-suited to measuring the dense optical spectrum of Gd, and the technique is applicable to other elements, especially lanthanides and actinides.

Accurate and precise knowledge of oscillator strengths is important for a variety of scientific fields and applications, both experimental and theoretical [49]. The oscillator strength

characterizes the relative and absolute emission intensity and absorption strength of spectral lines and is necessary both for prediction of optical spectra and for interpretation of measured spectra. Models of atomic and molecular structure may be used to predict oscillator strengths, and experimental measurements are critical for testing these models [53, 54]. Diagnostic measurements used for characterizing atomic and molecular species based on their spectra rely on oscillator strengths for quantitative calculations using the recorded spectral features. For example, absorption and emission spectroscopy often rely on databases of known transitions with oscillator strengths to identify component species, measure number densities, and determine temperatures. These diagnostics find use in a wide range of applications, including astronomy [55, 56], plasma characterization [18, 19], atmospheric sensing [8, 57], high-explosive fireball characterization [58–60], nuclear engineering and nonproliferation [9, 61], and many more. Although extensive data have been collected on oscillator strengths for electronic transitions in atoms, significant gaps remain for high-Z elements (lanthanides and actinides) and weak transitions in many other elements. Improved optical transition data on high-Z elements are especially important for spectral modeling and diagnostics in LPPs, which are used in a variety of applications including as surrogates for nuclear fireball conditions to predict physical and chemical pathways for nuclear fallout formation [62, 63].

There are multiple methods for measuring oscillator strengths, and Huber and Sandeman present an instructive and comprehensive overview and examination of many of the techniques [49]. Here, we focus on techniques using the optical absorption or emission spectra of atomic species. Methods can be divided into two main classes depending on whether they determine absolute or relative oscillator strengths. Absolute oscillator strengths for a given optical transition may be measured by combining radiative lifetimes of the upper state with branching fractions to all coupled lower states [64–66]. Typically, lifetimes are measured using laser-induced fluorescence spectroscopy, and branching fractions are determined using broadband and high-resolution Fourier transform spectroscopy (FTS). One challenge with this approach is the need to measure high-resolution spectra over large spectral ranges to determine accurate branching fractions, often requiring unique instrumentation such as the 1m FTS at Kitt Peak National Observatory [67, 68]. Uncertainties in oscillator strengths

determined from branching fraction and lifetime measurements typically range from 5-25% [69].

Relative oscillator strengths may be determined from emission spectra on sources meeting LTE conditions by combining relative emission intensities with knowledge of the excitation temperature of the source, from which a Boltzmann distribution of level populations is calculated [70–72]. Optically-thin conditions are required unless curve-of-growth (COG) methods or other methods are used to account for nonlinearities between number density and emission intensity [73]. Additional knowledge of the absolute atomic number density, or comparisons to known values of oscillator strengths obtained from other measurements, may be used to obtain absolute oscillator strengths. These methods have been widely used and results have been incorporated into many libraries and databases of oscillator strengths, especially for elements and/or transitions not studied extensively using other methods. For example, emission intensities from National Bureau of Standards (NBS) monographs based on measurements in arc sources [74] were used to determine oscillator strengths for many elements and incorporated into the online Kurucz database [75]. While these measurements provide valuable information for a wide range of elements, the cataloged transitions are far from complete and oscillator strengths may have high uncertainties up to 50% [76].

Absorption spectroscopy is also used for measuring oscillator strengths [49]. Measurement of absolute oscillator strengths using absorption spectroscopy requires knowledge of the temperature and total column density of the source being measured, which is challenging to achieve in practice [77, 78]. Relative oscillator strengths can be determined similarly to emission methods, assuming LTE conditions, and comparison with known oscillator strengths can then provide absolute values. Experiments have used broadband arc lamps to probe atomic vapor produced in ovens to measure equivalent linewidths using two identical spectrometers to measure relative oscillator strengths [79, 80]. Absolute values determined by using a reference line with a known oscillator strength have uncertainties reported from 5% down to 0.5% with carefully controlled measurements [81]. Tunable laser absorption spectroscopy can also be used when oscillator strengths of some lines are known, either by simultaneous measurement of known and unknown lines [82] or through the use of Boltzmann plots [83], but such measurements are often limited by the tuning range of the laser.

LIBS has been employed to measure oscillator strengths, and a recent review provides a summary of prior work with references [84]. In LIBS, a pulsed laser is used to generate a LPP by ablating the surface of a solid sample and emission spectra from the high-temperature plasma are measured. Typically, these methods rely on knowledge of transition probabilities for a subset of measured emission lines, from which a Boltzmann or Saha-Boltzmann plot is constructed. The slope and intercept of this plot is then used to determine the transition probability of additional measured lines. Often these methods require determination of secondary plasma properties such as electron density to predict Stark broadening [85]. Self-absorption is the primary limitation on accuracy of LIBS measurements for determination oscillator strengths, but curve-of-growth or  $C\sigma$  methods [86–88] improve accuracy, and typical uncertainties reported for oscillator strengths measured using LIBS range from 10-20% [10].

While LIBS is an extremely convenient method for measuring oscillator strengths, applicable to any element which can be ablated from a solid, there are some practical limitations. Due to the need for time-gated detection of LIBS, it is challenging to measure emission spectra with the high-resolution needed to resolve closely-spaced transitions. In addition, Stark broadening from high electron densities in the LPP may limit the ability to measure closely-spaced lines. High-Z elements with unfilled f-shells (lanthanides and actinides) exhibit highly dense optical spectra due to the large number of allowed optical transitions, and measurement of well-resolved optical lines is critical for accurate determination of transition probabilities. Thus, while LIBS has been applied successfully to measure transition probabilities in many elements (Na, Cr, Si, Ag, In, Ni, Pb, Sb, S, Xe, Sn, Pb, Cu, Zr, Cd, Au, Re, Ne, Mo, W) [84], including some with unfilled d-shells, it has not to our knowledge been applied to measurements in lanthanides and actinides, where oscillator strength data are often lacking.

Some of the challenges faced by LIBS are circumvented by absorption spectroscopy techniques, as described in Ch. 1. The primary limitation of absorption spectroscopy for measurements in LPPs has been the small spectral tuning range for CW laser sources, typically enabling measurement of 1-2 transitions before coarse adjustment of the laser center wavelength is required. For oscillator strength measurements, it is desirable and often necessary

to measure multiple transitions over large wavelength ranges so that an excitation temperature may be determined.

In this work, we leverage these newly developed capabilities to demonstrate a new method for measuring oscillator strengths of atomic transitions in a LPP using time-resolved dual-comb absorption spectroscopy. The method involves measurement and spectral fitting of high-resolution absorption spectra acquired at different time-delays after LPP formation, from which relative atomic column densities and oscillator strengths are determined. Comparison of measured absorption for lines with known oscillator strengths allows the temperature and total column density to be determined from a Boltzmann plot analysis, from which absolute oscillator strengths are calculated. Although conceptually similar to previous LIBS-based measurements of oscillator strengths in LPPs, the combination of high spectral coverage, high spectral resolution, and time-resolved absorption spectroscopy provides a powerful set of features for determination of oscillator strengths. In addition, due to the time-varying nature of the LPP, absorption spectra are measured at varying times in the LPP evolution as it cools, enabling multiple measurements of oscillator strengths over a range of temperatures and column densities, and thereby improving confidence in the measurement results.

We apply this method to determine oscillator strengths for the lanthanide rare-earth element Gd, which has a highly complex optical spectrum with closely-spaced optical transitions. Absorption spectra are measured with DCS from 530.5-535.2 nm at multiple time-delays from 33-252  $\mu$ s after formation of a LPP from laser-ablation of Gd metal. The time-resolved measurements show temperatures from 4200-1700 K as the LPP cools, and oscillator strengths show good consistency when measured over these different temperatures. Low-noise spectra with resolutions from 1.7-8.0 GHz (1.6-7.6 pm) are achieved depending on the time-delay, allowing differentiation of closely-spaced transitions and precise spectral fitting of absorption spectra. Oscillator strengths from a set of 24 Gd I lines are measured and compared to literature values, and new oscillator strengths for 19 Gd I transitions are reported. Absolute measurement uncertainty in  $\log(gf)$  was  $\sim 0.14$ , determined largely by uncertainties in the reference oscillator strength data. Measurement precision in  $\log(gf)$  determined from reproducibility of values determined from different delays/temperatures was

$\sim 0.07$ .

## 4.2 Experiment

The Yb-fiber based combs as well as their amplification and stabilization are described in Ch. 2. Figure 4.1 presents a simplified schematic of the layout and timing. When locked, Comb 2 had a repetition rate of 77.848,610 MHz with a difference frequency from Comb 1 of 404.544 Hz. Both combs were amplified and then frequency doubled using 0.5  $\mu\text{m}$  thick Barium Borate (BBO) crystals to reach the wavelengths of interest near 533 nm. An AOM set at 5/4 the repetition rate of Comb 2 shifted the frequency of Comb 1 to shift the detected RF spectrum away from the fold-over points that occur at half-integer multiples of the repetition rate [89]. A colinear dual-comb setup was employed in which the beam paths of the combs were combined with orthogonal polarizations before probing the ablation plume within a vacuum chamber. The combs passed through the ablation chamber after being combined with a polarizing beam splitter (PBS).

A LPP was generated by focusing a Nd:YAG laser onto a sample of 99.9% pure Gd metal. The Nd:YAG ablation laser at 1064 nm was operated at a  $\sim 10$  Hz repetition rate with 200 mJ pulse energy and  $\sim 5$  ns pulse duration. The ablation pulses were focused on to the sample surface by a 12.5 cm spherical lens, providing a spot size of  $\sim 1$  mm and power density of  $\sim 3.7$  GW/cm<sup>2</sup>. The sample was laterally translated by a stepper motor at a rate of 0.08 cm/s. The Gd sample was placed in a vacuum chamber under 30 Torr of flowing Ar. The dual-comb probe beam propagated through the ablation plume at a height of 4 mm above the Gd sample surface. The details of the detection setup are described in Sec. 2.3. The average power of each beam on the detector was limited to 26  $\mu\text{W}$  to remain within the detector's linear response region. The detector signal was recorded by a 14-bit DAQ (Alazar 9440) at a sampling rate of 125 MHz. Fig. 4.1(b) shows a schematic of the timing between the ablation event and the reference and signal interferograms, described in Sec. 1.3. The timing and synchronization of the measurement is described in Sec. 2.4 and utilized a Nexys 4 Artix-7 FPGA. Interferograms in the dual-comb signal repeated every 2.47 ms, determined by the difference frequency of 404.544 Hz between the combs.

Transmission through the ablation plume was measured at seven different time-delays – 33

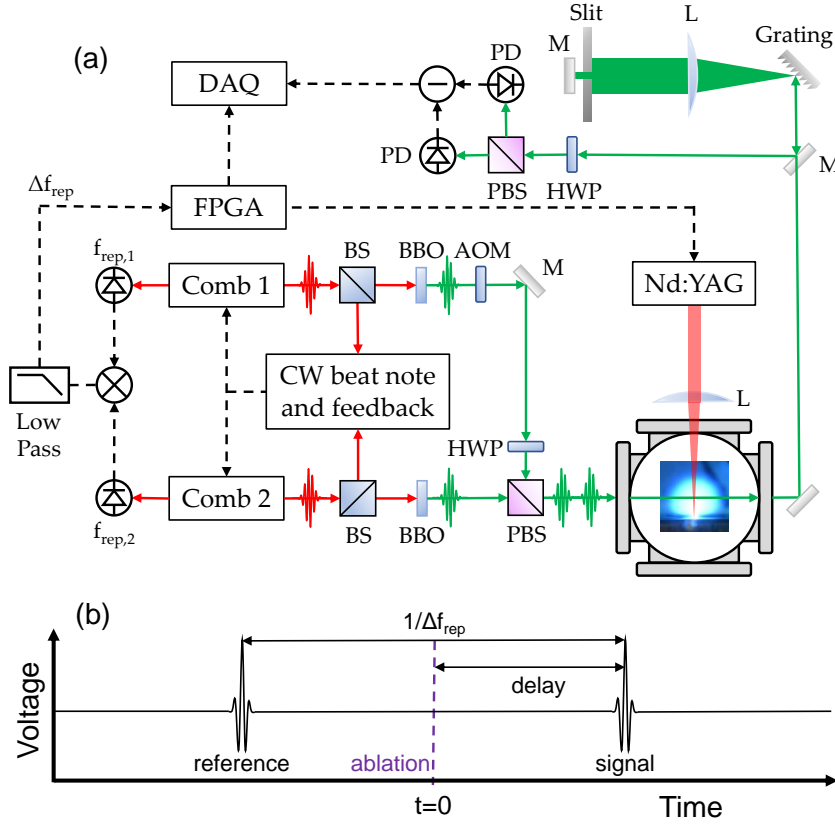


**Figure 4.1:** (a) Experimental schematic of the dual-comb setup. BS: beamsplitter; AOM: acousto-optic modulator; M: mirror; HWP: half-wave plate; PBS: polarizing beamsplitter; L: lens; PD: photodetector. (b) Schematic of the time-domain interferograms generated by the dual-comb signal. The interferograms repeat with a frequency equal to the inverse of the difference between the repetition rates of the two frequency combs. Only the interferograms coming directly before and after the ablation events repeating at  $\sim 10$  Hz are recorded. The first interferogram is used as a reference, and the second is the signal containing the absorption information due to the ablation plume. The measured time-delay is defined as the length of time between the ablation event and the centerburst of the signal interferogram. (Figure from [29])

$\mu\text{s}$ ,  $53 \mu\text{s}$ ,  $72 \mu\text{s}$ ,  $88 \mu\text{s}$ ,  $102 \mu\text{s}$ ,  $154 \mu\text{s}$ , and  $252 \mu\text{s}$  – and 750 interferograms were recorded for the signal and reference at each delay. Timing jitter between ablation and the interferogram centerbursts was  $\sim 0.6 \mu\text{s}$ . Section 1.4.4 gives the details of the signal processing procedures. A Blackman-Harris apodization window was used on each interferogram with a duration  $T_{meas}$  depending on the time-delay from ablation:  $33 \mu\text{s}$  ( $\pm 32 \mu\text{s}$ ),  $53 \mu\text{s}$  ( $\pm 53 \mu\text{s}$ ),  $72 \mu\text{s}$  ( $\pm 72 \mu\text{s}$ ),  $88 \mu\text{s}$  ( $\pm 88 \mu\text{s}$ ),  $102 \mu\text{s}$  ( $\pm 102 \mu\text{s}$ ),  $154 \mu\text{s}$  ( $\pm 154 \mu\text{s}$ ),  $252 \mu\text{s}$  ( $\pm 154 \mu\text{s}$ ), where ( $\pm XX \mu\text{s}$ ) is the extent of the apodization window to each side of the interferogram centerburst.



The frequency resolutions  $\delta f_{meas}$ , defined as the FWHM linewidth of the ILF, for the above listed apodization window widths were 8.02 GHz, 4.84 GHz, 3.57 GHz, 2.92 GHz, 2.52 GHz, 1.67 GHz, and 1.67 GHz. Each interferogram was zero-padded so that the resulting SBS had a frequency sampling of  $\sim 0.50$  GHz. After Fourier transformation, the 750 signal and reference SBS were averaged, and absorbance was calculated via  $A(\nu) = -\ln[\overline{SBS}_{sig}(\nu)/\overline{SBS}_{ref}(\nu)]$ . A 7<sup>th</sup> order polynomial baseline was fit to the absorbance baseline and subtracted.

The relative frequency axes of the absorbance spectra were determined using the repetition rates and the difference frequency of the combs for each measurement (Eq. 1.4). The absolute frequency calibration of the absorbance spectra was determined by comparing the experimental spectrum to known Gd line positions and applying a constant frequency shift to the experimental spectrum. Small variations in relative or absolute frequency calibration ( $< 1$  GHz) were tolerable (and expected due to unresolved hyperfine/isotope structure in the Gd spectrum) and could be accounted for in the spectral fitting routine as described in Sec. 3.2.

### 4.3 Theory

The procedure used in this study to obtain oscillator strengths from absorption spectra is as follows. First, an absorption spectrum is measured of a species in a spectral region containing transitions with known oscillator strengths. Based on the measured areas of the absorption peaks and reference oscillator strengths, a Boltzmann plot is constructed to determine the excitation temperature and total column density (see Sec. 3.3). If the absorption is then measured from a transition with unknown oscillator strength but known frequency, energy levels, and level degeneracies, Eq. 3.10 is used to calculate the oscillator strength based on the previously determined temperature and total column density.

In the following sections, we apply this approach to determine temperature and total column density in a Gd LPP using a set of 20 Gd I absorption lines with published oscillator strengths as reported by Meggers et al. [74] and compiled by Kurucz in an online database [75]. We then use the method described to determine the oscillator strengths for 23 additional measured Gd I transitions, 19 of whose oscillator strengths were not available in the literature. We also use the temperature and total column density measurements to re-

determine oscillator strengths for the initial 20 Gd I transitions and compare against other published values from the literature.

#### 4.4 Time-Resolved Absorption Spectra of Gd

Absorbance spectra of the Gd ablation plume are shown in Fig. 4.2 for the seven measured time-delays after ablation, and the 88  $\mu\text{s}$  spectrum is shown in detail in Fig. 4.3. The spectral range spanned a 5 THz (4.73 nm) region of optical frequencies from 560 to 565 THz (530.46 to 535.19 nm). The absorbance SNR varied across the spectrum due to variations in power of the frequency combs, and the region plotted has been truncated accordingly to avoid the high-noise regions at the edges of the probed spectral range.

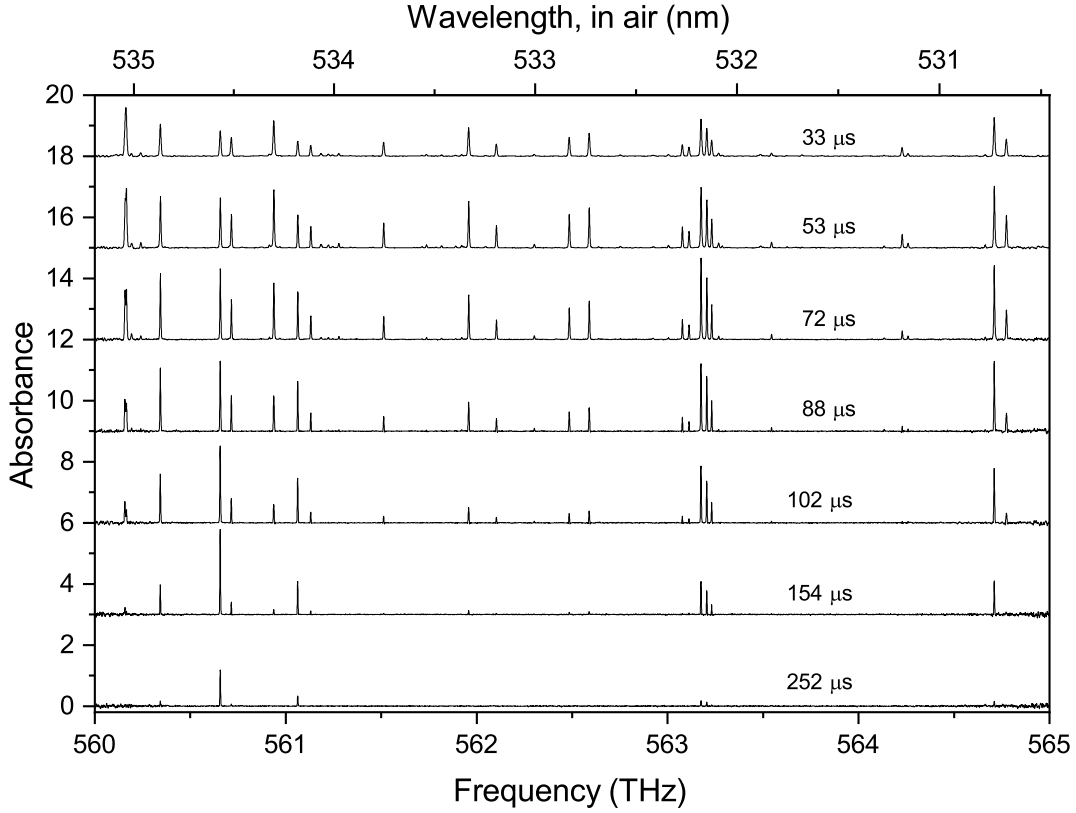


**Figure 4.2:** Experimental absorbance spectra (each averaged over 750 ablation shots) for the measured time-delays indicated in the figure. Spectra are offset for clarity. (Figure from [29])

A large number of absorption lines are visible in the spectra, with widths and heights

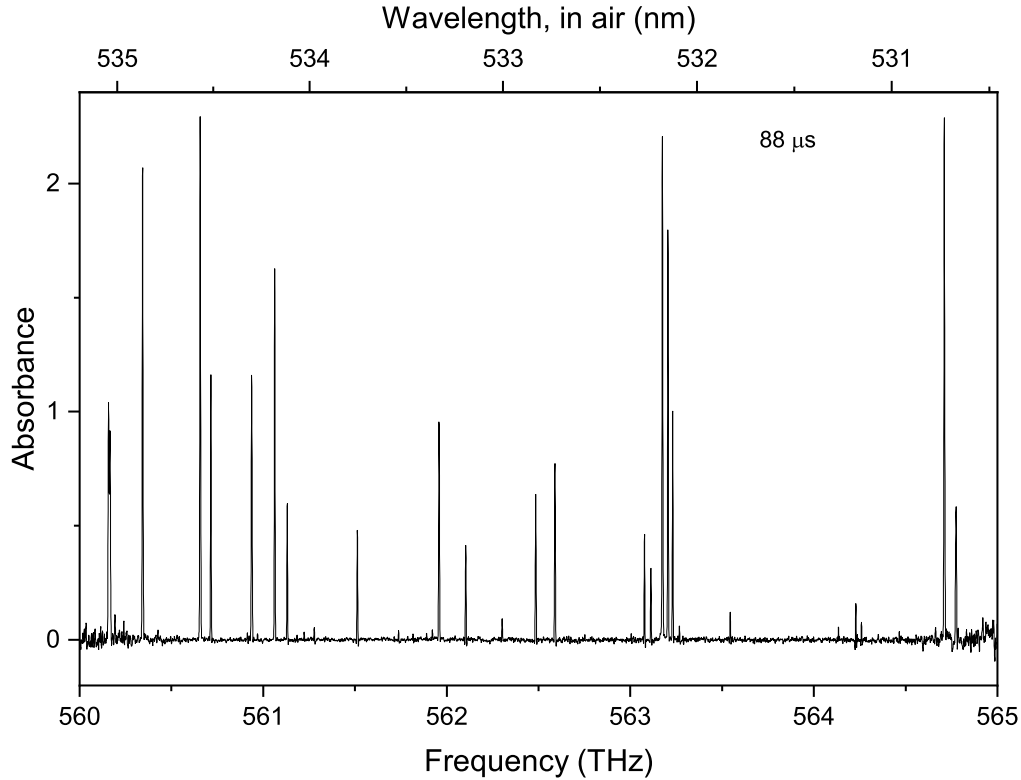


**Figure 4.3:** Experimental absorbance spectrum (averaged over 750 ablation shots) measured at 88  $\mu\text{s}$ .

varying with delay. Most of the observed absorption lines are from Gd I, with line identification described in Section 4.5. Two Gd II transitions listed in the literature [75] are within the measured frequency range, lying at 531.58 nm and 531.68 nm in air. However, the lower-state energies of  $19,223\text{ cm}^{-1}$  and  $19,750\text{ cm}^{-1}$  for these transitions, and  $\log(gf)$  values of -0.561 and -0.362, respectively, result in weakly observed absorption only at the earliest time probed of 33  $\mu\text{s}$ . Although the Gd II peaks were included in the fitting model (described in Section 4.5), there were not enough lines visible to determine the excitation temperature and column density; therefore, oscillator strengths for Gd II were not calculated. The absolute and relative line strengths vary with time-delay due to the changing excitation temperature and total Gd column density as the ablation plume expanded and cooled. The observed linewidths are determined primarily by the effective instrumental spectral resolution dictated by the apodization window width used (as discussed in Sec. 1.4.2).

The instrumental resolution varies with delay from 8.02 GHz (7.60 pm) at 33  $\mu\text{s}$ , to 1.67 GHz (1.58 pm) at 154  $\mu\text{s}$  and 252  $\mu\text{s}$ . The intrinsic linewidths of the absorption peaks also decrease with time due to changes in kinetic temperature (Doppler broadening) and electron density (Stark broadening) in the LPP.

A high density of spectral lines is observable at most time-delays shown in Fig. 4.2, especially at the earlier delays when a larger number of energy levels are populated due to the higher temperature. Fig. 4.4(a) shows a narrower portion of the experimental absorbance spectrum at 72  $\mu\text{s}$  delay, and Fig. 4.4(b) shows the spectrum at 154  $\mu\text{s}$ . The high spectral resolution of the DCS measurement enables many absorption lines to be measured with limited overlap/blending; however, the high density of lines for Gd makes some degree of line overlap inevitable. The effects of line overlap and unresolved hyperfine/isotope structure on the spectral fitting and data accuracy are discussed further in Section 4.8.

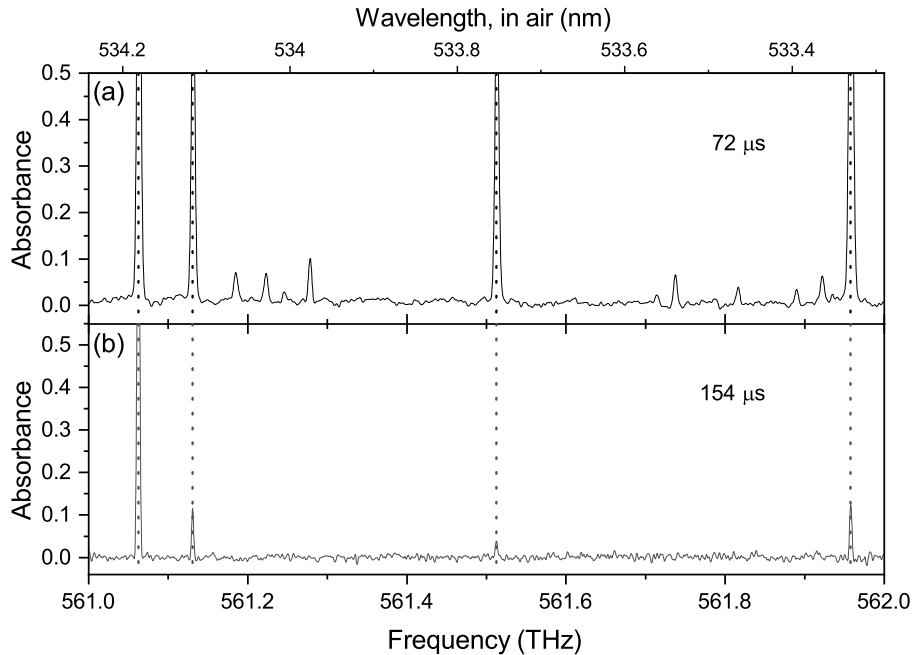


**Figure 4.4:** (a) Portion of experimental spectrum at 72  $\mu\text{s}$  showing strong and weak Gd I absorption lines. Dotted lines indicate transitions listed in the Kurucz database with known oscillator strengths. (b) Experimental spectrum at 154  $\mu\text{s}$  over the same range. At later times, weaker lines are no longer visible, and the spectral resolution is improved. (Figure from [29])

Figure 4.4 also shows the large dynamic range of absorbances involved in the measurement.

The spectra are dominated by transitions with relatively large oscillator strengths and/or transitions originating from low-lying energy levels, especially at later time-delays. Most of the strong observed lines correspond to transitions listed in the Kurucz database with known oscillator strengths, noted by vertical dotted lines in Fig. 4.4. However, a large number of additional absorption features are clearly visible in the spectra which are present at early times of the LPP but are not visible at later times when the temperature has decreased. As discussed in the next section, the frequencies of most of these lines correspond to dipole-allowed Gd I transitions. However, without oscillator strengths for these transitions they cannot be included in quantitative spectral models for simulation or fitting of experimental spectra. In addition, overlap of lines with unknown oscillator strengths may interfere with analysis of lines with known oscillator strengths. The next sections describe a method to determine oscillator strengths for these additional Gd I transitions, which may then be used to improve subsequent spectral modeling and analysis.

## 4.5 Analysis of Spectra

Experimental peaks were identified by the transition center frequency and were divided into three categories. The first category included peaks with known frequencies, energy levels, degeneracies, and oscillator strengths obtained from the Kurucz database [75]. The second category included peaks with frequencies corresponding to allowed dipole transitions, which were calculated from known energy levels and degeneracies obtained from the NIST database [52], but with unknown oscillator strengths. Frequencies for these dipole-allowed transitions were calculated from differences between even and odd energy levels (parity conservation), and with  $\Delta J = 0, \pm 1$ . The third category included peaks with frequencies at which absorption lines were clearly observed in the experimental spectra, but which did not correspond to any calculated dipole-allowed transition for Gd I or Gd II. These absorption lines may be due to impurities in the sample, molecular transitions, higher ionization states of Gd, partially-resolved isotope/hyperfine structure, or non-dipole allowed transitions. In the spectral range probed by the DCS measurement, the list of potential transitions included 20 Gd I and 2 Gd II transitions from the Kurucz database, 95 Gd I and 18 Gd II transitions from the list of possible dipole-allowed transitions, and 5 additional unidentified lines.

Figure 4.5 shows the spectral fit at 88  $\mu\text{s}$ , and Fig. 4.6 shows zoomed-in detail of the fits at 53  $\mu\text{s}$  and 154  $\mu\text{s}$ . The peaks shown in Fig. 4.6 are labelled according to the categories specified above. Root-mean-squared (RMS) fit residuals were  $< 0.01$ , which is comparable to the experimental noise determined from the absorbance baseline in regions away from spectral lines. Some structure was present in the fit residuals for some lines, possibly resulting from unresolved hyperfine/isotope structure or spectral ringing near peaks due to apodization, but the deviations were generally small relative to the peak heights. Differences between the input peak center frequencies and the fit center frequencies were typically  $< 0.4$  GHz, which is reasonable given the 0.5 GHz sampling of the frequency axis, uncertainty of the absolute frequency axis calibration, and expected variations in line-center positions. Uncertainties in the peak areas were determined from the standard error of the fit parameter. Linewidths (FWHM) determined from the fits (before instrumental broadening was applied) varied between particular absorption lines, but typically ranged from  $\sim 5$  GHz at 33  $\mu\text{s}$  to  $\sim 2.5$  GHz at 252  $\mu\text{s}$ .

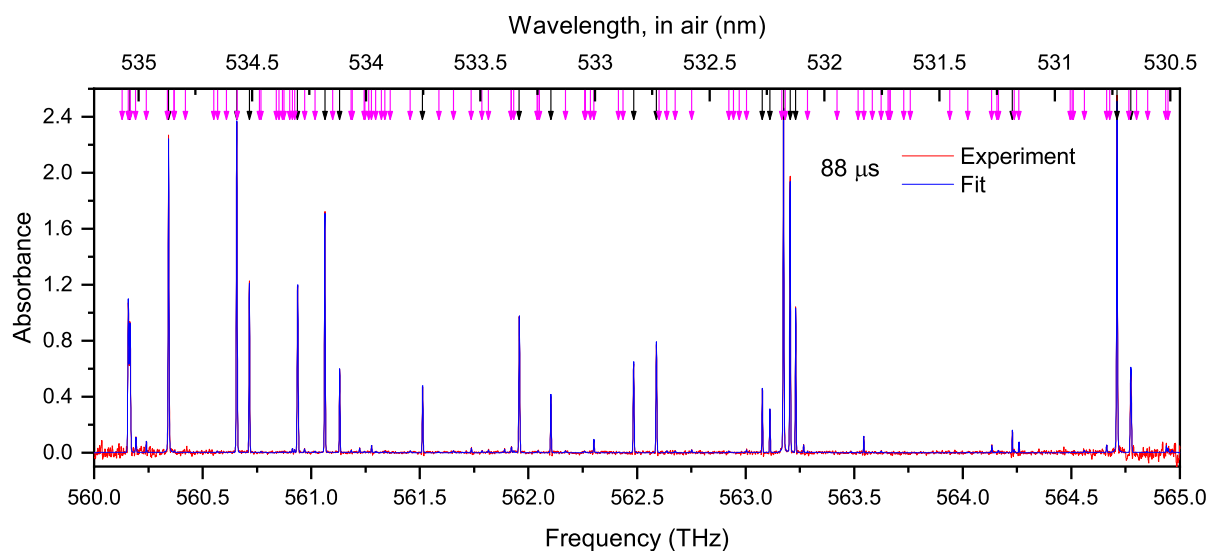


**Figure 4.5:** Spectral fit for the absorption spectrum at 88  $\mu\text{s}$ . The solid red line shows the experimental data, and the solid blue line shows the best-fit spectrum. The black arrows indicate frequencies of Gd I transitions with known oscillator strengths, and magenta arrows indicate frequencies of additional dipole-allowed Gd I transitions with unknown oscillator strengths.

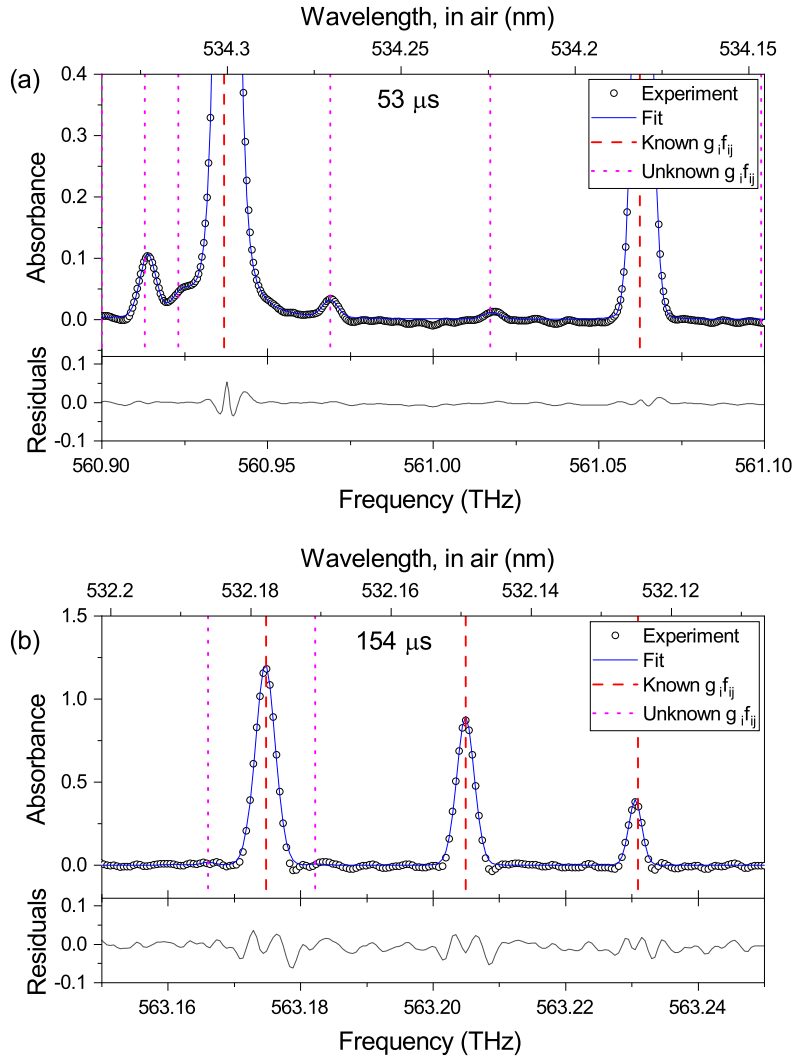


**Figure 4.6:** Examples of experimental data and fits for portions of the absorption spectrum at (a)  $53 \mu\text{s}$  and (b)  $154 \mu\text{s}$ . The dotted points show experimental data, and the solid blue line shows the best-fit spectrum. Vertical dashed lines show frequencies of Gd I transitions with known oscillator strengths, and vertical dotted lines show frequencies of additional dipole-allowed Gd I transitions with unknown oscillator strengths. The lower panels show the fit residuals. (Figure from [29])

#### 4.6 Determination of Temperature and Atomic Density

Based on the spectral fitting results, a set of peak areas at each delay was determined for the Gd I transitions specified in the search library. Not all peaks included in the input search library were fit with non-zero areas above the noise levels. Therefore, peaks were

excluded from further analysis if the fitted area was below a threshold determined by the experimental noise level of the baseline (area of 0.2 GHz for time-delays 33 and 53  $\mu\text{s}$  and 0.1 GHz for 72  $\mu\text{s}$  and later) or had an area standard error value greater than the peak area. A small number of additional peaks were discarded after visual inspection of spectra showing that the spectral feature was not observable over the noise, especially near the edge of the measurement bandwidth where spectrum noise levels were higher.

Boltzmann plots were constructed using the peak areas determined from the spectral fits, along with energy levels, level degeneracies, and oscillator strengths for the 20 measured transitions listed in the Kurucz database [75]. Within the measurement region, the Kurucz database was found to have the largest number of listed transitions relative to other literature sources, including the two lowest-energy transitions originating from energy levels of 999  $\text{cm}^{-1}$  and 1719  $\text{cm}^{-1}$ . Details on transition energies and  $\log(gf)$  values are given in Table 4.1.

| Freq. (THz) | Wavelength, air (nm) | $E_i$ ( $\text{cm}^{-1}$ ) | $J_i$ | $E_j$ ( $\text{cm}^{-1}$ ) | $J_j$ | $\log(gf)$ Kurucz [75] | $\log(gf)$ Lit.         | $\log(gf)$ This work | Std. Dev. | Avg. Error | No. of Time-Delays |
|-------------|----------------------|----------------------------|-------|----------------------------|-------|------------------------|-------------------------|----------------------|-----------|------------|--------------------|
| 560.1572    | 535.0447             | 6976.51                    | 5     | 25,661.34                  | 6     |                        | $-0.580 \pm 0.037$ [67] | -0.669               | 0.044     | 0.128      | 6                  |
| 560.1644    | 535.0377             | 12,486.55                  | 7     | 31,171.62                  | 8     | $0.545 \pm 0.217$      | $0.540 \pm 0.023$ [67]  | 0.25                 | 0.106     | 0.284      | 4                  |
| 560.3431    | 534.8671             | 6378.15                    | 2     | 25,069.18                  | 1     | $-0.380 \pm 0.217$     | $-0.230 \pm 0.025$ [67] | -0.414               | 0.095     | 0.099      | 6                  |
| 560.6564    | 534.5682             | 999.12                     | 5     | 19,700.61                  | 5     | $-1.464 \pm 0.217$     |                         | -1.510               | 0.046     | 0.099      | 7                  |
| 560.7151    | 534.5123             | 6550.4                     | 3     | 25,253.84                  | 3     | $-0.730 \pm 0.217$     |                         | -0.788               | 0.03      | 0.102      | 7                  |
| 560.9369    | 534.3009             | 11,296.47                  | 5     | 30,007.31                  | 6     | $0.400 \pm 0.217$      | $0.390 \pm 0.022$ [67]  | 0.348                | 0.052     | 0.106      | 6                  |
| 561.0624    | 534.1814             | 1719.09                    | 6     | 20,434.12                  | 7     | $-1.773 \pm 0.217$     |                         | -1.704               | 0.076     | 0.099      | 7                  |
| 561.1305    | 534.1165             | 7103.42                    | 5     | 25,820.72                  | 4     | $-1.113 \pm 0.217$     | $-1.170 \pm 0.040$ [67] | -1.053               | 0.066     | 0.106      | 6                  |
| 561.2773    | 533.977              | 16,228.82                  | 6     | 34,951.02                  | 5     |                        | $-1.680 \pm 0.060$ [66] | -0.290               | 0.07      | 0.136      | 4                  |
| 561.5125    | 533.7532             | 10,359.91                  | 2     | 29,089.95                  | 2     | $-0.450 \pm 0.217$     |                         | -0.439               | 0.054     | 0.112      | 6                  |
| 561.9574    | 533.3306             | 10,883.51                  | 4     | 29,628.39                  | 5     | $0.105 \pm 0.217$      | $0.130 \pm 0.022$ [67]  | 0.124                | 0.03      | 0.106      | 6                  |
| 562.1028    | 533.1926             | 10,222.23                  | 1     | 28,971.97                  | 0     | $-0.554 \pm 0.217$     |                         | -0.565               | 0.069     | 0.195      | 3                  |
| 562.4843    | 532.831              | 10,222.23                  | 1     | 28,984.69                  | 1     | $-0.393 \pm 0.217$     |                         | -0.281               | 0.039     | 0.108      | 6                  |
| 562.5888    | 532.7321             | 10,359.91                  | 2     | 29,125.85                  | 3     | $-0.148 \pm 0.217$     | $-0.170 \pm 0.023$ [67] | -0.127               | 0.019     | 0.106      | 6                  |
| 563.0767    | 532.2704             | 10,576.41                  | 3     | 29,358.63                  | 4     | $-0.508 \pm 0.217$     | $-0.550 \pm 0.023$ [67] | -0.489               | 0.067     | 0.109      | 6                  |
| 563.1114    | 532.2376             | 10,222.23                  | 1     | 29,005.61                  | 2     | $-0.728 \pm 0.217$     |                         | -0.691               | 0.055     | 0.109      | 6                  |
| 563.1748    | 532.1778             | 6786.18                    | 4     | 25,571.67                  | 4     | $-0.179 \pm 0.217$     | $-0.030 \pm 0.030$ [67] | -0.241               | 0.103     | 0.103      | 7                  |
| 563.2049    | 532.1493             | 6378.15                    | 2     | 25,164.64                  | 2     | $-0.562 \pm 0.217$     | $-0.390 \pm 0.023$ [67] | -0.520               | 0.046     | 0.099      | 7                  |
| 563.2309    | 532.1247             | 6550.4                     | 3     | 25,337.76                  | 2     | $-1.001 \pm 0.217$     | $-0.910 \pm 0.030$ [67] | -0.919               | 0.071     | 0.102      | 7                  |
| 563.6245    | 531.7532             | 12,345.97                  | 6     | 31,146.46                  | 7     |                        | $-1.750 \pm 0.093$ [67] | -1.524               | NA        | 0.152      | 1                  |
| 564.2278    | 531.1845             | 16,758.94                  | 7     | 35,579.55                  | 7     | $0.251 \pm 0.217$      |                         | 0.306                | 0.038     | 0.123      | 5                  |
| 564.2581    | 531.1561             | 11,830.39                  | 6     | 30,652.02                  | 6     |                        | $-1.230 \pm 0.041$ [67] | -0.986               | 0.035     | 0.124      | 5                  |
| 564.7101    | 530.7308             | 7103.42                    | 5     | 25,940.12                  | 5     | $-0.137 \pm 0.217$     | $0.050 \pm 0.024$ [67]  | -0.171               | 0.128     | 0.099      | 7                  |
|             |                      |                            |       |                            |       |                        | $0.070 \pm 0.060$ [66]  |                      |           |            |                    |
| 564.7737    | 530.6711             | 6976.51                    | 5     | 25,815.33                  | 6     | $-0.859 \pm 0.217$     | $-1.000 \pm 0.031$ [67] | -0.874               | 0.057     | 0.111      | 5                  |

**Table 4.1:** Oscillator strengths of Gd I transitions determined in this work, and comparison to literature.

Figure 4.7 shows the Boltzmann plots for all time-delays. Overall, linear fits to the Boltzmann plots were very good, with  $R^2$  values ranging from 0.949 to 0.995. The error bars include standard errors of the peak areas from the spectral fits, combined with the reported 50% relative uncertainties of the oscillator strengths. The uncertainty in oscillator strengths was much larger than uncertainties in peak areas for the majority of cases. The transition at 560.1644 THz ( $E_i = 12,486.55 \text{ cm}^{-1}$ ) has relatively large uncertainty due to strong overlap between this peak and a dipole-allowed transition ( $E_i = 7562.46 \text{ cm}^{-1}$ ) with unknown



| Freq. (THz) | Wavelength, air (nm) | $E_i$ (cm $^{-1}$ ) | $J_i$ | $E_j$ (cm $^{-1}$ ) | $J_j$ | $\log(gf)$ | Std. Dev. | Avg. Error | No. of Time-Delays |
|-------------|----------------------|---------------------|-------|---------------------|-------|------------|-----------|------------|--------------------|
| 560.1668    | 535.0356             | 7562.46             | 2     | 26,247.61           | 3     | -0.869     | 0.270     | 0.293      | 3                  |
| 560.1915    | 535.0119             | 7234.91             | 4     | 25,920.89           | 4     | -1.626     | 0.092     | 0.124      | 4                  |
| 560.2398    | 534.9658             | 16,078.05           | 2     | 34,765.64           | 3     | -0.160     | 0.068     | 0.123      | 4                  |
| 560.9129    | 534.3238             | 16,012.88           | 1     | 34,722.93           | 2     | -0.546     | 0.087     | 0.154      | 4                  |
| 560.923     | 534.3142             | 20,306.94           | 1     | 39,017.32           | 1     | -0.302     | 0.068     | 0.214      | 2                  |
| 560.9689    | 534.2705             | 7103.42             | 5     | 25,815.33           | 6     | -2.478     | 0.149     | 0.170      | 5                  |
| 561.2969    | 533.9583             | 20,299.87           | 3     | 39,022.72           | 4     | -0.678     | 0.017     | 0.248      | 2                  |
| 561.7363    | 533.5407             | 15,720.72           | 5     | 34,458.22           | 4     | -0.526     | 0.042     | 0.135      | 4                  |
| 561.7863    | 533.4931             | 15,972.27           | 0     | 34,711.45           | 1     | -1.027     | 0.081     | 0.202      | 2                  |
| 561.8151    | 533.4658             | 20,303.80           | 2     | 39,043.93           | 3     | 0.073      | 0.046     | 0.137      | 3                  |
| 562.3010    | 533.0048             | 6976.51             | 5     | 25,732.85           | 5     | -1.831     | 0.059     | 0.118      | 5                  |
| 562.6377    | 532.6859             | 19,507.99           | 4     | 38,275.57           | 3     | -0.376     | 0.163     | 0.149      | 3                  |
| 562.7515    | 532.5782             | 21,389.50           | 6     | 40,160.87           | 6     | 0.150      | 0.075     | 0.138      | 3                  |
| 562.9234    | 532.4155             | 19,718.72           | 4     | 38,495.82           | 4     | -0.108     | 0.231     | 0.207      | 3                  |
| 563.0035    | 532.3398             | 20,299.87           | 3     | 39,079.65           | 4     | 0.122      | 0.096     | 0.129      | 3                  |
| 563.1822    | 532.1709             | 21,544.68           | 4     | 40,330.42           | 5     | 1.195      | NA        | 0.176      | 1                  |
| 563.2857    | 532.0731             | 20,324.72           | 4     | 39,113.91           | 5     | -0.135     | 0.085     | 0.138      | 3                  |
| 563.5439    | 531.8293             | 10,883.51           | 4     | 29,681.31           | 3     | -1.002     | 0.020     | 0.117      | 5                  |
| 564.1335    | 531.2734             | 7103.42             | 5     | 25,920.89           | 4     | -2.152     | 0.024     | 0.151      | 5                  |

**Table 4.2:** List of Gd I transitions calculated  $\log(gf)$  values for previously unreported transition oscillator strengths.

oscillator strength, separated by 2.4 GHz. While both lines were included in the fitting model, the larger uncertainty of the fit accounts for the peak overlap as reflected in the standard error of the fit parameter. The transition at 560.6564 THz ( $E_i = 999.12$  cm $^{-1}$ ) has a closely neighboring dipole-allowed transition ( $E_i = 19,574.02$  cm $^{-1}$ ) with unknown oscillator strength located 1.7 GHz away. However, due to the high lower energy level of the dipole-allowed transition with unknown oscillator strength, its spectral area was assumed to be negligible relative to the transition from the lower energy over the temperature ranges measured, and thus was removed from the spectral fit.

The excitation temperatures and total column densities of Gd I determined from the Boltzmann plot fits and Eq. 3.10 at each time-delay are shown in Fig. 4.8. Error bars were determined from the standard errors of the linear fit parameters from the Boltzmann plots. The excitation temperature was determined to be  $4200 \pm 200$  K at 33  $\mu$ s after ablation and dropped to  $1700 \pm 50$  K at 252  $\mu$ s. The magnitude and time dependence of the excitation temperature is reasonable and comparable with previous studies performed in LPP systems; however, we note very few measurements have been performed of excitation temperature in LPPs using absorption-based spectroscopy [27, 28, 90]. The total column density calculation included evaluating the partition function  $Z(T)$  at the excitation temperature determined from the fits, with associated propagation of errors. The total Gd I column density was  $\sim 1$

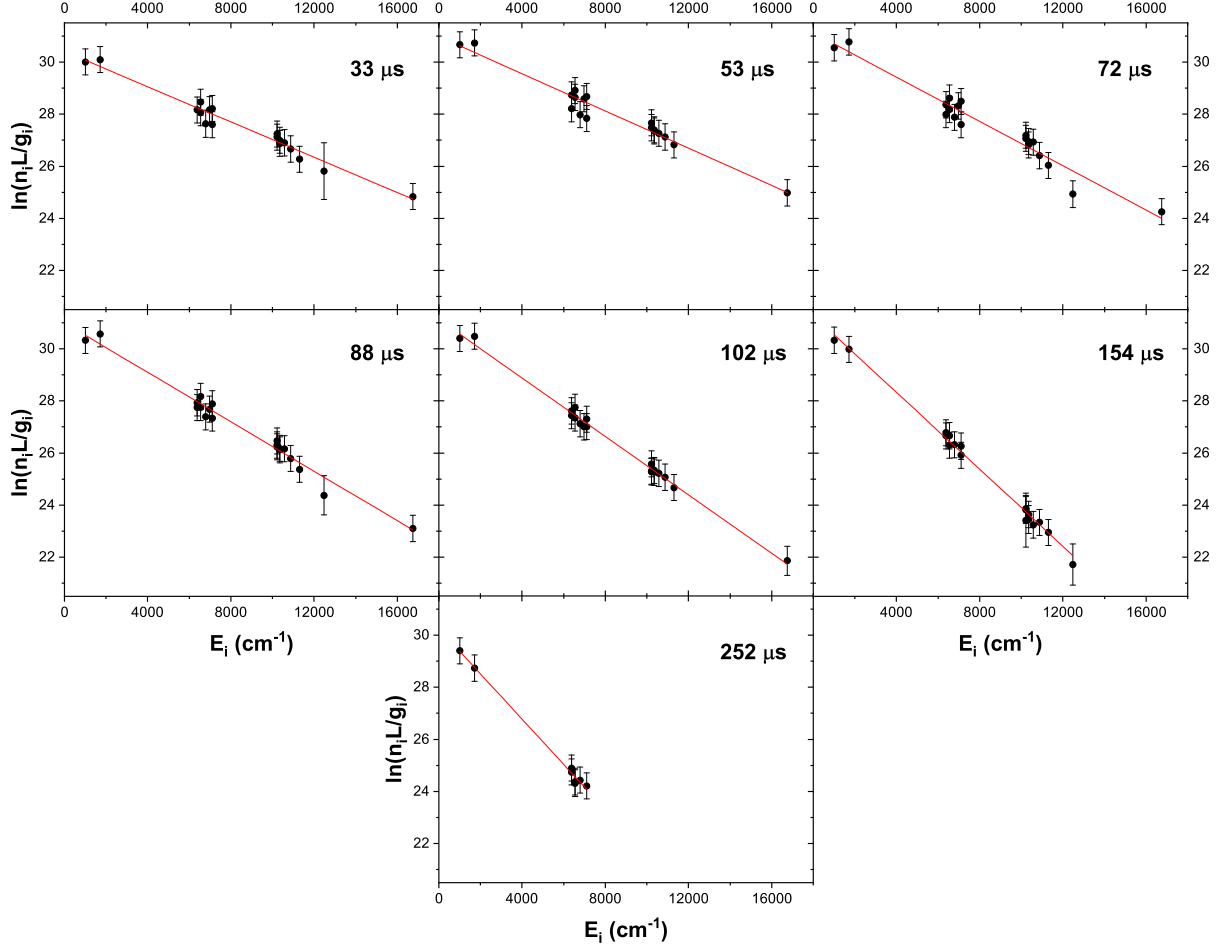


**Figure 4.7:** Boltzmann plots for all time-delays. Solid points were calculated from fits to peak areas for experimental data, along with oscillator strengths, level degeneracies, and lower-level energy from the Kurucz database. The solid red lines are linear fits to the data points. Error bars were calculated from the uncertainties in peak areas and oscillator strengths.

$\times 10^{15}$  atoms/cm<sup>2</sup> over the time-delays measured, which is also in reasonable agreement with similar prior laser ablation experiments [28].

#### 4.7 Determination of Gd I Oscillator Strengths

Based on the areas of the peaks from the spectral fits, and the temperature/column density results shown in Fig. 4.8, oscillator strengths were calculated using Eq. 3.10. Oscillator strengths were calculated for multiple time-delays, so long as the measured peaks met the minimum area conditions mentioned above. Thus, oscillator strengths for high-energy transitions were only calculated for early time-delays while lower-energy transitions were calculated

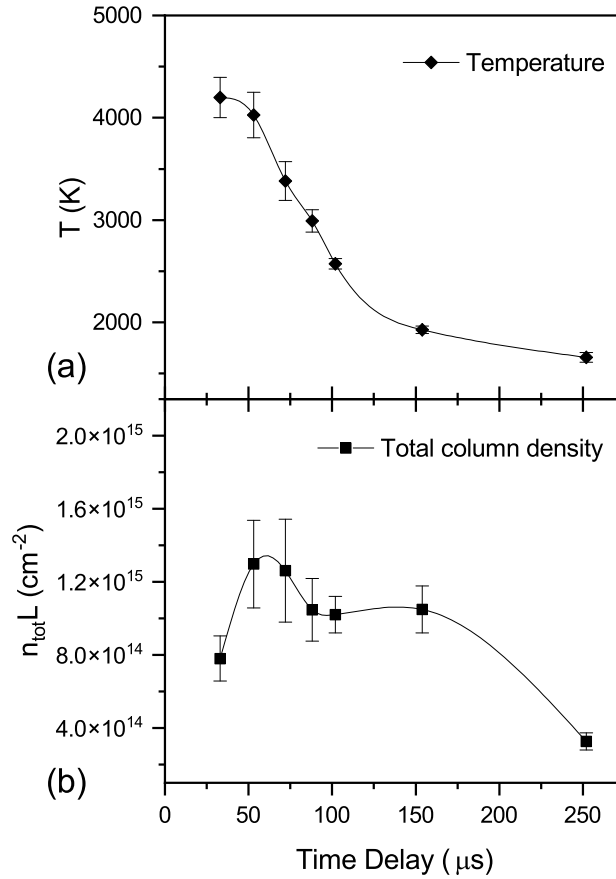


**Figure 4.8:** (a) Excitation temperature and (b) total column density of Gd I for each time-delay measurement. Data points were determined from fits to the Boltzmann plots at each time-delay and error bars were calculated based on standard errors of fits and propagation of errors. The solid lines are guides for the eye. (Figure from [29])

for all time-delays. Figure 4.9 shows examples of  $\log(gf)$  values for various transitions as a function of time-delay. Overall, most transitions showed excellent consistency in the  $\log(gf)$  values calculated at different delay times/temperatures, with values agreeing within the uncertainties. For most transitions, the uncertainty in determining  $\log(gf)$  at a given time was dominated by uncertainty in the temperature/column density from the Boltzmann plot fits, which in turn was driven by potential errors/uncertainties in the reference  $\log(gf)$  values used to construct the Boltzmann plot. This is further supported by the observation of similar  $\log(gf)$  calculated for a given transition at different times/temperatures, indicating possible systematic errors in one or more of the reference  $\log(gf)$  values, instead of an error in the

temperature or large departure from LTE conditions, for example.

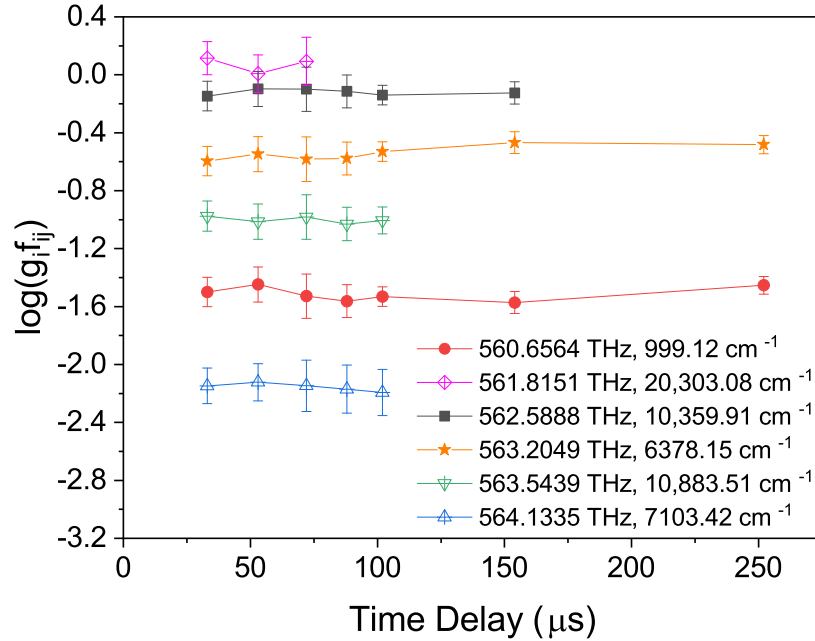


**Figure 4.9:**  $\log(gf)$  values vs. time-delay for selected transitions. The frequency and lower energy for each transition is noted in the figure. Plots with filled markers indicate transitions listed in the Kurucz database whose oscillator strengths were recalculated; those with unfilled markers are for previously unreported, dipole-allowed transitions. (Figure from [29])

Table 4.1 shows the determined  $\log(gf)$  results for transitions where comparison values were available in the literature, while Table 4.2 shows new  $\log(gf)$  results for the additional dipole-allowed transitions identified in this study. The  $\log(gf)$  values listed in the tables are weighted averages of the  $\log(gf)$  values determined at the different times, where the weighting corresponds to the uncertainties of the individual  $\log(gf)$  values at each time. The last column of the tables indicates the number of time-delays at which  $\log(gf)$  values were determined and used to calculate the average value of  $\log(gf)$ . Two values are reported for uncertainties. The first uncertainty gives the standard deviation of the  $\log(gf)$  values measured at the different time-delays and indicates the precision/repeatability of the measurement across the different time-delays. The second uncertainty value is the average of the uncertainty in the individual  $\log(gf)$  values over all times. This value tends to be the larger of the two as it includes the uncertainty of the Boltzmann fit, which is determined by the large uncertainties in the oscillator strengths from the Kurucz database.

## 4.8 Discussion

Previous measurements of Gd I oscillator strengths have been performed using various methods, but very few reported values are within the spectral range probed in the experiments here. The Gd I oscillator strengths listed in the Kurucz database are based on emission intensity of NBS spectra [74, 75]. Uncertainty in  $\log(gf)$  for these transitions is estimated to be up to 50% [76]. Szynarowska and Papaj measured the oscillator strength of the Gd I transition at 451.966 nm using a curve of growth method, reporting an uncertainty for  $\log(gf)$  of 0.07 [25, 91]. In 1992, Komarovskii and Smirnov reported the absolute transition probabilities of thirty-one levels from 350 to 770 nm by measuring the branching fractions and using previously determined radiative lifetime data [92]. Nishimura et al. used laser absorption with a dye laser to determine the oscillator strengths for six transitions from 570 to 612 nm with 24% uncertainty [93]. Jung et al. used tunable diode laser absorption spectroscopy to determine excitation temperature and oscillator strengths for five transitions from low-energy metastable states of Gd in the ultraviolet and near-infrared spectral regions [83, 94]. Haynam et al. reported the oscillator strengths of eight transitions from 575.2 to 1,469.2 nm with uncertainties of 15%, using measured radiative lifetimes and branching fractions [95]. Miyabe et al. in 1997 used the radiative lifetimes and branching fractions of nineteen transitions from 274.0 to 323.6 nm and 555.6 to 625.0 nm to determine oscillator strengths, reporting uncertainties of 20% [64]. More recently, Lawler et al., as part of their Wisconsin Atomic Transition Probability program, reported the atomic transition probabilities for 1290 lines from 300 to 1850 nm with uncertainties of 5 to 25% using radiative lifetimes and branching fraction measurements [67]. Lastly, Wang et al. reported oscillator strengths for sixty-six lines from 259.3 to 1005 nm, also using radiative lifetimes and branching fraction measurements [66].

Of these previous reports for Gd I oscillator strengths, three contain values for the transitions probed in this experiment. Figure 4.10 provides a graphical comparison of the  $\log(gf)$  values determined in this experiment with values given in Kurucz [75] and reported by Lawler et al. [67]. The  $\log(gf)$  values from 20 transitions listed in the Kurucz database were used as reference values to determine temperature and column density, and therefore our reported

$\log(gf)$  values for these transitions all agree within uncertainties by design. The relatively good fits to the Boltzmann plots shown in Fig. 4.7 suggest that the accuracy of the Kurucz database values is significantly higher than the assumed 50% uncertainty. Note that a relative uncertainty of 50% in oscillator strength or transition probability corresponds to an uncertainty of  $0.5/\ln(10) = 0.22$  in  $\log(gf)$ . The updated values reported here for  $\log(gf)$  provide lower uncertainty than the Kurucz database values, but their accuracy is still linked to the underlying accuracy of the reference  $\log(gf)$  values used in the analysis. Of the other values in the literature for  $\log(gf)$  of the Gd I transitions within the measurement range of the experiment, the Lawler et al. results [67] provide the best set of comparable transitions, with quoted relative uncertainties ranging from 0.050 to 0.091. Of the fifteen shared lines with Lawler et al., eleven agreed within the uncertainties and four did not agree. Wang et al. [66] reported two lines in common with the work here, both oscillator strengths having uncertainties of 0.06, but neither agreed with the oscillator strengths calculated in this work.

Potential sources of errors or uncertainty may include limitations of the experimental technique, assumptions made in the analysis, or errors in the reference oscillator strengths used to construct the Boltzmann plots. The primary sources of potential experimental error would result from inaccurate measurement of the areas of the absorbance peaks, or an incorrect relationship between absorbance and column density. Because the spectral fitting approach includes the instrumental broadening in transmittance, it accounts for most of the nonlinearity between column density and observed areas of absorption peaks [36]. However, additional error/uncertainty may be introduced which is not reflected in the values from the standard errors of the fit parameters. For example, large values of absorbance typically have increased measurement error due to difficulty in establishing photometric accuracy near regions of low transmitted intensity. No obvious systematic errors were observed for areas determined from the largest absorption peaks (for example, large deviations of these points on the Boltzmann plots). Similarly, trends in  $\log(gf)$  versus delay for peaks with varying area were not observed, which indicates that peak areas were measured accurately over a large range of optical densities. Nevertheless, additional experiments are needed to establish the accuracy of the absorbance measurements, for example using COG methods [73].

Errors may also result due to the limited spectral resolution of the measurement. For

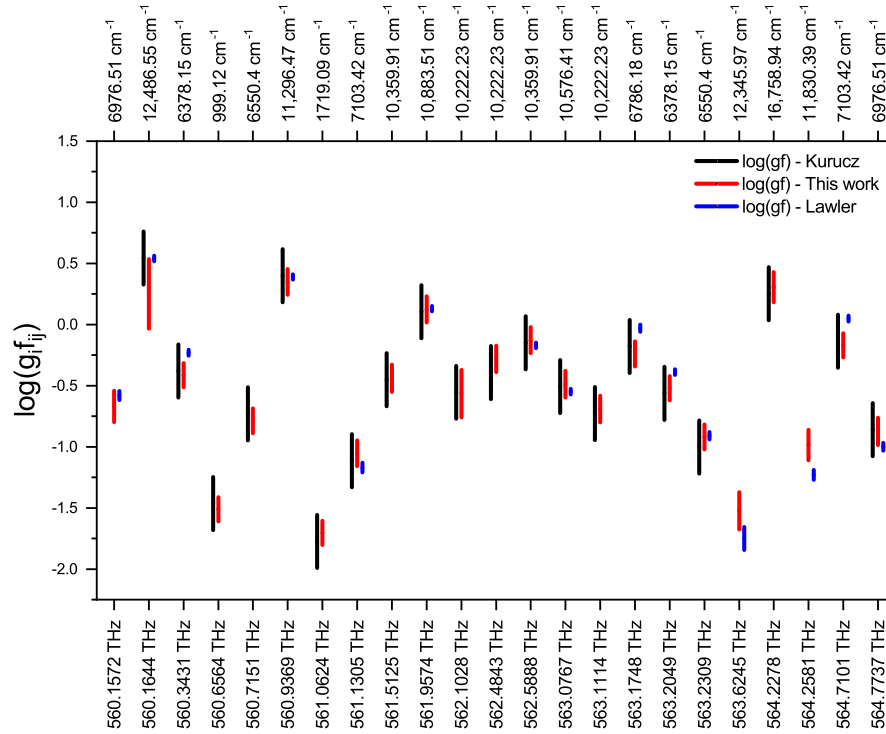


**Figure 4.10:** Plot comparing this work’s calculated  $\log(gf)$  values from the Boltzmann fit (in red) with reported values in Kurucz and Lawler et al. (in black and blue, respectively). The line frequency and lower transition level energy identify the transition corresponding to each  $\log(gf)$  value. Each bar’s width along the y-axis indicates the value and its spread, given as  $\log(gf)$  plus/minus its reported absolute log-space uncertainty. Note that the uncertainties used for the values from this work are the average errors shown in Table 4.1. (Figure from [29])

example, the inability to distinguish closely-spaced optical transitions may result in the areas being attributed to incorrect transitions. The spectral fitting routine accounts for partially-overlapping lines (line blends) as long as the transitions are identified, but fitting uncertainties were found to be higher for these cases, as expected. Efforts were made to identify spectral lines with nearby overlapping transitions, and account for these transitions in the analysis, as discussed in Section 4.5. Identification of transition frequencies for dipole-allowed transitions based on energy level differences was critical for identifying overlapping lines near the stronger lines listed in the literature. Likewise, inclusion of these additional transitions in the fitting model is important for determining absorbance peak areas with higher accuracy. Figure 4.11 shows an example, where the transition at 560.1644 THz ( $E_i = 12,486.55 \text{ cm}^{-1}$ ) overlaps two nearby dipole-allowed transitions at 560.157 THz ( $E_i =$

$6976.508 \text{ cm}^{-1}$ ) and  $560.167 \text{ THz}$  ( $E_i = 7562.46 \text{ cm}^{-1}$ ). Without sufficient spectral resolution and identification of the nearby peaks, areas from all 3 peaks could be incorrectly assigned to the single transition at  $560.1644 \text{ THz}$  ( $E_i = 12,486.55 \text{ cm}^{-1}$ ) listed in the literature, also possibly leading to overestimation of the oscillator strength. We note that the  $560.1644 \text{ THz}$  ( $E_i = 12,486.55 \text{ cm}^{-1}$ ) transition was found to fall below the Boltzmann plot trend line in our results, which may indicate that the  $\log(gf)$  taken from the literature was too high due to prior assignment of the overlapping peaks to a single transition.

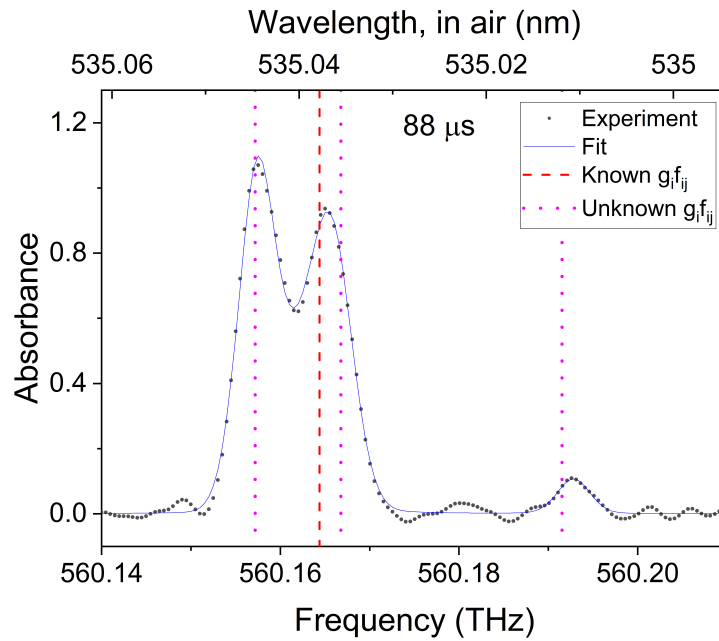


**Figure 4.11:** Example of overlapped Gd I peaks in experimental data. The transition listed by Kurucz et al. is differentiated in the figure from the those identified by calculating all dipole-allowed transitions. The Kurucz-listed transition is somewhat resolved from the nearby unlisted lower-frequency transition but is not well-resolved from the even closer higher-frequency transition. Inclusion of all three in the fitting model improves the fitted area accuracy of the peaks. The uncertainty of the fit takes into account the presence of nearby transitions, increasing as the separate transitions are less resolved from one another. (Figure from [29])

Similar errors from insufficient spectral resolution may arise due to partially-resolved hyperfine/isotope structure. Effects of peak structure due to unresolved hyperfine splitting or multiple isotopes may cause deviations in peak shapes from the expected Voigt profile, and lead to an increase in apparent peak width [26]. Gd has 5 stable isotopes with non-



negligible abundances [2.18%  $^{154}\text{Gd}$ , 14.8%  $^{155}\text{Gd}$ , 20.47%  $^{156}\text{Gd}$ , 15.65%  $^{157}\text{Gd}$ , 24.84%  $^{158}\text{Gd}$ , 21.86%  $^{160}\text{Gd}$ ] and the two odd isotopes have hyperfine structure, which results in highly complex spectra with distributions of lines spread over ranges up to a few GHz. The average transition isotope shift is 1.9 GHz with a maximum single transition isotope shift of 4.5 GHz, based on the energy level isotope shifts found in literature [96]. The spectral resolution in the experiment was insufficient to resolve much of the hyperfine/isotope structure of Gd lines, due to a combination of physical linewidths  $> 1$  GHz in the LPP environment and instrumental broadening. However, neglecting hyperfine/isotope structure may cause errors in peak areas determined from spectral fits, especially for closely-spaced transitions.

Other sources of error may result from incorrect approximations made in the analysis. Neglecting the stimulated emission contribution in Eq. 3.6 is calculated to result in errors no greater than 1% at a maximum temperature of 5000 K for the transitions studied. Departures from LTE conditions could make the Boltzmann distribution assumed in Eq. 3.7 invalid; however, the high linearity of the Boltzmann plots indicate that LTE approximations are valid within the measurement uncertainty. Despite the lower temperatures and electron densities in the LPP probed using absorption spectroscopy, the validity of the LTE assumption has been shown to be good in numerous prior studies [19, 70–72]; nevertheless, we cannot completely rule out potential errors due to LTE departure.

The line-of-sight integration of absorbance through the spatially-inhomogeneous plasma means that the column densities in Eq 3.9 are more correctly represented by an integral along the measurement path. Prior studies have shown that the line-of-sight integration for emission measurements in LPPs may lead to variations in measured excitation temperature depending on spatial distribution of species (ions versus neutrals), despite LTE conditions being valid [70, 97]. Similar considerations apply for absorption measurements, although it is worth noting that at later times in plasma evolution the spatial gradients in temperature and number densities are greatly reduced versus early times [26]. Nevertheless, the excitation temperatures determined from a Boltzmann-plot analysis of such path-integrated spectra will necessarily represent a weighted average of conditions along the line of sight. Similar considerations apply to temporal integration of the absorption measurements over the apodization windows in the DCS interferograms, leading to a weighted average of plasma

conditions over time. Although the spatial and temporal averaging will change the absolute values of excitation temperature and column densities, the effects will be similar for all atoms probed along the measurement path and thus relative values of column density will not be affected. Since the oscillator strengths are calculated from relative measurements of column density, we do not expect large errors to result from spatial and temporal averaging effects for a single species. However, this would not be true if comparing different species or different ionization states.

Using the method presented here with analysis of absorption spectra in LPPs using DCS, the average uncertainty of  $\log(gf)$  for the stronger transitions in Table 4.1 is 0.12, which is lower than the 0.22 value from the Kurucz database but larger than the uncertainties of 0.02-0.09 in  $\log(gf)$  for the results given by Lawler et al. using lifetimes and branching ratios [67, 75]. The average uncertainty in  $\log(gf)$  was 0.14 for all transitions, including the new weaker dipole-allowed transitions. However, the uncertainty in absolute values of  $\log(gf)$  for the measurements here is largely determined by the accuracy of the reference  $\log(gf)$  values used to construct the Boltzmann plots. The repeatability of the  $\log(gf)$  measurements here was 0.06 on average for the transitions in Table 4.1 and 0.07 for all transitions and considering that these measurements were made over multiple time-delays/temperatures, the result indicates the precision and repeatability of the method is much better than the absolute accuracy. Therefore, we expect the uncertainty in accuracy of  $\log(gf)$  results will be improved by using better reference data. For the analysis here, the higher-accuracy values for  $\log(gf)$  provided by Lawler et al. were not used when constructing the Boltzmann plots due to fewer number of transitions in the measurement range versus the Kurucz database, and more importantly the lack of oscillator strengths for transitions from the low-lying energy levels at  $999\text{ cm}^{-1}$  and  $1719\text{ cm}^{-1}$ .

For the plasma conditions measured, the Gd I absorption linewidths are expected to be determined by a combination of Doppler broadening and van der Waals pressure broadening with relative contributions varying with delay. For kinetic temperatures of 2000-5000 K, the Gd I Doppler broadening is calculated to be 1.4-2.3 GHz. Pressure broadening coefficients for the Gd I transitions measured were not available in the literature. However, assuming a typical pressure-broadening coefficient of 20 MHz/Torr at 300 K [50], the van der Waals

broadening is estimated to be  $< 0.2$  GHz at 30 Torr and 2000 K. Stark broadening is expected to be small at the late delays probed by absorption due to the low electron densities. Gaussian FWHM values determined from the spectral fits ranged from  $3 \pm 1$  GHz at  $33 \mu\text{s}$  to  $2.2 \pm 0.3$  GHz at  $251 \mu\text{s}$ . At every delay, the measured linewidths are significantly higher than Doppler-broadening values based on the temperatures, which is consistent with unresolved hyperfine and isotope structure of the Gd I transitions.

## 4.9 Summary and Conclusions

Dual-comb spectroscopy was used to measure broadband, high-resolution spectra in a laser-produced plasma, and analysis of the spectra was used to determine oscillator strengths of neutral gadolinium transitions. The use of DCS and a LPP to measure  $\log(gf)$  values combines techniques used in both LIBS and absorption spectroscopy. The technique is advantageous for spectral analysis due to its large spectral coverage and high spectral resolution which minimizes spectral overlap in the dense spectra consisting of closely-spaced lines in species such as the lanthanide and actinide elements. With DCS, high SNR measurements with a large dynamic range enable measurement of weak and strong spectral features simultaneously. The time-resolution of the technique allows spectra to be measured at multiple time-delays after ablation, increasing confidence in the analysis by providing measurements under varying plume conditions.

By using 20 known Gd I transitions to calculate the temperature and column density of the plume at each time-delay, 43 transition  $\log(gf)$  values were determined, 19 of which were previously unreported. Comparison to literature showed good agreement between those oscillator strengths reported elsewhere and those calculated here. Furthermore, the majority of calculated  $\log(gf)$  values showed good agreement across the measured time-delays. Absolute measurement uncertainty in  $\log(gf)$  was  $\sim 0.14$ , determined largely by uncertainties in the reference oscillator strength data used to construct the Boltzmann plots. Measurement precision in  $\log(gf)$  determined from reproducibility of values from different delays/temperatures was  $\sim 0.07$ . Possible sources of error and uncertainty were identified and discussed, which include fitting of absorption lines, deviations from LTE in the plume, line-of-sight measurements of a spatially varying plume, strong absorbance lines, and unresolved isotopic and

hyperfine splitting.

The limited amount of data available in the literature on oscillator strengths for Gd highlights the utility of the DCS absorption method in LPPs to obtain additional information the transitions of actinide/lanthanide series elements as well as other species. Laser ablation provides a simple laboratory-based method for generating an atomic vapor at high temperature suitable for measurement of oscillator strengths from a wide range of transitions spanning different energy levels. The DCS absorption method provides the high spectral resolution and broad spectral bandwidth necessary for these measurements, with the ability to provide time-resolved spectroscopy of the cooling plasma. The spectral region of 530-535 nm probed here is also interesting due to limited availability of tunable laser sources at these wavelengths. Additional wavelength ranges and broader spectral bandwidths may be obtained from the current frequency comb system using standard methods of supercontinuum generation or parametric wavelength conversion, enabled by the high peak powers of the pulsed comb sources. Overall, the DCS absorption measurements in LPP systems provide a powerful technique for obtaining fundamental optical data on a wide number of atomic and molecular species, and more exhaustive knowledge of the transitions of these species is expected to enhance spectral analysis of experimental data involving these species, improve spectral models, and provide valuable data for comparison with theory.

## Chapter 5

### Multi-Species Temperature and Number Density Analysis of a LPP using DCS

#### 5.1 Introduction

This chapter presents the measurement and analysis of a LPP containing multiple species using the Yb-DCS system, which was published in the Journal of Applied Physics [30]. Also included are further experiments on similar samples with varying concentrations, which is unpublished, as well as work from a measurement of CeO in a LPP performed using the Er-DCS system and published in Optics Letters [31], which is relevant to the discussion of the formation of oxides. The main study presented here applies the techniques utilized in previous DCS-LPP work for the measurement and analysis of multiple species simultaneously in a LPP. As has been shown, dual-comb spectroscopy (DCS) represents a novel method of using absorption spectroscopy as a diagnostic tool for analysis of excitation temperatures and column densities in laser-produced plasmas (LPPs). Chapter 1 describes the advantages and disadvantages of LPP spectroscopic measurements using LIBS and absorption spectroscopy measurements. With the ability to measure spectra over broad bandwidths at ultraviolet and visible wavelengths, multispecies detection is straightforward using LIBS [70, 97, 98]. Few studies, though, have been performed using tunable lasers or spectrometer-based absorption measurements for multispecies analysis [99]. The broad bandwidth of DCS measurements enable late-time absorption measurements of multiple species in LPPs with the additional advantage of high spectral resolution. Regarding temperature analyses, measurement of neutral and ionized atomic excitation temperatures in LPPs is routine using optical emission/LIBS [19], yet there are relatively few studies of excitation temperature using absorption-based spectroscopy [27–29, 90, 100]. The two prior studies of DCS on LPPs for determination of excitation temperatures have focused on characterizing single elements

present in the LPP. Inclusion of multiple species in the LPP with transitions within the DCS measurement bandwidth allows for determination of time-resolved excitation temperatures of each species. Comparison of these temperatures is useful for evaluating the assumption that the LPP species follow a thermal energy distribution of states, as part of the assumption of LTE [101], and aids in mapping thermal and density spatial inhomogeneities within the plume.

In this work, we present DCS measurements performed on a LPP resulting from ablation of an alloy containing multiple elements: Fe, Nd, and Gd. Multiple transitions of Fe I, Nd I, and Gd I were detected and spectrally fit, and Boltzmann plots were generated to determine excitation temperatures and total column densities for both species. Determined excitation temperatures for Nd I and Gd I showed good agreement at all delays, ranging from  $\sim 4000$ - $2000$  K from 30 to 150  $\mu\text{s}$ . Excitation temperatures determined for Fe I were  $\sim 1000$  K higher than for Nd/Gd which is explained based on spatial averaging effects over temperature gradients along the measurement path. Nd, Gd column densities were found to be  $\sim 10^{14}$   $\text{cm}^{-2}$ , and Fe column densities were roughly an order of magnitude larger. The measured relative column densities differed from the sample composition, which is explained based on elemental fractionation and molecular formation in the LPP. Additional experiments were performed to establish measurement repeatability, showing that Nd and Gd excitation temperatures were determined with a precision better than  $\pm 100$  K and column densities with a precision better than  $\pm 2 \times 10^{13}$   $\text{cm}^{-2}$ . The impact of incorrect Nd oscillator strengths on the determination of excitation temperatures was also observed and characterized for its effect on measurement accuracy.

## 5.2 Experiment

The experimental setup was the same as used in Ch. 4 (see Fig. 4.1). Comb 2 had a repetition rate of 77.848,563 MHz, differing from Comb 1 by  $\Delta f_{rep} = 404.853$  Hz. The sample was an alloy containing Fe, Nd, and Gd at atomic number percentages of 90, 5, and 5, respectively, with reported uncertainties of  $\pm 0.5\%$ . The delay-times measured were 31, 51, 71, 87, 110, 151, and 250  $\mu\text{s}$ , with a jitter of  $\sim 0.6$   $\mu\text{s}$ . All other parameters were the same as those described in Ch. 4.

Figure 5.1(a) presents example single-beam signal and reference spectra (SBS), obtained by Fourier transform of the time-domain interferograms and processed according to the method described in Sec. 1.4.4. The resolutions of the spectra were set by the widths of the Blackman-Harris apodization windows ( $T_{meas}$ ). The spectral resolutions, defined as the FWHM linewidth of the ILF, were 8.84, 5.23, 3.72, 3.02, 2.38, 1.73, and 1.72 GHz, for the respective time-delays listed above. The reference and signal SBS were averaged over 750 ablation shots, and the absorbance spectrum calculated according to Eqs. 1.12 and 1.13 (Fig. 5.1(b)).

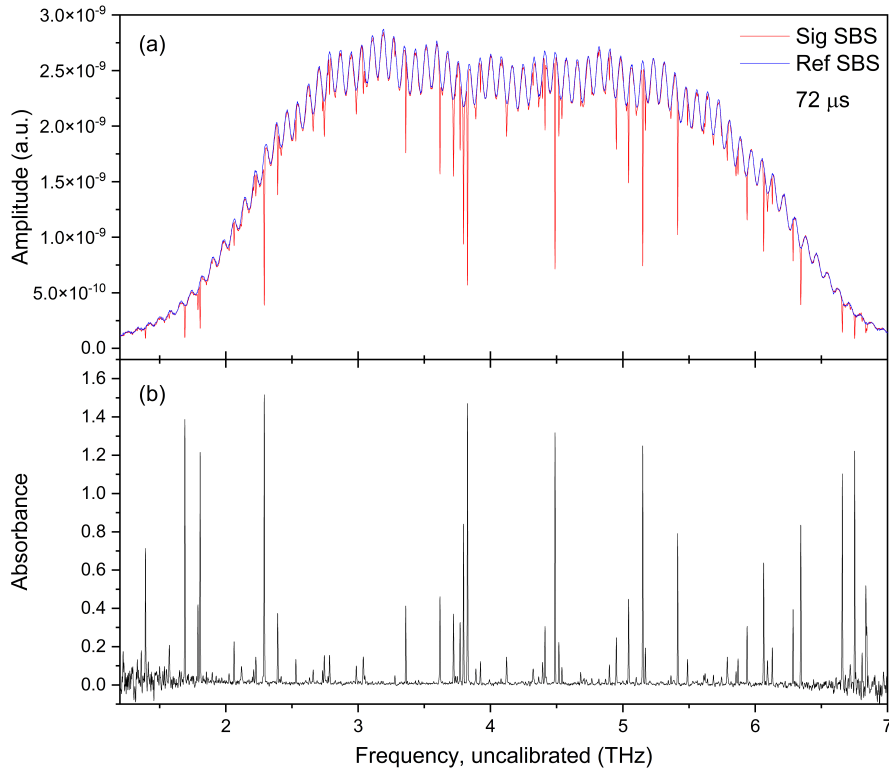


**Figure 5.1:** (a) Example SBS for the recorded reference and signal interferograms, each the result of spectral averaging across 750 ablation shots. Atomic absorption features due to atoms present in the plume coincident with the DCS beam path are clear in the signal SBS. Spectral fringing seen in the SBS due to residual reflections from optical components is eliminated by signal normalization with the reference in calculating absorbance, shown in (b).

### 5.3 Time-Resolved Absorption Spectra of Multi-Element Alloy and Analysis

Figure 5.2 presents the absorption spectra measured in the LPP at seven time-delays after ablation. The measurements spanned 5.4 THz (5.11 nm) from 560.0 to 565.4 THz (530.08 to 535.19 nm). Multiple well-resolved spectral lines of Fe, Nd, and Gd are observed, and their absolute and relative line strengths change in time due to spatial expansion and cooling of the LPP. Instrumental broadening is apparent at the 31  $\mu$ s delay (8.84 GHz), but at later times, the instrumental resolution is comparable to the expected linewidth, which is dominated by Doppler broadening. Observed lineshapes also include unresolved hyperfine and isotopically split transitions [96, 102]. Stark broadening is weak due to low electron densities at these late times, and pressure broadening is expected to be sub-GHz [50]. The ability to resolve many of the transitions is important to limit spectral overlap, enabling more accurate determination of peak areas used in the Boltzmann analysis discussed below. Both weak and strong spectral lines are observed, and the large dynamic range of the DCS measurement is useful in measuring many transitions of various energies, which increases the accuracy of the Boltzmann plot method.

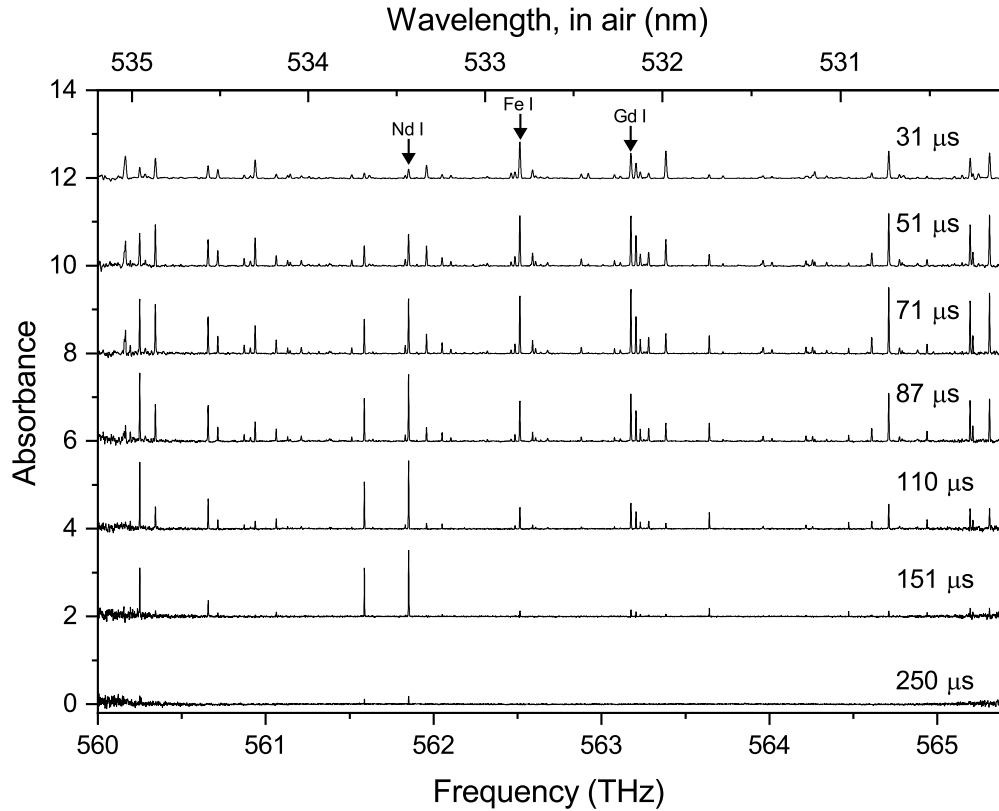
Here, 3 Fe I, 9 Nd I, and 22 Gd I known transitions were fit, listed in Table 5.1 and found in [75]. A few ion lines were visible at the earliest time measurements but were not included in this analysis due to being relatively weak and short-lived. Hyperfine and isotopic splittings were not large enough to be resolved; however, their effects could cause observed lineshapes to be aggregates of unresolved lineshapes rather than single Voigt lineshapes. The literature does not provide the necessary spectroscopic data for these effects to be included in the model for all measured transitions. Because the Boltzmann analysis uses integrated peak areas, small variations in lineshapes due to hyperfine/isotopic effects are not expected to impact the analysis significantly. Instrumental broadening was included in the model via convolution of the instrumental lineshape function with the modelled transmission spectrum, as described in Sec. 1.4.4.

Figure 5.3 shows examples of spectral fits in a subset of the full spectrum and at two time-delays. All fits had RMS fit residuals  $< 0.02$ , comparable to the baseline absorbance noise. Spectral fit results were not used for peak areas  $< 0.1$  GHz, if the fitted peak area



| Element | Frequency (THz) | Wavelength, air (nm) | $E_i$ (cm <sup>-1</sup> ) | $J_i$ | $E_j$ (cm <sup>-1</sup> ) | $J_j$ | log( $gf$ ) |
|---------|-----------------|----------------------|---------------------------|-------|---------------------------|-------|-------------|
| Fe      | 562.5130        | 532.8039             | 7376.764                  | 4     | 26,140.177                | 3     | -1.466      |
| Fe      | 562.4609        | 532.8531             | 12,560.933                | 3     | 31,322.611                | 3     | -1.85       |
| Fe      | 561.1454        | 534.1024             | 12,968.553                | 2     | 31,686.349                | 2     | -2.06       |
| Nd      | 565.2117        | 530.2598             | 8475.355                  | 5     | 27,328.788                | 4     | -0.01       |
| Nd      | 564.6092        | 530.8257             | 8800.392                  | 6     | 27,633.729                | 6     | 0.03        |
| Nd      | 563.2806        | 532.0778             | 8800.392                  | 6     | 27,589.409                | 6     | 0.03        |
| Nd      | 562.3199        | 532.9868             | 11,887.735                | 9     | 30,644.708                | 9     | 0.23        |
| Nd      | 562.0508        | 533.2420             | 9692.277                  | 7     | 28,440.275                | 8     | 0.13        |
| Nd      | 561.8511        | 533.4315             | 0                         | 4     | 18,741.337                | 4     | -1.171      |
| Nd      | 561.5879        | 533.6815             | 0                         | 4     | 18,732.556                | 5     | -0.87       |
| Nd      | 560.8719        | 534.3629             | 10,897.998                | 8     | 29,606.67                 | 7     | 0.05        |
| Nd      | 560.2499        | 534.9561             | 1128.056                  | 5     | 19,815.981                | 5     | -0.96       |
| Gd      | 565.3103        | 530.1673             | 7480.348                  | 6     | 26,337.071                | 6     | -0.09       |
| Gd      | 565.1948        | 530.2757             | 6550.395                  | 3     | 25,403.265                | 3     | -0.309      |
| Gd      | 564.7737        | 530.6711             | 6976.508                  | 5     | 25,815.33                 | 6     | -0.859      |
| Gd      | 564.7101        | 530.7308             | 7103.420                  | 5     | 25,940.122                | 5     | -0.137      |
| Gd      | 564.2278        | 531.1845             | 16,758.940                | 7     | 35,579.553                | 7     | 0.251       |
| Gd      | 563.2309        | 532.1247             | 6550.395                  | 3     | 25,337.755                | 2     | -1.001      |
| Gd      | 563.2049        | 532.1493             | 6378.146                  | 2     | 25,164.640                | 2     | -0.562      |
| Gd      | 563.1748        | 532.1778             | 6786.184                  | 4     | 25,571.672                | 4     | -0.179      |
| Gd      | 563.1114        | 532.2376             | 10,222.233                | 1     | 29,005.609                | 2     | -0.728      |
| Gd      | 563.0767        | 532.2704             | 10,576.410                | 3     | 29,358.628                | 4     | -0.508      |
| Gd      | 562.5888        | 532.7321             | 10,359.905                | 2     | 29,125.847                | 3     | -0.148      |
| Gd      | 562.4843        | 532.8310             | 10,222.233                | 1     | 28,984.69                 | 1     | -0.393      |
| Gd      | 562.1028        | 533.1926             | 10,222.233                | 1     | 28,971.965                | 0     | -0.554      |
| Gd      | 561.9574        | 533.3306             | 10,883.505                | 4     | 29,628.388                | 5     | 0.105       |
| Gd      | 561.5125        | 533.7532             | 10,359.905                | 2     | 29,089.945                | 2     | -0.45       |
| Gd      | 561.1305        | 534.1165             | 7103.420                  | 5     | 25,820.72                 | 4     | -1.113      |
| Gd      | 561.0624        | 534.1814             | 1719.087                  | 6     | 20,434.115                | 7     | -1.773      |
| Gd      | 560.9369        | 534.3009             | 11,296.465                | 5     | 30,007.307                | 6     | 0.4         |
| Gd      | 560.7151        | 534.5123             | 6550.395                  | 3     | 25,253.838                | 3     | -0.73       |
| Gd      | 560.6564        | 534.5682             | 999.121                   | 5     | 19,700.606                | 5     | -1.464      |
| Gd      | 560.3431        | 534.8671             | 6378.146                  | 2     | 25,069.179                | 1     | -0.38       |
| Gd      | 560.1644        | 535.0377             | 12,486.547                | 7     | 31,171.622                | 8     | 0.545       |

**Table 5.1:** Atomic transitions of Fe, Nd, and Gd used in the spectral fit and Boltzmann analysis.



**Figure 5.2:** Experimental absorbance DCS spectra measured at seven time-delays after ablation. Each is the average of 750 shots. Atomic transitions of Fe, Nd, and Gd are visible, along with some ionic lines at early times, but only the two Nd I resonant transitions are visible at 250  $\mu\text{s}$ . A single atomic transition for each species is indicated as an example. Spectra offset for clarity. (Figure from [30])

was less than the standard error provided by the fitting routine, or if visual inspection indicated a bad fit due to high spectral noise. Figure 5.4 shows the lower-level state column densities for various transitions of the three elements calculated from the fitted peak areas according to Eq. 3.9. Populations in higher energy states decay more quickly in time as the LPP cools, while the lowest energy states initially gain population before also decaying. Temperature variations from plasma expansion and cooling drives the relative population changes across all energy states, including the ground state [103]. At 250  $\mu\text{s}$ , only resonance transitions ( $E_i = 0$ ) were detected, which indicates the LPP has cooled sufficiently to reduce the population in higher-energy levels according to Eq. 3.7.

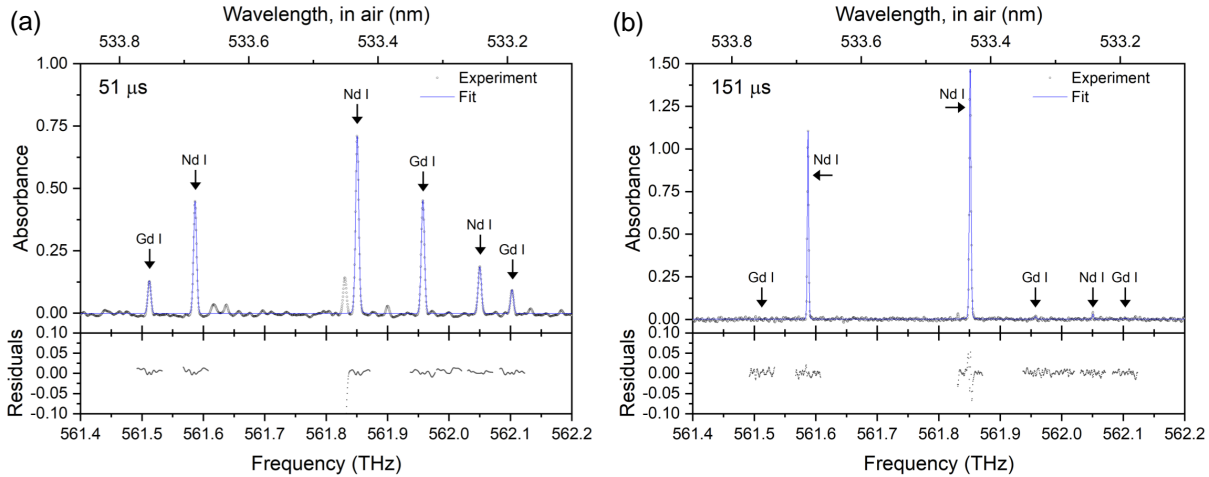


**Figure 5.3:** Example spectral fits at (a) 51 and (b) 151  $\mu\text{s}$ , plotted over a narrow spectral region to show agreement between measurements (points) and spectral fits (lines). Transitions used in the spectral fitting are labelled by element. Additional absorption lines visible in the spectrum were not included in the fits because oscillator strength data were not available. Note the absorbance range in (a) is smaller. (Figure from [30])

#### 5.4 Determination of Temperature and Atomic Density

Boltzmann plots were created at each time-delay separately for each species to determine species excitation temperatures and total column densities as a function of time as described in Sec. 3.3.

Figures 5.5 and 5.6 show the Boltzmann plots for Nd I, Gd I, and Fe I at all time-delays up to 151  $\mu\text{s}$  and the linear fits used to determine temperature and total column density. At 250  $\mu\text{s}$ , only the two resonant Nd I lines are visible, and so no Boltzmann plots were made for this time-delay. The error bars include both the standard error from the spectral fitting routine and the reported 50% relative uncertainty of the oscillator strengths [76]. The linear fits of the Boltzmann plots had  $R^2$  values ranging from 0.93 to 0.99. The  $R^2$  of the Nd I fits were consistently smaller, partly due to the disagreement between the two ground state transitions on the Boltzmann plot, which is discussed further in the next section. The errors in the fits for Fe were high due to the low number of points included in the Boltzmann plots.

The slope and y-intercept of the Boltzmann plot linear fits were used to determine excitation temperature and total column density, respectively, for each species. These values

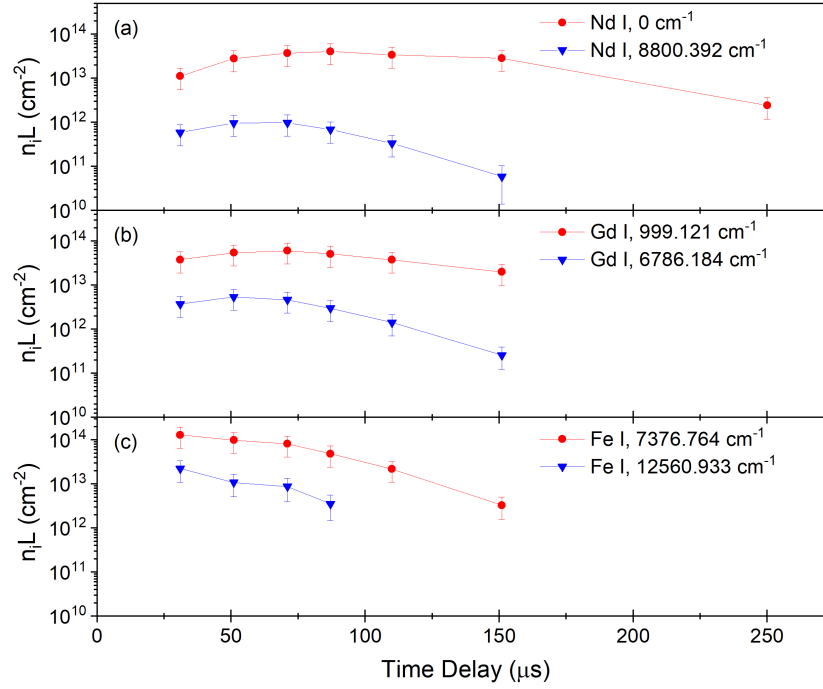


**Figure 5.4:** State column densities for selected high-lying (blue triangles) and low-lying (red circles) energy levels of (a) Nd I, (b) Gd I, and (c) Fe I as a function of time after ablation. Higher energy levels lose population as the plume cools in time, whereas atoms accumulate in the lower energy states. The Nd I resonant transition trace comes from the calculated column density using the 561.8511 THz transition fitted peak area. (Figure from [30])

are shown in Fig. 5.7 as a function of time-delay. The error bars were determined from the standard errors of the slope and y-intercept in the Boltzmann plot fits. The excitation temperatures determined for Nd I and Gd I were similar at all time-delays, ranging from  $4040 \pm 420$  K and  $4040 \pm 160$  K at  $31 \mu\text{s}$  to  $2080 \pm 290$  K and  $2170 \pm 90$  K at  $151 \mu\text{s}$ . The excitation temperatures determined for Fe I were markedly higher, ranging from  $5600 \pm 1100$  to  $3700 \pm 1000$  K, but are not unreasonable accounting for the high uncertainties. Total column densities determined from the Boltzmann plots were Nd I  $\sim 7 \times 10^{13} \text{ cm}^{-2}$ , Gd I  $\sim 3 \times 10^{14} \text{ cm}^{-2}$ , and Fe I  $\sim 3 \times 10^{15} \text{ cm}^{-2}$ . The magnitudes of excitation temperatures and column densities are comparable to previous measurements [28, 29]. The column densities for Nd and Gd in the LPP were found to be significantly lower than for Fe, as expected; however, the relative values do not match the percentages based on the sample composition of the alloy. Figure 5.7(d) plots the ratio between the Gd and Nd column densities, which was

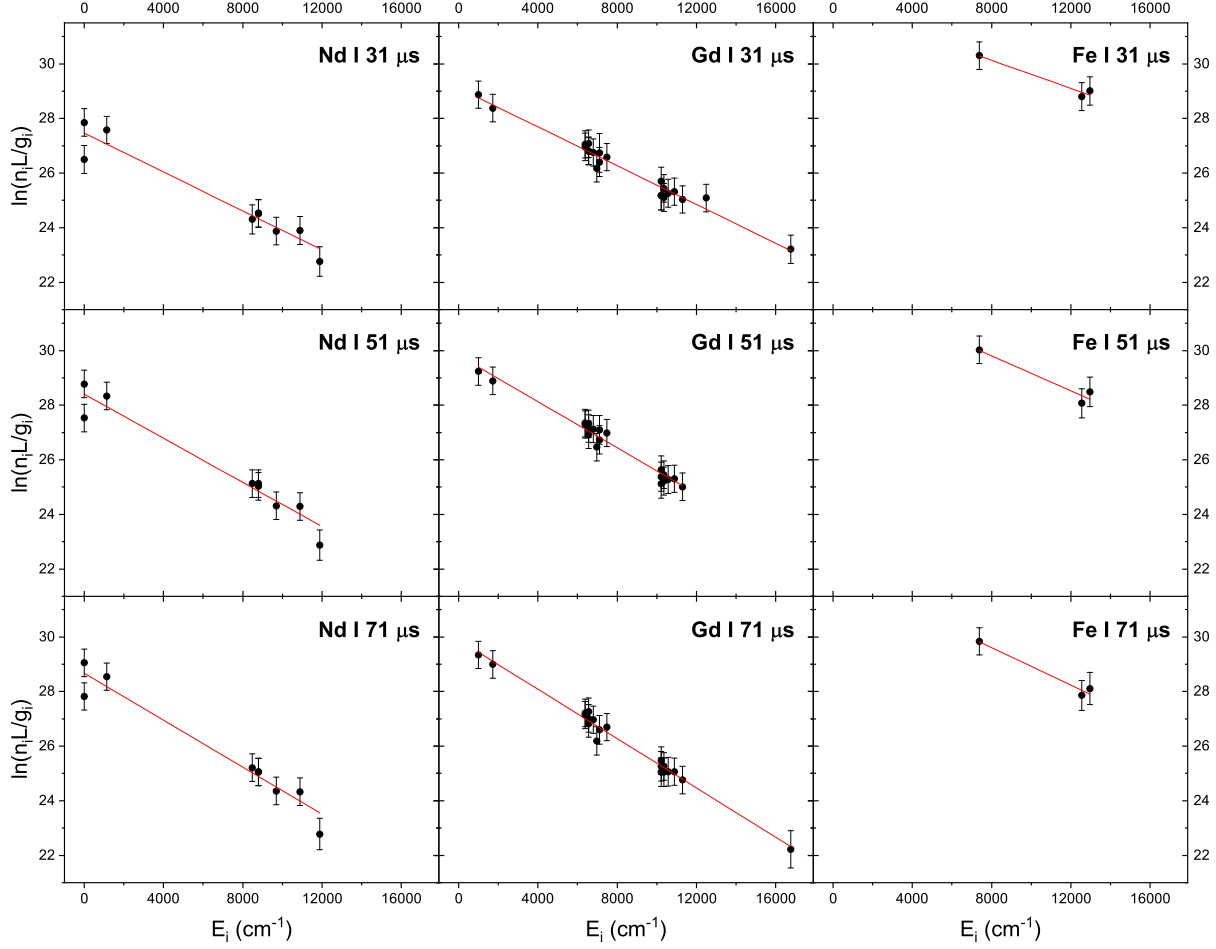


**Figure 5.5:** Boltzmann plots for Nd I, Gd I, and Fe I at 31, 51, and 71  $\mu\text{s}$ . Red lines are linear fits calculated from the plots to determine temperature and total column density for each species. Error bars include both reported oscillator strength uncertainties and standard error from the spectral fits.

found to vary with time-delay from 2-5, despite having equal concentrations in the sample.

## 5.5 Discussion

Previous work using LIBS has shown how spatial effects can cause different apparent temperatures to be measured for two species in the same plume [20, 70, 97, 104]. The Boltzmann distribution used to determine excitation temperatures and species densities assumes the LPP is in local LTE, such that each species follows a thermal distribution of states within each small volume of the LPP [101]. Thermal distributions with varying excitation temperature across the LPP are valid within the LTE assumption, however, and tempera-

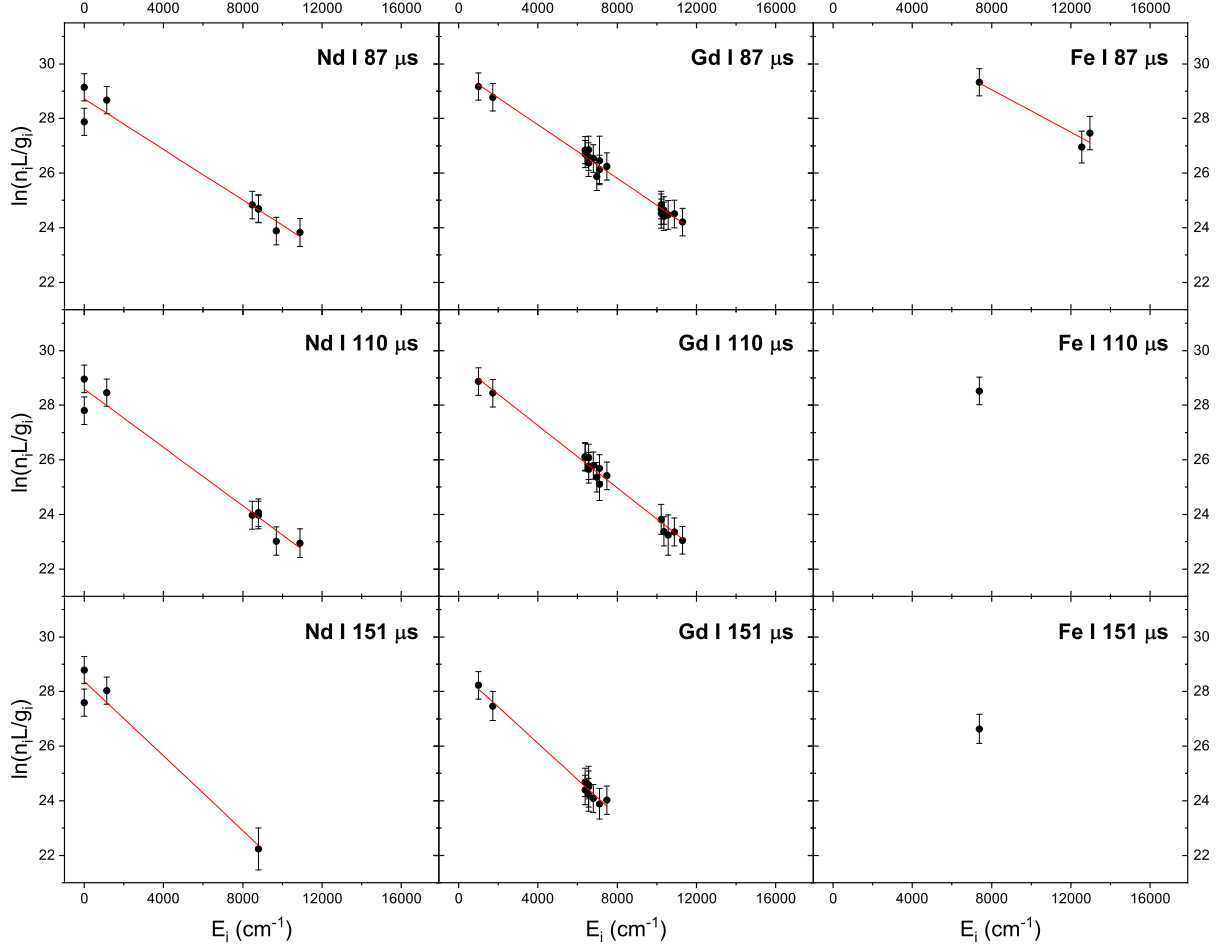


**Figure 5.6:** Boltzmann plots for Nd I, Gd I, and Fe I at 87, 110, and 151  $\mu\text{s}$ . Red lines are linear fits calculated from the plots to determine temperature and total column density for each species. Error bars include both reported oscillator strength uncertainties and standard error from the spectral fits.

ture gradients across the LPP are well documented [19, 103]. Accordingly, any excitation temperature determined from a spectroscopic measurement probing species across a thermal gradient is a weighted average temperature derived from the constituent local temperatures. The determined average temperature will be weighted toward the local temperature of the more populated regions. For absorption-based measurements, the lower-states in the transition drive the weighting, which are more populated in lower-temperature regions. In a LPP with a thermal gradient, the Boltzmann distribution leads to higher populations in lower-temperature regions, which results in a lower weighted average temperature. Similar considerations apply for emission-based measurements but with the upper-state populations

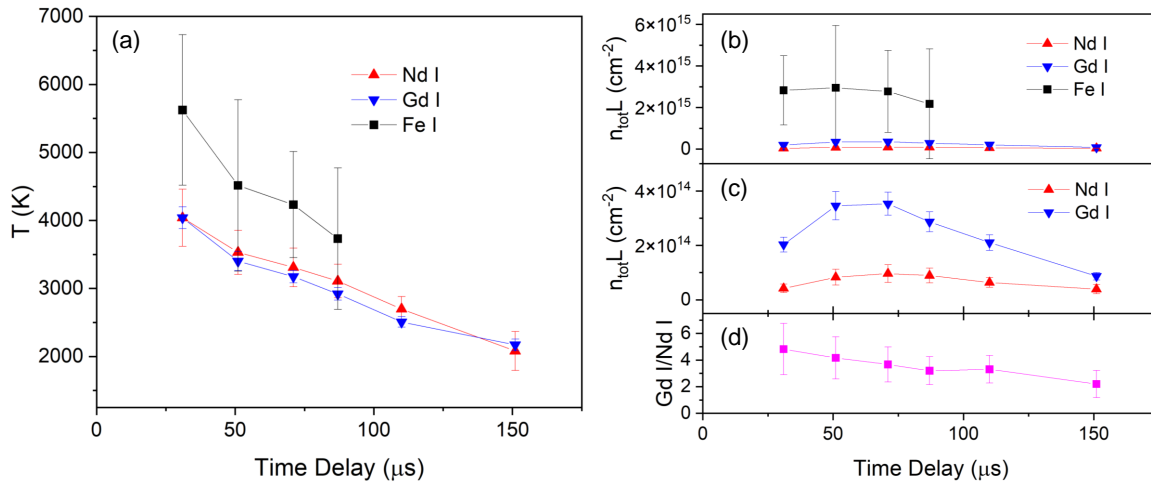


**Figure 5.7:** Temperature (a) and total column density (b) as a function of time after ablation for Nd I, Gd I, and Fe I. (c) is a vertically-zoomed copy of (b) to show detail of Nd I and Gd I total column densities. The ratio of Gd I/Nd I is shown in (d). (Figure from [30])

driving the weighting.

The results in Fig. 5.7(a) show that the excitation temperatures determined for Nd I and Gd I agree very well within the measurement uncertainties, which is significant since such a result cannot be assumed due to the measurement of a column of atoms across the inhomogeneous LPP. The excitation temperatures determined for Nd I and Gd I are both likely affected by the averaging effects along the measurement path; however, the similar range of energy levels measured for both species results in similar weighting functions.

Spatial effects in the line-of-sight averaging may thus explain the higher apparent excitation temperature for Fe versus Nd and Gd. The Fe I temperature analysis included only transitions originating from high energy levels  $> 7377 \text{ cm}^{-1}$ . By probing exclusively higher energy transitions, the line-of-sight average is weighted towards the higher temperature regions of the LPP where these energy levels of the Fe I transitions are more populated. Fe atoms are also present in cooler regions but are not detected in the measurement and thus do not contribute to the weighting of temperatures along the measurement path. The excitation temperatures determined for Fe I are also consistent with previous measurements using DCS absorption spectroscopy, but which used a slightly different experimental con-

figuration and analysis [28]. The previous measurements of Fe excitation temperature also probed exclusively higher energy states and so are expected to share the same bias toward higher temperatures relative to species in which ground or low-energy states are probed. A measurement which included more transitions that spanned more energies would give more confident results that would likely show lower excitation temperatures. While the spatial averaging effects likely explain the difference in measured excitation temperatures for Fe versus Nd/Gd, chemical differences between elements cannot be dismissed as potential causes for divergence (e.g., different oxidation rates/energies).

The ratios of column densities for species measured in the LPP are not necessarily expected to be identical to those determined from the sample composition. Elemental fractionation effects during ablation are known to occur, especially when using IR nanosecond pulsed lasers [105, 106]. As a result, the ablation plume may be non-stoichiometric relative to the sample due to matrix effects and differences in ablation efficiency for different elements in the sample [107, 108]. While the ablation process itself may be non-stoichiometric, Fig. 5.7(d) also shows that the relative column densities of Gd and Nd change with time-delay. This result may indicate the presence of molecular formation as the LPP cools [109–111]. All the species measured here—Fe, Nd, and Gd—form molecular oxides, and trace levels of oxygen are likely present in the ablation chamber due to leaks and oxidation of the sample surface. Rates for molecular formation may vary between different species and depend on the temperature of the LPP, leading to variations in the relative number densities of the species over time [112–115].

Subsequent DCS measurements of LPPs have shown oxide formation under similar conditions and delay-times. Using the Er-DCS system described in Ch. 2, Ce and CeO were measured simultaneously in a LPP generated by ablating a pure Ce sample [31]. Fig. 5.8 shows measured absorbance spectra in that experiment as a function of time-delay after ablation. Transition frequencies of atomic Ce I lines identified in the literature [75, 116, 117] and calculated dipole-allowed Ce I transitions are indicated by arrows. In addition to atomic Ce lines, the spectra show the clear presence of molecular absorption bands, with the most prominent being the CeO transition from the ground electronic state  $X_2(^3\Phi_3)$  to the first electronic excited state  $A_2(^3\Delta_2)$  (also denoted [12.8]2) [118–122]. The relative heights of atomic



and molecular absorption features vary in time due to plasma expansion, plasma cooling, and oxidation chemistry. A late-time spectrum (302  $\mu\text{s}$ ) with higher resolution (1.24 GHz) is shown in Fig. 5.9, showing a portion of the Q-branch and overlapping P-branch of the  $X_2(^3\Phi_3) - A_2(^3\Delta_2)(0-0)$  CeO transition identified through comparison with the literature [121]. Fig. 5.9(b) shows details of smaller spectral regions in which individual rotational transitions are labeled by dashed lines at the frequencies listed in [121], along with J-value assignments.

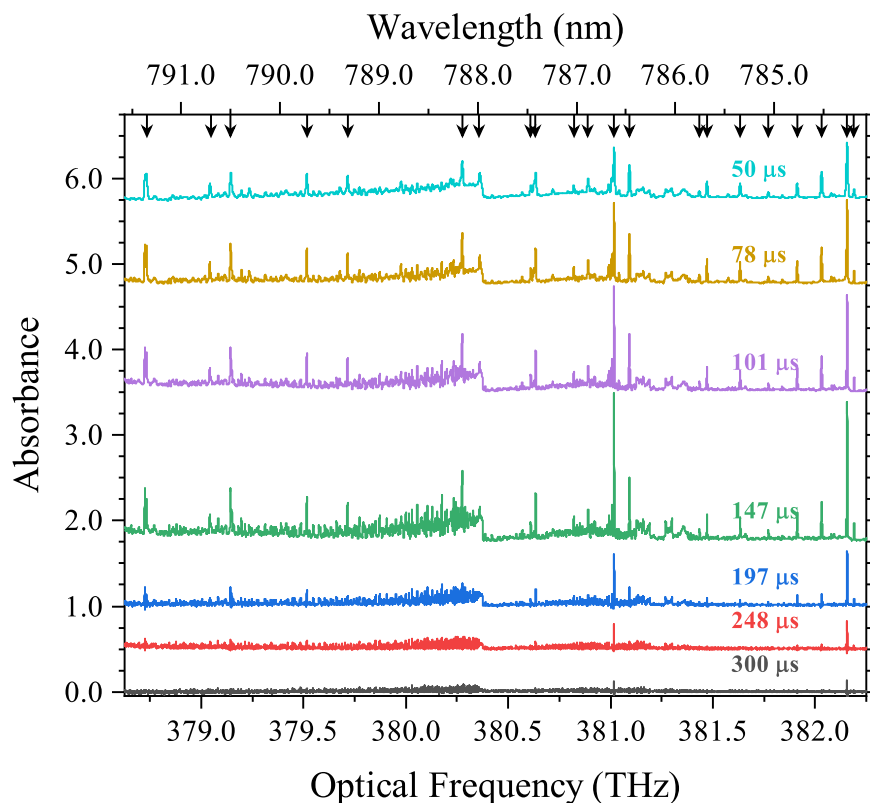


**Figure 5.8:** Time evolution of absorbance spectra of LPP containing CeO molecular bands and prominent Ce atomic lines (positions indicated by arrows). The measurement spectral resolution varies with time-delay (from top to bottom: 7.60 GHz, 4.96 GHz, 3.72 GHz, 2.56 GHz, 1.91 GHz, 1.50 GHz, and 1.25 GHz). Spectra offset for clarity. (Figure from [31])

Strong CeO absorption was observed in a background gas of 50 Torr of  $\text{N}_2$  (no added oxygen) with surface oxide layers on the Ce metal target removed by performing 10 ablation passes along the sample region prior to data collection for each time-delay. These results indicate that Ce oxidizes rapidly to CeO in trace amounts of oxygen, likely present due to small leaks in the sample chamber (base pressure 1 Torr) or residual surface oxidation

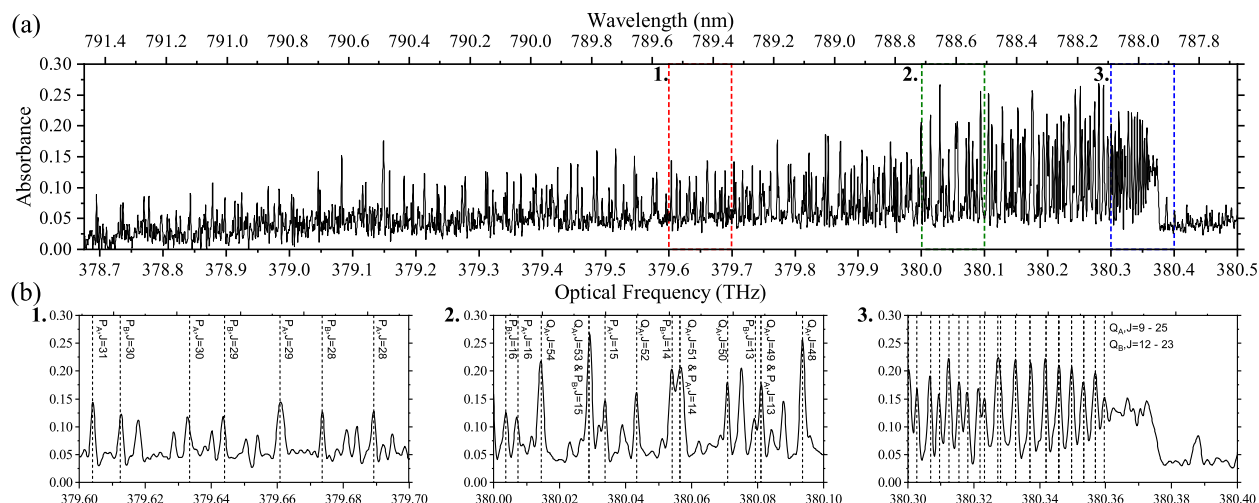


**Figure 5.9:** (a) Absorbance measurement of LPP showing molecular CeO rovibrational electronic transition lines originating predominantly from the P and Q branches of the  $X_2(^3\Phi_3) - A_2(^3\Delta_2)(0-0)$  band. The spectrum is the result of 400 averaged shots and was acquired at 302  $\mu\text{s}$  after ablation with a resolution of 1.24 GHz. No cleaning shots were performed for this measurement, resulting in increased CeO absorption and decreased Ce I absorption. (b) Zoomed-in portions of (a) emphasizing different 0.1 THz portions of the spectra and lines position reported by Linton et al. [121]: (b1) P-branch lines at approximately 379.65 THz; (b2) P and Q-branch lines at approximately 380.05 THz; (b3) Q-branch lines with bandhead at approximately 380.35 THz. (Figure from [31])

not removed completely via the cleaning process. These observations are consistent with prior studies [122], which found similar CeO formation in the presence of trace levels of oxygen. Experiments performed in the presence of 50 Torr air (not shown) resulted in the disappearance of all atomic and molecular absorption features, suggesting that higher oxygen concentrations provide favorable conditions for formation of larger Ce oxides such as  $\text{CeO}_2$  [123]. These results indicate oxide formation is likely for Nd and Gd, which are chemically similar to Ce. Note that DCS is well-suited to measuring time-resolved molecular formation in LPPs due to its ability to resolve closely spaced rovibrational lines of molecular bands that cover large spectral bandwidths. Comparisons of atomic and molecular densities and temperatures are especially valuable for understanding gas-phase chemical kinetics.

Figures 5.5 and 5.6 show a discrepancy in the values for the two ground-state Nd I transitions in the Boltzmann plots, this behavior being observed at all time-delays. The source of the discrepancy may be due to an erroneous value in the literature for the oscillator strength of one or both transitions. The higher frequency transition at 561.8511 THz was

observed to have a stronger relative absorbance than the lower frequency resonant transition at 561.5879 THz at all time-delays, despite being cited as having the smaller oscillator strength. Figure 5.10 shows the fitted peak areas of the two transitions and their ratio, which is theoretically equal to the ratio of their true oscillator strengths. According to the measurements made here, the ratio of the oscillator strengths for the 561.8511 THz to the 561.5879 THz resonant transitions is  $1.71 \pm 0.12$  (mean and standard deviation over all measured time-delays). In contrast, available literature sources report a ratio of 0.50 [75, 124]. The linear fits of the Boltzmann plots, which include several other transitions, suggest the 561.5879 THz transition could have an incorrect oscillator strength in the literature. For comparison, the Boltzmann analysis was repeated for Nd I with this transition excluded, resulting in the temperature and total column density changing by  $\sim 10\%$  (averaged across all time-delays). The variation in temperature and column density clearly shows the sensitivity of the analysis to the input oscillator strengths. Thus, the accuracy of temperature and column density measurements based on this method depends critically on having high-accuracy measurements of oscillator strengths, which may be lacking for weaker transitions of many elements [29].

To determine the precision, or repeatability, of the determination of excitation temperature and column density, additional measurements were performed. For this analysis, seven duplicate datasets were acquired and analyzed. Each data set consisted of 750 ablation shots taken sequentially at 110  $\mu\text{s}$  after ablation. Excitation temperatures and total column densities for Nd I and Gd I were calculated for each measurement, and results are shown in Fig. 5.11. The repeatability in excitation temperature was found to be  $\pm 60$  K for Nd I and  $\pm 70$  K for Gd I. For column densities, the repeatability was  $\pm 5 \times 10^{12} \text{ cm}^{-2}$  for Nd I and  $\pm 2 \times 10^{13} \text{ cm}^{-2}$  for Gd I. The repeated measurements give the precision to which excitation temperatures and total column densities can be determined with the current DCS/LPP measurement. The measurement precision is slightly better than the standard errors calculated from the Boltzmann plot linear fits used to indicate the error bars on individual measurements. As such, these error bars included other potential sources of error including the validity of the Boltzmann model, the accuracy/precision to which the peak areas are measured and fit, and the accuracy of the input spectroscopic constants.

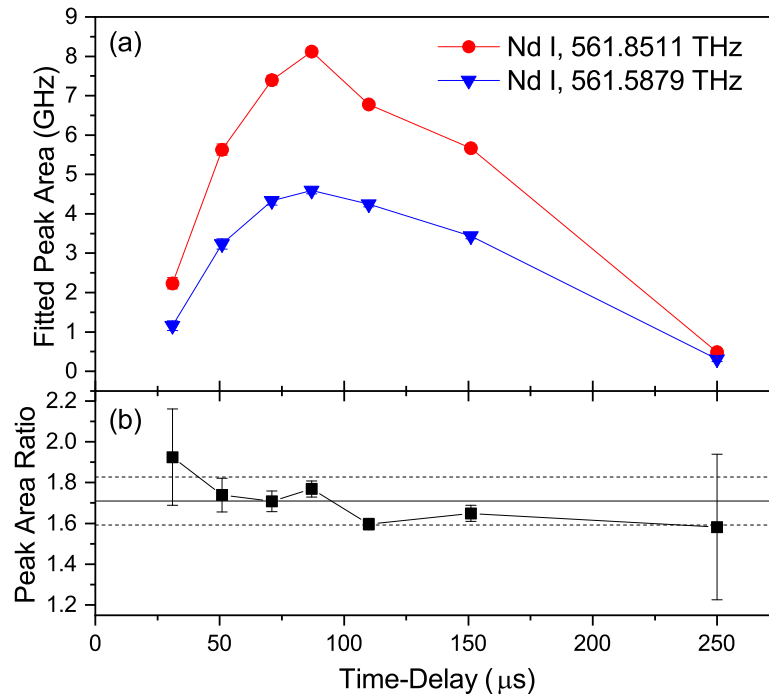


**Figure 5.10:** Plot of (a) fitted peak areas and (b) their ratio for the two resonant transitions of Nd I within the DCS measurement bandwidth. Solid line denotes mean value across all time-delays and dashed lines one standard deviation,  $1.71 \pm 0.12$ . Error bars on the fitted peak areas come from the fit error, which is propagated and plotted for the ratios. (Figure from [30])

As discussed above, both thermal and density spatial distributions exist in the LPP. Thus, no single values for excitation temperature and number density exist, complicating quantification of accuracy. For absorption measurements which probe a columnar volume of the LPP, both values are a line-of-sight average. Comparison to measurements made by other techniques would be strengthened by a model which includes spatial inhomogeneity, but this is beyond the scope of the current work. Despite the challenge in determining accuracy for the measurements, there is great value in comparisons of excitation temperature and column densities between different species and how these parameters vary in time as the LPP cools. The similar excitation temperatures determined for Gd I and Nd I show the consistency of the Boltzmann plot method when using transitions spanning similar energy ranges. In contrast, the higher apparent temperature for Fe I is consistent with measurement of only higher-energy transitions. Regarding column density measurements, observation of chang-

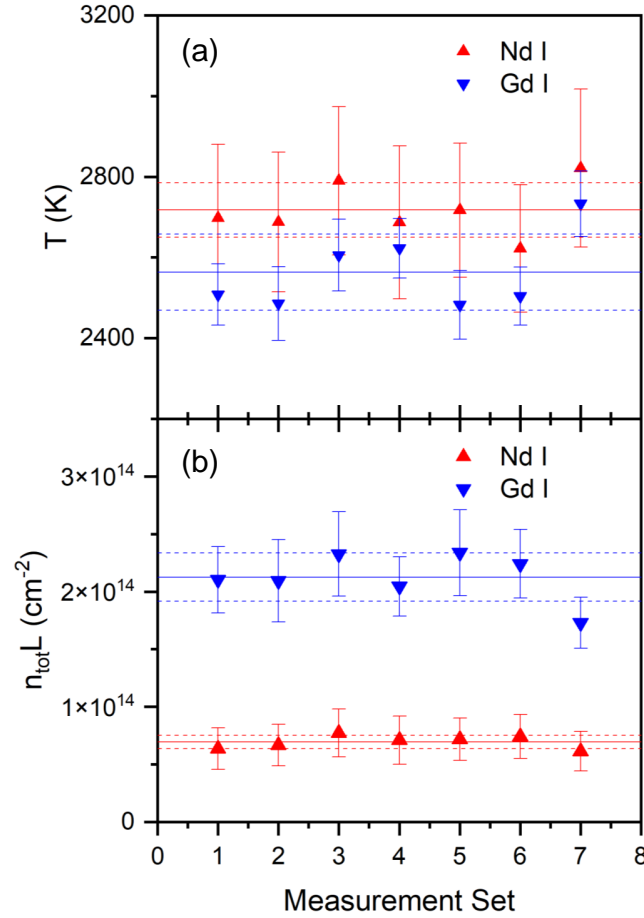


**Figure 5.11:** Excitation temperature (a) and total column density (b) for Nd I and Gd I for seven repeated measurements of 750 ablation shots each at  $110 \mu\text{s}$ . Solid horizontal lines denote mean values across all seven measurements, and dashed lines mark one standard deviation. (Figure from [30])

ing ratios between species in time reflects possible rate differences in molecular formation between the two. Such rates are a critical piece in studies to understand LPP evolution [109–111].

It is also important to note that the column densities measured within the LPP are not a direct measurement of the elemental number densities of species in the solid target used for ablation. As discussed above, elemental fractionation effects may be present during ablation, and it is difficult to determine the absolute ablation efficiency based on theoretical calculations alone. Combined with the complexities caused by evolving spatial distributions in the LPP, a direct link between measured column densities and the number densities present

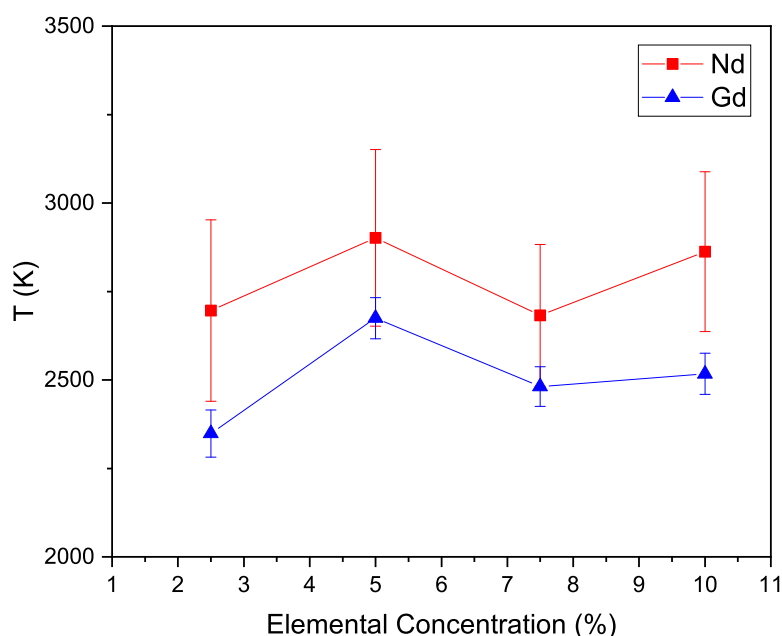
in the sample are difficult to establish without additional calibration techniques. Analytical measurements of sample composition using calibration-based methods are common in LIBS [125], and similar methods could be applied to the DCS measurement. The absorption-based DCS measurement is less susceptible to optical depth effects commonly observed in LIBS, including self-absorption and self-reversal, which may require additional analysis and correction via curve of growth and  $C\sigma$  techniques, for example [86, 87, 126]. Therefore, it is possible that a DCS-based calibration may provide higher measurement confidence, or require fewer calibration measurements spanning different sample compositions, than a corresponding LIBS-based measurement. The results presented here provide a first step toward establishing the accuracy, precision, and repeatability of the DCS measurement combined with laser ablation, but additional studies are needed.

## 5.6 Sample Concentration/Measured Number Densities Calibration

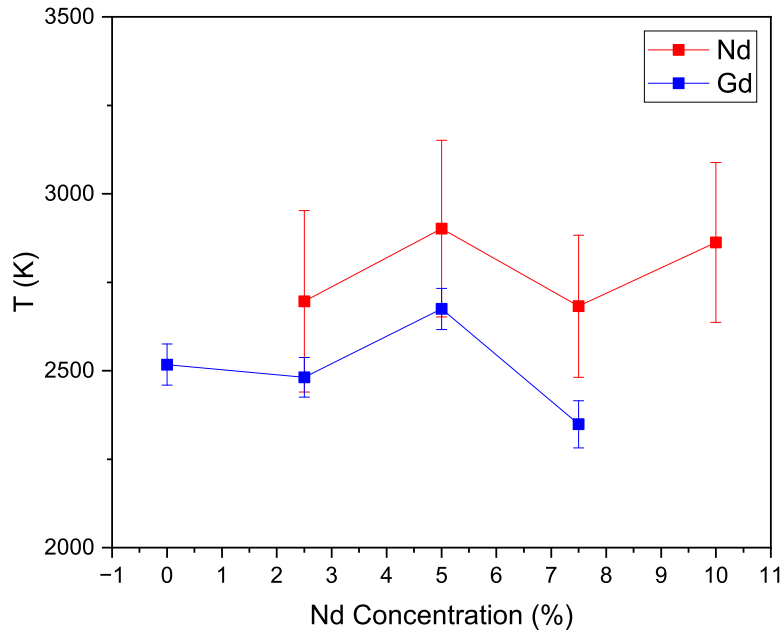
Along with the measurements and analysis described above, more measurements were performed with a set of alloys of varying concentrations for the purpose of calibration. The measured total column densities can be calibrated to the sample concentrations given a range of concentrations, and inclusion of a 0% concentration provides an important baseline. Five alloys were studied, all with Fe concentration of 90%. Nd and Gd concentrations varied inversely from 0 to 10%, i.e., 0/10, 2.5/7.5, 5/5, 7.5/2.5, and 10/0% for Nd/Gd. Three time-delays, 50, 70 and 110  $\mu\text{s}$  were measured, but only the 110  $\mu\text{s}$  sets were analyzed, with the exception of the analyses for the 90/5/5% data presented above. The spectra were fit in the method discussed above, with 2 Fe, 6 Nd, and 12 Gd transitions included. Excitation temperatures  $T$  and total column densities  $n_{\text{tot}}L$  were determined using Boltzmann plots for each species at each concentration. Fitted transitions were excluded from the Boltzmann plots if their peak areas were  $< 0.1$  GHz or if their uncertainty was greater than the peak area. Due to these restrictions, as well as only fitting 2 Fe transitions, Fe was excluded from most of the following analyses.

Figure 5.12 shows the excitation temperatures calculated for Nd I and Gd I as a function of concentration. The unweighted average  $T$  and standard deviation for Gd I was  $2790 \pm 100$  K and  $2510 \pm 120$  for Nd I. The error bars are calculated from the uncertainty of the fitted

slope for the Boltzmann plots. The temperatures for Nd agree within their uncertainties and those of Gd do not, but this is at least partially due to the errors for Nd being larger than for Gd at all concentrations. This may be because of the inclusion of an Nd ground-state transition with what we think is an erroneous oscillator strength, discussed above and shown in Fig. 5.10. Temperatures were not determined at 0% concentration due to none of the fitted peaks fulfilling the above requirements for inclusion in the Boltzmann plots. Note that the temperatures measured for each species share similar trends. However, Fig. 5.13 shows the two temperatures also share the same trend when plotted as a function of sample measurement (tracked in terms of Nd concentration, e.g., Nd= 2.5% indicates a single sample measurement that also had Gd=7.5%). One possible explanation is that average plume geometry was slightly different between sample measurements so that different portions of the plume at different temperatures were probed. Note that the standard deviations here are poorer than those of  $\pm 60$  K and  $\pm 70$  K for Nd I and Gd I, respectively, reported in the previous section, indicating that there is at least one contributing factor besides measurement repeatability at work.



**Figure 5.12:** Determined excitation temperatures for Nd and Gd as a function of sample concentration.



**Figure 5.13:** Determined excitation temperatures for Nd and Gd as a function of Nd concentration. Note that Gd has an inverse concentration to Nd, so pairs of points that share a common x-value were taken in the same measurement.

Figure 5.14 shows the total column densities calculated for Nd and Gd as a function of concentration, along with their unweighted linear fits. These fits had a forced y-intercept of 0, since the density is expected to be 0 atoms/cm<sup>-2</sup> at 0% concentration, and had  $R^2$  (coefficient of determination) values of 0.961 and 0.975 for Nd and Gd, respectively. Counter-intuitively, allowing the y-intercept to vary gave poorer  $R^2$  values of 0.807 and 0.865. Figure 5.14 shows that the linear fits are just within the uncertainties of the Nd data and not within those of the Gd data. This indicates that the measured total column densities do not have a strong linear correlation with sample concentration, given the uncertainties. It is not yet understood why measured total column densities do not scale more linearly with sample concentration. Perhaps the mechanisms discussed above, including elemental fractionation, may be effected by the sample concentrations. For example, ablation efficiencies may vary as the composition and structure of the samples varies. Additionally, the rate of oxide formation may increase with increased number density, noting that oxide formation was shown to be likely above.

The measured peak areas which determine  $T$  and  $n_{tot}L$  were studied to learn more. Fig-



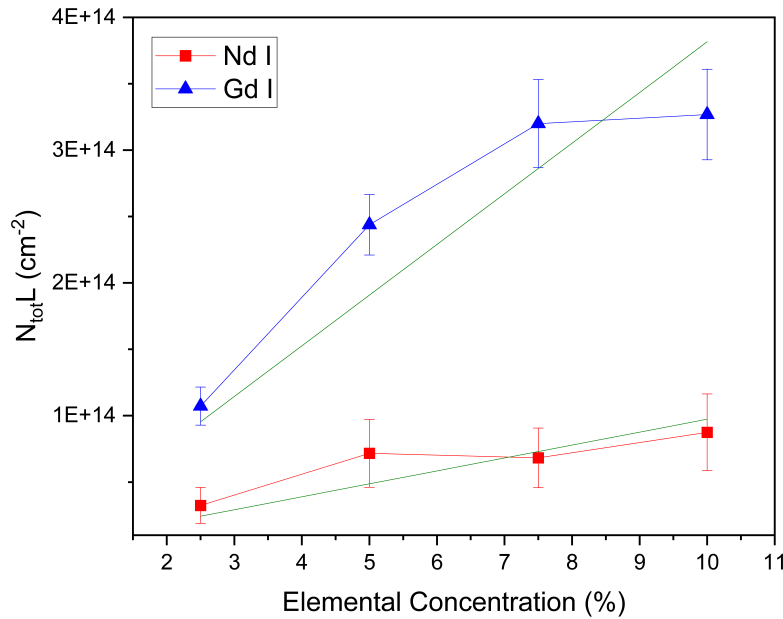


**Figure 5.14:** Determined total column densities for Nd and Gd as a function of sample concentration. The linear fits have y-intercepts forced to 0.

ure 5.15 shows the peak area for a representative transition for each element as a function of sample concentration. The uncertainties are the standard error for the fitted peak area from the statistics of the fit. The Fe I transition at 562.5130 THz did not have a constant fitted peak area across the samples given the uncertainties, as would be expected since the concentration was constant. It is unclear whether these differences are due to variations in the measurement parameters (e.g., probing slightly different regions of the plume), unaccounted effects such as variations in elemental fractionation processes, or errors in the measurement process (e.g., such as incorrectly measured peak areas). The result indicates, however, that mechanisms exist which may be expected to break any linear relationship that may exist between sample concentration and measured total column densities of Nd I and Gd I. Note that nearly all Gd I and Nd I transitions showed a roll-off in peak area for higher concentrations, as exhibited in the two transitions plotted here. As mentioned above, there is a possibility that molecular formation rates may vary with number density present. However, more measurements and analysis should be performed to study the effects of larger absorbances on the results and whether such peak areas are being measured accurately. Future calibration

experiments may benefit from avoiding elements that are suspected to form oxides so easily as well as preventing air from entering the chamber.

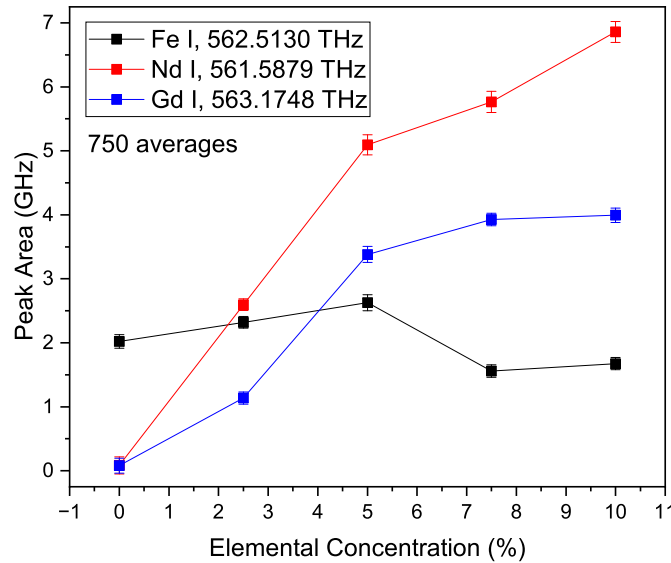


**Figure 5.15:** Fitted peak areas for three transitions with 750 averages as a function of sample concentration. Note, Fe was kept at a constant 90% concentration.

The fitted peak areas for the 0% concentrations for both Nd and Gd show values close to 0, as expected. Given the behavior observed for 0% concentrations in the results and  $T$  and  $n_{tot}L$ , the rules for inclusion of transitions in the Boltzmann plots may need to be revised for these special cases. The 0% case is an important measurement to include as it gives a baseline for the calibration, indicating whether peak areas and total column densities of 0 are accurately measured.

To better understand the determined values of  $T$  and  $n_{tot}L$ , the effects due the number of spectral averages was examined. The datasets for all alloy concentrations at 110  $\mu\text{s}$  were processed for averaging numbers 1, 2, 5, 10, 50, 100, and 325, resulting in 750, 325, 150, 75, 15, 7, and 2 averaged spectra for each averaging number, respectively. Spectral fitting was then performed on each spectrum. A specialized set of codes was written to handle the analysis (spectral fitting and Boltzmann-plot analysis) of so many spectra (see App. B.5). The mean and standard deviation of the fit parameters were calculated across the spectra of

each averaging size as well as their standard errors. Boltzmann plots for each spectra were constructed and fit to determine  $T$  and  $n_{tot}L$  for each spectrum, with mean and standard deviations for the various averaging sizes. The total column densities are plotted for Nd and Gd as a function of averaging number in Figs. 5.16 and 5.17, with each concentration shown. Similarly, the excitation temperatures are shown in Figs. 5.18 and 5.19. The error bars are the standard deviations across the averaging bins. The error bars can also be calculated as the average of the uncertainties from the individual Boltzmann plots across the averaging bins. The results for  $n_{tot}L$  show smaller differences than at higher averaging numbers. At low ( $< 10$ ) number of averages, however, the determined values nearly always trend to higher values, even showing orders of magnitude of difference in the case of 1 and 2 averages. The inverse relationship between measured values and number of averages holds true for  $T$  as well, though the observed differences in  $T$  are much smaller. This effect may be explained by the fact that if all peak areas are measured with the same systematic bias, the slope of the Boltzmann plot will be unchanged. The y-intercept will be strongly affected, however. Across all measurements and averaging numbers, analysis applied to 0% concentration produces values which vary greatly over many orders of magnitude with extreme uncertainties.

Though peak areas of  $\sim 0$  GHz were obtained for 0% concentrations with large averaging numbers, it was thought that the noise contribution to fitted peak areas is not 0 in the case of less averaging. For nearly all concentrations, the total column densities were observed to increase at lower averaging numbers. The peak areas for single-shot data were plotted in a histogram for all lines to observe the distribution of fits. For transitions in 0% concentration cases, the distribution was roughly Gaussian about 0 GHz, with a prominent dip at 0 GHz observed in nearly all cases (Fig. 5.20). The lack of very nearly 0 GHz fits may be the result of the frequency of the noise being on the order of the linewidths being fit, so that peaks and valleys of the noise are nearly always present to give erroneous positive or negative fit values. The noise is expected to be roughly Gaussian and centered about 0 such that it does not bias the peak area fits. For strongly absorbing peaks, the fitted peak areas were observed to exhibit a long tail in the distribution towards very large peak areas (Fig. 5.21). This tail skews the mean value and increases the standard deviation, which is thought to

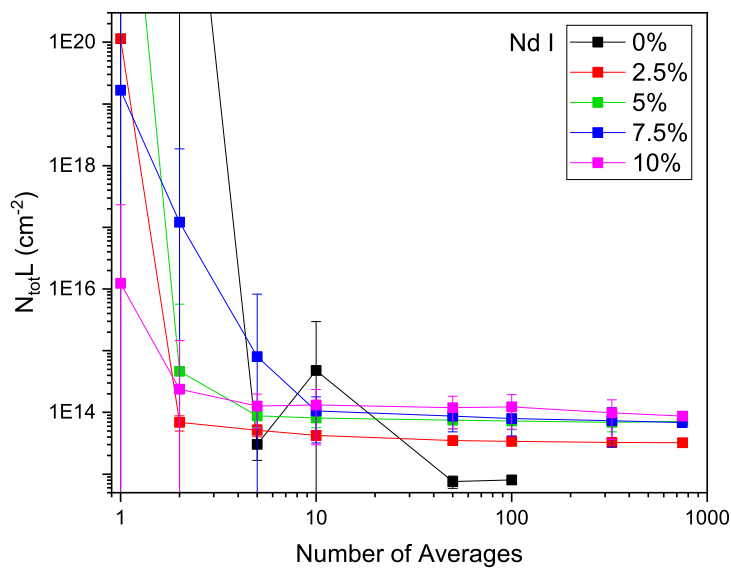


**Figure 5.16:** Determined total column densities for Nd I for various sample concentrations as a function of averaging number.

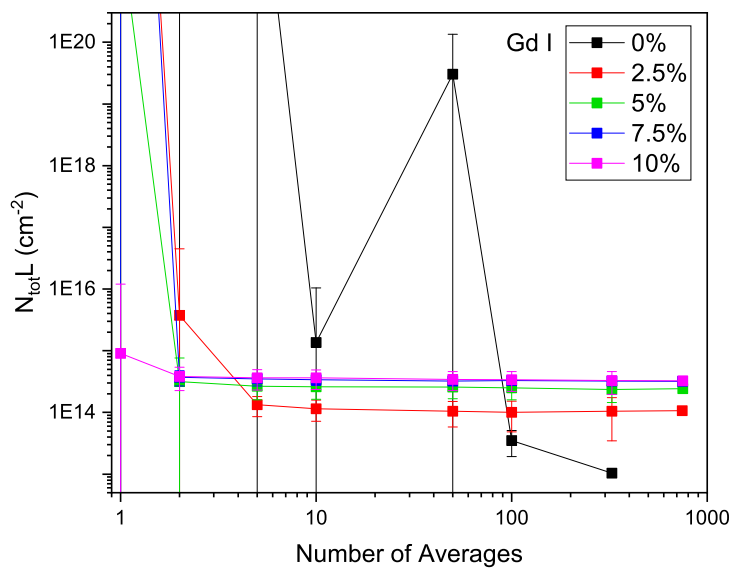


**Figure 5.17:** Determined total column densities for Gd I for various sample concentrations as a function of averaging number.

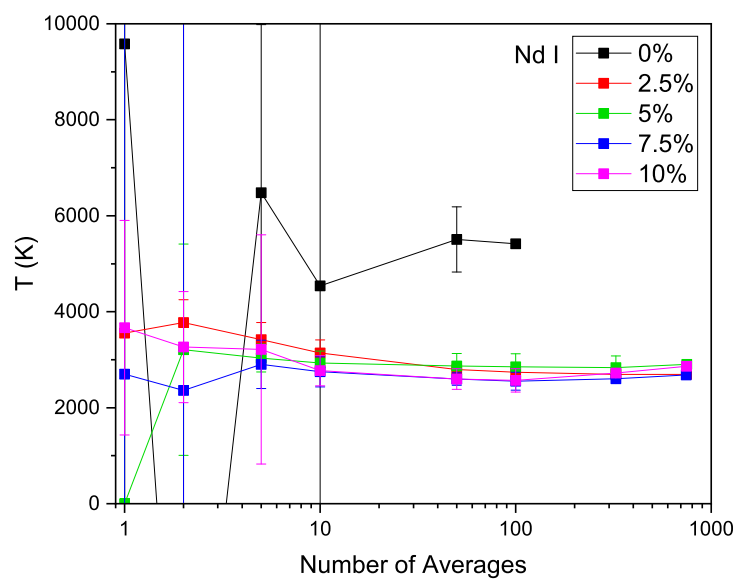


**Figure 5.18:** Determined excitation temperatures for Nd I for various sample concentrations as a function of averaging number.

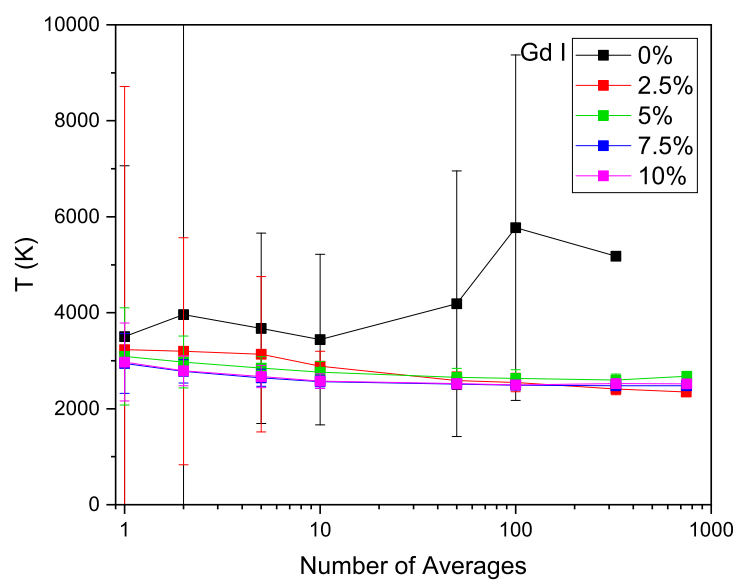


**Figure 5.19:** Determined excitation temperatures for Gd I for various sample concentrations as a function of averaging number.

be indirectly observed in the plots of total column density. Future studies may benefit from analyzing the fitted peak areas for many lines as a function of averaging number directly, similarly as to what was done for  $T$  and  $n_{tot}L$  here. To better understand the results, fitted peak areas should be plotted for each concentration as a function of the number of averages. Visualization of this data is challenging, however, because each fitted transition must be plotted for each concentration and number of averages, rather than a single value of  $T$  or  $n_{tot}L$ .

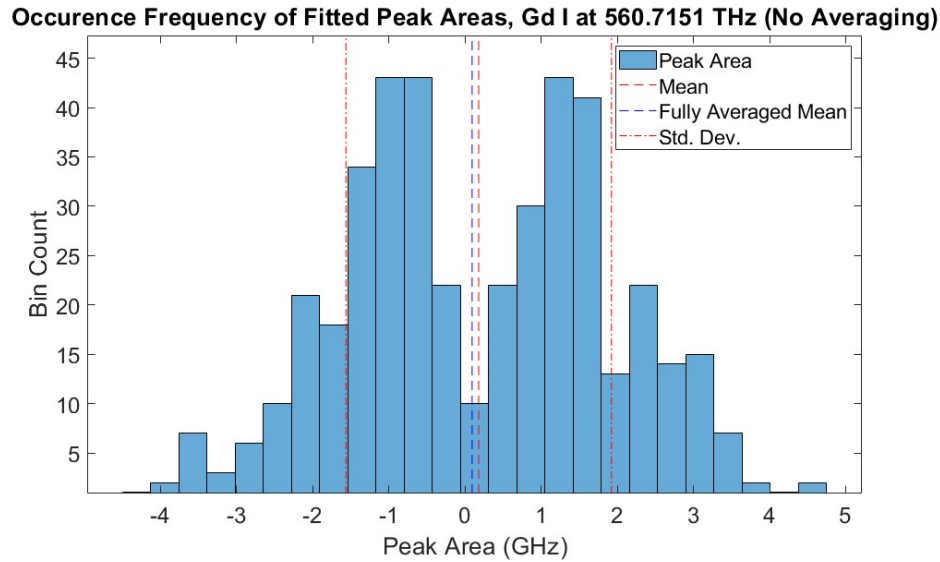


**Figure 5.20:** Histogram showing the distribution of fitted peak areas for the 560.7151 THz Gd I transition with 0% Gd sample concentration.

More work is needed to better understand the accuracy and precision of the DCS measurements within LPPs and their effect on Boltzmann-plot analysis results. Future studies may verify measurements using better-controlled systems, such as static cells, particularly if they contain known gas concentrations. The inclusion of a constant concentration element, as Fe was here, is useful as a check across all measurements. The primary issue for analyzing Fe I in this set of measurements is that only three transitions existed within the measurement bandwidth, all of which were excited-state transitions. These weight the analysis to hotter regions of the plume and are difficult to detect at later times when frequency resolution is improved. Avoidance of oxide formation would simplify understanding of the methodology, either by choosing less reactive species or better controlling the chamber environment.

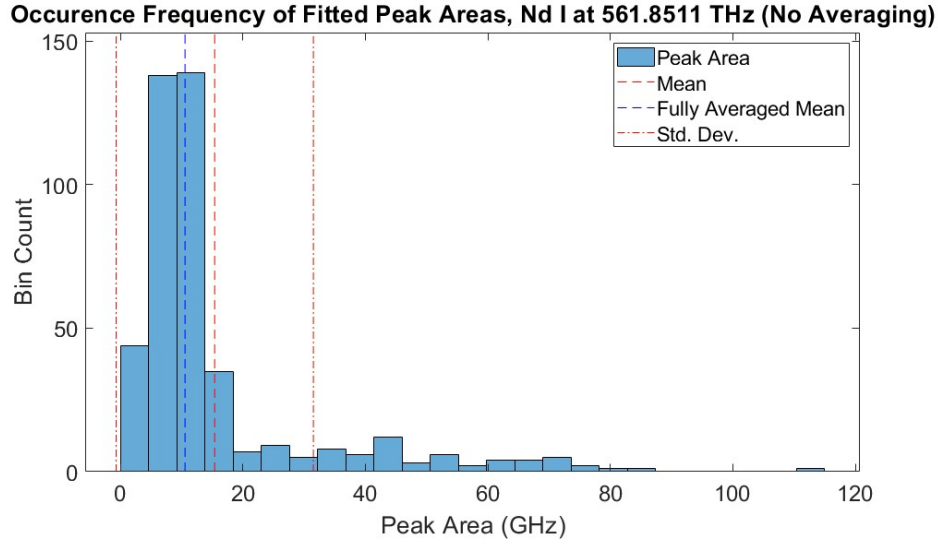


**Figure 5.21:** Histogram showing the distribution of fitted peak areas for the 561.8511 THz Nd I transition with 10% Nd sample concentration.

Lastly, experiments could be performed in parallel with LIBS and CW-LAS for comparison.

## 5.7 Summary and Conclusions

The presented work demonstrates a method using broadband, high-resolution dual-comb spectroscopy for time-resolved multispecies analysis of LPPs, with determination of excitation temperatures and column densities. Here, absorption spectra within a 5 nm spectral bandwidth were collected over seven time-delays from 30-250  $\mu\text{s}$  of a LPP generated by ablating an alloy containing Nd, Gd, and Fe. A high density of atomic absorption lines was probed, and 34 well-resolved peaks were used in Boltzmann plots for determination of excitation temperatures and column densities for the three atomic species. Nd I and Gd I excitation temperatures agreed within uncertainties at all time-delays and ranged from  $\sim 4000$  K at 31  $\mu\text{s}$  to  $\sim 2100$  K at 151  $\mu\text{s}$ . Line-of-sight averaging effects are known to cause differing apparent excitation temperatures in inhomogeneous LPPs, making the temperature agreement of Nd I and Gd I a point of note. The excitation temperatures determined for Fe I were higher but not unreasonable given measurement uncertainties and potential line-of-sight averaging effects. In particular, the Fe analysis included only three transitions in the Boltzmann plot, none with low initial state energies, which is expected to bias the apparent

excitation temperature toward higher values and is consistent with the experimental results. Determined column densities were comparable to previous studies, but the ratio of Gd I/Nd I was observed to vary in time. Elemental fractionation may explain mismatch between the density ratio determined for the LPP versus within the sample, and differences in formation rates of molecules could cause the LPP ratio to change in time. Oxide formation was shown to occur with trace amounts of oxygen in the case of a similar Ce-containing LPP, indicating that oxides may play a role in these alloy measurements as well.

Repeated measurements were analyzed to estimate the precisions for determination of excitation temperature and column density, and results showed precisions better than  $\pm 70$  K and  $\pm 2 \times 10^{13} \text{ cm}^{-2}$  for Nd and Gd. Accuracy values are difficult to define given the lack of a single excitation temperature and number density for an inhomogeneous LPP. A model of the spatial temperature and density distributions used for calculating line-of-sight averages would aid in quantification of accuracy and in linking the results to spatially resolved measurements made using other spectroscopic techniques.

A similar series of DCS measurements were also performed in which the concentrations of Nd and Gd were varied. Variation of measured excitation temperature was greater when the sample concentration was varied as compared to multiple measurements made on a single sample. This effect may be explained by slight differences in the measurement parameters between different samples, such as probing slightly different regions of the plume. A non-linear relationship was observed between sample concentration and measured total column density for Nd I and Gd I. To better understand the causes, the fitted peak areas were studied and observed to also vary nonlinearly with concentration. All values were the results of analysis on 750 averaged spectra. Results were then studied as a function of averaging size, and biases toward large total column densities were observed at low averaging numbers. When fitting transitions for species with 0% concentration, which should be equivalent to fitting noise, roughly Gaussian distributions of fitted peak areas were observed, indicating the cause is not due to noise effects. However, a high number of large peak area outliers were observed for strongly absorbing transitions, which skew the averages to high values. More analysis is needed to understand the fitting effects, as well as more controlled experiments better understand which effects are due to measurements of LPPs and their associated vari-



ations versus the measurement effects introduced by DCS. Such experiments may include measurement of previously known number densities and temperatures as well as parallel measurements with other techniques such as LIBS and CW-LAS.

Exploring and developing the abilities of DCS for multispecies analysis adds a new tool to the plasma diagnostic toolbox used to understand the physical and chemical processes of LPPs more fully. Determination of time-resolved excitation temperatures and quantitative column densities using the DCS absorption-based measurement significantly expands the capabilities for LPP diagnostics, especially for later time-delays where LIBS/emission becomes unfavorable. In addition, the DCS absorption measurement is not subject to effects of self-absorption and self-reversal, which often prevent quantitative measurements of low-lying energy levels in emission-based analysis. Demonstration of consistent excitation temperatures between different species is important both for verifying LTE approximations and for extending temperature measurements to other species for which not enough lines are measured to construct a Boltzmann plot. For example, if measurement of similar excitation temperatures can be shown to be reliable under certain conditions, then excitation temperatures may be assumed for one species based on determination from another measured simultaneously. However, spatial averaging effects and energy levels of the probed transitions must be considered carefully for these assumptions to be valid.

## Appendix A

### Multicolor DCS with Optical Pumping

The ability of DCS to perform spectroscopic measurements and analysis is improved by having a bandwidth which covers many wavelengths to probe many transitions. Many atomic and molecular transitions exist in the visible and IR, and some wavelength regions are difficult to access without nonlinear frequency-generating techniques (e.g., optical parametric oscillator cavities). Frequency combs are prime candidates for driving nonlinear frequency conversion due to the short, intense pulses, which can be used for second harmonic [29], high-harmonic [127], supercontinuum [39], and difference-frequency generation [128]. In studying LPPs, the accuracy of the Boltzmann-plot analyses is improved by including more transitions that cover a range of energies, as described in Ch. 5.

In this experiment, absorption of Rb within a LPP was detected using both the fundamental and second-harmonic light of the Er-DCS system described in Ch. 2. Figure A.1 shows how the fundamental 1550 nm light was used in a parallel setup to the 780 nm to probe the LPP simultaneously. The interferograms of the two frequency bands were made to probe the LPP at the same time-delay by adjusting the distance from the dichroic beamsplitter to the 1550 nm fiber coupler using a translation stage. This particular configuration utilized a double-pass arrangement of the LPP using a retro-reflecting mirror to make re-coupling into fiber more convenient. Note that a single filtering/detection setup can be used for measuring multiple wavelength regions if the optics and detectors are appropriately chosen. A mask, rather than a single slit, can be used to filter light of the wavelength regions to measure. Care must be taken, though, that the detected frequencies do not overlap in the RF domain. Here, the large difference between 780 nm and 1550 nm necessitated using separate setups that contained the appropriate optics and detectors for the two wavelength regions, e.g., Si

or InGaAs detectors. The DAQ read in the data from each beamline on separate channels to be recorded simultaneously.

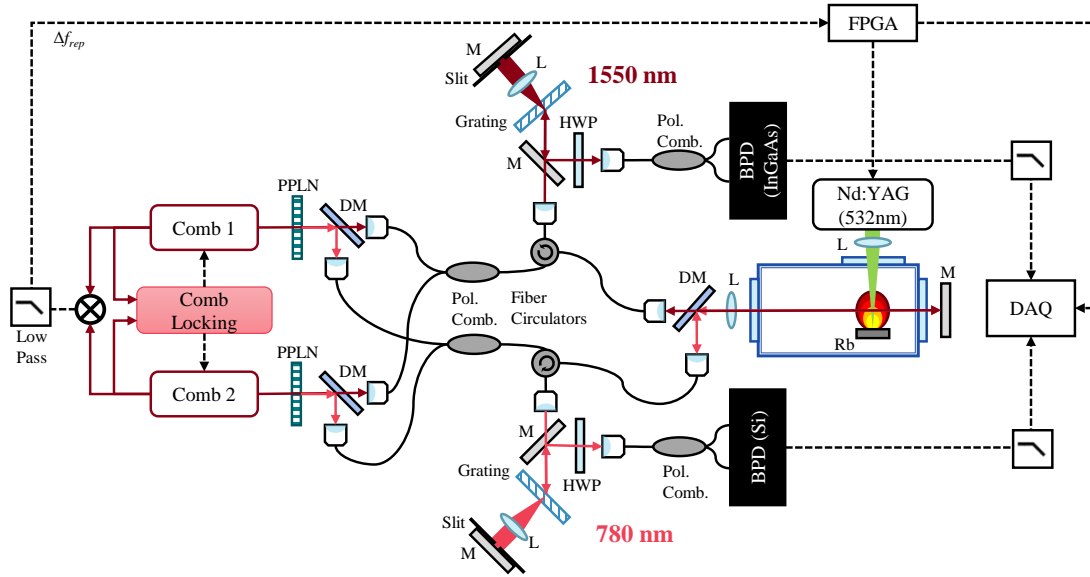


**Figure A.1:** Schematic showing the layout of the Er-DCS system used for probing a LPP with 780 nm and 1550 nm light simultaneously. PPLN: periodically-poled lithium niobate, DM: dichroic mirror, Pol. Comb.: fiber-based polarization combiner, M: mirror, L: lens, HWP: half-wave plate, BPD: balanced photodetector, FPGA: field-programmable gate array, DAQ: data-acquisition board.

The Rb transitions of interest were the D2 ground-state line ( $5^2S_{1/2}$  to  $5^2P_{3/2}$ ) at 780.03 nm and two transitions from the D2 upper state to  $4^2D_{5/2}$  and  $4^2D_{3/2}$  at 1528.89 nm and 1529.00 nm, respectively (Fig. A.2). A NIST glass sample (SRM610) containing 425 ppm of Rb was ablated and contained a high enough Rb concentration that the excited-state transitions were detectable at early times. The sample was ablated with 85 mJ, 532 nm pulses at 10 Hz while scanning at 0.08 mm/s and under 30 Torr of flowing  $N_2$ .

Absorption spectra at both wavelengths were recorded at 40, 80, 160, and 1200  $\mu s$  after ablation, and averages of 400 shots are shown in Fig. A.3. The two spectral regions were measured simultaneously at each time-delay. All spectra were processed with the same apodization window, resulting in an instrumental resolution of 7.6 GHz, except the 1200  $\mu s$  780 nm spectrum, which had a resolution of 0.24 GHz. This was done to allow direct

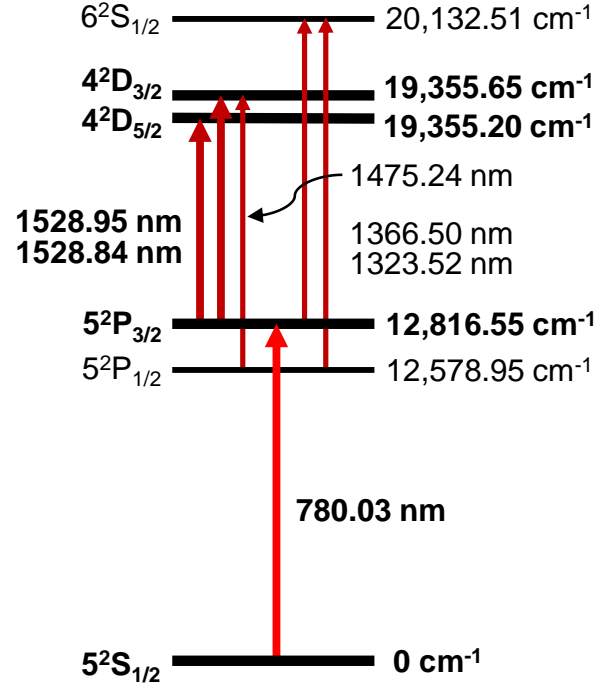


**Figure A.2:** Energy level diagram for Rb, showing the energy levels and transitions of interest in boldface. The other levels and transitions are other possible candidates for measurement.

comparison of the spectra while also demonstrating the higher resolution capability of the DCS system to resolve the hyperfine structure of the D2 line when measured at a late delay-time when a wide apodization window can be utilized [129, 130]. The absorbance strength of the 1530 nm lines diminishes in time due to these being excited-state transitions, which lose population as the LPP cools in time. Population fills the ground state as the LPP cools, so that the D2 line absorbance does not weaken much. Since excited-state transitions are populated only at early-times in the LPP, and only narrow apodization windows can be used at early times, it is difficult to measure such transitions with high frequency resolution (sub-GHz). However, forcing population to remain in the ground-state of an excited-state transition enables measurement at longer time-delays for better frequency resolution.

Optical pumping with a CW laser is one technique for placing population into an excited state by pumping the atoms up from a lower energy state. Here, by locking a 780 nm

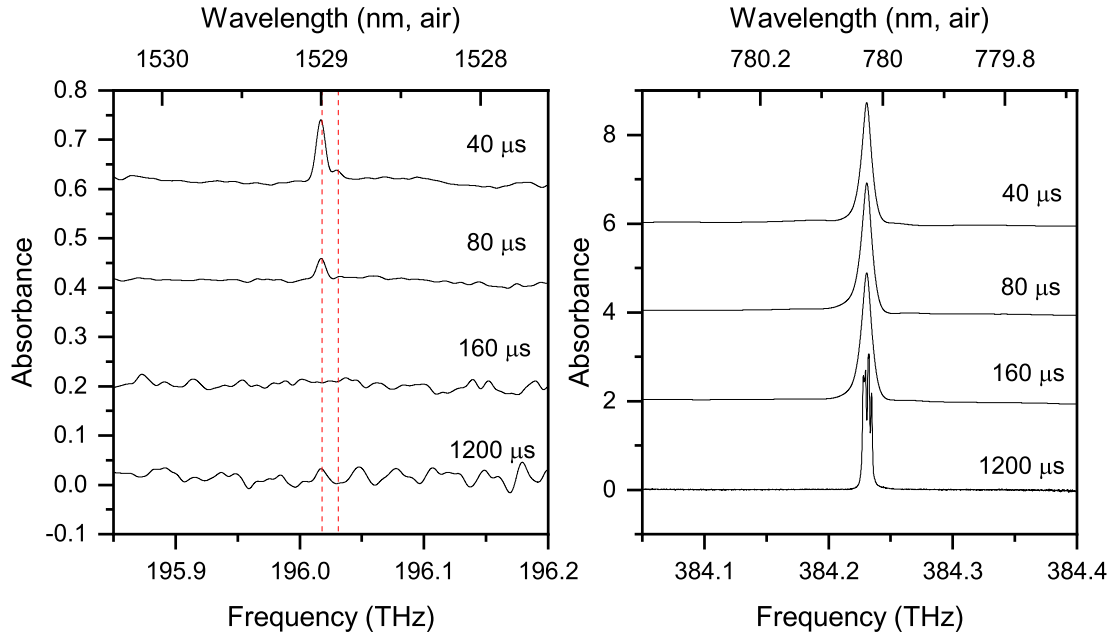


**Figure A.3:** Absorption spectra of three Rb transitions measured using the fundamental and second-harmonic of the Er-DCS. The dashed lines show the theoretical frequency location of the 1530 nm transitions.

laser to the D2 transition, sufficient population can be transferred into the lower state of the 1530 nm transitions to enable measurement via absorption. A DCS measurement of these lines was performed by Nishiyama et al. previously [131]. Here, the technique is used in a LPP to sustain the population in the excited state being probed out to longer times. Figure A.4 shows the optical layout used to pump the Rb atoms in the LPP. The pumping laser is locked to the D2 transition using a static Rb cell, and a portion of the beam is sent through the LPP colinearly with the DCS probe beam. In this setup, excited-state transitions originating from the upper state of the pumped transition can be detected for as long as a suitable number of atoms are within the beamlines, regardless of the plume temperature.

Figure A.5 shows the absorption spectrum of the two 1530 nm excited-state Rb transitions within a LPP measured by the DCS system with optical pumping of the D2 line. Here, a Rb-containing mica sample (lepidolite, concentration unknown, estimated to be  $\sim 3\%$  or

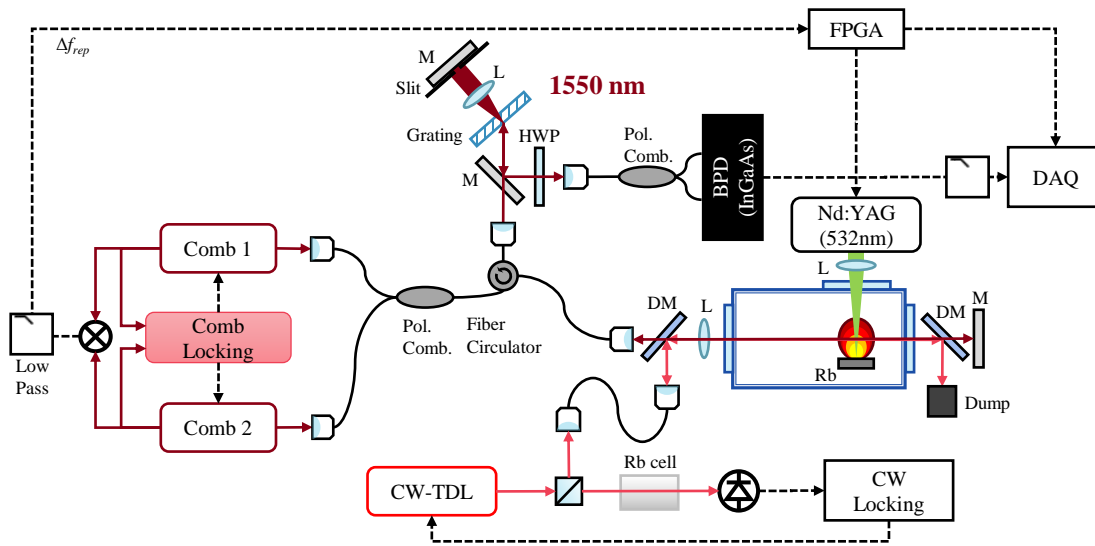


**Figure A.4:** Optical layout for pumping Rb atoms in a LPP with a CW laser locked to the D2 transition, allowing detection of excited state transitions by the Er-DCS system for longer times.

less Rb) was ablated to increase the total Rb number density since previous measurements had shown higher absorbance values for the D2 transition at similar time-delays. We do not ablate pure Rb as it is highly reactive with water in the atmosphere. The measured linewidth for the stronger line was  $\sim 0.67$  GHz, which was directly measured and does not include the instrumental lineshape broadening effect that would be accounted for in spectral fitting. The predicted Doppler-broadened linewidth at 2000 K is 0.679 GHz, and the pressure broadening is expected to be  $\sim 0.1$  GHz [132] at 2000 K under 30 Torr of  $N_2$ . The stronger transition has three allowed hyperfine components, whereas the weaker has two, with splittings of  $\sim 0.1$  GHz. Though these splittings should not be quite resolvable here, they will contribute to the effective linewidth reported without spectral fitting using a model that includes the hyperfine transitions. The side-peak feature on the stronger transition should not correspond to any hyperfine spacing, as it is over 2 GHz away from the main peak. The feature may be explained by isotopic shifting, but the isotopic shift values have not been found in the literature.

This experiment is interesting because the measured 1530 nm transitions should be Doppler-

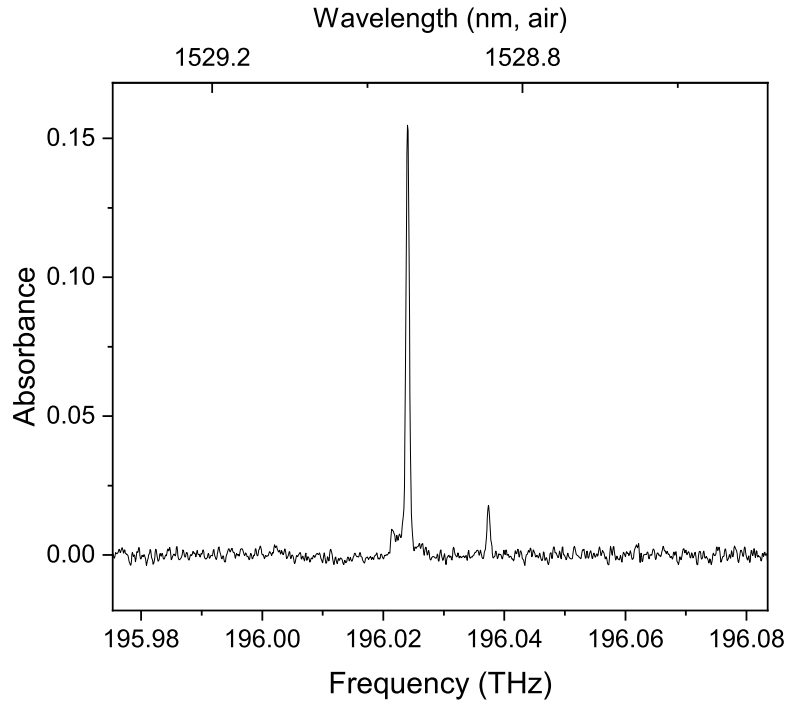


**Figure A.5:** DCS absorbance spectrum of the 1530 nm excited-state transitions of Rb, measured in a late-time LPP using optical pumping.

free, though the results here may not conclusively indicate so. If the linewidth of the pumping laser is narrower than the Doppler broadening of the D2 line, then the pumping laser interacts with only a subset of the velocity classes of the Rb atoms. As such, only a certain velocity class of atoms are pumped into excited-state of the D2 transition for the broadband comb to probe. With no other velocity classes present in the lower state of the 1530 nm transitions, no Doppler broadening is observed. Future work should focus on paying closer attention to which hyperfine transition the pumping laser is locked to and using spectral fitting to retrieve more accurate values for the measured linewidths. Use of an isotopically pure ablation sample would also make analysis more straightforward. Care must be taken to avoid effects related to power broadening, Autler-Townes splitting, and polarization effects described in [131]. Doppler-free measurements would aid in studies focused on measuring pressure broadening via the Lorentzian linewidths, as well as resolving closely-spaced transitions which would overlap with Doppler broadening. Figure A.2 shows just a few additional

Rb transitions which could be studied in the NIR to observe this effect.



## Appendix B

### Codes

In this appendix, details on the implementation in code of the mathematical methods discussed throughout the text are presented. The codes, which I fully developed, are too long for inclusion here and can be made available upon request. The figures presented here are the output from the codes. Though they are formatted for full-screen viewing on a computer monitor, they are shown here as they are generated to show the capabilities of the codes in preparing plots with automatic scaling and labels in addition to the content of the plots.

#### B.1 Signal Processing

For DCS-LPP data, interferograms which probe the LPP (signal) are recorded in conjunction with their preceding interferogram, which acts a reference since it came before ablation (see Sec. 1.3). In the saved dataset, then, the records are interleaved signal and reference data. The code `ref_and_sig_separator.m` separates the reference and signal records and saves them in separate files. Usually, the first record is a reference since there is a large time window between a signal interferogram and the next reference interferogram (due to the low duty-cycle of the ablation pulses) during which the recording may have started. In the case that recording began just after a reference interferogram, the dataset will begin with a signal record. Here, the first and last records must be discarded since they have no reference/signal partners, assuming an even total number of records. Rarely, a bug occurs in which the DAQ trigger fails, resulting in a single reference or signal record being skipped. This causes the signal/reference interleaving to be offset by one at the point of the skipped record. The user can indicate the skipped record number so the offset is accounted for. Otherwise, each sig-

nal/reference dataset will contain records of each type, switching over at the skipped record point.

The code `DCS_post_processing_code.m` handles most of the post-processing work, reading in time-domain interferogram data and producing averaged single-beam, transmittance, and absorbance spectra. The user specifies the location of the signal and, optionally, reference data, which can be read in from files of several formats. The user can specify a range of records to be used or individual records to exclude. For datasets too large for MATLAB, the user should use the code `dataset_breakup_code.m` to break the dataset into same-sized chunks which can be processed individually. The results of these can be averaged using the code `spectra_averaging.m`. The user must indicate details about the data, which are: the repetition rate of the probe comb, the difference between the repetition rates of the two combs, whether the DAQ was externally clocked and if not the internal clock frequency of the DAQ, the number of centerbursts in each record (useful for burst-mode DCS [32]), the estimated time between centerburst (useful for accurate centerburst finding), and if the experiment was on an ablation-generated LPP and if so the time-delay between ablation and the first centerburst. The time-axis is generated according to the sampling-clock frequency and record number of points.

The user can have the raw time-domain data plotted for viewing reference or to check the data. In the case of multiple-record datasets, a “click-plot” is generated, in which the user uses the keyboard or mouse to progress forward or backward through plots of each record. This can be useful for determining when there exists a noise spike that occurred when the ablation laser fired. The user can define a time range to be removed from the data to remove the spike. A voltage noise floor bias other than zero may also be observed. The bias can be removed by subtracting the mean of the time-domain data from itself. Plots showing the data with ablation-spike and voltage-bias removed can be generated.

Preparation of the time-window is accomplished by determining the times of the centerbursts and parsing the data before and after. The code can handle multiple centerbursts, as is the case in burst-mode DCS, as well as apply window parsing to reference data. Consequently, less care is required in preparing the reference and signal data acquisition windows during the experiment so that they are identical since they can be parsed to match

in post-processing. The MATLAB function `findpeaks` is used to determine the maximum of every centerburst in each record and its corresponding time. As an aid, the number, prominence, and estimated time between centerbursts are utilized. The user can plot the results of the peak finding function to check that all (and only) centerbursts are accurately found. Processed time-windows are then parsed out of the raw data, which include data some user-specified time before and after the centerbursts. Time-windows asymmetric about the centerburst can be utilized, though the Mertz phase correction applied after Fourier transform is not intended for asymmetric windows.

The difference between the comb repetition rates,  $\Delta f_{rep}$ , can be calculated and plotted as a function of time. In the case of non-ablation data that lack interleaved reference interferograms, the difference frequency for record  $i$  is given by

$$\Delta f_{rep,i} = \frac{1}{2} \left( \frac{1}{t_{i+1} - t_i} + \frac{1}{t_i - t_{i-1}} \right) \quad (\text{B.1})$$

for centerburst-maximum time  $t_i$ . For the first and final records out of  $n$  total,

$$\Delta f_{rep,1} = \frac{1}{t_2 - t_1} \quad (\text{B.2})$$

and

$$\Delta f_{rep,n} = \frac{1}{t_n - t_{n-1}}. \quad (\text{B.3})$$

The time-record must not be reset between records for the calculations to apply. In the case of ablation data in which each signal interferogram *sig* has a paired reference *ref* recorded immediately before,

$$\Delta f_{rep,i} = \frac{1}{t_{sig,i} - t_{ref,i}}. \quad (\text{B.4})$$

$\Delta f_{rep}(i)$  can be plotted to show the mean, standard deviation, and range (Fig. B.1).

For the case of multiple records, the data can be averaged in the time or frequency domains (see Sec. 1.4.4 for a discussion of the two methods). The code is equipped to perform time-domain alignment of the interferograms either utilizing the MATLAB `finddelay` function or cross-correlations to aid time-domain averaging. Frequency-domain averaging is recommended with use of the Mertz phase correction (Sec. 1.4.4).

Next, the time-window can be apodized and zero-padded. The code can apply Blackman, Blackman-Harris, Hamming, Hanning, flat-top-weighted, weak, medium, and strong Norton-Beer, and Happ-Genzel apodization windows, as well as none (rectangular, or same as multiplying by 1s) (Fig. 1.5). The apodization windows are generated over the parsed time-axis and then multiply the data. Padding the data with zeros simply appends a user-defined number of zeros to both ends of the time-domain data. The effect of zero-padding is discussed in Sec. 1.4.4.

Before Fourier transform, narrow time-window data for Mertz phase correction and, optionally, pseudo-reference, are acquired (see Sec. 1.4.4). The Mertz time-domain data are obtained by multiplying the full data with a rectangular function consisting of 1s centered about the centerburst maximum with a width defined by the user (10 points is often used for DCS-LPP experiments). The pseudo-reference time-domain data are acquired in the same way but with a wider width of 1s as also defined by the user. The final processed time-domain datasets  $V_{sig,ref}(t)$  can then be plotted for viewing just before Fourier transform.

The frequency axis, in the natively detected RF units, is generated with the same number of points as the time-domain data, extending from negative to positive values of one-half of the inverse of the time step-size  $\Delta t$ . The axis can be converted to optical frequencies (uncalibrated, centered about 0 Hz) by multiplying by  $f_{rep}/\Delta f_{rep}$  (Eq. 1.1). The fast Fourier transform (FFT) of each time-domain record, both signal and reference, is then calculated using the MATLAB `fft` function. Note that the functions `fftshift` and `ifftshift` must be employed to deal with the way MATLAB handles FFTs about 0. Specifically, the full and properly scaled FFT is calculated as

$$\hat{f}'_{sig,ref}(\nu) = \frac{\Delta t}{\sqrt{2\pi}} \text{fftshift}(\text{fft}(\text{ifftshift}(V_{sig,ref}(t)))). \quad (\text{B.5})$$

The unwrapped phase of the FFT of the Mertz time-window data is also calculated. The final single-beam spectra  $SBS_{sig,ref}(\nu)$  are calculated according to the Mertz phase correction in Eq. 1.11. Note that the original interferogram is reproduced by

$$V_{sig,ref}(t) = \frac{\sqrt{2\pi}}{\Delta t} \text{fftshift}(\text{ifft}(\text{ifftshift}(\hat{f}'_{sig,ref}(\nu)))). \quad (\text{B.6})$$

The transmittance spectrum is calculated using the frequency averaged signal and reference SBS according to Eq. 1.12. However, the code is capable of dividing single-shot reference and signal spectra and then averaging over single-shot transmittance functions if desired. Before averaging, the user has the option to limit the maximum absorbance by removing data points in the signal SBS within the optical window that have values less than the noise floor RMS times a user-defined factor. Limiting is performed on the SBS where the linearity of Beer's Law is still maintained before the calculation of absorbance. The purpose is to improve absorbance lineshape fitting by removing the problematic upper regions of strongly absorbing lines. In the case of time-domain averaging, the user may choose to shift the noise floor to 0 by subtracting the mean of the original noise floor. In all cases, values less than 0 in the transmittance function  $T(\nu)$  are replaced with NaNs to prevent obtaining a complex absorbance function, which is given by Eq. 1.13.

The final portion of the code is dedicated to saving and plotting the post-processed data. The apodization window, frequency axis, averaged and unaveraged SBS, transmittance, and absorption matrices are all saved to a user-defined folder. The code can generate plots of SBS, transmittance, and absorbance (Figs. B.2-B.4). Plots include a text annotation which includes many of the data parameters and post-processing options for record-keeping. Save filenames, plot labels, and plot scaling are automatically generated by the code.

To determine the instrumental/effective resolution ( $\delta f_{meas} = \delta f_{inst}$ , see Sec. 1.4.2), defined as the FWHM of the ILF which is the Fourier transform of the apodization window, the user should use the code `apodization_window_modeller.m`. The inputs are largely the same as the post-processing code, and the code builds the same apodization window and takes the Fourier transform to obtain the ILF. The width-reference tool of the `findpeaks` MATLAB function is used to determine the instrumental resolution. The user should set the peak-height-minimum of the `findpeaks` function in the code inputs to ensure that the main lobe of the ILF is measured rather than a side lobe. The apodization window and ILF can be plotted and saved (Figs. B.5 and B.6).

The code `THz_calibration_fitting_code.m` is used to apply the final post-processing steps to the absorption spectrum. The code is designed to process spectra from multiple time-delays of an LPP experiment and can handle multiple spectra at once. The spectral frequency axis in

optical units has calibrated spacings but requires an absolute shift ( $f_{offset}$  in Eq. 1.1) for true calibration. The user can input this calibration, but the code is equipped to determine the necessary calibration. The user gives a rough calibration, usually 100s of THz and determined based on knowledge of the frequencies that were roughly measured, often determined using an optical spectrum analyzer. The code loads in transition database files supplied by the user, chosen based on what species were measured, and attempts to align the peak locations of the spectrum to the database transition locations. This is achieved by minimizing the sum of the differences between the database transition frequencies and the calibrated absorption spectrum peak frequencies. The user controls the peak-finding parameters and initial-guess calibration to aid the optimization. Since the spectra are double-sided, symmetric about 0 with negative and positive frequency values, the user must determine which side has the correct orientation.

A newer code can be used as a better alternative for calibrating spectra. The code `DCSlocking_model.m` builds a simple model of the two frequency combs and calculates the measured frequency for a feature at any optical frequency. The primary CW locking laser is used as the reference point for calculating the comb teeth frequencies, so the accuracy of the calibration relies on how well the CW wavelength is known. The user provides this wavelength, the repetition rate of one comb, the repetition rate difference, and the lock frequencies for the two locks between the CW laser and each comb. The relative signs of these values are crucial. The comb teeth locations can be plotted using stem plots for visualization. The user can enter any frequency, and the code will calculate the beatnote frequency between the two closest comb teeth to that frequency. By supplying a frequency corresponding to a target optical transition, the user can determine the expected RF and uncalibrated optical frequencies at which this transition would be measured by the dual-comb spectrometer. The absolute calibration of the DCS spectra ( $f_{offset}$ ), then, is the frequency of the target transition minus the DCS-measured frequency (in relative optical units, i.e., the measured RF frequency multiplied by  $f_{rep}/\Delta f_{rep}$ ). The user is encouraged to use multiple target transitions and verify the alignment of the calibrated experimental data with the known transition frequencies.

The code `DCSlocking_model_drift.m` builds on the previous code, adding in the capability

of predicting the effects of drift in the repetition rate and difference frequency. The user additionally supplies a  $\pm$  change in these two values, which can be measured by several means, e.g., utilizing the  $\Delta f_{rep}$  calculator in the main post-processing code. Comb models are built for each case, the measured frequencies for a target transition calculated, and then the differences between these measured frequencies reported. With this code, the user can predict how much a measured transition's frequency will fluctuate due to  $f_{rep}$  and  $\Delta f_{rep}$  drift under specific comb-locking conditions.

Once the spectra are calibrated, the user can define the bounds of the optical region of interest to reduce the original double-sided spectrum which often contains large regions of only noise. Any broad y-axis offsets between the optical windows of the signal and reference SBS will result in a non-zero baseline. The code can fit an  $n^{\text{th}}$  degree polynomial to the non-zero baseline and subtract it from spectrum. Before fitting, the findpeaks function is used to detect absorption features, whose values are replaced with nearby baseline values. Otherwise, absorption peaks would skew the fitting to greater values around absorption features. The final absorbance spectrum is saved for use in the spectral fitting code described in Sec. B.3 (Fig. B.7).

Within the same code, the final absorbance spectrum can be plotted against an absorption spectrum model for convenience (Fig. B.8). The user controls the parameters of the model as described in Sec. B.2. Lastly, the code can calculate the peak heights, FWHM linewidths, and integrated areas for absorption features in the spectrum (Fig. B.9). This capability is included for convenience of rough measurements, but spectral fitting should be applied to accurately determine lineshape component linewidths and peak areas to account for ILF broadening and overlapping absorption features.

## B.2 Absorption Spectra Modelling

In `absorption_spectra_modelling.m`, the user provides transition information files for each species to be modelled. The code requires names for each species file for the purpose of labelling. Each file is intended to be a different atomic species, but the user could use separate files for transition information from different sources for a single species and provide labels accordingly to differentiate lines within the modelled spectrum. The provided files must

contain a list of transitions, with the upper and lower energies of the levels of each transition (in  $\text{cm}^{-1}$ ), the degeneracy values  $J$  for those levels, and each transition's associated  $\log(gf)$  value. The user indicates in the code inputs which columns are associated with these values for each file.

A file containing the partition function  $Z(T)$  for each species is also required. This file contains the coefficients of an  $n^{\text{th}}$  degree polynomial fitted to the partition function. The code `partition_function.m` calculates  $Z(T)$  for a species and saves the fitted polynomial coefficients. The user must provide a database file containing the energies (in  $\text{cm}^{-1}$ ) and degeneracies  $g$  of all energy levels of the species. This information can be downloaded from the NIST online database [52]. The user indicates the columns within the file containing the necessary information, as well as the minimum and maximum temperature values for calculating  $Z(T)$ , the number of points to be calculated over (temperature step-size), and degree  $n$  of the fitting polynomial. Good starting values are 100 to 20,000 K, 19,900 points, and  $n = 20$ . The code plots  $Z(T)$  as well as the fitted polynomial and saves the polynomial coefficients and plot to a user-defined folder. Figure B.10 shows the partition function for Gd I with the 20<sup>th</sup> degree fitted polynomial.

The frequency axis over which the spectrum is modelled can be generated based on minimum and maximum values and step-size, or an axis file can be loaded in so that a spectrum can be modelled over the same points as any experimental data. The spectrum, however, is modelled over a larger range than this, with the user defining some axis value to pad on either end, such as 1 THz. This is so that transitions just outside the frequency window of interest are also modelled so that absorption in their wings are included in the final spectrum.

The code requests whether various parameters should be "forced" to be the same, a phrase referring to whether a model being fit to experimental data should force a parameter, e.g., kinetic temperature, to be constant over various species. Here, it is used to designate whether all species are to be modelled using a single value for each parameter or if each species will have different user-defined values. For instance, the user could designate Fe I, Gd I, and Nd I be modelled at 4000, 5000, and 6000 K, respectively, or all simply modelled at 5000 K. The user must then give the model parameters for excitation temperature, kinetic temperature (which indicates Gaussian width), Lorentzian width, total number density, and absorbance



baseline, as well as providing the atomic mass for each species in kg. The modelled spectrum, which can be automatically saved to a file, can be plotted in frequency or wavelength, both in vacuum and air. The user has the option to label the absorption lines with peak values greater than a specified amount with their species and lower-level energy for easy identification. An example modelled spectrum is shown in Fig. B.11.

After some preliminary setup, the input parameters are passed to two nested functions which calculate the absorption spectrum. The outer function (`absorption_spectra_modelling_function_multi_element_wrapper.m`) takes the full input parameter set input for all species and breaks them up per species to be passed to the inner function (`absorption_spectra_modelling_function_single_element.m`), which calculates the absorption spectrum on a per species basis. The outer function holds each single-species spectra as the inner function generates them, summing them together at the end. The outer function also includes the ILF broadening effect if the user chooses to. In theory, this is done by convolving the transmittance spectrum with the ILF, which is the Fourier transform of the apodization window applied in the time domain (a rectangular function if the experimental time-domain data are not apodized). It is important that the convolution be calculated with the transmittance spectra as this is where the ILF broadening occurs in practice, and the effect is nonlinear in absorbance as given by  $T(\nu) = e^{-A(\nu)}$  (see Sec. 1.4.2). The most notable effect is the shortening of strong absorbance features. However, it is computationally cheaper to inverse Fourier transform the modelled transmittance spectrum and multiply it by the time-domain apodization window then Fourier transform back to frequency to obtain the convolved spectrum. It is important that the number of points and point spacing of the spectrum and apodization window match. Since building an appropriate apodization window has several pitfalls, the code requires the user to load an apodization window used in processing experimental data along with the experimental frequency axis which is used for the model's axis. It is important for the calculation to include zero-padding and the symmetry about 0 in the Fourier transform process, as these change the total number of points.

The inner function calculates the absorption spectrum for a single species given level energies, level degeneracies, oscillator strengths, species mass, and sample length. The calculation steps follow the theory given in Sec. 3.1. The Faddeeva function  $w(z)$  (Eq. 3.2)

is utilized as a function `fadf.m` downloaded from the MathWorks file exchange [133]. Absorbance functions for each transition are calculated separately and then summed together for a final single-species spectrum.

### B.3 Spectral Fitting

Calculating all dipole-allowed transitions within the measurement bandwidth is a key step in a thorough spectral fitting. The code `transition_calculator.m` calculates these transition frequencies as  $\nu = c(E_f - E_i)$ , for speed of light  $c$  and state energies in  $\text{cm}^{-1}$ , between states of differing parity that obey the selection rule  $\Delta J = 0, \pm 1$ . The code `transition_calculator_MkII.m` has the additional capability to calculate only transitions which originate or terminate in specific user-defined electronic states. It is possible for there to be hundreds of dipole-allowed transitions, and fitting over so many may be prohibitively expensive, particularly since calculated lines lack their corresponding oscillator strengths found in the literature and used for a Boltzmann-plot analysis. It is desirable to use the code `transition_database_filterer.m` to filter the transitions of one database according to those listed in another. For example, a database of all dipole-allowed transitions can be filtered to only include transitions within a certain frequency range of each transition of a literature-based database. Thus, any transitions nearby to transitions with known oscillator strengths (which are used in analysis) are included for better fitting, while all others are excluded to reduce the computational workload.

The fitting code, `area_fitting_routine.m`, requires the user to load the calibrated frequency axis and absorbance values by specifying their file locations; these are appropriately saved by the post-processing codes. Transition database files are also uploaded, which require, for each transition, the center frequency, lower-level energy, lower-level degeneracy, oscillator strength as  $\log(gf)$ , and the relative uncertainty in  $\log(gf)$ . Note that this final parameter is not necessary for fitting, but is tracked with each transition for convenient bookkeeping; values of NaNs can be used. Multiple database files can be uploaded, and the user specifies their names and the species to which they correspond. It is possible to upload multiple database files for one species as well so the user can distinguish between different transition sources, such as multiple online databases, literature sources, and self-calculated dipole-

allowed transitions which may not be listed in the literature.

The user is given the option to set a maximum on the lower-level energy of the transitions to be fit. This is included so that transitions with much too high energies, given the experimental conditions, are excluded and not erroneously fit. For a LPP at late times, a limit of  $E_i \leq 15,000 \text{ cm}^{-1}$  was often used. A frequency range can be indicated by the user over which to perform the fit to exclude any areas that are not of interest. An apodization window can also be uploaded, which is saved appropriately by the post-processing codes, so that ILF effects can be modelled and accounted for.

A proper initial guess of the fitting parameters is required. The user inputs these values and has the option of plotting the initial guess model with the experimental data to manually adjust the initial guess to achieve a relatively close match. For the fitting process, the user indicates bounds for the parameters, which aid in achieving a good fit as well as the window size around each transition to fit. The entire experimental spectrum is not fit but rather only regions around absorption peaks so that large regions void of fitting transitions do not erroneously affect the fit. The user can also indicate that absorption lines of at least a certain strength be labelled with its element, database, and lower-level energy for convenient identification.

The trust-region-reflective algorithm is used for fitting in MATLAB, utilizing the `lsqcurvefit` function. The Levenberg-Marquardt algorithm is often used for spectral fits, but MATLAB does not offer parameter bounding for this algorithm. The fitting algorithm generates models with new parameters iteratively and requires that the modelling code be defined as a callable function. The modelling code consists of two nested functions. The first function (`area_fitting_freq_parse_wrapper.m`) serves to pass the parameters to the base modelling code (`area_modelling_function.m`), receive the model, and then select out the portions of the model corresponding to transitions being fit using a frequency index key. This step is necessary since it is easier to model the spectrum over the full range rather than with spectral gaps but only the absorption lines of interest are to be fit.

The base modelling function builds Voigt lineshapes at each transition center-frequency plus the center-frequency offset. The offset is one of the fit parameters and is important for mitigating a poor fit that can be caused by an imperfect frequency calibration. The Voigt

lineshapes are calculated using the input Gaussian and Lorentzian width parameters along with the Faddeeva function, described in Sec. 3.1. Each Voigt lineshape is then scaled by each transition's peak area parameter. All lineshapes are summed together and the baseline offset is added. ILF broadening is included by the same method described in Sec. 3.2. Once the fitting is complete, the fitted parameters are saved to a text file, and a fit report is generated with input parameters and fit controls as well as goodness of fit data for record-keeping. A figure showing the experimental data with the overlaid fitted model and residuals is plotted and saved, such as the one shown in Fig. B.12. Figure B.13 shows a zoomed-in portion of Fig. B.12 to show detail and fit agreement. All labels and filenames are generated automatically based on the data and user inputs.

Note that a common error that can occur is that some variable is of an incorrect size. Often the cause is that the uploaded frequency axis or absorbance data (X or Y data) are row vectors rather than column vectors, which may occur if the data was acquired without the use of the previously discussed `THz_calibration_fitting_code.m`. A simple matrix transposition can solve this error.

## B.4 Boltzmann-Plot Analysis

The Boltzmann-plot code `Boltzmann.m` reads in the peak areas for each transition as calculated and saved by the spectral fitting code, then generates the Boltzmann plot according to the theory presented in Sec. 3.3. The code can function over multiple species, generating Boltzmann plots for each. The plots are linearly fit using the MATLAB `polyfit` function, and  $n_{tot}L$  and  $T$  and their uncertainties are calculated based on the y-intercept and slope, respectively, all according to the theory presented in Sec. 3.3. The Boltzmann plots are generated and saved (Fig. B.14) as well as text files containing all the relevant and calculated information. The code has the capability to exclude transitions from the analysis based on if 1.) the peak area is less than a user-defined value or 2.) the peak area uncertainty is greater than the peak area multiplied by a user-defined factor. The user can also manually specify transitions to be excluded by simply entering a list of the transition frequencies (in THz, with four decimal places) to exclude. These exclusions can be performed in addition to the automatic exclusions listed above, which can be enable or disabled independently.

A second code, `Boltzmann_time_series.m`, loads in the Boltzmann-plot analysis results from across multiple time delays to plot  $n_{tot}L$  and  $T$  as a function of time. Example plots are shown in Figs. [B.15](#) and [B.16](#).

## B.5 Averaging-Size Looping Variations

A set of codes was written to handle analysis of data utilizing multiple averaging sizes. These codes are variations of the above codes, roughly performing the same functions while looping over the various averaging sizes. The code `area_fitting_routine_avgs.m` performs spectral fits, reading in the unaveraged SBS spectra from the main DCS data-processing code and averaging them according to the number of user-specified number of averages. For example, the user can specify an averaging number of 5, and given 100 unaveraged shots, the data will be averaged in bins of 5, resulting in 20 SBS which are used to calculate absorbance. Note that the code `DCS_post_processing_averaging_plotter.m` also performs these averaging functions and can create movies that show SBS, transmittance, and absorbance plots as a function of shot number for various averaging sizes. The power of the spectral fitting code lies in the ability to define multiple averaging sizes, all of which are processed and their spectra fit in a single run. Calibration and baseline subtraction are also performed post-averaging. As such, the processing/total fitting times can be much longer ( $\sim$ hours), particularly if an averaging size of 1 (single-shot data) is included. For averaging numbers which give more than 1 averaging bin (more than 1 averaged spectrum), means and standard deviations are calculated for all fit parameters and statistics. A separate code (`Boltzmann_analysis_avgs.m`) reads in the various fitting results and performs the Boltzmann-plot analyses on each of the fits. `PeakAreaVSConcPlotter.m` plots fitted peak area as a function of sample concentration for all transitions (similar to Fig. [5.15](#)). Similarly, `PeakAreaHistogramsPlotter.m` generates histograms to show the distribution of fitted peak areas for all transitions (Figs. [5.20](#) and [5.21](#)).

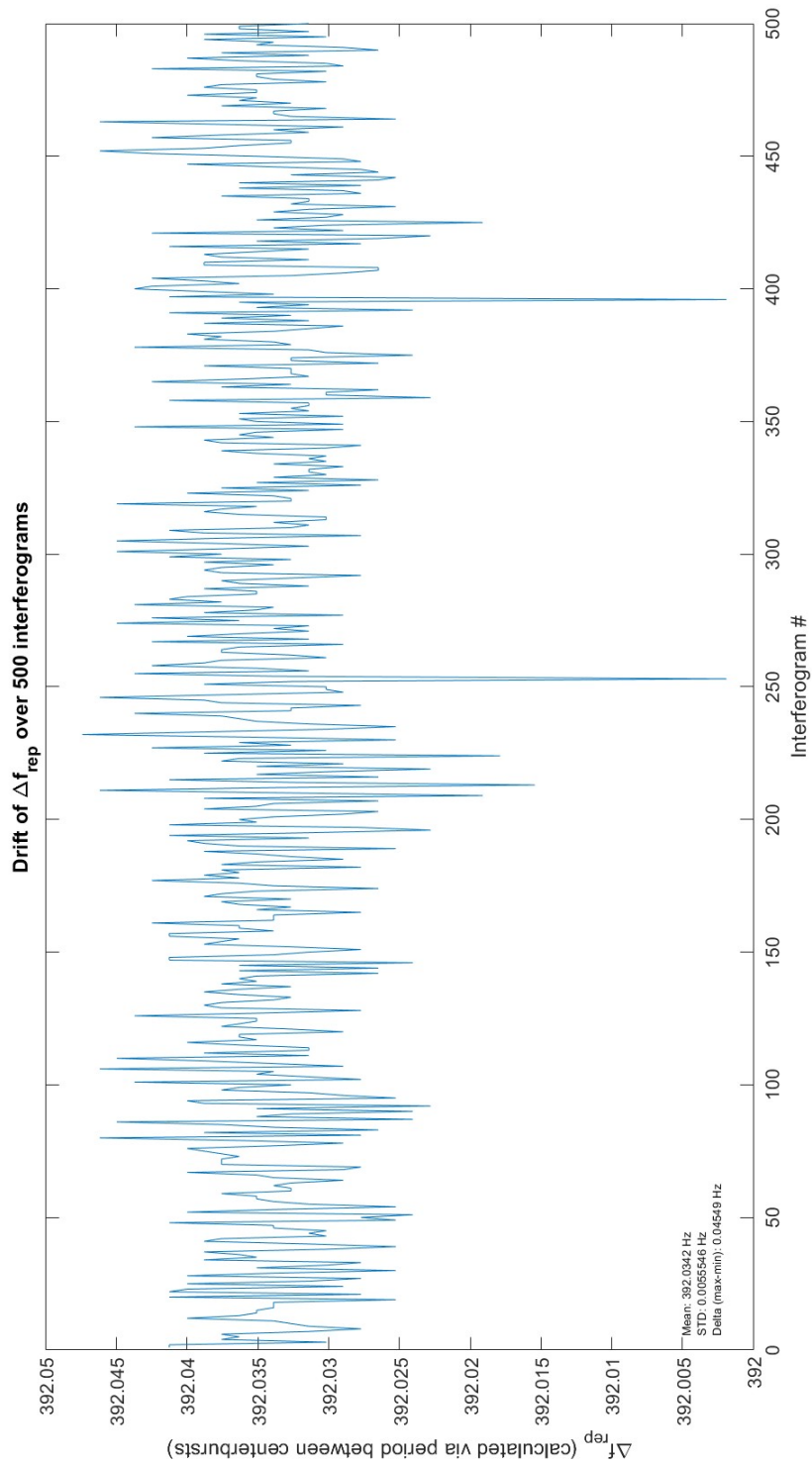


**Figure B.1:** Example of calculated  $\Delta f_{\text{rep}}(i)$  with statistics listed in the annotation.

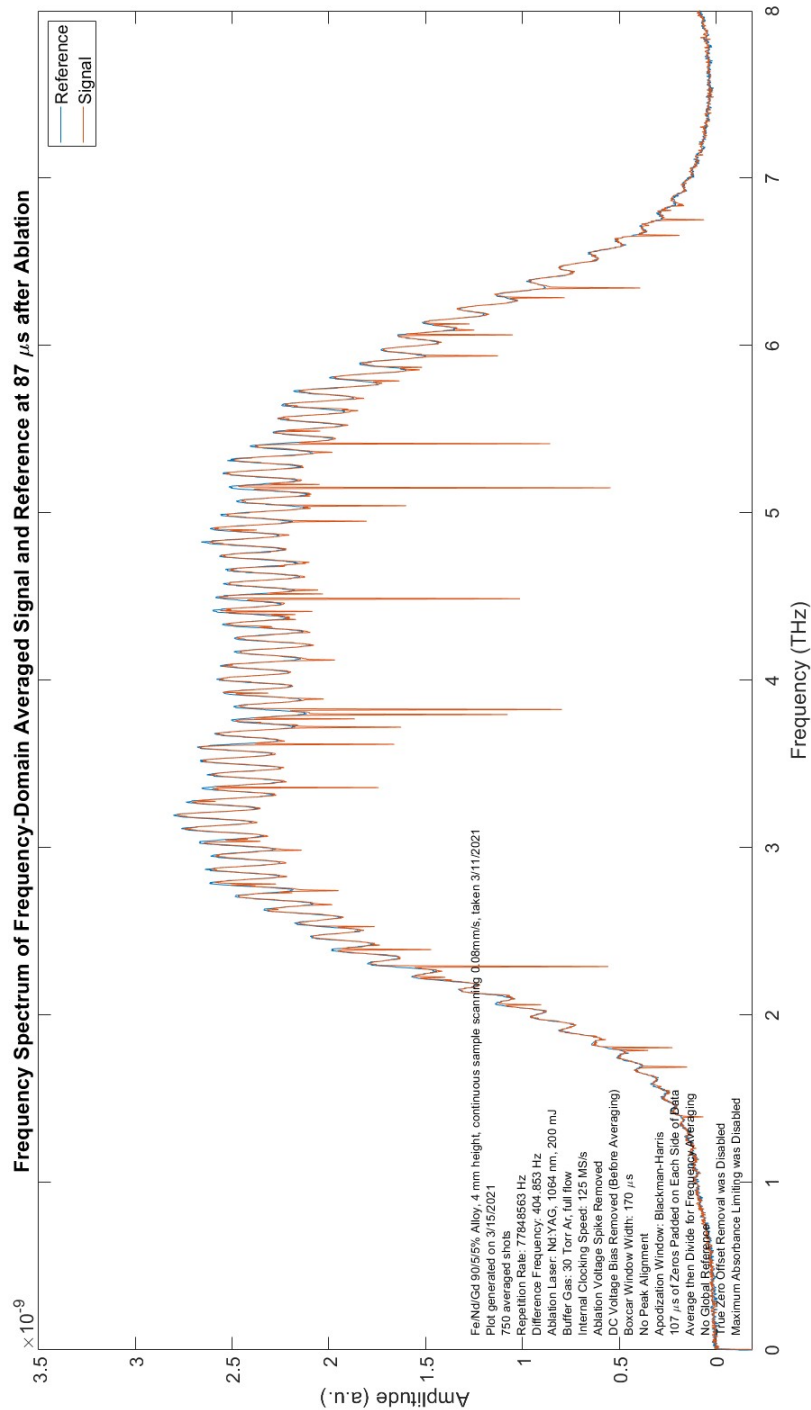


**Figure B.2:** Example SBS for both signal and reference of a DCS-LPP experiment. Both are Mertz phase-corrected by their own low-passed phase information.

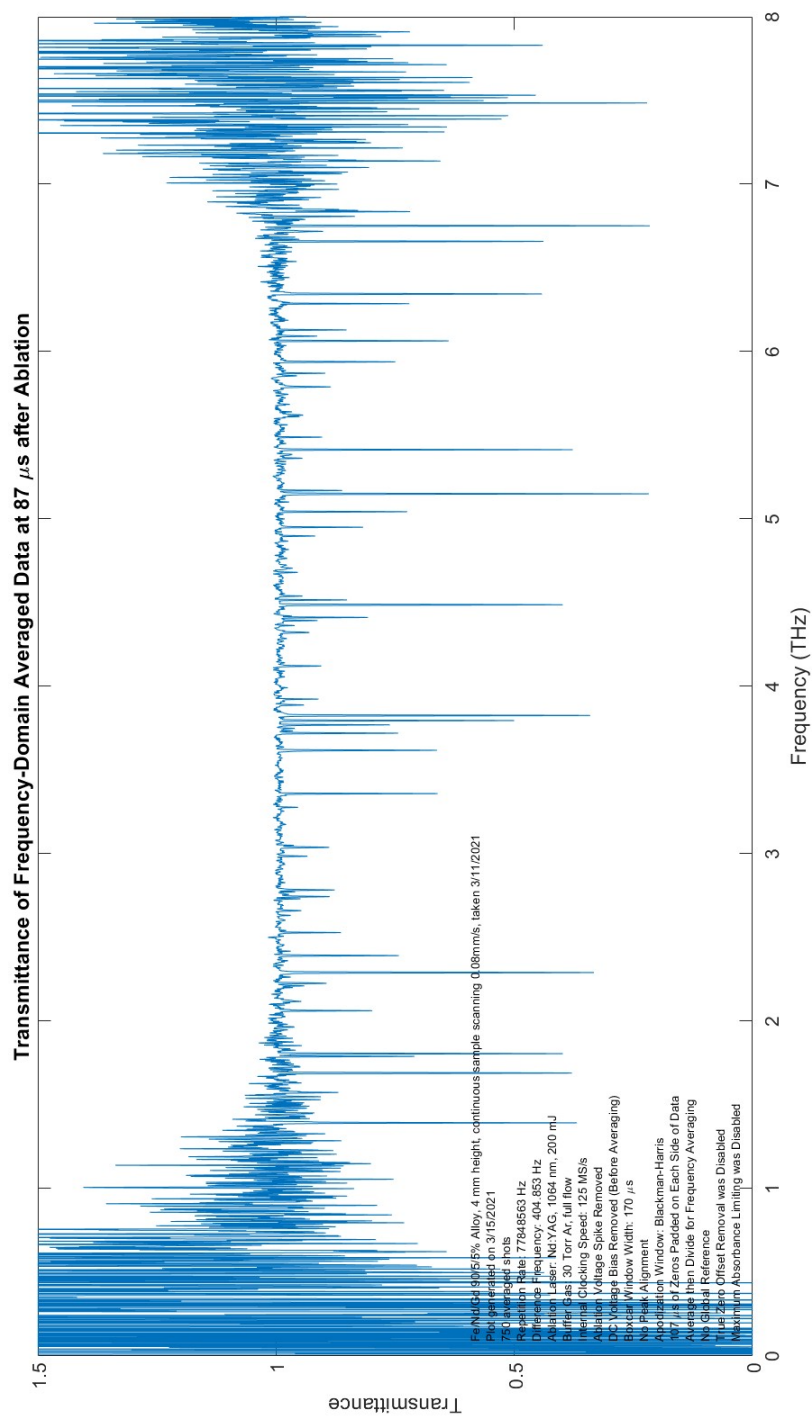


**Figure B.3:** Example transmittance function.



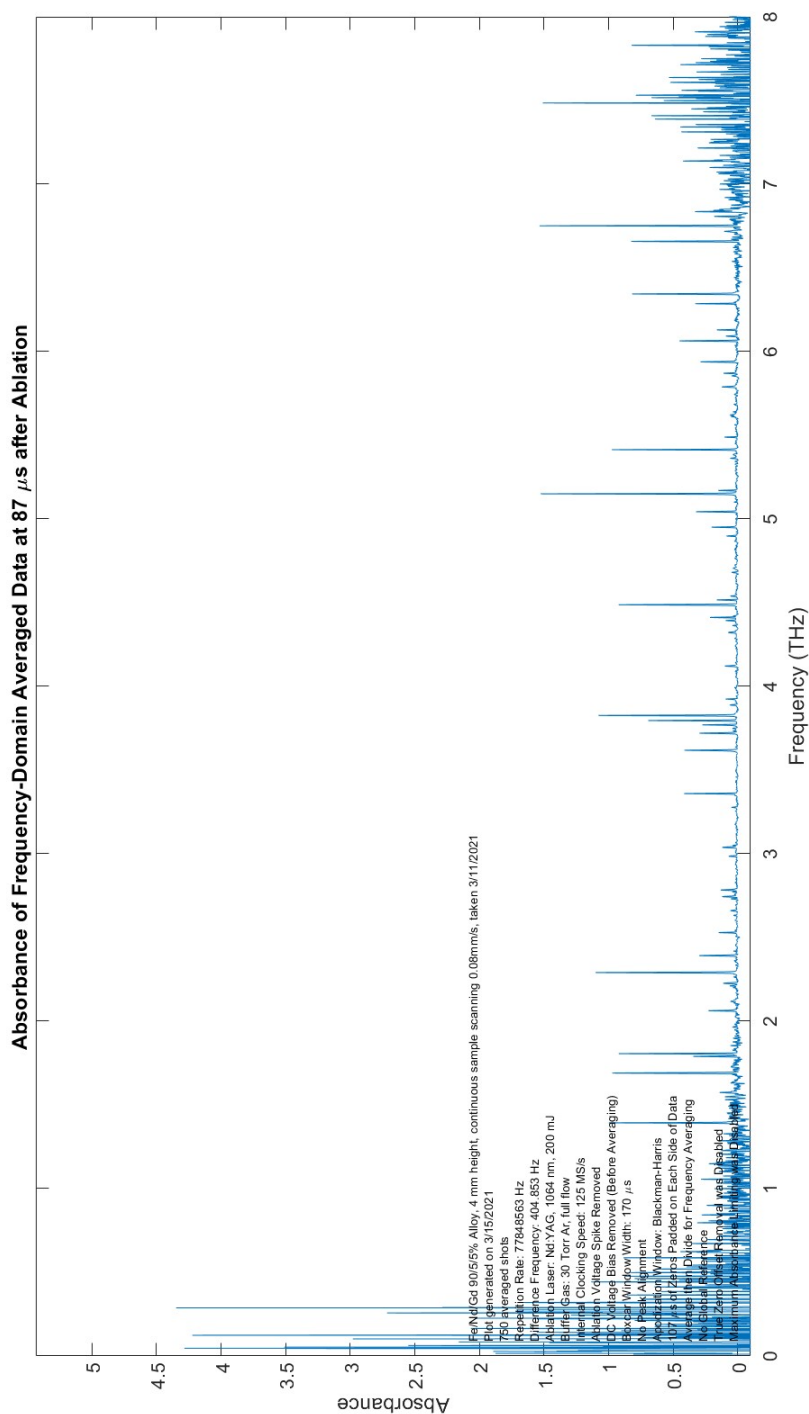


**Figure B.4:** Example absorbance function, plotted against the uncalibrated optical frequency axis. The frequency spacings are calibrated but a global offset is required for absolute calibration.

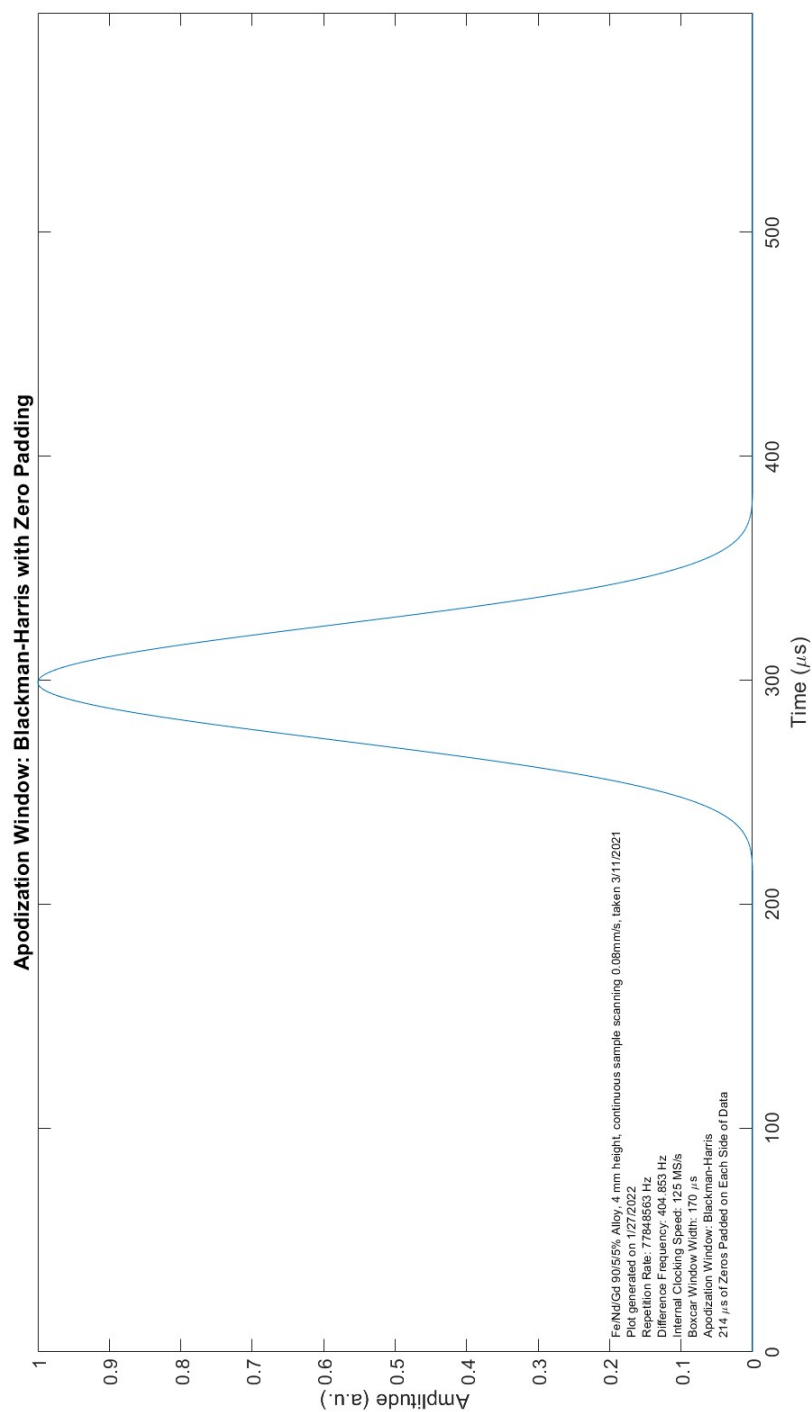


**Figure B.5:** Example Blackman-Harris apodization window with zero-padding.

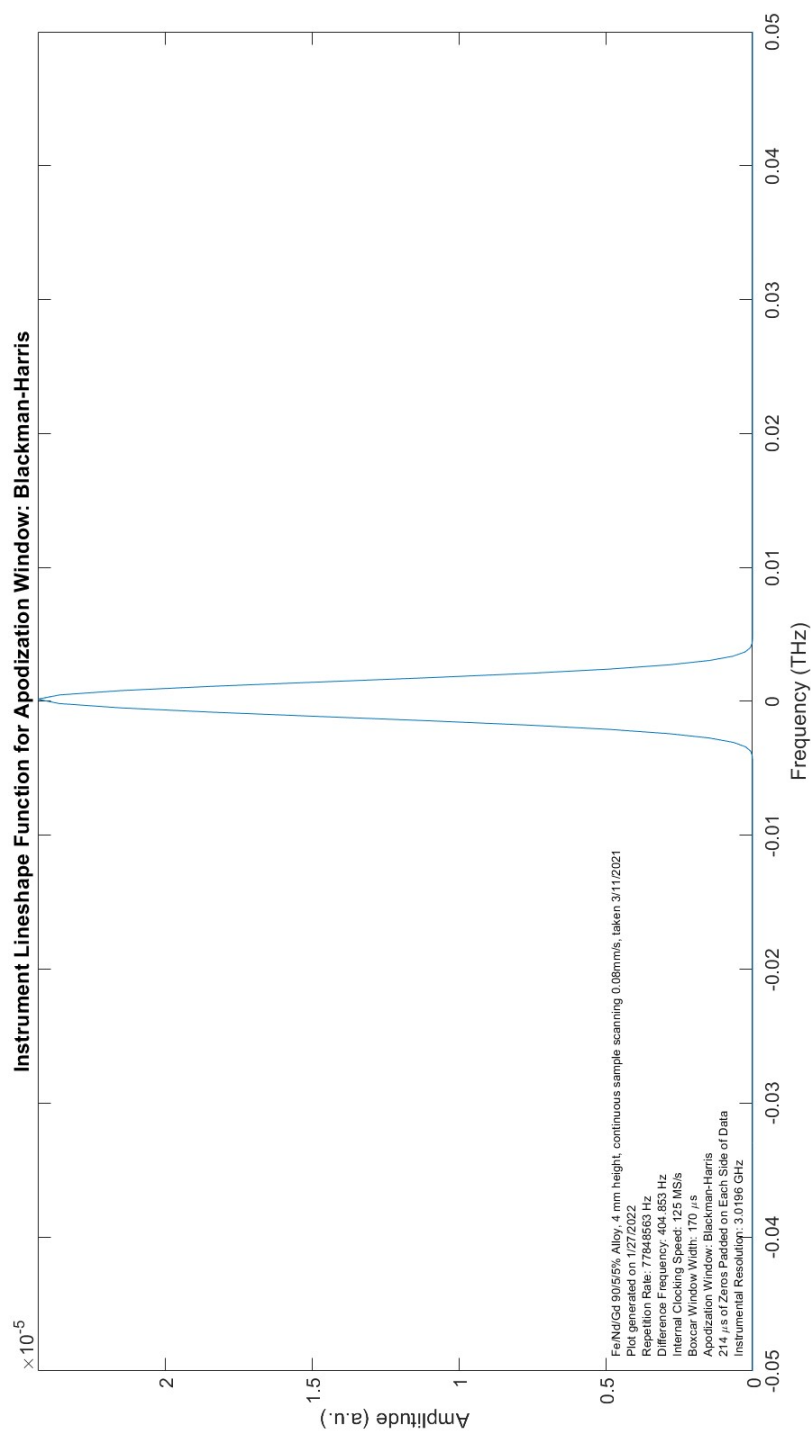


**Figure B.6:** Example ILF, which is the Fourier transform of the Blackman-Harris apodization window in Fig. B.5. Note the measured FWHM reported in the annotation, which is the instrumental resolution.

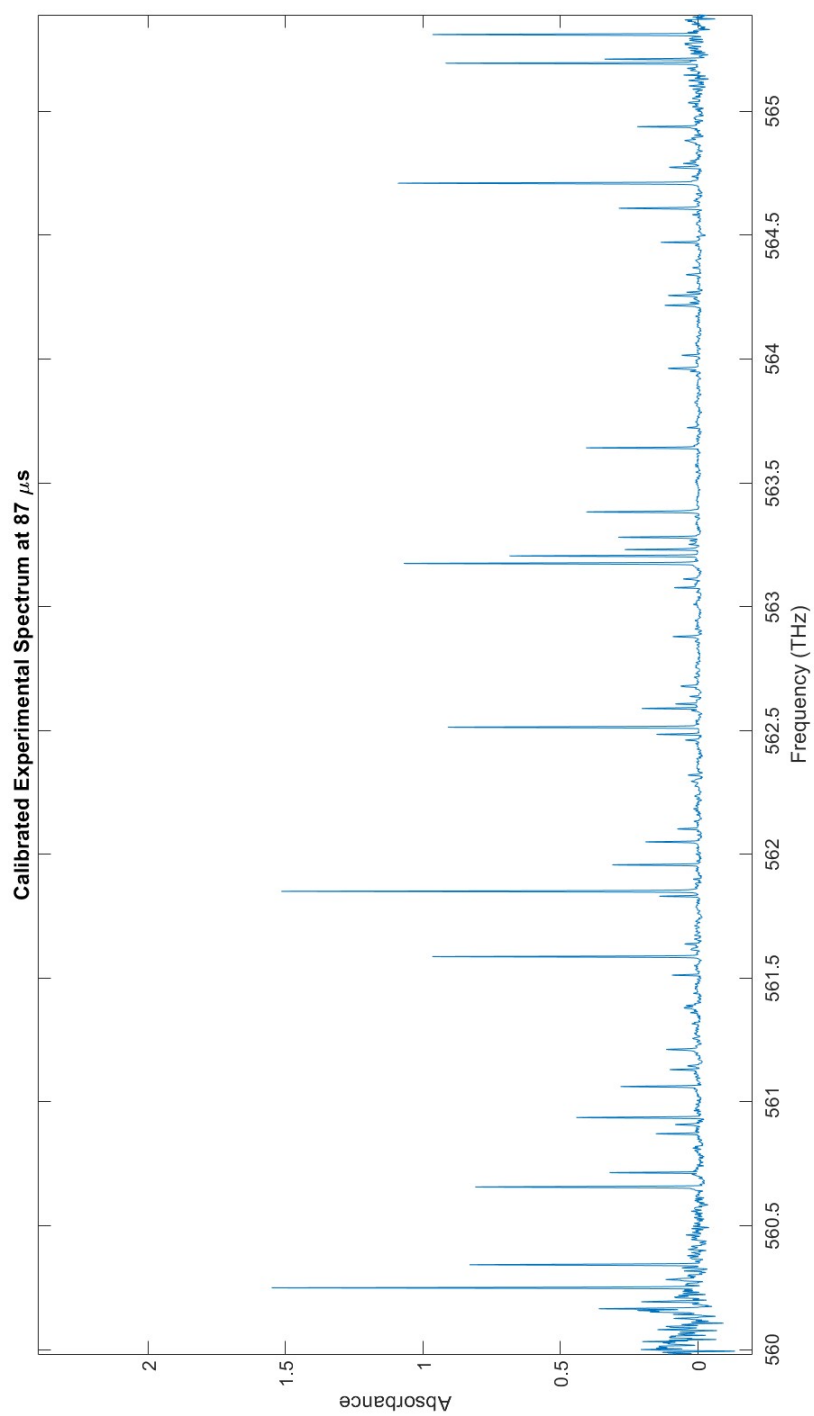


**Figure B.7:** Example absorbance function with background subtraction and absolute calibration.

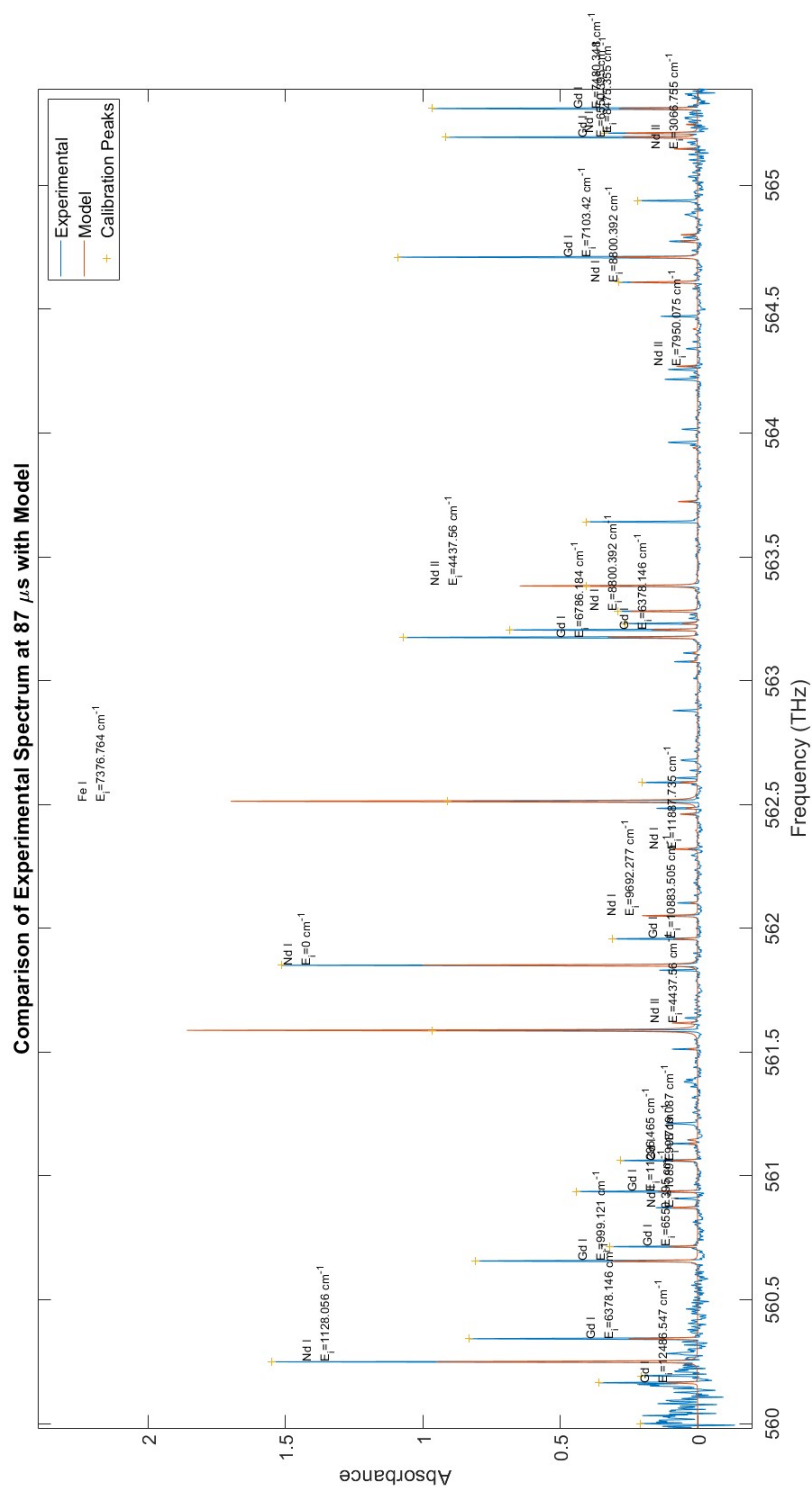


**Figure B.8:** Example calibrated absorbance overlaid with a modelled spectrum to check feature alignment.

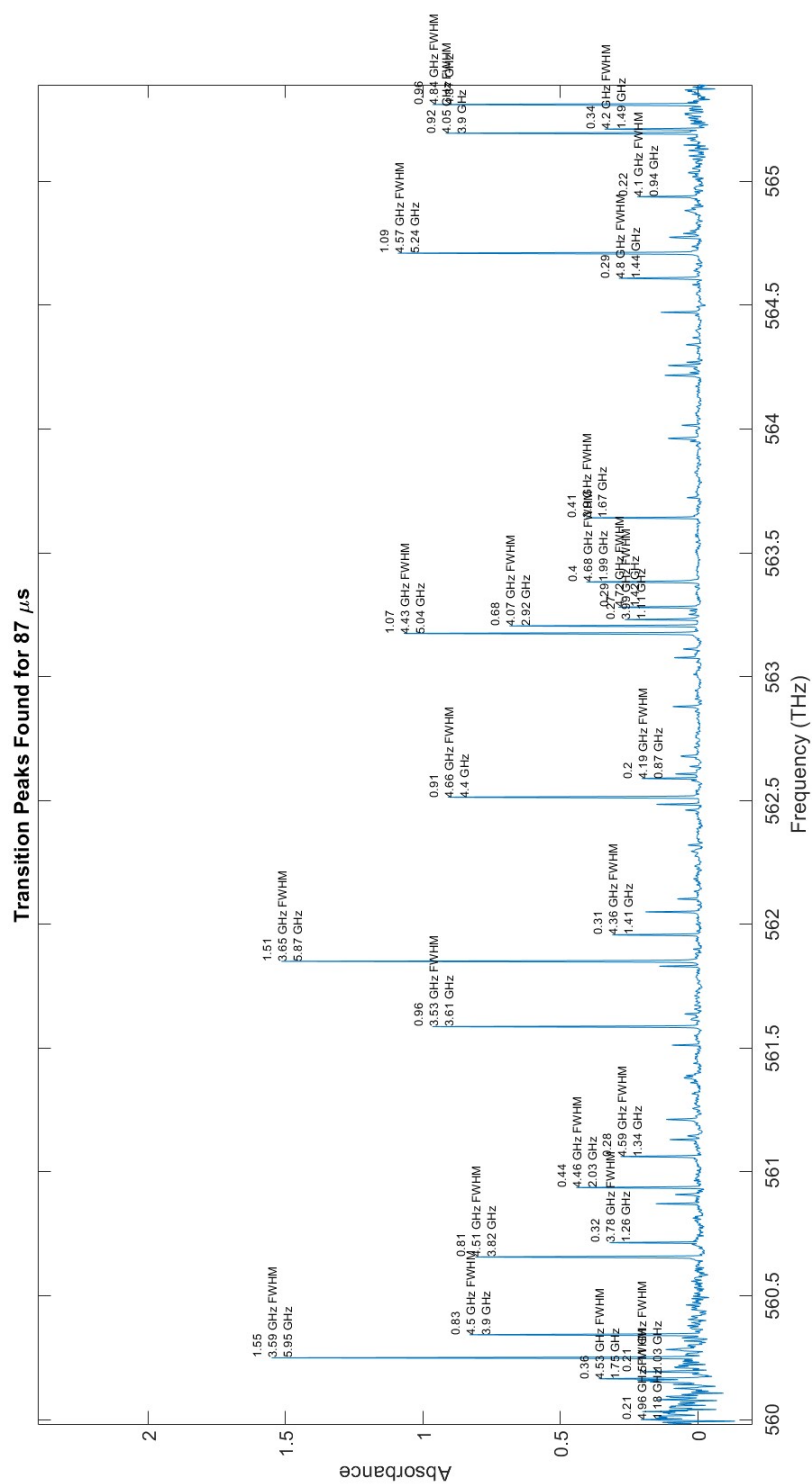


**Figure B.9:** Example calibrated absorbance function with calculated peak heights, linewidths, and integrated peak areas.

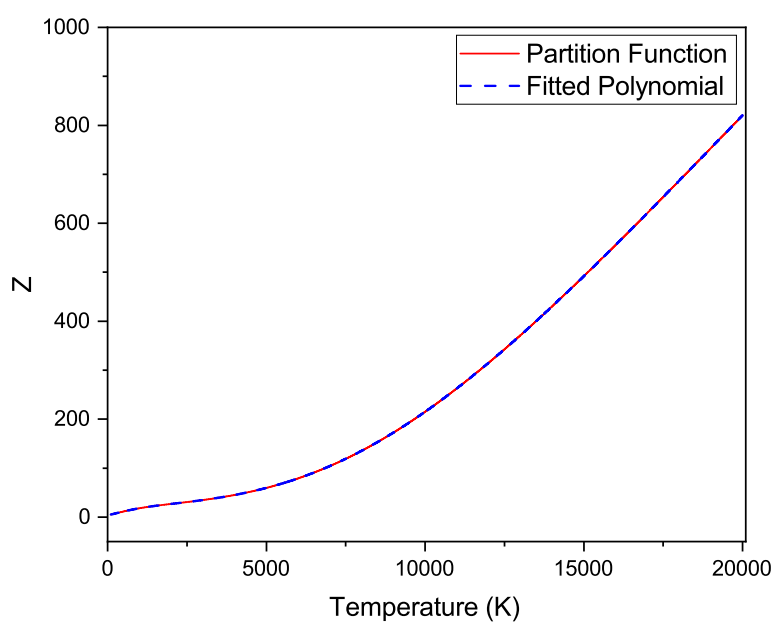


**Figure B.10:** Partition function  $Z(T)$  and the 20<sup>th</sup> degree fitted polynomial for Gd I used in the absorption spectrum calculations.

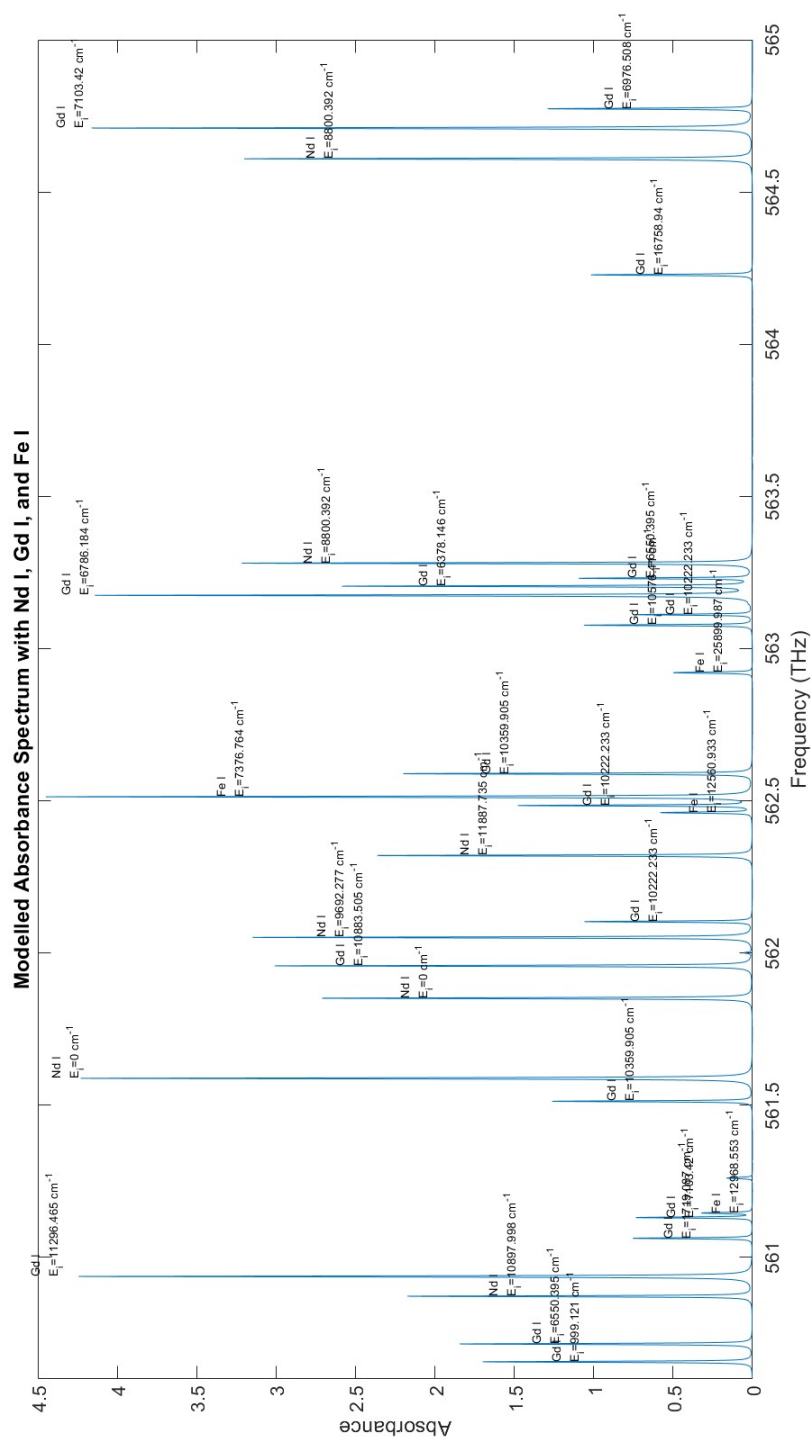


**Figure B.11:** Modelled absorption spectrum for Nd I, Gd I, and Fe I, all at 5000 K excitation temperature with total number densities of  $10^{15}$ ,  $10^{15}$ , and  $10^{16} \text{ cm}^{-3}$ , respectively. All species were modelled with Lorentzian widths (FWHM) of 2 GHz and kinetic temperatures of 5000 K. This model also included ILF broadening effect due to a  $170 \text{ } \mu\text{s}$  wide Blackman-Harris apodization window with a 3.02 GHz linewidth (FWHM).





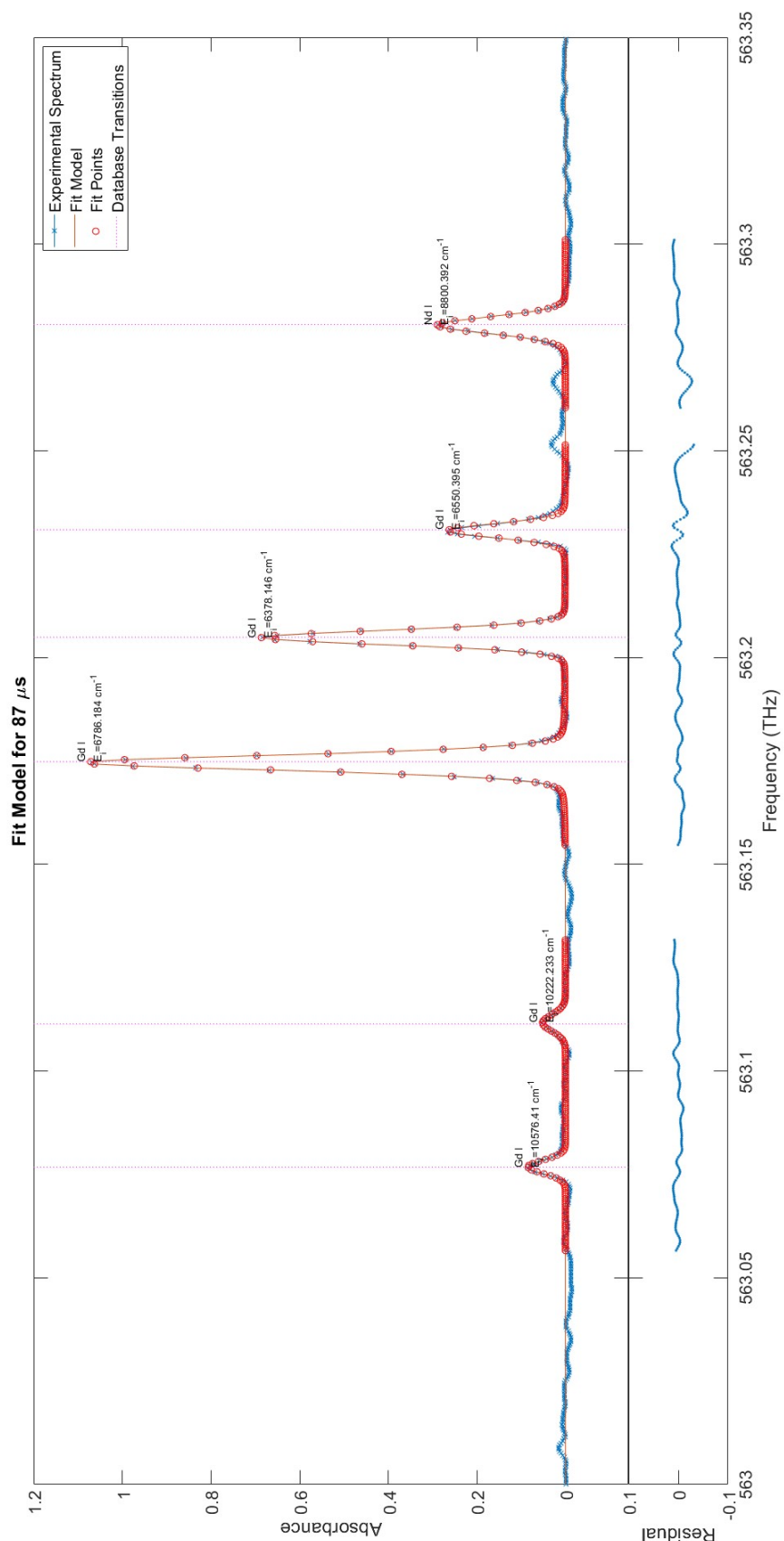


**Figure B.13:** Zoomed-in portion of Fig. B.12.

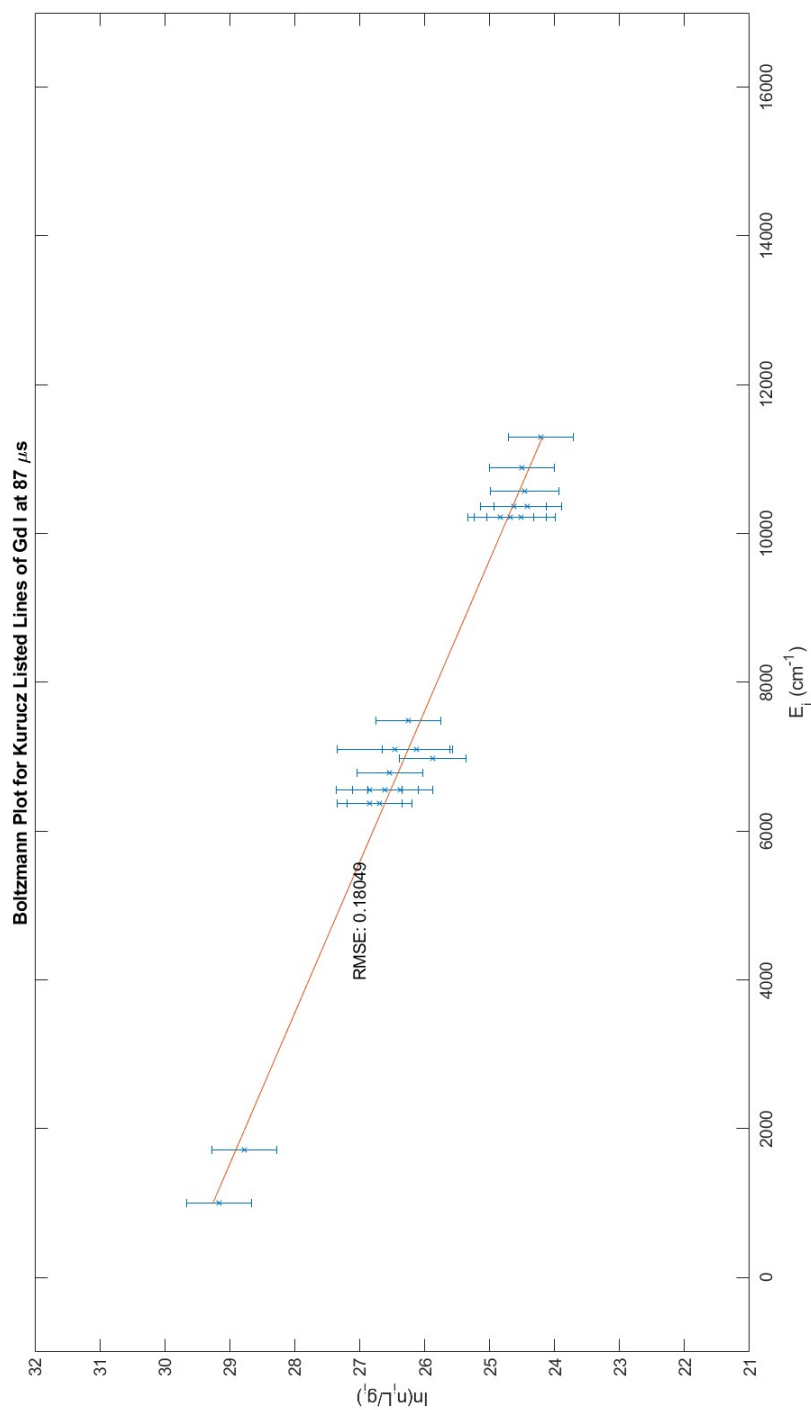


**Figure B.14:** Example plot produced by the Boltzmann-plot analysis code, showing the Boltzmann plot for 20 transitions of Gd I measured in a LPP at 87  $\mu$ s after ablation. The code generates a plot like this for each species in the analysis.

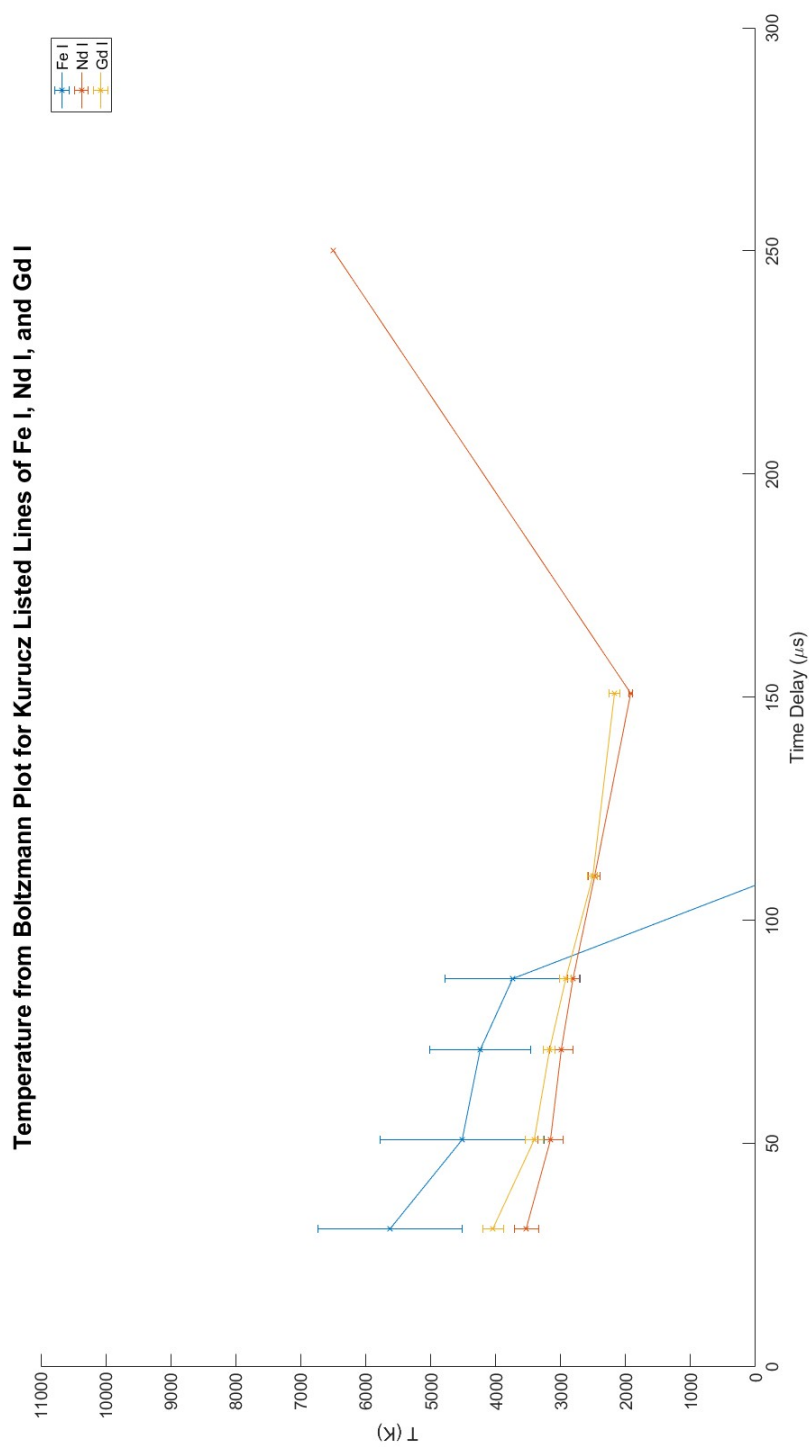


**Figure B.15:** Example plot produced by the Boltzmann-plot time-series code, showing the calculated temperatures for Fe I, Nd I, and Gd I as a function of time-delay. Note that Fe I results after 87  $\mu\text{s}$  were discarded after analysis due to having too few points for the Boltzmann fit.

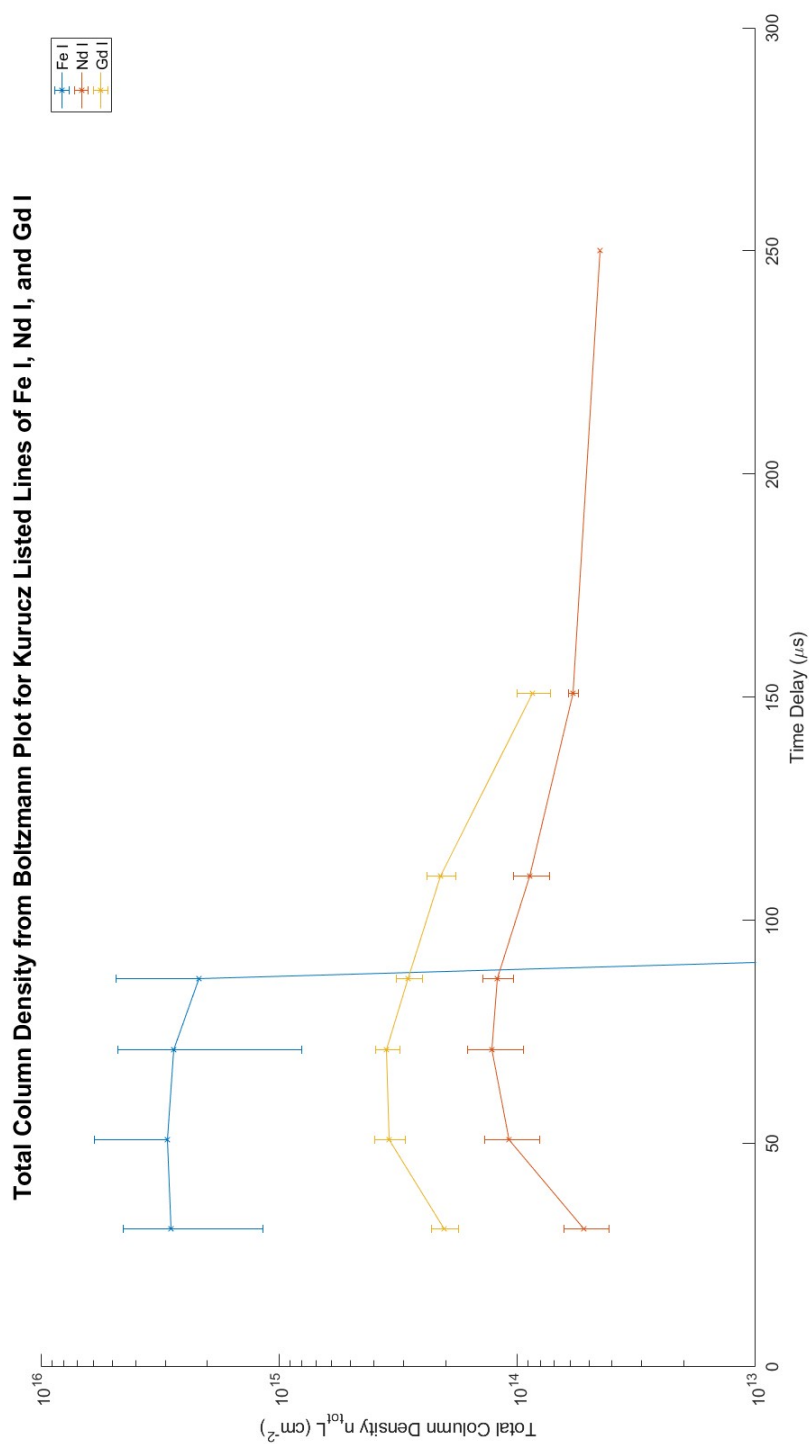


**Figure B.16:** Example plot produced by the Boltzmann-plot time-series code, showing the calculated total column-densities for Fe I, Nd I, and Gd I as a function of time-delay. Note that Fe I results after 87  $\mu\text{s}$  were discarded after analysis due to having too few points for the Boltzmann fit.

## References

- [1] Ian Coddington, Nathan Newbury, and William Swann. Dual-comb spectroscopy. *Optica*, 3(4):414–426, 2016.
- [2] Nathalie Picqué and Theodor W Hänsch. Frequency comb spectroscopy. *Nature Photonics*, 13(3):146–157, 2019.
- [3] Martin Ferus, Jakub Koukal, Libor Lenža, Jiří Srba, Petr Kubelík, Vojtěch Laitl, Ekaterina M Zanozina, Pavel Váňa, Tereza Kaiserová, Antonín Knížek, et al. Calibration-free quantitative elemental analysis of meteor plasma using reference laser-induced breakdown spectroscopy of meteorite samples. *Astronomy & Astrophysics*, 610:A73, 2018.
- [4] Surya Harikrishnan, Adarsh Ananthachar, Khoobaram S Choudhari, Sajan Daniel George, Santhosh Chidangil, and VK Unnikrishnan. Laser-induced breakdown spectroscopy (libs) for the detection of rare earth elements (rees) in meteorites. *Minerals*, 13(2):182, 2023.
- [5] Cong Li, Chun-Lei Feng, Hassan Yousefi Oderji, Guang-Nan Luo, and Hong-Bin Ding. Review of libs application in nuclear fusion technology. *Frontiers of Physics*, 11:1–16, 2016.
- [6] Demetrios Anglos. Laser-induced breakdown spectroscopy in art and archaeology. *Applied spectroscopy*, 55(6):186A–205A, 2001.
- [7] Ashwin Kumar Myakalwar, S Sreedhar, Ishan Barman, Narahara Chari Dingari, S Venugopal Rao, P Prem Kiran, Surya P Tewari, and G Manoj Kumar. Laser-induced breakdown spectroscopy-based investigation and classification of pharmaceutical tablets using multivariate chemometric analysis. *Talanta*, 87:53–59, 2011.

- [8] Marc N Fiddler, Israel Begashaw, Matthew A Mickens, Michael S Collingwood, Zerihun Assefa, and Solomon Bililign. Laser spectroscopy for atmospheric and environmental sensing. *Sensors*, 9(12):10447–10512, 2009.
- [9] SS Harilal, BE Brumfield, NL LaHaye, KC Hartig, and MC Phillips. Optical spectroscopy of laser-produced plasmas for standoff isotopic analysis. *Applied Physics Reviews*, 5(2):021301, 2018.
- [10] Mark C Phillips, Brian E Brumfield, Nicole LaHaye, Sivanandan S Harilal, Kyle C Hartig, and Igor Jovanovic. Two-dimensional fluorescence spectroscopy of uranium isotopes in femtosecond laser ablation plumes. *Scientific reports*, 7(1):3784, 2017.
- [11] Nancy J McMillan, Shannon Rees, Kristen Kochelek, and Catherine McManus. Geological applications of laser-induced breakdown spectroscopy. *Geostandards and Geo-analytical Research*, 38(3):329–343, 2014.
- [12] Gulab Singh Maurya, Alicia Marín-Roldán, Pavel Veis, Ashok Kumar Pathak, and Pratik Sen. A review of the libs analysis for the plasma-facing components diagnostics. *Journal of Nuclear Materials*, 541:152417, 2020.
- [13] Richard E Russo, XL Mao, J Yoo, and JJ Gonzalez. Laser ablation. In *Laser-induced breakdown spectroscopy*, pages 41–70. Elsevier, 2007.
- [14] Vahid Majidi and Martha R Joseph. Spectroscopic applications of laser-induced plasmas. *Critical Reviews in Analytical Chemistry*, 23(3):143–162, 1992.
- [15] Shudi Zhang, Xiaohua Wang, Miaohong He, Yunbin Jiang, Bochao Zhang, Wei Hang, and Benli Huang. Laser-induced plasma temperature. *Spectrochimica Acta Part B: Atomic Spectroscopy*, 97:13–33, 2014.
- [16] Daniel E Shelby, Sven Merk, Benjamin W Smith, Igor B Gornushkin, Ulrich Panne, and Nicolás Omenetto. Temperature evaluation by simultaneous emission and saturated fluorescence measurements: A critical theoretical and experimental appraisal of the approach. *Spectrochimica Acta Part B: Atomic Spectroscopy*, 89:50–59, 2013.

- [17] M Ribière, Loïc Méès, D Allano, and BG Chéron. Evolutions in time and space of laser ablated species by dual-laser photoabsorption spectroscopy. *Journal of Applied Physics*, 104(4):043302, 2008.
- [18] David W Hahn and Nicoló Omenetto. Laser-induced breakdown spectroscopy (libs), part i: review of basic diagnostics and plasma—particle interactions: still-challenging issues within the analytical plasma community. *Applied spectroscopy*, 64(12):335A–336A, 2010.
- [19] Carlos Aragón and Jose Antonio Aguilera. Characterization of laser induced plasmas by optical emission spectroscopy: A review of experiments and methods. *Spectrochimica Acta Part B: Atomic Spectroscopy*, 63(9):893–916, 2008.
- [20] Nicole L LaHaye, Sivanandan S Harilal, and Mark C Phillips. Early-and late-time dynamics of laser-produced plasmas by combining emission and absorption spectroscopy. *Spectrochimica Acta Part B: Atomic Spectroscopy*, 179:106096, 2021.
- [21] LA King, IB Gornushkin, D Pappas, BW Smith, and JD Winefordner. Rubidium isotope measurements in solid samples by laser ablation-laser atomic absorption spectroscopy. *Spectrochimica Acta Part B: Atomic Spectroscopy*, 54(13):1771–1781, 1999.
- [22] NR Taylor and MC Phillips. Differential laser absorption spectroscopy of uranium in an atmospheric pressure laser-induced plasma. *Optics letters*, 39(3):594–597, 2014.
- [23] Sivanandan S Harilal, Nicole L LaHaye, and Mark C Phillips. Two-dimensional fluorescence spectroscopy of laser-produced plasmas. *Optics Letters*, 41(15):3547–3550, 2016.
- [24] Jonathan Merten. Laser-ablation absorption spectroscopy: Reviewing an uncommon hyphenation. *Spectrochimica Acta Part B: Atomic Spectroscopy*, page 106358, 2022.
- [25] EW Foster. The measurement of oscillator strengths in atomic spectra. *Reports on Progress in Physics*, 27(1):469, 1964.



- [26] Sivanandan S Harilal, Elizabeth J Kautz, and Mark C Phillips. Time-resolved absorption spectroscopic characterization of ultrafast laser-produced plasmas under varying background pressures. *Physical Review E*, 103(1):013213, 2021.
- [27] Emily N Weerakkody, David G Weisz, Jonathan Crowhurst, Batikan Koroglu, Timothy Rose, Harry Radousky, Ryan L Stillwell, Jason R Jeffries, and Nick G Glumac. Time-resolved formation of uranium and silicon oxides subsequent to the laser ablation of  $u_3si_2$ . *Spectrochimica Acta Part B: Atomic Spectroscopy*, 170:105925, 2020.
- [28] Yu Zhang, Caroline Lecaplain, Reagan RD Weeks, Jeremy Yeak, Sivanandan S Harilal, Mark C Phillips, and R Jason Jones. Time-resolved dual-comb measurement of number density and temperature in a laser-induced plasma. *Optics letters*, 44(14):3458–3461, 2019.
- [29] Reagan RD Weeks, Mark C Phillips, Yu Zhang, Sivanandan S Harilal, and R Jason Jones. Measurement of neutral gadolinium oscillator strengths using dual-comb absorption spectroscopy in laser-produced plasmas. *Spectrochimica Acta Part B: Atomic Spectroscopy*, 181:106199, 2021.
- [30] Reagan RD Weeks, Yu Zhang, Sivanandan S Harilal, Mark C Phillips, and R Jason Jones. Multi-species temperature and number density analysis of a laser-produced plasma using dual-comb spectroscopy. *Journal of Applied Physics*, 131(22):223103, 2022.
- [31] Ryan T Rhoades, Reagan RD Weeks, Seth E Erickson, Caroline Lecaplain, Sivanandan S Harilal, Mark C Phillips, and R Jason Jones. Dual-comb absorption spectroscopy of molecular  $ceo$  in a laser-produced plasma. *Optics Letters*, 47(10):2502–2505, 2022.
- [32] Yu Zhang, Reagan RD Weeks, Caroline Lecaplain, Sivanandan S Harilal, Jeremy Yeak, Mark C Phillips, and R Jason Jones. Burst-mode dual-comb spectroscopy. *Optics Letters*, 46(4):860–863, 2021.
- [33] Jenna Bergevin, Tsung-Han Wu, Jeremy Yeak, Brian E Brumfield, Sivanandan S Har-

- ilal, Mark C Phillips, and R Jason Jones. Dual-comb spectroscopy of laser-induced plasmas. *Nature Communications*, 9(1):1273, 2018.
- [34] Brian R Washburn, Scott A Diddams, Nathan R Newbury, Jeffrey W Nicholson, Man F Yan, and Carsten G Jørgensen. Phase-locked, erbium-fiber-laser-based frequency comb in the near infrared. *Optics letters*, 29(3):250–252, 2004.
- [35] Peter R. Griffiths and James A. De Haseth. *Fourier transform infrared spectroscopy*. Wiley-Interscience, 2nd edition, 2007.
- [36] Changjiang Zhu and Peter R Griffiths. Extending the range of beer’s law in ft-ir spectrometry. part i: Theoretical study of norton-beer apodization functions. *Applied spectroscopy*, 52(11):1403–1408, 1998.
- [37] Takuro Ideguchi, Antonin Poisson, Guy Guelachvili, Nathalie Picqué, and Theodor W Hänsch. Adaptive real-time dual-comb spectroscopy. *Nature communications*, 5(1): 3375, 2014.
- [38] J Olson, YH Ou, A Azarm, and K Kieu. Bi-directional mode-locked thulium fiber laser as a single-cavity dual-comb source. *IEEE Photonics Technology Letters*, 30(20): 1772–1775, 2018.
- [39] Axel Ruehl, Michael J Martin, Kevin C Cossel, Lisheng Chen, Hugh McKay, Brian Thomas, Craig Benko, Liang Dong, John M Dudley, Martin E Fermann, et al. Ultrabroadband coherent supercontinuum frequency comb. *Physical Review A*, 84(1): 011806, 2011.
- [40] Nathan R Newbury, Ian Coddington, and William Swann. Sensitivity of coherent dual-comb spectroscopy. *Optics express*, 18(8):7929–7945, 2010.
- [41] DB Chase. Nonlinear detector response in ft-ir. *Applied spectroscopy*, 38(4):491–494, 1984.
- [42] Mark C Abrams, GC Toon, and RA Schindler. Practical example of the correction of fourier-transform spectra for detector nonlinearity. *Applied optics*, 33(27):6307–6314, 1994.

- [43] H Sakai, GA Vanasse, and ML Forman. Spectral recovery in fourier spectroscopy. *JOSA*, 58(1):84–90, 1968.
- [44] DB Chase. Phase correction in ft-ir. *Applied Spectroscopy*, 36(3):240–244, 1982.
- [45] Jyrki Kauppinen. Correction of the linear phase errors of one-sided interferograms. *Infrared Physics*, 16(3):359–366, 1976.
- [46] JK Shaw, Connor Fredrick, and SA Diddams. Versatile digital approach to laser frequency comb stabilization. *OSA Continuum*, 2(11):3262–3271, 2019.
- [47] J.-D. Deschênes. Digital pll code base. <https://github.com/jddes/Frequency-comb-DPLL>.
- [48] Zaijun Chen, Ming Yan, Theodor W Hänsch, and Nathalie Picqué. A phase-stable dual-comb interferometer. *Nature communications*, 9(1):3035, 2018.
- [49] Martin CE Huber and RJ Sandeman. The measurement of oscillator strengths. *Reports on Progress in Physics*, 49(4):397, 1986.
- [50] W. Demtröder. *Laser spectroscopy, Vol. 1: Basic Principles*. Springer Berlin Heidelberg, 2008. doi: 10.1007/978-3-540-73418-5.
- [51] Ove Axner, Jörgen Gustafsson, Nicolò Omenetto, and James D Winefordner. Line strengths, a-factors and absorption cross-sections for fine structure lines in multiplets and hyperfine structure components in lines in atomic spectrometry—a user’s guide. *Spectrochimica Acta Part B: Atomic Spectroscopy*, 59(1):1–39, 2004.
- [52] J. Reader A. Kramida, Yu. Ralchenko and NIST ASD Team (2019). Nist atomic spectra database (version 5.7.1). <https://physics.nist.gov/asd>.
- [53] A Hibbert. Atomic structure theory. *Progress in Atomic Spectroscopy: Part A*, pages 1–69, 1978.
- [54] Gediminas Gaigalas, Daiji Kato, Pavel Rynkun, Laima Radžiūtė, and Masaomi Tanaka. Extended calculations of energy levels and transition rates of nd ii-iv ions

- for application to neutron star mergers. *The Astrophysical Journal Supplement Series*, 240(2):29, 2019.
- [55] James E Lawler, Christopher Sneden, John J Cowan, Inese I Ivans, and EA Den Hartog. Improved laboratory transition probabilities for ce ii, application to the cerium abundances of the sun and five r-process-rich, metal-poor stars, and rare earth lab data summary. *The Astrophysical Journal Supplement Series*, 182(1):51, 2009.
- [56] Christopher Sneden, James E Lawler, John J Cowan, Inese I Ivans, and Elizabeth A Den Hartog. New rare earth element abundance distributions for the sun and five r-process-rich very metal-poor stars. *The Astrophysical Journal Supplement Series*, 182(1):80, 2009.
- [57] Zoltán Bacsik, János Mink, and Gábor Keresztury. Ftir spectroscopy of the atmosphere part 2. applications. *Applied Spectroscopy Reviews*, 40(4):327–390, 2005.
- [58] Mark C Phillips, Bruce E Bernacki, Sivanandan S Harilal, Brian E Brumfield, Joel M Schwallier, and Nick G Glumac. Characterization of high-explosive detonations using broadband infrared external cavity quantum cascade laser absorption spectroscopy. *Journal of Applied Physics*, 126(9):093102, 2019.
- [59] Christopher S Goldenstein, R Mitchell Spearrin, Jay B Jeffries, and Ronald K Hanson. Infrared laser-absorption sensing for combustion gases. *Progress in Energy and Combustion Science*, 60:132–176, 2017.
- [60] Christopher Murzyn, Adam Sims, and Nick Glumac. Diode laser monitoring of atomic iodine in explosive fireballs. *Measurement Science and Technology*, 30(11):115501, 2019.
- [61] P Campbell, ID Moore, and MR Pearson. Laser spectroscopy for nuclear structure physics. *Progress in Particle and Nuclear Physics*, 86:127–180, 2016.
- [62] Batikan Koroglu, Zurong Dai, Mikhail Finko, Michael R Armstrong, Jonathan C Crowhurst, Davide Curreli, David G Weisz, Harry B Radousky, Kim B Knight, and

- Timothy P Rose. Experimental investigation of uranium volatility during vapor condensation. *Analytical chemistry*, 92(9):6437–6445, 2020.
- [63] Mikhail S Finko and Davide Curreli. Simulation of uranium plasma plume dynamics in atmospheric oxygen produced via femtosecond laser ablation. *Physics of Plasmas*, 25(8):083112, 2018.
- [64] Masabumi Miyabe, Ikuo Wakaida, and Takashi Arisawa. Measurement of radiative lifetime and branching ratio of gd i using three-step resonance ionization spectroscopy. *Zeitschrift für Physik D Atoms, Molecules and Clusters*, 39:181–187, 1997.
- [65] EA Den Hartog, KA Bilty, and JE Lawler. Radiative lifetimes of neutral gadolinium. *Journal of Physics B: Atomic, Molecular and Optical Physics*, 44(5):055001, 2011.
- [66] Qian Wang, Jianrui Yin, Liyun Jiang, Xue Shang, Yanshan Tian, and Zhenwen Dai. Experimental branching fractions, transition probabilities and oscillator strengths in gd i and gd ii. *Journal of Physics B: Atomic, Molecular and Optical Physics*, 47(3):035003, 2014.
- [67] JE Lawler, KA Bilty, and EA Den Hartog. Atomic transition probabilities of gd i. *Journal of Physics B: Atomic, Molecular and Optical Physics*, 44(9):095001, 2011.
- [68] EA Den Hartog, JE Lawler, C Sneden, and JJ Cowan. Improved laboratory transition probabilities for gd ii and application to the gadolinium abundances of the sun and three r-process rich, metal-poor stars. *The Astrophysical Journal Supplement Series*, 167(2):292, 2006.
- [69] Carl Martin Sikström, Hampus Nilsson, Ulf Litzén, Anders Blom, and Hans Lundberg. Uncertainty of oscillator strengths derived from lifetimes and branching fractions. *Journal of Quantitative Spectroscopy and Radiative Transfer*, 74(3):355–368, 2002.
- [70] Jose Antonio Aguilera and Carlos Aragón. Characterization of a laser-induced plasma by spatially resolved spectroscopy of neutral atom and ion emissions.: Comparison of local and spatially integrated measurements. *Spectrochimica Acta Part B: Atomic Spectroscopy*, 59(12):1861–1876, 2004.

- [71] R Mayo-Garcia, C Aragon, JA Aguilera, and M Ortiz. Measured oscillator strengths in singly ionized molybdenum. *Journal of Physics B: Atomic, Molecular and Optical Physics*, 48(21):215002, 2015.
- [72] C Aragon, JA Aguilera, M Ortiz, and R Mayo-Garcia. Experimental oscillator strengths of highly excited levels of mo ii. *Journal of Physics B: Atomic, Molecular and Optical Physics*, 49(10):105003, 2016.
- [73] J Manrique, JA Aguilera, and C Aragón. Determination of transition probabilities by laser-induced breakdown spectroscopy with curve-of-growth measurements. *Journal of Quantitative Spectroscopy and Radiative Transfer*, 112(1):85–91, 2011.
- [74] WF Meggers, Ch H Corliss, and BF Scribner. Nbs monograph 145. *US Gov. Print. Off., Washington, DC*, 1975.
- [75] Peter L. Smith, Claas Heise, Jim R. Esmond, and Robert L. Kurucz. Atomic spectral line database from CD-ROM 23 of R. L. Kurucz. <https://www.cfa.harvard.edu/amp/ampdata/kurucz23/sekur.html>.
- [76] Charles R Cowley. The use of precision oscillator strengths as a means for obtaining large numbers of moderately accurate gf-values. *Monthly Notices of the Royal Astronomical Society*, 202(2):417–425, 1983.
- [77] BL Wexler, BE Wilcomb, and N Djeu.  $6\ 1\ s\ 0-6\ 3\ p\ 0$  transition in 199 hg: Determination of the  $a$  coefficient and self-pressure broadening. *JOSA*, 70(7):863–865, 1980.
- [78] Chou-Mou Huang and Charles C Wang. Oscillator strength for principal series transitions to the high rydberg states of potassium. *Physical Review Letters*, 46(18):1195, 1981.
- [79] DE Blackwell and BS Collins. Precision measurement of relative oscillator strengths—i fundamental technique: A first application to mn i. *Monthly Notices of the Royal Astronomical Society*, 157(3):255–271, 1972.

- [80] G Smith. Oscillator strengths for neutral calcium lines of 2.9 eV excitation. *Journal of Physics B: Atomic, Molecular and Optical Physics*, 21(16):2827, 1988.
- [81] DE Blackwell, PA Ibbetson, AD Petford, and MJ Shallis. Precision measurement of relative oscillator strengths—iv. attainment of 0.5 per cent accuracy. Fe I transitions from levels a 5 d 0–4 (0.00–0.12 eV). *Monthly Notices of the Royal Astronomical Society*, 186(3):633–650, 1979.
- [82] DM Lucas, DN Stacey, CD Thompson, and RB Warrington. High-precision relative oscillator strength measurements in Sm I by absorption spectroscopy. *Physica Scripta*, 1997(T70):145, 1997.
- [83] EC Jung, Kwang-Hoon Ko, SP Rho, C Lim, and Cheol-Jung Kim. Measurement of the populations of metastable levels in gadolinium vapor by diode laser-based UV and near-IR absorption spectroscopy. *Optics communications*, 212(4-6):293–300, 2002.
- [84] Sabrina Messaoud Aberkane, Ali Safi, Asia Botto, Beatrice Campanella, Stefano Legnaioli, Francesco Poggialini, Simona Raneri, Fatemeh Rezaei, and Vincenzo Palleschi. Laser-induced breakdown spectroscopy for determination of spectral fundamental parameters. *Applied Sciences*, 10(14):4973, 2020.
- [85] AM El Sherbini, H Hegazy, and Th M El Sherbini. Measurement of electron density utilizing the  $\text{H}\alpha$ -line from laser produced plasma in air. *Spectrochimica Acta Part B: Atomic Spectroscopy*, 61(5):532–539, 2006.
- [86] C Aragón and JA Aguilera. Csigma graphs: A new approach for plasma characterization in laser-induced breakdown spectroscopy. *Journal of Quantitative Spectroscopy and Radiative Transfer*, 149:90–102, 2014.
- [87] C Aragón and JA Aguilera. Quantitative analysis by laser-induced breakdown spectroscopy based on generalized curves of growth. *Spectrochimica Acta Part B: Atomic Spectroscopy*, 110:124–133, 2015.
- [88] Ali Safi, S Hassan Tavassoli, Gabriele Cristoforetti, Elisabetta Tognoni, Beatrice Campanella, Stefano Legnaioli, Stefano Pagnotta, Francesco Poggialini, and Vincenzo

- Palleschi. Exploiting self-absorption for plasma characterization in laser-induced breakdown spectroscopy experiments: a comparison of two recent approaches. *Analytical chemistry*, 91(13):8595–8601, 2019.
- [89] I Coddington, WC Swann, and NR Newbury. Coherent dual-comb spectroscopy at high signal-to-noise ratio. *Physical Review A*, 82(4):043817, 2010.
- [90] TP Duffey, TG McNeela, T Yamamoto, J Mazumder, and AL Schawlow. Absorption spectroscopic measurements of plume density and temperature in production of nanocrystalline nba 3 by laser ablation deposition. *Physical Review B*, 51(20):14652, 1995.
- [91] M Szynarowska and R Papa. Measurement of the absolute oscillator strength of the spectral line  $\lambda = 451.966$  nm of gadolinium. *Physica Scripta*, 25(3):485, 1982.
- [92] VA Komarovskii and Yu M Smirnov. Experimental study of transition probabilities of the gadolinium atom. *Optics and spectroscopy*, 73(5):507–510, 1992.
- [93] Akihiko Nishimura, Hironori Ohba, Koichi Ogura, and Takemasa Shibata. Measurement of the absolute oscillator strengths of gadolinium using an atomic vapor produced by electron beam heating. *Optics communications*, 110(5-6):561–564, 1994.
- [94] Eung Chang Jung, Kwang-Hoon Ko, Taek-Soo Kim, and Duck-Hee Kwon. Real-time measurement of the population densities in gd atomic vapor using diode laser absorption spectroscopy at 394.554 nm. *Japanese journal of applied physics*, 43(2R):822, 2004.
- [95] Christopher A Haynam, Brian J Comaskey, John Conway, Jon Eggert, Joseph Glaser, Edmund W Ng, Jeffrey A Paisner, Richard W Solarz, and Earl F Worden. Gadolinium enrichment technology at lawrence livermore national laboratory. In *Laser Isotope Separation*, volume 1859, pages 24–36. SPIE, 1993.
- [96] BK Ankush and MN Deo. Fourier transform high-resolution spectroscopic studies of gd i: Optical isotope shifts in the spectral region of 18 700–20 200  $\text{cm}^{-1}$ . *Physica Scripta*, 81(5):055301, 2010.



- [97] JA Aguilera and C Aragón. Apparent excitation temperature in laser-induced plasmas. In *Journal of Physics: Conference Series*, volume 59, page 210. IOP Publishing, 2007.
- [98] Kemal E Eseller, F-Y Yueh, and Jagdish P Singh. Non-intrusive, on-line, simultaneous multi-species impurity monitoring in hydrogen using libs. *Applied Physics B*, 102:963–969, 2011.
- [99] AH El-Astal, Thomas Morrow, WG Graham, and D George Walmsley. The role of gas-phase oxidation and combination during laser deposition of  $\text{YBa}_2\text{Cu}_3\text{O}_{7-x}$  in ambient oxygen. *Superconductor Science and Technology*, 8(7):529, 1995.
- [100] Emily N Weerakkody and Nick G Glumac. Quantitative absorption spectroscopy of laser-produced plasmas. *Journal of Physics D: Applied Physics*, 54(12):125201, 2021.
- [101] Gabriele Cristoforetti, Alessandro De Giacomo, M Dell’Aglio, Stefano Legnaioli, Elisabetta Tognoni, Vincenzo Palleschi, and Nicolo Omenetto. Local thermodynamic equilibrium in laser-induced breakdown spectroscopy: beyond the mcwhirter criterion. *Spectrochimica Acta Part B: Atomic Spectroscopy*, 65(1):86–95, 2010.
- [102] SA Ahmad and GD Saksena. Isotope shifts in energy levels of the neutral neodymium atom. *Spectrochimica Acta Part B: Atomic Spectroscopy*, 35(2):81–92, 1980.
- [103] Sivanandan S Harilal, Elizabeth J Kautz, and Mark C Phillips. Spatiotemporal evolution of emission and absorption signatures in a laser-produced plasma. *Journal of Applied Physics*, 131(6):063101, 2022.
- [104] SS Harilal, BE Brumfield, and MC Phillips. An evaluation of equilibrium conditions and temperature-dependent speciation in a laser-produced air plasma. *Physics of Plasmas*, 25(8):083303, 2018.
- [105] Bret C Windom and David W Hahn. Laser ablation—laser induced breakdown spectroscopy (la-libs): A means for overcoming matrix effects leading to improved analyte response. *Journal of Analytical Atomic Spectrometry*, 24(12):1665–1675, 2009.

- [106] Beatriz Fernández, Fanny Claverie, Christophe Pécheyran, and Olivier FX Donard. Direct analysis of solid samples by fs-la-icp-ms. *TrAC Trends in Analytical Chemistry*, 26(10):951–966, 2007.
- [107] JA Aguilera, C Aragón, V Madurga, and J Manrique. Study of matrix effects in laser induced breakdown spectroscopy on metallic samples using plasma characterization by emission spectroscopy. *Spectrochimica Acta Part B: Atomic Spectroscopy*, 64(10):993–998, 2009.
- [108] Jonathan Merten and Bruce Johnson. Massing a laser-induced plasma with atomic absorption spectroscopy. *Spectrochimica Acta Part B: Atomic Spectroscopy*, 149:124–131, 2018.
- [109] Sivanandan S Harilal, Brian E Brumfield, Bret D Cannon, and Mark C Phillips. Shock wave mediated plume chemistry for molecular formation in laser ablation plasmas. *Analytical chemistry*, 88(4):2296–2302, 2016.
- [110] Patrick J Skrodzki, Milos Burger, I Jovanovic, Mark C Phillips, Jeremy Yeak, Brian E Brumfield, and Sivanandan S Harilal. Plume dynamics and gas-phase molecular formation in transient laser-produced uranium plasmas. *Physics of Plasmas*, 26(8):083508, 2019.
- [111] Sivanandan S Harilal, Elizabeth J Kautz, Bruce E Bernacki, Mark C Phillips, Patrick J Skrodzki, Milos Burger, and I Jovanovic. Physical conditions for uo formation in laser-produced uranium plumes. *Physical Chemistry Chemical Physics*, 21(29):16161–16169, 2019.
- [112] Igor Rahinov, Alexey Fomin, Marina Poliak, and Sergey Cheskis. Absorption electronic spectrum of gaseous feo: in situ detection with intracavity laser absorption spectroscopy in a nanoparticle-generating flame reactor. *Applied Physics B*, 117:317–323, 2014.
- [113] Yu Gong, Mingfei Zhou, and Lester Andrews. Spectroscopic and theoretical studies of

- transition metal oxides and dioxygen complexes. *Chemical reviews*, 109(12):6765–6808, 2009.
- [114] LA Kaledin, EA Shenyavskaya, and I Kovacs. Electronic spectrum of ndo. *Acta Physica Hungarica*, 54(1-2):189–212, 1983.
- [115] P Carette, A Hocquet, M Douay, and B Pinchemel. Laser-induced fluorescence of gdo. *Journal of Molecular Spectroscopy*, 124(2):243–271, 1987.
- [116] JE Lawler, J Chisholm, DE Nitz, MP Wood, J Sobeck, and EA Den Hartog. Atomic transition probabilities of ce i from fourier transform spectra. *Journal of Physics B: Atomic, Molecular and Optical Physics*, 43(8):085701, 2010.
- [117] David E Nitz, John J Curry, M Buuck, A DeMann, N Mitchell, and W Shull. Transition probabilities of ce i obtained from boltzmann analysis of visible and near-infrared emission spectra. *Journal of Physics B: Atomic, Molecular and Optical Physics*, 51(4):045007, 2018.
- [118] William W Watson. Spectra of the monoxides of cerium and praseodymium. *Physical Review*, 53(8):639, 1938.
- [119] LL Ames and RF Barrow. Rotational analysis of absorption bands of ceo. *Proceedings of the Physical Society*, 90(3):869, 1967.
- [120] RF Barrow, RM Clements, SM Harris, and PP Jenson. The electronic spectrum of gaseous ceo. *The Astrophysical Journal*, 229:439–447, 1979.
- [121] C Linton, M Dulick, RW Field, P Carette, PC Leyland, and RF Barrow. Electronic states of the ceo molecule: Absorption, emission, and laser spectroscopy. *Journal of Molecular Spectroscopy*, 102(2):441–497, 1983.
- [122] Leonid A Kaledin, JE McCord, and Michael C Heaven. Laser spectroscopy of ceo: characterization and assignment of states in the 0-3 ev range. *Journal of Molecular Spectroscopy*, 158(1):40–61, 1993.

- [123] RL DeKock and W Weltner. Spectroscopy of rare earth oxide molecules in inert matrices at 4 degrees k. *Journal of Physical Chemistry*, 75(4):514, 1971.
- [124] VN Gorshkov, VA Komarovskii, AL Osherovich, and NP Penkin. Lifetimes of excited levels of nd i and nd ii-oscillator strengths of the spectral lines of nd i. *Astrophysics*, 17(4):799–806, 1982.
- [125] David W Hahn and Nicolás Omenetto. Laser-induced breakdown spectroscopy (libs), part ii: review of instrumental and methodological approaches to material analysis and applications to different fields. *Applied spectroscopy*, 66(4):347–419, 2012.
- [126] JA Aguilera and C Aragón. Characterization of laser-induced plasmas by emission spectroscopy with curve-of-growth measurements. part i: Temporal evolution of plasma parameters and self-absorption. *Spectrochimica Acta Part B: Atomic Spectroscopy*, 63(7):784–792, 2008.
- [127] R Jason Jones, Kevin D Moll, Michael J Thorpe, and Jun Ye. Phase-coherent frequency combs in the vacuum ultraviolet via high-harmonic generation inside a femtosecond enhancement cavity. *Physical Review Letters*, 94(19):193201, 2005.
- [128] Flavio C Cruz, Daniel L Maser, Todd Johnson, Gabriel Ycas, Andrew Klose, Fabrizio R Giorgetta, Ian Coddington, and Scott A Diddams. Mid-infrared optical frequency combs based on difference frequency generation for molecular spectroscopy. *Optics express*, 23(20):26814–26824, 2015.
- [129] Daniel A Steck. Rubidium 87 d line data. 2001.
- [130] Daniel A Steck. Rubidium 85 d line data. 2008.
- [131] Akiko Nishiyama, Satoru Yoshida, Yoshiaki Nakajima, Hiroyuki Sasada, Ken’ichi Nakagawa, Atsushi Onae, and Kaoru Minoshima. Doppler-free dual-comb spectroscopy of rb using optical-optical double resonance technique. *Optics Express*, 24(22):25894–25904, 2016.

- [132] MV Romalis, E Miron, and GD Cates. Pressure broadening of  $rd\ 1$  and  $d\ 2$  lines by  $3\ he$ ,  $4\ he$ ,  $n\ 2$ , and  $xe$ : Line cores and near wings. *Physical Review A*, 56(6):4569, 1997.
- [133] Sanjar Abrarov. The voigt/complex error function (second version). <https://www.mathworks.com/matlabcentral/fileexchange/47801-the-voigt-complex-error-function-second-version>, 2016. MATLAB Central File Exchange. Accessed June 30, 2020.